國 立 交 通 大 學

機 械 工 程 學 系

博士論文

卤化物非線性光學晶體合成與光學特性探討

Synthesis and Characterization of Nonlinear Optical Halide

Crystals

研 究 生：林志光

指導教授：周長彬
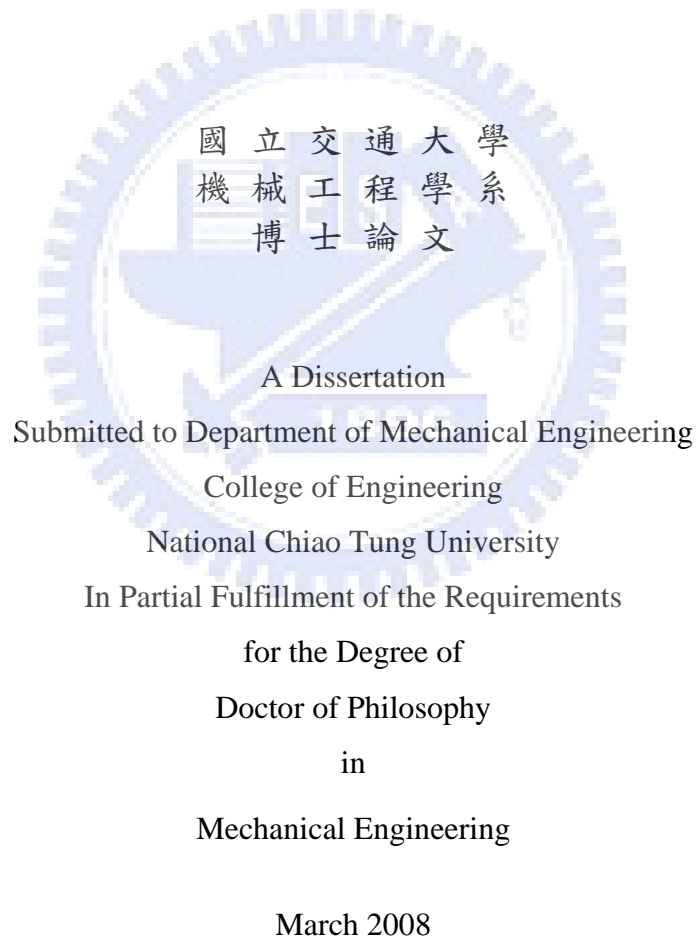
中 華 民 國 九 十 七 年 三 月

鹵化物非線性光學晶體合成與光學特性探討

Synthesis and Characterization of Nonlinear Optical Halide Crystals

研 究 生：林志光　　　　　　　Student：Zhi-Guang Lin

指導教授：周長彬　　　　　　　Advisor：Chang-Pin Chou

國 立 交 通 大 學
機 械 工 程 學 系
博 士 論 文

A Dissertation
Submitted to Department of Mechanical Engineering
College of Engineering
National Chiao Tung University
In Partial Fulfillment of the Requirements
for the Degree of
Doctor of Philosophy
in
Mechanical Engineering

March 2008

Hsinchu, Taiwan, Republic of China

中華民國九十七年三月

中文摘要

　　本論文係採用化學合成法來成長光學非線性$AGeX_3$ (A = Rb, Cs; X = Cl, Br)晶體，並藉由電子微探儀(EPMA)量測晶體成分比例、微差掃描熱卡計(DSC)量測晶體相變溫度、粉末X光繞射儀(PXRD)量測晶體結構、拉曼散射光譜儀(Raman)量測晶體振動型態、傅立葉紅外線光譜儀(FTIR)量測晶體可穿透範圍、紫外光可見光光譜儀(UV-visible)量測晶體能隙、光激發螢光光譜儀(PL)量測晶體發光特性、粉末二倍頻(PSHG)量測晶體非線性係數、橢圓儀(ellipsometry)量測晶體折射係數。由成分分析結果顯示，陰陽離子置換比例如同預期；且熱分析結果顯示，晶體的居禮轉換溫度及熔點皆會隨著溴原子含量的增加而提高，顯示所合成的$AGeX_3$晶體皆以固溶體型態存在。從X光繞射結果得知，$CsGe(Br_xCl_{1-x})_3$晶體結構會隨著溴原子含量的增加而歪斜扭曲；但$(Rb_zCs_{1-z})GeBr_3$晶體結構則是隨著銣原子含量的增加而朝正方對稱結構變化。由拉曼散射光譜儀分析顯示，晶體的拉曼訊號會隨著溴原子含量的增加而有紅位移的現象產生。而光激發螢光光譜分析顯示，晶體的光激發光訊號會隨著晶體使用環境溫度的降低而有紅位移的現象產生。紫外光可見光光譜儀分析顯示，陰離子取代的比例能調變晶體能隙值的大小。而傅立葉紅外線光譜儀分析顯示，晶體的穿透範圍會隨著溴原子含量的增加而擴大。由粉末二倍頻檢測結果得知，晶體的二階非線性係數會隨著溴原子含量的增加而變大，但會隨著銣原子含量的增加而變小。

Abstract

In this thesis, we grow the NLO crystals by chemical synthesis. Most studies have examined the structural, linear optical and nonlinear optical properties of the $AGeX_3$ (A = Rb, Cs; X = Cl, Br) crystals by varying the alloy composition to satisfy the demands of specific applications.

In the analysis of EPMA, bromine replaced chlorine in $CsGeCl_3$, and vice versa in $CsGeBr_3$ while cesium was substituted by rubidium in $CsGeBr_3$. According to DSC analysis, the Curie temperature and the melting temperature of the crystals rose with Br content.

The XRD analysis indicated that the structural distortion of $CsGe(Br_xCl_{1-x})_3$ (R3m) increases with Br content, while the structure of $(Rb_zCs_{1-z})GeBr_3$ slowly becomes centro-symmetric as Rb content increases. The results of Raman spectroscopy agree with the expectation based on effective-mass that the oscillation frequency increases as the Br content falls because Br is heavier than Cl. The atomic vibration modes of $AGeX_3$ (A = Rb, Cs; X = Cl, Br) system were also defined herein.

Regarding transparency characteristics, the longest infrared transparency wavelength is typically limited by the phonon absorption of the crystal and the absorption edge is limited by the energy band-gap of the crystal. UV-visible spectra show that the absorption edge declines from 3.43 to 2.38 eV with the composition of bromine (x = 0 to 1), but remains constant for z = 0 to 3/4. The infrared phonon absorption edge of $CsGe(Br_xCl_{1-x})_3$ with x = 0 to 1 is approximately from 30 to 47 μm. Hence, the transmission range of the crystals increases with Br. Furthermore, the force constant increases as the Br content declines, such that the oscillation frequency increases as Br content decreases. The photoluminence spectra revealed that the emission bands of $CsGe(Br_xCl_{1-x})_3$ and $(Rb_zCs_{1-z})GeBr_3$ were red-shifted as the temperature fell, because cooling reduced the lattice constant.

Detection of the generated second-harmonic of the powder demonstrates that all of the crystals, $CsGe(Br_xCl_{1-x})_3$ (x = 0, 1/6, 1/4, 2/6, 3/6, 4/6, 3/4, 5/6, 1) and $(Rb_zCs_{1-z})GeBr_3$ (z = 1/4, 2/4, 3/4), were phase-matchable. The structural distortion and the off-center Ge ion in the unit cell govern the SHG responses. The XRD results that the lattice constant increased with Br content while the cell angle decreased as Br increased. Therefore, the structural distortion of $CsGe(Br_xCl_{1-x})_3$ increases with Br content and the position of the B-site cation, Ge, becomes closer to the cell corner. However, $(Rb_zCs_{1-z})GeBr_3$ yields opposing results as the Rb content is increased. Thus, the nonlinearity properties increased with Br content, but fell as Rb content increased. This result is identical to that for PSHG, for which that second-order NLO susceptibility increased with Br content, but declined as Rb content increased.

This dissertation is dedicated with love to

my mother and my friends.

Table of Contents

List of Tables

List of Figures

Chapter 1   Introduction to NLO crystals

1.1 Definition of nonlinear optics

Nonlinear optics includes the study of new optical effects and novel phenomena that arise from the interactions of intense coherent optical radiation with mater. For historical reasons, this new branch of optical physics is called "nonlinear optics".

Before the 1960s, in the field of conventional optics, numerous basic mathematical equations or formulae were linear. The following three examples reveal this linearity of conventional optics.

First, in interpreting the refraction, reflection, dispersion, scattering and birefringence of light that propagates in a medium, an important physical quantity, the electric polarization that is induced in the medium, must be considered. In the regime of conventional optics, the electric polarization vector $\vec{P}$ is simply assumed to be linearly proportional to the electric field strength $\vec{E}$ of an applied optical wave:

$$\vec{P} = \varepsilon_0 \chi \vec{E} \tag{1-1}$$

where ε_0 denotes the permittivity of free space, and χ is the susceptibility of a particular medium. Based on this assumption of

1

linearity, Maxwell's equations yield a set of linear differential equations

in which only the terms that are proportional to the first power of the field

$\bar{E}$ are involved. Therefore, no coupling occurs between different light

beams or between different monochromatic components when they pass

through a medium. Restated, if several monochromatic optical waves of

various frequencies simultaneously pass through a medium, then no

coherent radiation is generated at any new frequency.

Second, in conventional optics, the attenuation of an optical beam

that propagates in an absorptive medium can be described as

$$\frac{dI}{dz} = -\alpha I \tag{1-2}$$

where I is the beam intensity; z is the distance in the propagation

direction, and α is a constant for a given medium. The physical

meaning of Eq. (1-2) is that the decline in the beam intensity over a in a

unit length of propagation is linearly proportional to the local intensity

itself. Equation (1-2) yields a well known exponential attenuation

expression,

$$I(z) = I(0) \cdot e^{-\alpha z} \tag{1-3}$$

This expression states that for a given propagation length of $z=l$, the

transmitted intensity $I(l)$ is linearly proportional to the initial intensity

$I = I(0)$.

The third example is related to the Fabry-Perot (F-P) interferometer which has a central place in modern optics. The transmission T of this device is given by [1-1]

$$T = \frac{1}{1 + F \sin^2(\delta / 2)} \tag{1-4}$$

where F is a constant that is obtained from the reflectivity of the two mirrors of the interferometer, and δ is a phase-shift factor determined by

$$\delta = \frac{4\pi}{\lambda} n_0 d \cos\theta \tag{1-5}$$

where λ is the wavelength of the incident beam; d is the spacing between the two mirrors; θ is the angle between the beam and the normal to the mirrors, and n_0 is the refractive index of the medium inside the F-P cavity. In the regime of conventional optics, n_0 is a constant that is independent of the incident beam intensity for a particular wavelength. Accordingly, the transmission T of the whole device is also a constant for given values of λ, θ, and d. In this case, the transmitted intensity I_t is linearly proportional to the incident intensity I_0, such that,

$$I_t = T \cdot I_0 \propto I_0 \tag{1-6}$$

3

The above three examples manifest the simple linear feature, described by Eqs. (1-1), (1-2) and (1-6), respectively. These simple linear assumptions or conclusions reached using the conventional optics are widely accepted, and have been confirmed by most experimental observations and measurements based on the use of ordinary light sources. However, these situations have been changed dramatically since the beginning of the 1960s.

Shortly following the demonstration of the first laser device (a pulsed ruby laser) in 1960 [1-2], these simple linear assumptions or conclusions, described above, were found to be no longer appropriate in circumstances in which an intense laser beam was incident on particular optical media. For clarity, the three examples are adopted to show why some higher-order approximations should be made when an intense laser field interacts with an optical medium.

The first breakthrough was achieved in 1961 when a pulsed laser beam was sent into a piezoelectric crystal sample. Researchers, for the first time in the history of optics, observed the generation of the second -harmonic at an optical frequency [1-3]. Shortly after this discovery, various other coherent optical frequency-mixing effects (including optical

sum-frequency generation, optical difference-frequency generation and optical third-harmonic generation) were observed. The researchers realized that all of these new effects could be reasonably explained if the linear term on the right-hand side of Eq. (1-1) was replaced by a power series

$$\vec{P} = \varepsilon_0 \left[\chi^{(1)} \vec{E} + \chi^{(2)} \vec{E}\vec{E} + \chi^{(3)} \vec{E}\vec{E}\vec{E} + \cdots \right] \qquad (1\text{-}7)$$

Here, $\chi^{(1)}$, $\chi^{(2)}$ and $\chi^{(3)}$ are the first-order (linear), second-order (nonlinear), and third-order (nonlinear) susceptibility, and so on. They are material coefficients and in general are tensors. In general, the magnitude of $\chi^{(n+1)}$ is approximately $\chi^{(n)}/E_{atm}$, where E_{atm} represents the atomic electrical field. Since $E_{atm} \sim e/a_0^2$, where $-e$ is the charge of an electron and a_0 is the Bohr radius of an hydrogen atom, $E_{atm} \sim 5\times10^9 V/cm$. Hence, the effect of $\chi^{(2)}$ is a factor of E/E_{atm} smaller than that of $\chi^{(1)}$. This fact explains why the optical nonlinear effect was discovered only after the laser was invited. Only focusing a laser beam can generate an E field with sufficiently high strength that the nonlinear optical effect can be observed. Substituting Eq. (1-7) into Maxwell's equations yields a set of nonlinear differential equations in high-order-power terms of optical electric field strength; these terms are responsible for various observed

coherent optical frequency-mixing effects [1-4].

At roughly the same time, researchers found that the depletion behavior of an intense laser beam that propagates in an absorptive optical medium was not consistent with Eq. (1-2) or Eq. (1-3). For example, in a one-photon absorptive medium, when the intensity of the incident beam is sufficiently high, the attenuation coefficient α is no longer a constant and may become a variable that depends on the incident intensity. Therefore, the exponential attenuation formula, Eq. (1-3), can not be applied and the linear relationship between $I(z=l)$ and $I(0)$ does not hold. In this case, either a saturable absorption or a reverse-saturable absorption effect may occur. Furthermore, a two-photon absorption process occurs in the medium, then the attenuation of an intense incident beam is given by

$$\frac{dI}{dz} = -\alpha I - \beta I^2 \qquad (1-8)$$

where β is the two-photon absorption coefficient, which can be regarded as a constant only if the saturation or reverse-saturation effect can be neglected. In more general cases, when multi-photon (three-photon or more) absorption processes are considered, Eq. (1-8) must be generalized as follows;

$$\frac{dI}{dz} = -\alpha I - \beta I^2 - \gamma I^3 - \cdots \qquad (1\text{-}9)$$

where γ is the three-photon absorption coefficient.

Consider again the transmission behavior of an F-P device under the action of an intense laser beam. In such a case, Eq. (1-6) no longer applies. The prediction that the refractive index of a medium at a particular wavelength is a constant, arises from the assumption of linearity of the electric polarization, given by Eq. (1-1). However, based on the more general assumption expressed by Eq. (1-7), the refractive index for centrosymmetric or isotropic media can be written as

$$n = n_0 + n_2 I \qquad (1\text{-}10)$$

where the first term n_0 is the linear refractive index that is independent of the beam intensity; the second term describes the contribution of the additional nonlinear refractive index which is proportional to the beam intensity, and n_2 is a coefficient of proportionality. When the beam intensity is quite low, the second term in Eq. (1-10) is negligible. However, when the intensity of the incident laser beam is sufficiently high, the second term may be significant. In fact, the intensity-dependent refractive-index change is the basic mechanism of numerous major nonlinear optical effects. For an F-P device that interacts with an intense

laser beam, the phase-shift factor, according to Eq. (1-10), is determined by

$$\delta = \frac{4\pi}{\lambda} d \cos\theta \cdot \left(n_0 + n_2 I_i\right) \qquad (1\text{-}11)$$

where I_i is the intracavity intensity of the incident laser beam. In this case, the transmission T of the F-P device is no longer a constant, even for the given values of λ, d and θ; restated, a complex nonlinear relationship will exist between the incident intensity and the transmitted intensity. The nonlinear response of an F-P device that contains a nonlinear medium is one of the most important issues in optical bistability studies.

Based on the comparisons made above, the main issue in conventional optics is the propagation and interaction with matter of light from ordinary light sources and the intensities of the light beams are so low that even a simple linear approximation suffices to offer a good theoretical explanation of the related optical effects and phenomena. In this sense, conventional optics may also be called "linear optics" or "optics of weak light", while, "nonlinear optics" concerns mainly the interaction between intense laser radiation and matter. In the latter, the intensities of laser beams may be so high that very many new effects and

novel phenomena can be observed, and some high-order nonlinear approximations must be made to explain these new effects and phenomena. In this sense, nonlinear optics may also be called "optics of intense light".

1.2 Background

In 1986, Kato determined that the shortest wavelength generated by frequency doubling was 204.8 nm [1-5]. This record, achieved in BBO, was surpassed only ten years later. In 1996, a Chinese group reported on the new nonlinear crystal potassium fluoroboratoberyllate (KBBF) [1-6], which supports direct SHG down to 172.5 nm [1-7]. However, KBBF has a plate-like nature, and the growth of crystals thicker than a millimeter is very difficult, making tuning of the phase-matching angle difficult. In particular, for deep-UV applications of this crystal, an optical contact technique based on the coupling of two CaF_2 prisms has been proposed [1-7]; it is rather inconvenient and cannot be utilized for very efficient nonlinear conversion.

Sum-frequency generation can also be employed to generate very short UV wavelengths (below 205 nm). This approach was developed in

the mid-1970s [1-8, 1-9]. The summing wavelengths should differ as much as possible to satisfy phase matching conditions; that is, one should lie near the UV edge of the transmission range and the other near the IR edge. Recently, a German group, using SFG between the near IR idler wavelengths from OPO, pumped by a Ti:sapphire femtosecond laser and the UV fourth harmonic of the same laser, produced wavelengths of 175 nm in CLBO [1-10], 172.7 nm in LBO [1-11], 170 nm in LB4 [1-12] and 166 nm in KB5 [1-13]. Their results are available elsewhere [1-14].

A few powerful quasi-CW deep-UV sources have recently been demonstrated, using CLBO in the final sum-frequency mixing stage. A mean power of 250 mW at 205 nm has been generated [1-15]; a 1-W source at 196.3 nm has been developed [1-16] and an absolute maximum mean power of 1.5 W at the same wavelength has been achieved [1-17]. A nanosecond, widely tunable deep-UV source has been described [1-18]. Using a set of BBO harmonic generators and a broadly tunable Ti:sapphire laser with amplifier, the authors of this investigation generated pulses with more than 1 mJ energy in the 193–233 nm spectral range with a repetition rate of 10 Hz.

The search for new inorganic second harmonic generating materials

that can be used in the IR region is a current frontier topic in the field of nonlinear optical materials. Alternative materials have been developed, including compound semiconductors such as GaSe [1-19], AgGaS$_2$ [1-20], AgGaSe$_2$ [1-21], ZnGeP$_2$ [1-22, 1-23] and Tl$_3$AsSe$_3$ [1-24] (Table 1-1). Although these crystals seem to exhibit suitable non-linearity, they are either difficult to generate or exhibit low optical damage thresholds [1-25, 1-26], since they have narrow bandgaps. Accordingly, the search for new infrared NLO crystals with favorable properties, especially a high damage threshold, has became a key research area in IR NLO material science and laser technology [1-22].

1.3 Motivation

Ternary halides ABX$_3$ (A: Rb, Cs ; B: Ge, Sn, Pb ; X: Cl, Br, I) crystals have potential for use in non-linear optical applications [1-27] and with the exception of the fluorides are expected to be transparent in the mid-infrared region [1-28]. This statement is speculative in the following sense. Oxide compounds exhibit typical resonances near 10 μm. Replacing O^{2-} with Cl$^-$, Br$^-$ or I$^-$ increases the mass and reduces the spring constant of the vibrating system. Both effects shift the resonances to

11

longer wavelengths, and crystals with a pyramidal basis are also known to exhibit fairly large optical non-linearity. A pyramidal basis in a unit cell contains one tetrahedron with one cation and three anions located at its vertices — such as in the pyramidal bases $-GeCl_3$ and $-GeBr_3$ [1-29, 1-30] in $CsGeCl_3$ (CGC) and $CsGeBr_3$ (CGB) crystals, respectively. Furthermore, the damage threshold of CGC is 200 $MWcm^2$ [1-31]. Since the optical damage threshold and the transparent range of materials are related to the magnitude of the band gap, while the optical non-linearity is inversely proportional to the cubic power of the band gap [1-20], the linear and nonlinear properties of $CsGe(Br_xCl_{1-x})_3$ and $(Rb_yCs_{1-y})GeBr_3$ can be adjusted by varying the composition of the alloy to meet the demands of specific applications.

This dissertation describes the synthesis of crystals of various compositions and measurements of the optical properties. Nonlinear coefficients of $CsGe(Br_xCl_{1-x})_3$, $x = 0, 1/6, 1/4, 2/6, 3/6, 4/6, 3/4, 5/6, 1$ and $(Rb_yCs_{1-y})GeBr_3$, $y = 0, 1/4, 2/4, 3/4, 1$ are also considered to reveal the potential of these crystals in NLO applications.

1.4 Organization of this dissertation

This work discusses the growth and characteristics of solid solution $CsGe(Br_xCl_{1-x})_3$ and $(Rb_yCs_{1-y})GeBr_3$ crystals with various substitution ratios. Furthermore, these crystals were also investigated in powdered form to study the generation of the second harmonic. The outline is as follows. Chapter 2 briefly describes the procedure for chemically growing ABX_3 (A = Rb, Cs; B = Ge; X = Br, Cl) crystals. The composition and thermal behaviors of these substituted crystals were analyzed by electron-probe X-ray microanalysis and differential scanning calorimetry, respectively. In Chapter 3, structure was also determined by X-ray diffractometry and the atomic vibration was elucidated by Raman spectroscopy. In Chapter 4, the optically transparent region was detected by UV-vis spectrometry and Fourier-transform infrared spectrometry. In Chapter 5, the optical characteristics were determined by photo-luminescence and ellipsometry. In Chapter 6, the nonlinear optical properties were analyzed by powder second harmonic generation measurements. The final chapter briefly draws conclusions.

1.5 Tables and Figures

Table 1-1 Conventional IR NLO crystals [1-19, 1-20, 1-21, 1-22, 1-23, 1-24].

Crystals	GaSe	AgGaS$_2$	AgGaSe$_2$	ZnGeP$_2$	Tl$_3$AsSe$_3$	LiIO$_3$	LiNbO$_3$
Optical transparency (μm)	0.65~18	0.53~13	0.73~18	0.74~12	1.26~17	0.3~6.0	0.33~5.5
Energy bandgap (eV)	2.0	2.7	1.68	2.2	0.98	4.1	3.8
d (pm/V)	d_{22}=63~72	d_{36}=13~31	d_{36}=33~43	d_{36}=111	20	d_{15}=5.53	d_{15}=5.53 d_{22}=2.76
optical damage threshold (MW/cm^2)	28	100	25	60	16	250	10^4

1.6 References

[1-1] M. Born and E. Wolf, *Principles of Optics*, 6th ed., (Pergamon, Oxford, 1980, pp.323-333).

[1-2] T. H. Maiman, *Nature* 187 (1960) 493.

T. H. Maiman, *British Communication & Electronics* 7 (1960) 674.

[1-3] P. A. Franken, A. E. Hill and C. W. Peters, *Phys. Rev. Lett.* 7 (1961) 118.

[1-4] J. A. Armstrong, N. Bloembergen, J. Ducuing and P. S. Pershan, *Phys. Rev.* 127 (1962) 1918.

[1-5] K. Kato, *IEEE J. Quant. Electr.* QE-22 (1986) 1013.

[1-6] B. Wu, D. Tang, N. Ye and C. Chen, *Opt. Mater.* 5 (1996) 105.

[1-7] T. Togashi, T. Kanai, T. Sekikawa, S. Watanabe, C. Chen, C. Zhang, Z. Xu and J. Wang, *Opt. Lett.* 28 (2003) 254.

[1-8] F. B. Dunning, R. E. Jr. Stickel, *Appl. Opt.* 15 (1976) 3131.

[1-9] G. H. Lesch, J. C. Johnson and G. A. Massey, *IEEE J. Quant. Electr.* QE-12 (1976) 83.

[1-10] V. Petrov, F. Noack, F. Rotermund, M. Tanaka and Y. Okada, *Appl. Opt.* 39 (2000) 5076.

[1-11] F. Seifert, J. Ringling, F. Noack, V. Petrov and O. Kittelmann, *Opt.*

Lett. 19 (1994) 1538.

[1-12] V. Petrov, F. Rotermund, F. Noack, R. Komatsu, T. Sugawara and S. Uda, *J. Appl. Phys.* 84 (1998) 5887.

[1-13] V. Petrov, F. Rotermund and F. Noack, *Electron. Lett.* 34 (1998) 1748.

[1-14] V. Petrov, F. Rotermund, F. Noack, J. Ringling, O. Kittelmann and R. Komatsu, *IEEE J. Sel. Topics Quant. Electr.* 5 (1999) 1532.

[1-15] K. F. Wall, J. S. Smucz, B. Pati, Y. Isyanova, P. Moulton and J. G. Manni, *IEEE J. Quant. Electr.* 39 (2003) 1160.

[1-16] J. Sakuma, A. Finch, Y. Ohsako, K. Deki, M. Yoshino, M. Horiguchi, T. Yokota, Y. Mori and T. Sasaki, *Advanced Solid-State Lasers, OSA Trends in Optics and Photonics Series* 26 (1999) 89.

[1-17] J. Sakuma, K. Deki, A. Finch, Y. Ohsako and T. Yokota, *Appl. Opt.* 39 (2001) 5505.

[1-18] A. V. Kachynski, V. A. Orlovich, A. A. Bui, V. D. Kopachevsky, A. V. Kudryakov and W. Kiefer, *Opt. Commun.* 218 (2003) 351.

[1-19] K. Cenzual, L. M. Gelato, M. Penzo and E. Parthe, *Acta Crystallogr. B* 47 (1991) 433.

L. D. Boyd, E. Buehler and F. G. Storz, *Appl. Phys. Lett.* 18 (1971) 301.

[1-20] P. J. Kupecek, C. A. Schwartz and D. S. Chemla, *IEEE J. Quantum Electron.* 10 (1974) 540.

G. C. Bhar and R. C. Smith, *IEEE J. Quantum Electron.* 10 (1974) 546.

J. E. Jaffe and A. Zunger, *Phys. Rev. B* 29 (1984) 1882.

Y. R. Shen, *The Principles of Nonlinear Optics* (New York: Wiley, 1984, ch. 2).

[1-21] H. Komine, J. M. Fukumoto, W. H. Long and E. A. Stappaerts, *Conference on Lasers and Electro-Optics* 8 (1994) CPD 14-1/31.

[1-22] G. Dmitriev, G. G. Gurzadyan and D. N. Nikogosyan, *Handbook of Nonlinear Optical Crystals* (Berlin: Springer, 1991).

[1-23] P. D. Mason, D. J. Jackson and E. K. Gorton, *Opt. Commun.* 110 (1994) 163.

[1-24] D. R. Suhre, *Appl. Phys. B* 52 (1991) 367.

[1-25] E. Buehler and J. H. Wernick, *J. Cryst. Growth* 8 (1970) 324.

[1-26] K. C. Yoo, R. P. Storrick, T. Henningsen, J. A. Spitznagel and R. H. Hopkins, *J. Cryst. Growth* 125 (1992) 208.

[1-27] M. Hagemann and H. J. Weber, *Applied physics A* 63 (1996) 67.

[1-28] D. K. Seo, N. Gupta, M. H. Whangbo, H. Hillebrecht and G. Thiele, *Inorg. Chem.* 37 (1998) 407.

[1-29] A. N. Christensen and S. E. Rasmussen, *Acta Chem. Scand.* 19

(1965) 421.

[1-30] M. D. Ewbank, P. Cunningham, R. Borwick, M. J. Rosker and P.

Gunter, *Conference on Lasers and Electro-Optics* CFA7 (1997) 462.

[1-31] Q. Gu, Q. Pan, X. Wu, W. Shi and C. Fang, *J. Cryst. Growth* 212

(2000) 605.

Chapter 2   Experimental Procedure

2.1 Preparation of raw materials

Figure 2-1 presents the synthetic procedure, which was modified from the work done by Gu *et al.* [2-1, 2-2, 2-3], Chritensen and Tananaev *et al.* [2-4, 2-5], who used different synthesis methods that seemed complex and had low productivity. In this investigation, H_3PO_2 (50%) was loaded with HBr (48%), HCl (37%) and GeO_2 (99.999%) into a 250 ml beaker, and then heated to 95°C. The solution was vigorously mixed for 5 hours and then cooled to room temperature. After the precipitates were removed, CsCl (99.9%), CsBr (99.9%) and RbBr (99.8%) were added separately and the temperature was raised to the boiling point. The mixture was then stood to cool to room temperature again. A light yellow precipitate was formed. The reaction equations were as follows.

(1) Br^- is replaced by Cl^- in CGB: C-series
$$2(3x\text{-}1)HBr + 6(1\text{-}x)HCl + 2GeO_2 + H_3PO_2 + 2CsBr =$$
$$2CsGe(Br_xCl_{1\text{-}x})_3 \downarrow + 2H_2O + H_3PO_4 \; ; x = 0, \frac{1}{6}, \frac{1}{4}, \frac{2}{6}, \frac{3}{6}, \frac{4}{6}, \frac{3}{4}, \frac{5}{6}, 1$$
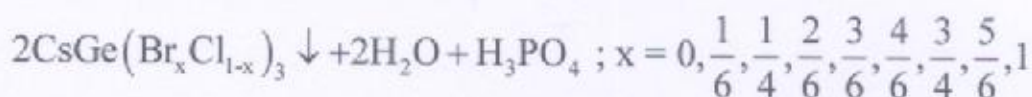
(2) Cl^- is replaced by Br^- in CGC: B-series

$$6yHBr + 2(2\text{-}3y)HCl + 2GeO_2 + H_3PO_2 + 2CsCl =$$

$$2CsGe(Br_yCl_{1\text{-}y})_3 \downarrow + 2H_2O + H_3PO_4 \ ; y = 0, \frac{1}{6}, \frac{1}{4}, \frac{2}{6}, \frac{3}{6}, \frac{4}{6}, \frac{3}{4}, \frac{5}{6}, 1$$

(3)

$$4HBr + H_3PO_2 + 2GeO_2 + 2zRbBr + 2(1\text{-}z)CsBr =$$

$$2(Rb_zCs_{1\text{-}z})GeBr_3 \downarrow + 2H_2O + H_3PO_4 \ ; z = 0, \frac{1}{4}, \frac{2}{4}, \frac{3}{4}, 1$$
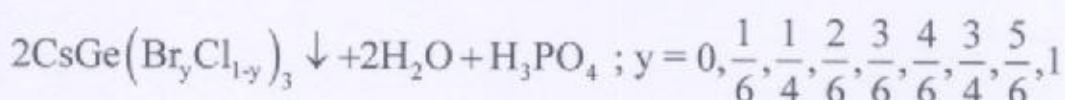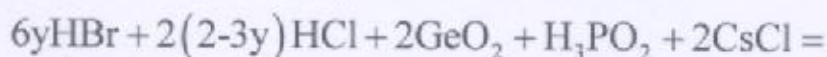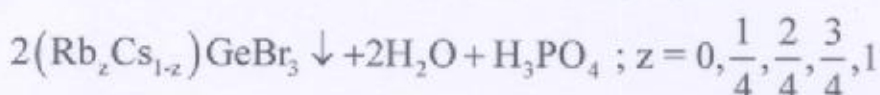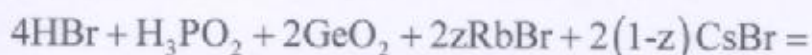
2.2 Refinement

Recrystallization (Fig. 2-2) was conducted by mixing the precipitates with 1:1 concentrated HX : alcohol solution to yield yellow crystals of $CsGe(Br_xCl_{1\text{-}x})_3$ and $(Rb_yCs_{1\text{-}y})GeBr_3$. This procedure was performed seven times to ensure that no residual precursor remained. Then, the crystals were dried at $85^\circ C$ for 48 hours in a vacuum to prevent deliquescence from any side effect. The crystals were then maintained at $20\,^\circ C$ in a vacuum. The precipitated products can be changed from yellow to white as soon as the substitutional ratio, x, fell from one to zero.

2.3 Measuring crystal characteristics

Rhombohedral crystals were synthesized and sieved into particles of various sizes to analyze its structural and optical properties. The crystal

20

structures were observed using an X-ray diffractometer. A differential scanning calorimeter (DSC) was employed to elucidate the thermal and structural behaviors of crystals. The composition of all samples was measured by electron-probe X-ray microanalysis (EPMA). Raman spectra were used to determine the atomic vibration. The absorption edge was measured using a UV-vis spectrometer. The optical transmission spectra in the infrared region were obtained using a Fourier-transform infrared spectrometer (FTIR). Linear optical properties were measured using an ellipsometer. Nonlinear optical properties were determined by making powder second harmonic generation measurements. Figure 2-3 depicts the measurement procedure, described above.

2.3.1 Composition measurement

The composition of specimens was determined using an electron probe microanalyer (EPMA, JAX-8800, JEOL, Japan) with the aid of the ZAF (atomic number, absorption and fluorescence) program.

2.3.2 Thermal analysis

The melting points and phase-transformed points were determined

using a Differential Scanning Calorimeter (Seiko SSC 5000-DSC) as the

temperature is increased at 5°C per minute in an atmosphere of $N_{2(g)}$.

2.3.3 X-ray powder diffraction

The phase and structures of as-fabricated crystals were analyzed

using an X-ray diffractometer (Rigaku, Dmmax-B, Tokyo, Japan), in both

the conventional θ-2θ continuous and the fixed time scanning mode.

X-ray was generated using a Cu target operated at 40 KV and 30 mA.

2.3.4 Raman scattering measurements

The macro-Raman scattering measurements were made using an

Ar-ion laser (Coherent INNOVA 90) as the excitation source, emitting at

a wavelength of 488 nm at 500 mW. The spectra were obtained at room

temperature. As displayed in Fig. 2-4, the incident beam was reflected at

45° from the samples that were mounted on the holder, to a spectrometer.

The laser beam was focused by a converging lens ($f = 5$ cm) with a beam

spot size with a diameter of ~ 30-50 μm and a mean power of about 10

mW on the surface of the sample. The scattered light was collected using

backscattering geometry by a camera lens, and imaged onto the entrance

slit of the triplemate spectrometer (Spex 1877).

2.3.5 Transmission analysis

The transmission of crystals in the IR region was determined using a Fourier - Transform Infrared Spectrometer (Bomem, DA8.3) from 100 to 4000 cm^{-1} at room temperature. Crystals must be dried in a vacuum at 85°C for 48 hours, and then ground. After pressing at 10^5 N for five minutes, a crystal pellet was formed.

2.3.6 Absorption edge analysis

The absorption edge of the specimen was measured using a Hitachi U-3010 UV-vis spectrophotometer with an integral sphere from 200 nm to 800 nm at room temperature.

2.3.7 Luminescence measurement

An He–Cd laser (λ = 325 nm) was used as the excitation source in measuring the continuous-wave (cw) photoluminescence (PL). Figure 2-5 schematically depicts the cw-PL system. The excitation laser beam was directed normally and focused onto the sample surface as the power was varied using an optical attenuator. The spot size on the sample was about

100 μm. Spontaneous and stimulated emissions were collected by a fiber bundle and coupled into a 0.32 cm focal-length monochromator with a 1200 lines/mm grating, before being detected using a photomultiplier tube (PMT) detector. The temperature-dependent PL measurements were made using a closed cycle cryogenic system. The closed cycle refrigerator was used to set the temperature between 17 K and 293 K.

2.3.8 Second-order nonlinear optical measurement

Powder SHG measurements, as described by Chen et al. [2-6], were made on a modified Kurtz-NLO [2-7] system using 1260 nm light (Fig. 2-6). A CrF-Femtosecond laser was used to make all measurements. The laser is self mode-locked by maintaining lasing longitudinal cavity modes in phase to generate ultrashort near-transform-limited optical pulses with durations of about 50 fs. The Cr^{4+}:Forsterite oscillator yields pulses with a typical full-width-at-half maximum (FWHM) bandwidth of around 45 nm at a repetition rate of 76 MHz and a mean power of 270 mW. The ultrashort pulse duration can yield an enormous peak power density after focusing. The Cr^{4+}:Forsterite laser is pumped using a 7-8 W ytterbium-doped fiber laser. Since the SHG efficiency of powders has been

demonstrated to depend strongly on particle size [2-7, 2-8], crystals were ground and sieved (Newark Wire Cloth Company) into six particle-size ranges, 37 μm, 37–74 μm, 74–105 μm, 105–210 μm, 210–420 μm and 420–840 μm. Crystalline KDP was also ground and sieved into the same particle-size ranges for comparison with known SHG materials. All of the powders were placed in separate capillary tubes. The capillary was filled with crystal powder. Although the powder was suspended in air in the two extremities, the compact part was used for nonlinear optical characterization. The SHG radiation (630 nm) was collected during transmission and detected by a photomultiplier tube (Oriel Instruments). The SHG signal was collected using a data-acquisition (DAQ) interface and was monitored by an analytical program on a personal computer.

2.3.9 Ellipsometric measurement

The dielectric constants and refractive indices of crystals were measured using variable angle spectroscopic ellipsometer. The incident angles were 65° and 75° from 200 nm to 1300 nm at room temperature.

2.4 Analysis of component characteristics

Figures 2-7, 2-8 and 2-9 present the compositions of $CsGe(Br_xCl_{1-x})_3$ (x = 0, 1/6, 1/4, 2/6, 3/6, 4/6, 3/4, 5/6, 1) and $(Rb_yCs_{1-y})GeBr_3$ (y = 0, 1/4, 2/4, 3/4, 1) based on EPMA measurements. These results reveal that these samples exhibit a Cs to Ge ratio of almost 1:1 (for CGBC) and a Ge to Br ratio of almost 1:3 (for RCGB). EPMA measurement can qualitatively confirm that bromine atoms were successfully doped in $CsGeCl_3$ crystals to form B-series crystals; chlorine atoms were also successfully doped in $CsGeBr_3$ crystals to form C-series crystals; rubidium atoms were successfully doped in $CsGeBr_3$ crystals. The impurity contents were all less than 1% ($O_{max} \leq 0.57\%$, $P_{max} \leq 0.61\%$).

2.5 Analysis of thermal characteristics

DSC was conducted to determine the melting and phase-transformed temperatures of $CsGe(Br_xCl_{1-x})_3$. The analysis was performed on polycrystalline $CsGe(Br_xCl_{1-x})_3$ in $N_{2(g)}$ atmosphere at a heating rate of $5^{\circ C}/_{min}$ to $450^{\circ}C$ using a Seiko SSC5000 DSC. The results, presented in Fig. 2-10, reveal that the phase-changed temperatures of $CsGeCl_3$ and $CsGeBr_3$ were similar to those reported by Thiele et al. [2-9, 2-10]. Since

the molecular weight of $CsGe(Br_xCl_{1-x})_3$ increases with the Br content, the attraction between $CsGe(Br_xCl_{1-x})_3$ and its outside electrons becomes stronger. Therefore, T_c (the Curie temperature) and T_m (melting temperature) of $CsGe(Br_xCl_{1-x})_3$ crystals increase with Br content. In summary, the NLO $CsGe(Br_xCl_{1-x})_3$ crystals could be properly operated at 255.2 $^\circ$C, 253.1 $^\circ$C, 250.6 $^\circ$C, 250.5 $^\circ$C, 239.1 $^\circ$C, 227.3 $^\circ$C, 215.5 $^\circ$C, 206.2 $^\circ$C and 154.1 $^\circ$C for x=1, 5/6, 3/4, 4/6, 3/6, 2/6, 1/4, 1/6 and 0, respectively.

2.6 Tables and Figures

Stage 1: Synthesis (A = Cs, Rb; B = Ge; X = Cl, Br)

$$H_3PO_2 + 4HX + 2BO_2 + 2AX \rightarrow H_3PO_4 + 2H_2O + 2ABX_{3\,(s)}$$
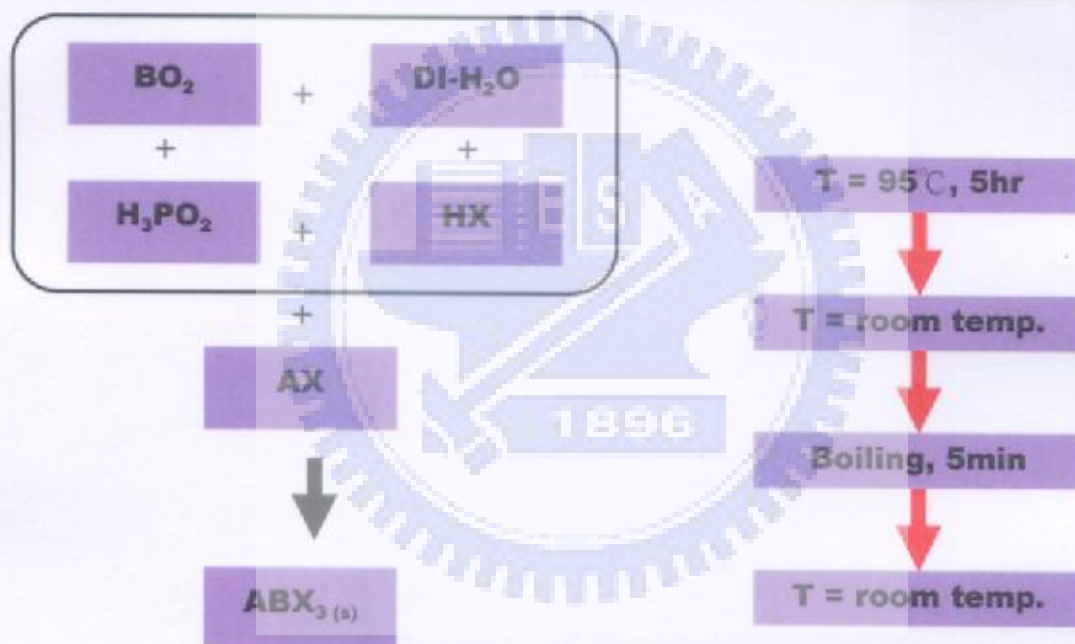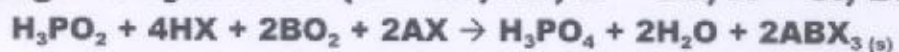
Fig. 2-1 The procedure of synthesizing raw rhombohedral nonlinear optical crystals ABX_3.
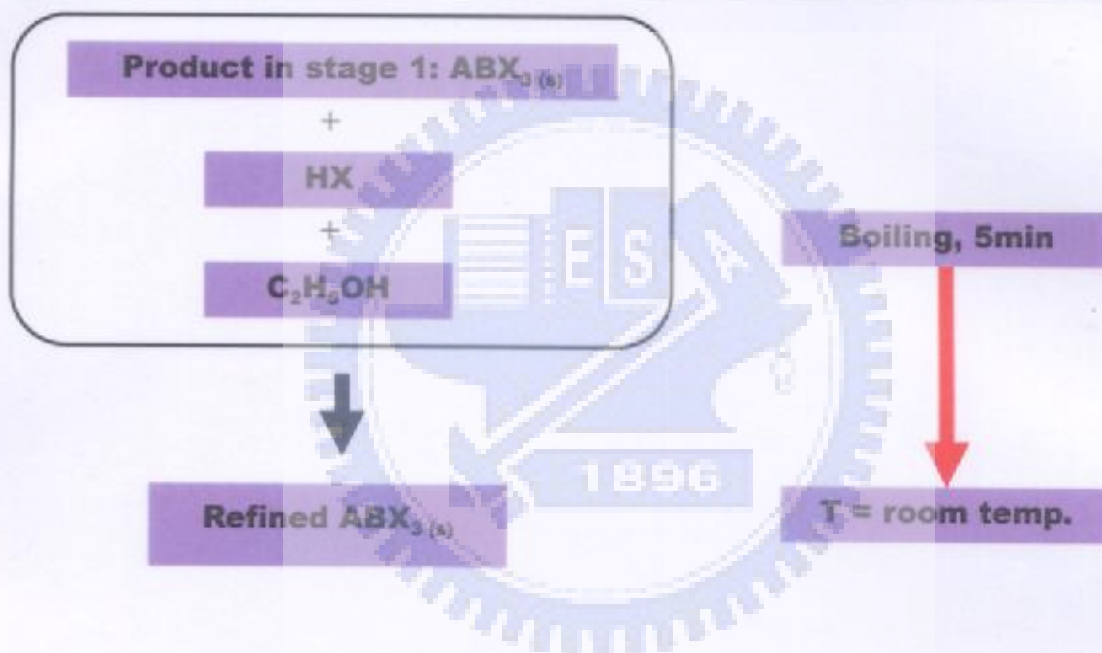
Fig. 2-2 The procedure of recrystallizing rhombohedral nonlinear optical crystals ABX_3.
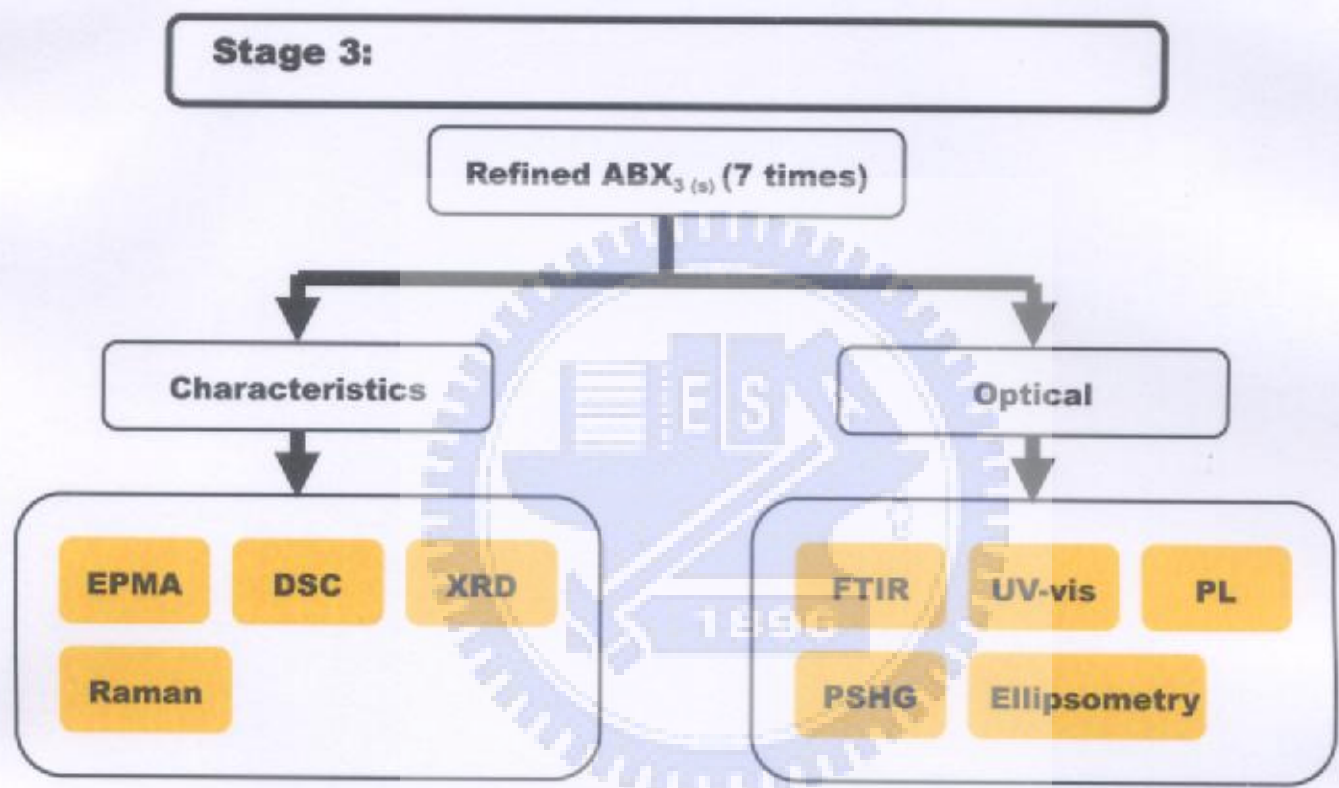
Fig. 2-3 The analyzing procedures.
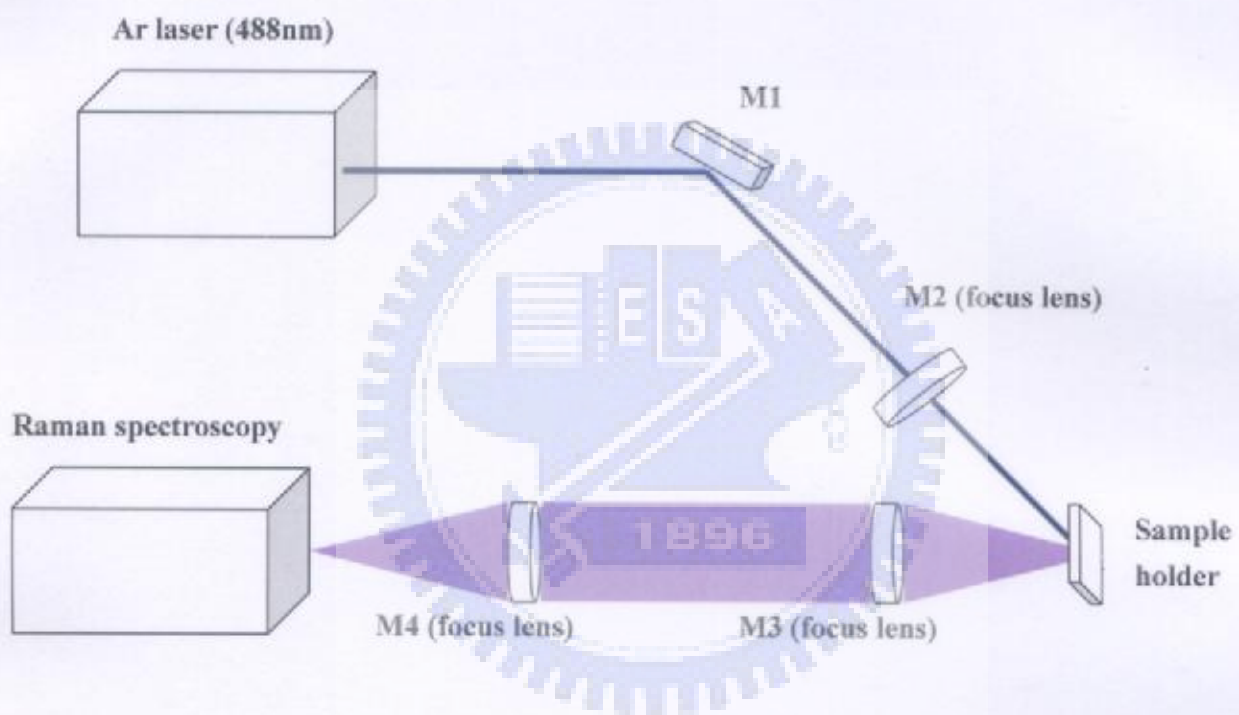
Fig.2-4 The scheme of the Raman system.
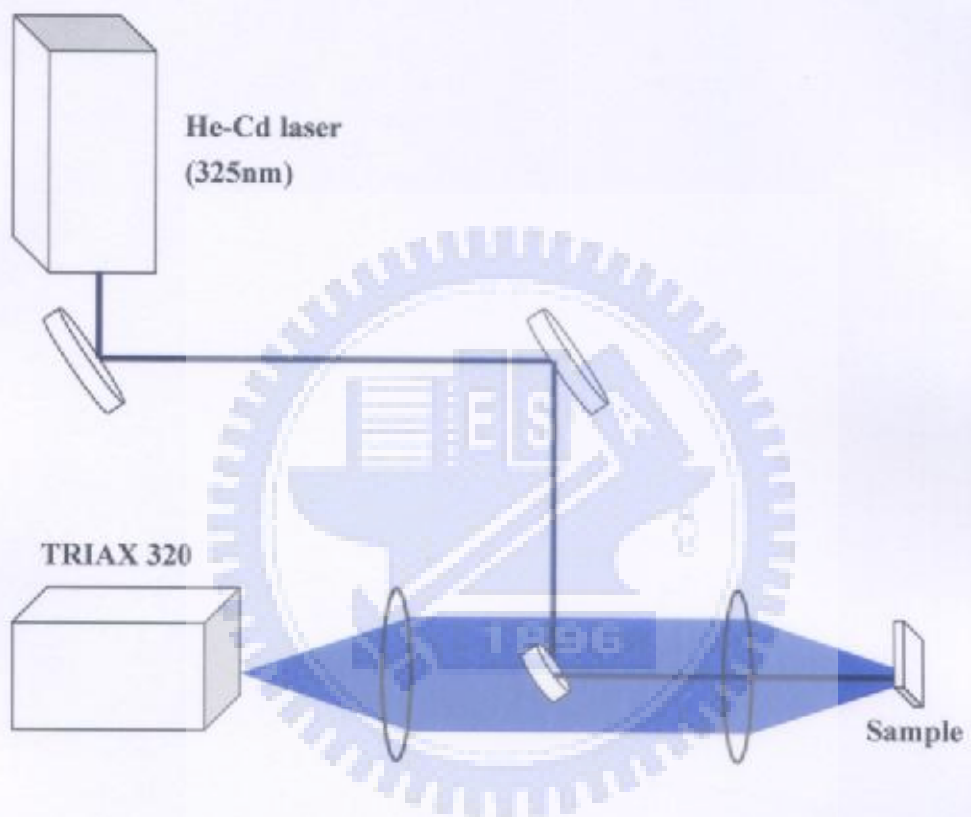
Fig.2-5 The scheme of the PL system (optical pumping system).
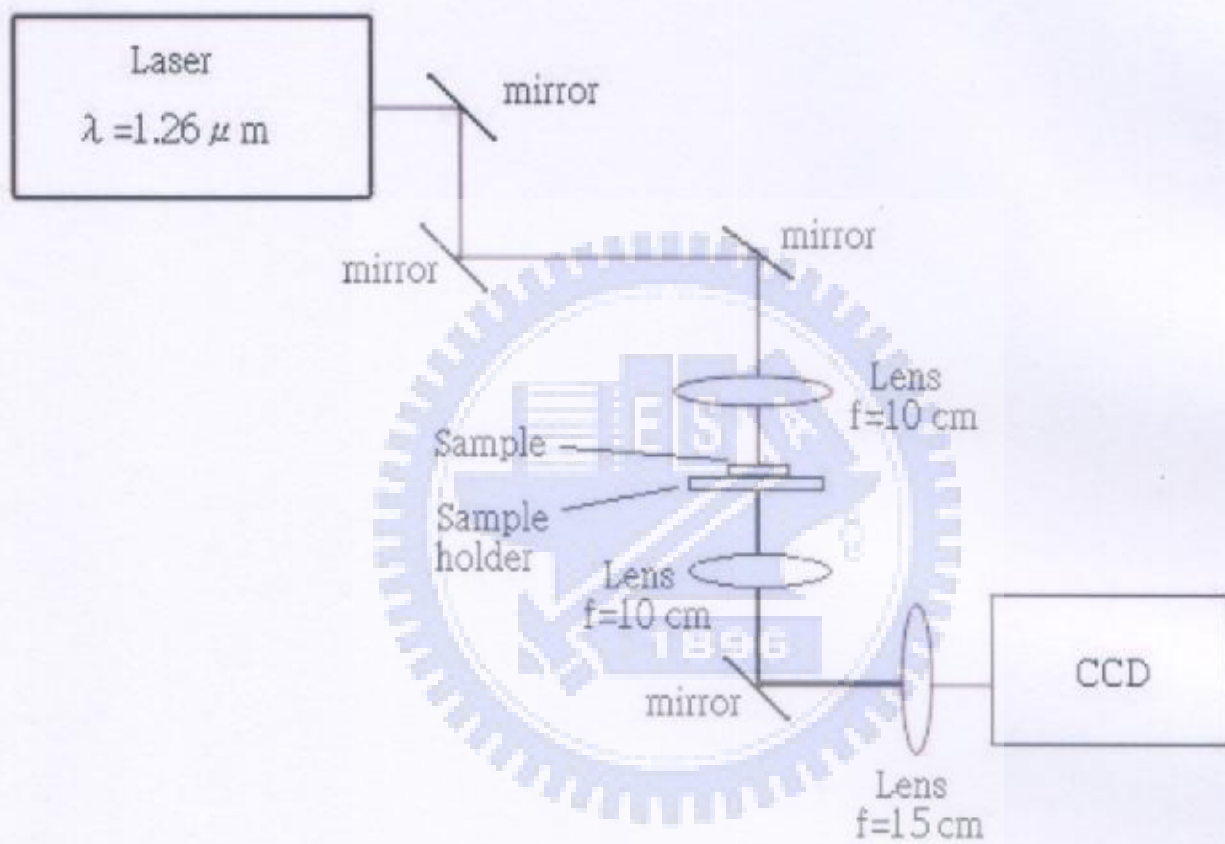
Fig. 2-6 The scheme of the PSHG system.
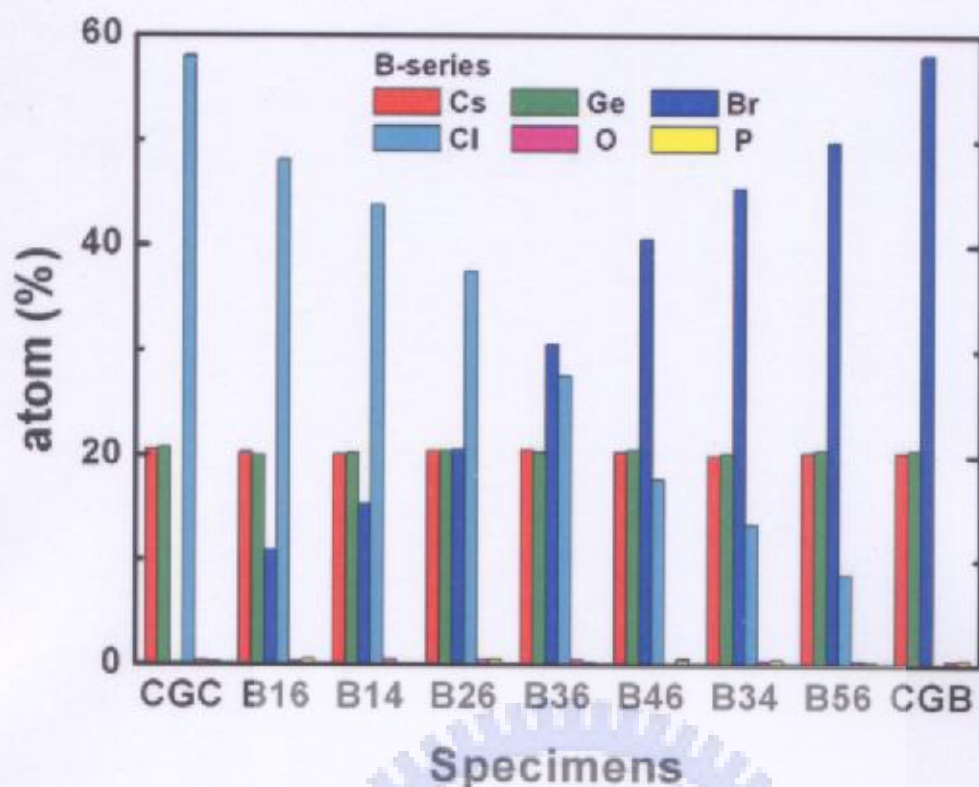
Fig. 2-7 EPMA measurements, $CsGe(Br_yCl_{1-y})_3$ (B-series) : y = 0, 1/6, 1/4, 2/6, 3/6, 4/6, 3/4, 5/6, 1.
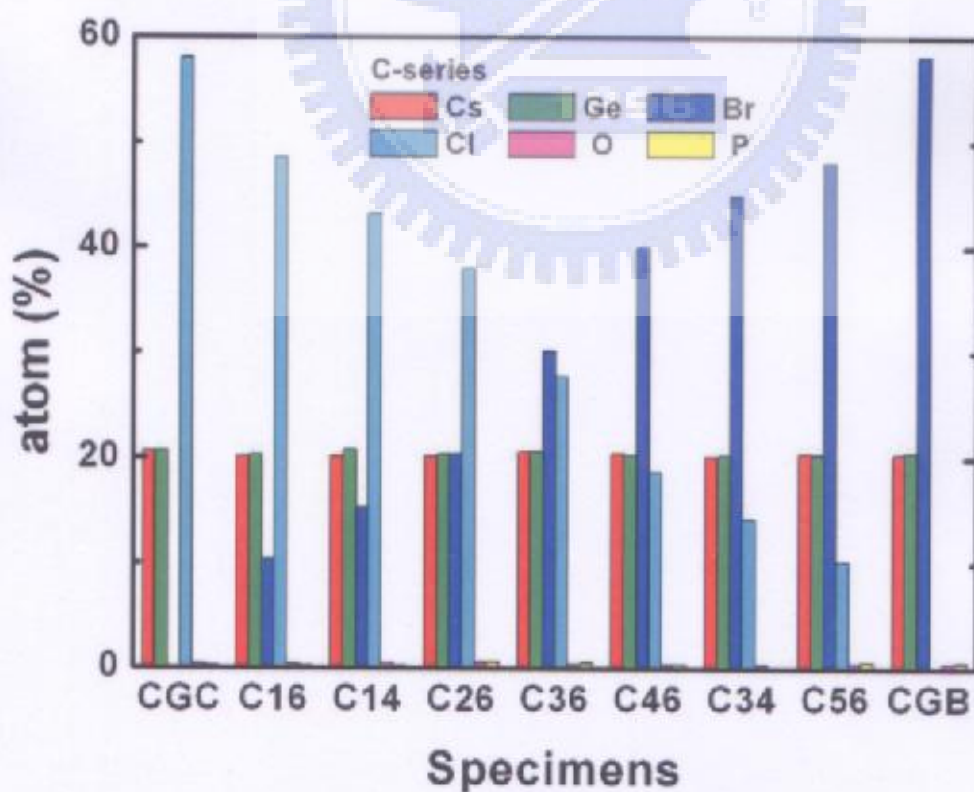
Fig. 2-8 EPMA measurements, $CsGe(Br_xCl_{1-x})_3$ (C-series) : x = 0, 1/6, 1/4, 2/6, 3/6, 4/6, 3/4, 5/6, 1.
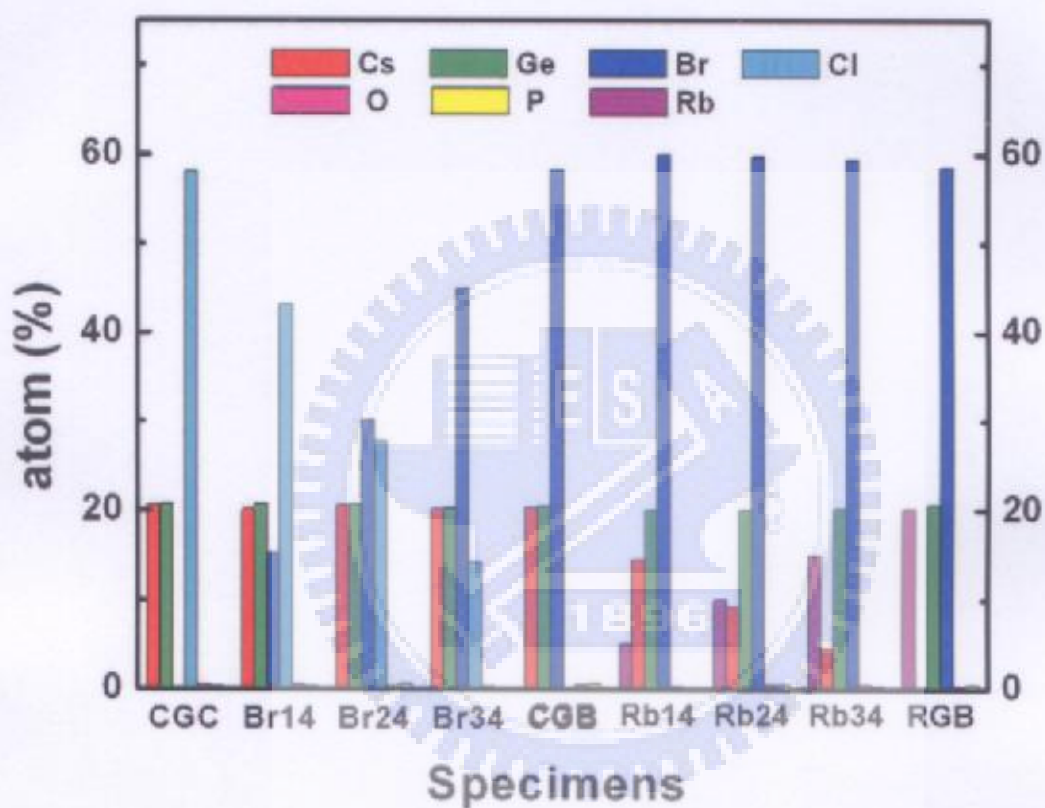
Fig. 2-9 EPMA measurements, $CsGe(Br_xCl_{1-x})_3$: x = 0, 1/4, 2/4, 3/4, 1 and $(Rb_zCs_{1-z})GeBr_3$: z = 0, 1/4, 2/4, 3/4, 1.
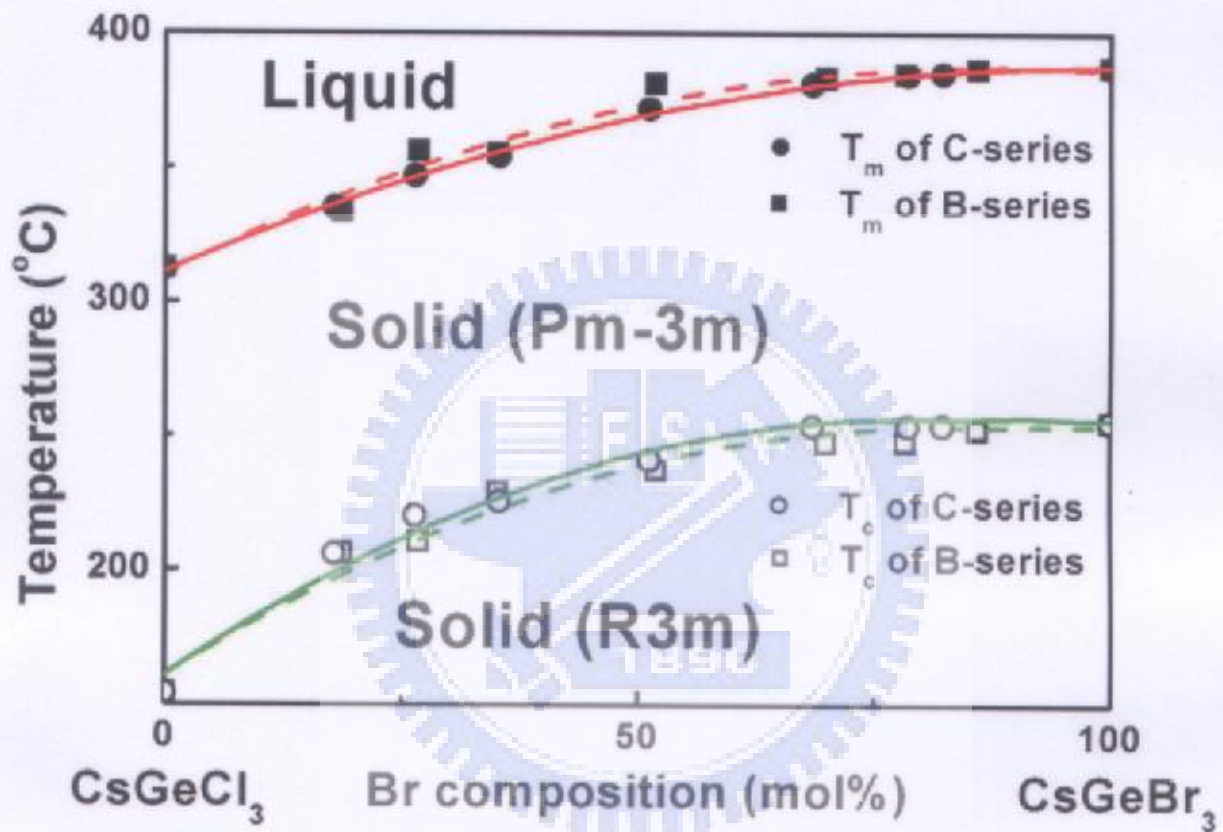
Fig. 2-10 The thermal analysis of rhombohedral nonlinear optical crystals $CsGe(Br_xCl_{1-x})_3$.

2.7 References

[2-1] Q. Gu, Q. Pan, X. Wu, W. Shi and C. Fang, *J. Cryst. Growth* 212 (2000) 605.

[2-2] Q. Gu, Q. Pan, W. Shi, X. Sun and C. Fang, *Prog. Cryst. Growth Charact. Mater.* 40 (2000) 89.

[2-3] Q. Gu, C. Fang, W. Shi, X. Wu and Q. Pan, *J. Cryst. Growth* 225 (2001) 501.

[2-4] A. N. Christensen and S. E. Rasmussen, *Acta Chem. Scand.* 19 (1965) 421.

[2-5] I. V. Tananaev, D. F. Dzhurinskii and Y. N. Mikhailov, *Zh. Neorgan. Khim* 9 (1964) 1570.

[2-6] W. K. Chen, C. M. Cheng, J. Y. Huang, W. F. Hsieh and T. Y. Tseng, *J. Phys. Chem. Solids* 61 (2000) 969.

[2-7] S. K. Kurtz and T. T. Perry, *J. Appl. Phys.* 39 (1968) 3798.

[2-8] J. P. Dougherty and S. K. Kurtz, *J. Appl. Crystallogr.* 9 (1976) 145.

[2-9] G. Thiele, H. W. Rotter and K. D. Schmidt, *Z. Anorg. Allg. Chem.* 545 (1987) 148.

[2-10] G. Thiele, H. W. Rotter and K. D. Schmidt, *Z. Anorg. Allg. Chem.* 559 (1988) 7.

Chapter 3   Structural Properties

3.1 X-ray diffraction analysis

3.1.1 Theory [3-1, 3-2]

The peaks in an X-ray diffraction pattern are directly related to the atomic distances. Consider an incident monochromatic X-ray beam's interacting with the atoms arranged in a periodic manner, as presented in two dimensions in Fig. 3-1. The atoms, represented as circles in the graph, form different sets of planes in the crystal. For a given set of lattice planes with an inter-plane distance of d, the condition for a diffraction (peak) to occur can be simply expressed as

$$2 d \sin \theta = n \lambda \qquad (3\text{-}1)$$

which is known as Bragg's law. In this equation, λ denotes the wavelength of the X-ray; θ is the diffraction angle, and n is an integer that represents the order of the diffraction peak.

A set of reciprocal vectors $\vec{b}_1, \vec{b}_2, \vec{b}_3$ are defined in terms of the crystal axes $\vec{a}_1, \vec{a}_2, \vec{a}_3$:

$$\vec{b}_1 = \frac{\vec{a}_2 \times \vec{a}_3}{\vec{a}_1 \cdot \vec{a}_2 \times \vec{a}_3}, \quad \vec{b}_2 = \frac{\vec{a}_3 \times \vec{a}_1}{\vec{a}_1 \cdot \vec{a}_2 \times \vec{a}_3}, \quad \vec{b}_3 = \frac{\vec{a}_1 \times \vec{a}_2}{\vec{a}_1 \cdot \vec{a}_2 \times \vec{a}_3} \qquad (3\text{-}2)$$

Each reciprocal vector is perpendicular to the plane that is defined by the

two crystal axes that have different indices. The scalar products specify and important relationship between the two sets of vectors. If the indices are the same,

$$\vec{a}_1 \cdot \vec{b}_1 = \vec{a}_1 \cdot \frac{\vec{a}_2 \times \vec{a}_3}{\vec{a}_1 \cdot \vec{a}_2 \times \vec{a}_3} = 1$$

If the indices are different,

$$\vec{a}_1 \cdot \vec{b}_2 = \vec{a}_1 \cdot \frac{\vec{a}_3 \times \vec{a}_1}{\vec{a}_1 \cdot \vec{a}_2 \times \vec{a}_3} = 0$$

since the vector $\vec{a}_3 \times \vec{a}_1$ is perpendicular to $\vec{a}_1$ such that the scalar product of $\vec{a}_1$ and $\vec{a}_3 \times \vec{a}_1$ involves $\cos 90^\circ$. These results can be generalized by writing

$$\vec{a}_i \cdot \vec{b}_j = \begin{cases} 1, & i = j \\ 0, & i \neq j \end{cases} \tag{3-3}$$

The relations expressed as Eq. (3-3) are the normal and orthogonal conditions between the primary and reciprocal vectors. Considerable use of these relations shall be made.

A vector $\vec{H}_{hkl}$ is defined in terms of the reciprocal vectors and the Miller indices:
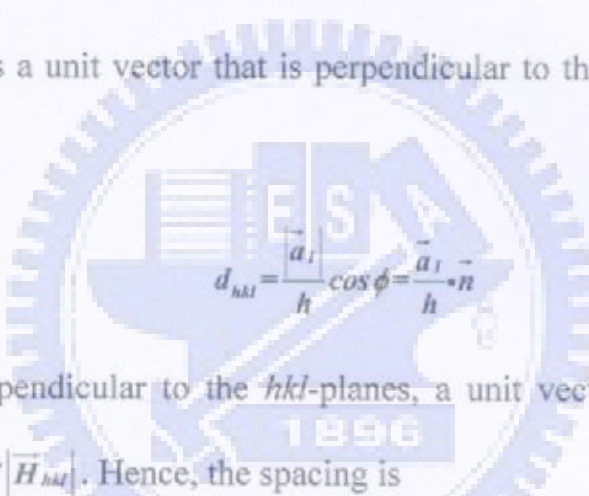
$$\vec{H}_{hkl} = h\vec{b}_1 + k\vec{b}_2 + l\vec{b}_3 \tag{3-4}$$

From Fig. 3-2, $\left(\vec{a}_1/h - \vec{a}_2/k \right)$ and $\left(\vec{a}_2/k - \vec{a}_3/l \right)$ are vectors that are parallel to the hkl-planes. However, from the relations expressed by Eq. (3-3),

39

$$\left(\frac{\vec{a}_1}{h}-\frac{\vec{a}_2}{k}\right)\cdot\vec{H}_{hkl}=\left(\frac{\vec{a}_1}{h}-\frac{\vec{a}_2}{k}\right)\cdot\left(h\vec{b}_1+k\vec{b}_2+l\vec{b}_3\right)=1\text{-}1\text{=}0\,,$$

$$\left(\frac{\vec{a}_2}{k}-\frac{\vec{a}_3}{l}\right)\cdot\vec{H}_{hkl}=\left(\frac{\vec{a}_2}{k}-\frac{\vec{a}_3}{l}\right)\cdot\left(h\vec{b}_1+k\vec{b}_2+l\vec{b}_3\right)=1\text{-}1\text{=}0\,.$$

Therefore, the vector $\vec{H}_{hkl}$ is perpendicular to the set of *hkl*-planes, since it is perpendicular to two vectors that are parallel to the planes. The spacing between the planes d_{hkl} is the perpendicular distance between the planes. If $\vec{n}$ is a unit vector that is perpendicular to the planes, Fig. 3-2 indicates that

$$d_{hkl}=\frac{\left|\vec{a}_1\right|}{h}\cos\phi=\frac{\vec{a}_1}{h}\cdot\vec{n}$$

Since $\vec{H}_{hkl}$ is perpendicular to the *hkl*-planes, a unit vector $\vec{n}$ can be expressed as $\vec{H}_{hkl}/\left|\vec{H}_{hkl}\right|$. Hence, the spacing is

$$d_{hkl}=\frac{\vec{a}_1}{h}\cdot\frac{\left(h\vec{b}_1+k\vec{b}_2+l\vec{b}_3\right)}{\left|\vec{H}_{hkl}\right|}=\frac{1}{\left|\vec{H}_{hkl}\right|}$$

The value of the planar spacing d_{hkl} must be known to apply the Bragg law ($\lambda=2d_{hkl}\sin\theta$). Based on the assumption that the lengths of the three crystal axes and the angles between them are known, the spacing can be expressed in the form

$$d_{hkl}=f\left(\vec{a}_1,\vec{a}_2,\vec{a}_3,\alpha_{12},\alpha_{23},\alpha_{31},h,k,l,\right).$$

The obvious starting point is to write

$$\frac{1}{d_{hkl}^2} = \left|\vec{H}_{hkl}\right|^2 = \left(h\vec{b}_1 + k\vec{b}_2 + l\vec{b}_3\right) \cdot \left(h\vec{b}_1 + k\vec{b}_2 + l\vec{b}_3\right),$$

$$\frac{1}{d_{hkl}^2} = h^2 \vec{b}_1 \cdot \vec{b}_1 + k^2 \vec{b}_2 \cdot \vec{b}_2 + l^2 \vec{b}_3 \cdot \vec{b}_3 + 2hk\vec{b}_1 \cdot \vec{b}_2 + 2kl\vec{b}_2 \cdot \vec{b}_3 + 2lh\vec{b}_3 \cdot \vec{b}_1.$$

Using Eq. (3-2) and factoring out $\vec{v}_a = \vec{a}_1 \cdot \vec{a}_2 \times \vec{a}_3$, yields

$$\frac{1}{d_{hkl}^2} = \frac{1}{\vec{v}_a^2}\left\{ \begin{array}{l} h^2 \left|\vec{a}_2 \times \vec{a}_3\right|^2 + k^2 \left|\vec{a}_3 \times \vec{a}_1\right|^2 + l^2 \left|\vec{a}_1 \times \vec{a}_2\right|^2 + \\ 2hk\left(\vec{a}_2 \times \vec{a}_3\right) \cdot \left(\vec{a}_3 \times \vec{a}_1\right) + 2kl\left(\vec{a}_3 \times \vec{a}_1\right) \cdot \left(\vec{a}_1 \times \vec{a}_2\right) + 2lh\left(\vec{a}_1 \times \vec{a}_2\right) \cdot \left(\vec{a}_2 \times \vec{a}_3\right) \end{array} \right\} \tag{3-5}$$

From the equations of vector analysis

$$\left(\vec{a}_i \times \vec{a}_j\right) \cdot \left(\vec{a}_j \times \vec{a}_k\right) = \vec{a}_i \cdot \vec{a}_j \vec{a}_j \cdot \vec{a}_k - \vec{a}_i \cdot \vec{a}_k \vec{a}_j^2 = \vec{a}_i \vec{a}_j \vec{a}_k^2 \left(\cos\alpha_{ij}\cos\alpha_{jk} - \cos\alpha_{ik}\right)$$

$$\left|\vec{a}_i \times \vec{a}_j\right|^2 = \vec{a}_i^2 \vec{a}_j^2 \sin^2\alpha_{ij}$$

Using these relations and factoring out $\vec{a}_1^2 \vec{a}_2^2 \vec{a}_3^2$, yields

$$\frac{1}{d_{hkl}^2} = \frac{\vec{a}_1^2 \vec{a}_2^2 \vec{a}_3^2}{\vec{v}_a^2}\left\{ \begin{array}{l} \dfrac{h^2 \sin^2\alpha_{23}}{\vec{a}_1^2} + \dfrac{k^2 \sin^2\alpha_{31}}{\vec{a}_2^2} + \dfrac{l^2 \sin^2\alpha_{12}}{\vec{a}_3^2} + \dfrac{2hk}{\vec{a}_1 \vec{a}_2}\left(\cos\alpha_{23}\cos\alpha_{31} - \cos\alpha_{12}\right) \\ + \dfrac{2kl}{\vec{a}_2 \vec{a}_3}\left(\cos\alpha_{31}\cos\alpha_{12} - \cos\alpha_{23}\right) + \dfrac{2lh}{\vec{a}_3 \vec{a}_1}\left(\cos\alpha_{12}\cos\alpha_{23} - \cos\alpha_{31}\right) \end{array} \right\} \tag{3-6}$$

The square of the triple scalar product is conveniently expressed in determinant form in terms of simple scalar products:

$$\vec{v}_a^2 = \left(\vec{a}_1 \cdot \vec{a}_2 \times \vec{a}_3\right)^2 = \begin{vmatrix} \vec{a}_1 \cdot \vec{a}_1 & \vec{a}_1 \cdot \vec{a}_2 & \vec{a}_1 \cdot \vec{a}_3 \\ \vec{a}_2 \cdot \vec{a}_1 & \vec{a}_2 \cdot \vec{a}_2 & \vec{a}_2 \cdot \vec{a}_3 \\ \vec{a}_3 \cdot \vec{a}_1 & \vec{a}_3 \cdot \vec{a}_2 & \vec{a}_3 \cdot \vec{a}_3 \end{vmatrix},$$

$$\vec{v}_a^2 = \vec{a}_1^2 \vec{a}_2^2 \vec{a}_3^2 \left(1 + 2\cos\alpha_{12}\cos\alpha_{23}\cos\alpha_{31} - \cos^2\alpha_{12} - \cos^2\alpha_{23} - \cos^2\alpha_{31}\right) \tag{3-7}$$

To enable those to be written in the usual crystallographic notation, let

$$\vec{a}_1 = \vec{a}, \quad \alpha_{23} = \alpha,$$
$$\vec{a}_2 = \vec{b}, \quad \alpha_{31} = \beta,$$
$$\vec{a}_3 = \vec{c}, \quad \alpha_{12} = \gamma,$$

Combining Eqs. (3-6) and (3-7) and switching to the usual

41

crystallographic notation,

$$\frac{1}{d_{hkl}^2} = \frac{1}{\left(1 + 2\cos\alpha\cos\beta\cos\gamma - \cos^2\alpha - \cos^2\beta - \cos^2\gamma\right)}$$

$$\times \left\{ \begin{array}{l} \dfrac{h^2\sin^2\alpha}{\bar{a}^2} + \dfrac{k^2\sin^2\beta}{\bar{b}^2} + \dfrac{l^2\sin^2\gamma}{\bar{c}^2} + \dfrac{2hk}{\bar{a}\bar{b}}\left(\cos\alpha\cos\beta - \cos\gamma\right) \\[2mm] + \dfrac{2kl}{\bar{b}\bar{c}}\left(\cos\beta\cos\gamma - \cos\alpha\right) + \dfrac{2lh}{\bar{a}\bar{c}}\left(\cos\gamma\cos\alpha - \cos\beta\right) \end{array} \right\} \quad (3\text{-}8)$$

Equation (3-8) is the spacing formula for the general triclinic crystal. The formula simplifies significantly for the other systems.

For a rhombohedral structure, $a = b = c$ and $\alpha = \beta = \gamma$. Accordingly, Eq. (3-8) reduces to

$$\frac{1}{d_{hkl}^2} = \frac{\left(h^2 + k^2 + l^2\right)\sin^2\alpha + 2\left(hk + kl + lh\right)\left(\cos^2\alpha - \cos\alpha\right)}{a^2\left(1 + 2\cos^3\alpha - 3\cos^2\alpha\right)}$$

In Bragg's law ($\lambda = 2d_{hkl}\sin\theta$), $\lambda_{Cu_{K\alpha}} = 1.5418\ \text{Å}$,

$$\left(\frac{\sin\theta_{hkl}}{0.7709}\right)^2 = \frac{(h^2 + k^2 + l^2)\sin^2\alpha + 2(hk + kl + lh)(\cos^2\alpha - \cos\alpha)}{a^2(1 + 2\cos^3\alpha - 3\cos^2\alpha)} \quad (3\text{-}9)$$

The rhombohedral cell volume is also determined:

$$V = a^3\sqrt{1 + 2\cos^3\alpha - 3\cos^2\alpha} \quad (3\text{-}10)$$

3.1.2 Discussion

X-ray diffraction (XRD) was utilized to determine the structural parameters of all the crystals $CsGe(Br_xCl_{1-x})_3$ and $(Rb_yCs_{1-y})GeBr_3$. The synthesized crystals were crushed, ground and sieved. X-ray

diffractograms were obtained at room temperature using Cu–K$_\alpha$ radiation with Siemens D5000 equipment. An extra CsCl crystal was used as an internal standard to determine the lattice parameters. The measured pattern was indexed and analyzed, as in the full-profile Rieltvelt refinement, using the non-profited program *PowderCell* [3-3], which was developed by W. Kraus and G. Nolze. The structural parameters of CsGe(Br$_x$Cl$_{1-x}$)$_3$ and (Rb$_y$Cs$_{1-y}$)GeBr$_3$ were compared with those of CsGeCl$_3$(R3m, No.160), CsGeBr$_3$(R3m, No.160) and RbGeBr$_3$(Pn21a, No.33) which have been presented in JCPDS [3-4, 3-5, 3-6, 3-7, 3-8]. The peak-splitting caused by structural non-centrosymmetry, occurs mainly from $2\theta = 15°$ to $35°$ (Figs. 3-3 and 3-4). The X-ray diffraction peaks shifted gradually as the substitute composition changed (Fig. 3-5). Certain strong diffraction peaks were observed at $2\theta = 31.76°$, $27.66°$, $26.86°$, $22.60°$, $22.10°$, $15.76°$ in CsGeBr$_3$. These diffraction patterns were compared with those with JCPDS and were indexed as (200), $(1\bar{1}1)$, (111), $(1\bar{1}0)$, (110) and (100) planes, respectively. They were also verified that CsGe(Br$_x$Cl$_{1-x}$)$_3$ (x=0, 1/6, 1/4, 2/6, 3/6, 4/6, 3/4, 5/6, 1) and (Rb$_y$Cs$_{1-y}$)GeBr$_3$ (y=0, 1/4, 2/4, 3/4) are crystallized in the non-centrosymmetric rhombohedral space group R3m. The splitting

43

differences between $(1\bar{1}1)$ and (111) and between $(1\bar{1}0)$ and (110) decline as the Br content decreases in $CsGe(Br_xCl_{1-x})_3$.

In an ideal perovskite structure, the cell parameters were $a = b = c$ and $\alpha = \beta = \gamma = 90°$ with cubic space group Pm−3m (No. 221). Examples are the high-temperature phase of cubic $CsGeCl_3$ and $CsGeBr_3$ [3-4, 3-5, 3-6, 3-7, 3-8]: the cell parameters of cubic $CsGeBr_3$ are $a = b = c = 5.362$ Å and $\alpha = \beta = \gamma = 90°$. The cell edges of rhombohedral (room-temperature phase) $CsGeBr_3$ were longer than those of cubic (high-temperature) phase (Fig. 3-6), and the cell angles of rhombohedral (room-temperature phase) $CsGeBr_3$ were slightly smaller than 90° (Fig. 3-7). The structural distortion contributes to the optical nonlinearity of $CsGeBr_3$. Structural parameters obtained from Figs. 3-6, 3-7 and 3-8 revealed that the lattice constant (or cell volume) increased with Br content while the cell angle became smaller. Accordingly, the structural distortion of $CsGe(Br_xCl_{1-x})_3$ (R3m) increases with Br content. In contrast, Figs. 3-9 and 3-10 indicate that the lattice constant (or cell volume) became smaller as the Rb content increased, while the cell angle became larger. Hence, the structure of $(Rb_yCs_{1-y})GeBr_3$ gradually becomes centro-symmetric as Rb content increases.

3.2 Theoretical methods for designing materials from NLO crystals

3.2.1 Theory [3-9, 3-10, 3-11, 3-12, 3-13, 3-14]

Over the last few years, first-principles calculations based on Kohn-Sham (KS) density functional theory [3-9] have attracted enormous interest among solid-state physicists and chemists. This investigation utilizes a package, which was developed by the theoretical group led by Professor M. C. Payne [3-10] of Cambridge University, U.K.. This program (hereafter called the Cambridge Sequential Total Energy Package, CASTEP) is used to perform total energy pseudo-potential calculations to solve KS equations concerning the electronic states of systems that contain arbitrary arrangements of atoms. These calculations yield the ground state energy and charge density of the system, enabling any physical quantity related to total energies (such as lattice constants, elastic constants, molecular geometries and others) to be computed. The only input to the calculations is the atomic number of each constituent atomic species. Ionic potentials are replaced with pseudo-potentials. The electronic wavefunctions are expanded in terms of a plane wave basis set and the electron-electron interactions are considered through the use of

density functional theory [3-11]. The use of pseudo-potentials significantly reduces the calculation burden for large numbers of plane waves. Two direct methods are usually adopted to calculate the KS ground-state total energy: (1) direct determination of the minimum of the KS total-energy functional, proposed by Car and Parrinello [3-12]; (2) an iterative approach to the diagonalization of the KS Hamiltonian in conjunction with iterative improvement of the charge density or the potential self-consistently [3-10]. Both methods have been implemented using the CASTEP package.

CASTEP uses preconditioned conjugate gradient approaches [3-10] to relax the electronic configuration to its ground state. Moreover, it employs fast Fourier transforms to reduce the computational cost and memory required to calculate Hamiltonian product that acts on the electronic wavefunctions. The integration over the Brillouin zone (BZ) is further reduced to a summation over a finite number of k-points by a special k-points sampling technique that was developed by Monkhorst and Pack [3-13]. In this pseudo-potential-plane wave calculation scheme, two parameters typically used to control the convergence are the kinetic energy cutoff of the plane waves basis set E_{cut} and the number of special k

points in the Brillouin-zone integration N_{kpt}. The combination of the above concepts is crucial to the efficiency of modern total energy pseudo-potential calculations.

The structural stability and bulk modulus of a new material can be predicted quite accurately based on a calculation of ground state total energy. The calculation proceeds as follows.

(1) First, the cell volume is isotropically varied and the internal coordinates relaxed to minimize the total energy and the stress for a given cell volume.

(2) The obtained total energy versus cell volume $E_{tot}(v)$ is called the equation of state (EOS) of a solid.

(3) Fit the calculated $E_{tot}(v)$ to the following equation [3-14];

$$E_{tot}(v) = \frac{B_0 v}{B_0'}[(\frac{v_o}{v})^{B_0'}\frac{1}{(B_0'-1)}+1]+\text{constant}$$

with B_0 and B_0' as the free parameters. Here, B_0 and $B_0' = dB_0/dP|_{v_o}$ are the bulk modulus and its derivative with respect to pressure in equilibrium geometry.

3.2.2 Discussion

Figures 3-11 through 3-19 present the unit cell of constituent atoms

that are input to the calculation. Figures 3-20 through 3-28 display the results of the corresponding simulations. Figures 3-20 and 3-28 demonstrate that the diffraction peaks from the JCPDS database and the calculations are all identical to those obtained experimentally. Hence, the simulation was successfully. Since JCPDS includes no information on $CsGe(Br_xCl_{1-x})_3$ for $x = 1/6 \sim 5/6$, the results of the simulation are compared to the experimental results. According to Figs. 3-21 to 3-27, the location of the simulated diffraction peaks are identical to those of the experimental diffraction peaks (including the C-series and the B-series), revealing that the anion of $CsGe(Br_xCl_{1-x})_3$ is substituted well, and the crystals are in solid solution. The difference between the intensities of a particular diffraction peak arises from the fact that each crystal is assumed to be large, perfect and single in the simulation, so the diffraction intensity is high; however, the experimental specimens are polycrystalline crystals and the destructive interference that comes from various crystal boundaries reduces the diffraction intensity.

3.3 Raman scattering analysis

3.3.1 Theory [3-15, 3-17, 3-23]

The classical description of the Raman effect treats a scattering molecule as a collection of atoms that undergo simple harmonic vibrations and the quantization of the vibrational energy is neglected.

When a molecule is placed in an electric field, its electrons are displaced relative to its nuclei, producing an electric dipole moment. In small fields, the induced dipole moment μ_i is proportional to the field strength ε.

$$\mu_i = \alpha\varepsilon \qquad (3\text{-}11)$$

The coefficient of proportionality α is the polarizability of the molecule with which the electron cloud of the molecule can be distorted. A fluctuating electric field can generate a fluctuating dipole moment of the same frequency. An electric field which generated electromagnetic radiation can be expressed as,

$$\varepsilon = \varepsilon^0 cos2\pi t v_0 \qquad (3\text{-}12)$$

where ε^0 is the equilibrium field strength and v_0 is the angular frequency of the radiation. Therefore, electromagnetic radiation can induce a fluctuating dipole of frequency v_0 in the molecule. This

49

induced dipole will emit or scatter radiation of frequency v_0. This process is called Rayleigh scattering.

Consider a diatomic molecule that vibrates with a frequency of v_v. If it undergoes simple harmonic vibrations, then a coordinate q_v along the axis of vibration at time t, is

$$q_v = q_0 cos2\pi v_v t \qquad (3\text{-}13)$$

If the polarizability varies during the vibration, its value for a small vibrational amplitude will be

$$\alpha = \alpha^0 + \left(\frac{\partial\alpha}{\partial q_v}\right)_0 q_v \qquad (3\text{-}14)$$

Substituting Eq. (3-13) into Eq. (3-14) yields

$$\alpha = \alpha^0 + \left(\frac{\partial\alpha}{\partial q_v}\right)_0 q_0 cos2\pi v_v t \qquad (3\text{-}15)$$

If the incident radiation of frequency v_0 interacts with the molecule, then according to Eqs. (3-11) and (3-12),

$$\mu_i = \alpha\varepsilon = \alpha\varepsilon^0 cos2\pi v_0 t \qquad (3\text{-}16)$$

Substituting Eq. (3-15) into Eq. (3-16) yields

$$\mu_i = \alpha^0 \varepsilon^0 cos2\pi v_0 t + \left(\frac{\partial\alpha}{\partial q_v}\right)_0 \varepsilon^0 q_0 cos2\pi v_v t\ cos2\pi v_0 t$$

which can be rewritten as

$$\mu_i = \alpha^0 F^0 cos2\pi v_0 t + \left(\frac{\partial \alpha}{\partial q_v}\right)_0 \frac{\varepsilon^0 q_0}{2} \times \left[cos2\pi\left(v_0+v_v\right)t+cos2\pi\left(v_0-v_v\right)t\right] \quad (3\text{-}17)$$

The first term in Eq. (3-17) specifies the Rayleigh scattering and the remaining terms describe the Stokes and the anti-Stokes Raman scattering. Equation (3-17) indicates that light is scattered with frequencies,

v_0 = Rayleigh scatter

and

$v_0 \pm v_v$ = Raman scatter

Accordinglly, Eq. (3-17) demonstrates that for Raman scattering to occur,

$$\left(\frac{\partial \alpha}{\partial q_v}\right)_0 \neq 0 \quad (3\text{-}18)$$

such that the polarizability of the molecule must vary during the vibration if that vibration is to be Raman active.

The quantum theory approach to Raman scattering acknowledges that the vibrational energy of a molecule is quantized. A non-linear molecule will undergo 3N-6 normal vibrations and a linear molecule will have 3N-5, where N represents the number of atoms in the molecule. The energy of each of these vibrations will be quantized according to the relationship,

$$E_v = hv(n+1/2) \quad (3\text{-}19)$$

where v is the frequency of the vibration and n is the vibrational quantum number that controls the energy of that particular vibration and takes values 0, 1, 2, 3, …. . Perturbation theory is applied to introduce quantization into Raman scattering theory. For simplicity, this approach applies perturbations to the ground state molecular wavefunctions until new wavefunctions are obtained which describe the vibrational excited state. The transition from the ground state can then be regarded as have been achieved by perturbing a wavefunction by the sum of the applied perturbations. This perturbed wavefunction has a corresponding energy and provides a useful visual description of Raman scattering as the vibrational transitions occur via this virtual energy level (Fig. 3-29).

Rayleigh scattering arises from transitions that start and finish at the same vibrational energy level. Stokes Raman scattering arises from transitions that start in the ground state and end at a higher vibrational energy level, whereas anti-Stokes Raman scattering involves a transition from higher to lower vibrational energy. At room temperature, most molecular vibrations are in the ground n = 0 state and anti-Stokes transitions are therefore less likely to occur than the Stokes transitions, such that the Stokes Raman scattering is more intense. This difference in

intensity becomes greater as the energy of the vibrations increases and the higher vibrational energy levels become less populated at a particular temperature. Consequently, the Stokes Raman scattering is usually studied when Raman spectroscopy is considered.

3.3.2 Vibration modes [3-15, 3-16, 3-17, 3-18, 3-19, 3-20, 3-21]

Perovskite (ABX_3) has four types of crystal structures, as cubic (O_h), tetragonal (C_{4v}), orthorhombic (C_{2v}) and trigonal (C_{3v}) symmetries (Fig. 3-30). Each ABX_3 unit cell consists of five atoms, such that the cell has 15 degrees of freedom (Table 3-1). Three degrees of freedom are associated with the translation motion of the unit cell; another three concern the torsional motion of the unit cell, and the others concern the vibrational motion. Three of the vibrational motion modes involved $A \longleftrightarrow BX_3$ vibration, and the others were caused by BX_3 inner vibration.

If BX_3 is regarded as a single atom at a B-site, the $A \longleftrightarrow BX_3$ vibration can be simplified as a double-atom-vibration, such as of CsCl. When the phase exhibits perfect cubic symmetry, the vibration is triply degenerate vibration since $a=b=c$. In the perovskite structure, the B

53

atom is surrounded by six X atoms. The cubic symmetry (O_h point group) has six optical modes — A_{1g}, E_g, F_{1u}, F_{1u}, F_{2u} and F_{2g}. The F_{2u} mode is silent and the F_{1u} modes are only infrared active, so no Raman activity occurs in the phase with perfect cubic symmetry.

Figure 3-31 has two F_{1u} modes. The B-X bond defined the direction of the z-axis; two X atoms on the z-axis were labeled O_1, while the others in the x-y plane were named O_2. The vibration in Fig. 3-31(a) was stretching, while that in Fig. 3-31(b) was bending. Both were triply degenerate vibrations since $a=b=c$ (cubic). When the cubic perovskite structure is transformed into a less symmetrical one, these vibration modes are split (Table 3-2). In tetragonal symmetry (C_{4v}), the length of the B-O_1 bond differs from that of the B-O_2 bond. Hence, each of the F_{1u} modes splits into a doubly degenerate E (from the xy plane) mode and a nondegenerate A_1 (from the z axis) mode, and the F_{2u} mode splits into E and B_1 modes. All of the A_1 and E modes are both Raman and infrared active while the B_1 mode is only Raman active. When the structure is transformed from tetragonally symmetric to orthorhombically (C_{2v}) symmetric, the E mode splits into two nondegenerate B_1 and B_2 modes. However, the E mode, which came from the F_{2u} mode, splits into two

54

nondegenerate A_1 and A_2 modes, because the tetragonal (C_{4v}) axis angle

differs from the orthorhombic axis angle (C_{2v}). From group theory, the

vibration modes associated with triagonal (C_{3v}) and tetragonal (C_{4v})

symmetries are identical. The A_2 mode is silent and the B_1 mode is only

Raman-active.

3.3.3 Discussion

For the Raman scattering measurements, the $CsGe(Br_xCl_{1-x})_3$ and

$(Rb_yCs_{1-y})GeBr_3$ samples were illuminated at room temperature using an

argon ion laser at 488 nm with an average power of 30 mW. Figures 3-32

and 3-33 plot the results. The Raman peaks were shifted with the Br

content, consistent with the fact that the phonon frequency is inversely

proportional to the square root of the mass of GeX_3 (X = Cl, Br). The

results of peak-fitting (Figs. 3-34 through 3-37) agree well with the

Raman spectra of CGC and CGB [3-6, 3-22]. Tables 3-3 through 3-5

summarize the results. The strongest Raman (column "vs peak") are

attributed to the A_1 mode. Raman peaks from 262 cm^{-1} to 292 cm^{-1}

(column "w_2 peak") are also associated with the A_1 mode. Another group

of Raman peaks (from 159 cm^{-1} to 165 cm^{-1} (column "ls peak")) can be

attributed to the E mode. The other group of Raman peaks (from 209 cm^{-1} to 237 cm^{-1} (column "s_2 peak")) is associated with the A_1+E mode and the A_1 mode for $CsGe(Br_xCl_{1-x})_3$ and $(Rb_yCs_{1-y})GeBr_3$, respectively. Raman peaks of CGB at 419.21 cm^{-1} and 209.79 cm^{-1} are associated with the corresponding (50.5 cm^{-1}) overtones. Raman peaks of CGC at 236.98 cm^{-1} can be assigned to the corresponding (58.5 cm^{-1}) overtone. Accordingly, column "s_2 peak" and column "w_3 peak" are associated with the corresponding (column "w_1 peak") overtones (Figs. 3-38 and 3-39). However, column "w_3 peak" is assigned to the corresponding (column "s_2 peak") overtone for $(Rb_yCs_{1-y})GeBr_3$ (Fig. 3-40).

From Figs. 3-38 to 3-40 and Tables 3-3 to 3-5, columns "m, s_1, vs, ls, w_2 peak" are associated with the anion substitution. Column "ls peak" is associated with bromine atoms while column "w_2 peak" relates to only chlorine atoms. Columns "m, s_1, vs peak" are related to $Ge-X_3$ bonds. This result is consistent with the effective-mass concept: the oscillation frequency is expected to increase as the Br content declines because the Br atom is heavier than Cl. Columns "w_1, s_2, w_3 peak" are associated with the oscillation between Cs^+ and $Ge(Br_xCl_{1-x})_3^-$ because they are less influenced by the anion substitution. In column "s_2 peak", Raman signals

56

were changed from the anion vibration A_1+E modes to the cation vibration A_1 modes, indicating that the relative vibration between Cs^+ and the anion cluster $Ge(Br_xCl_{1-x})_3^{-1}$ was transformed to the doubly degenerate vibration of Ge$-$Br bonds.

3.4 Tables and Figures

Table 3-1 The vibration modes of cubic ABO_3 structure [3-15~20].

ABO_3
(15 freedoms)

translation motion   torsional motion   vibration
(3 freedoms)   (3 freedoms)   (9 freedoms)
F_2u

A<->BO_3 BO_3
(3 freedoms) F_1u inner vibration
(6 freedoms)

Strengthing vibration   Bending vibration
(3 freedoms) F_1u (3 freedoms)
F_1u
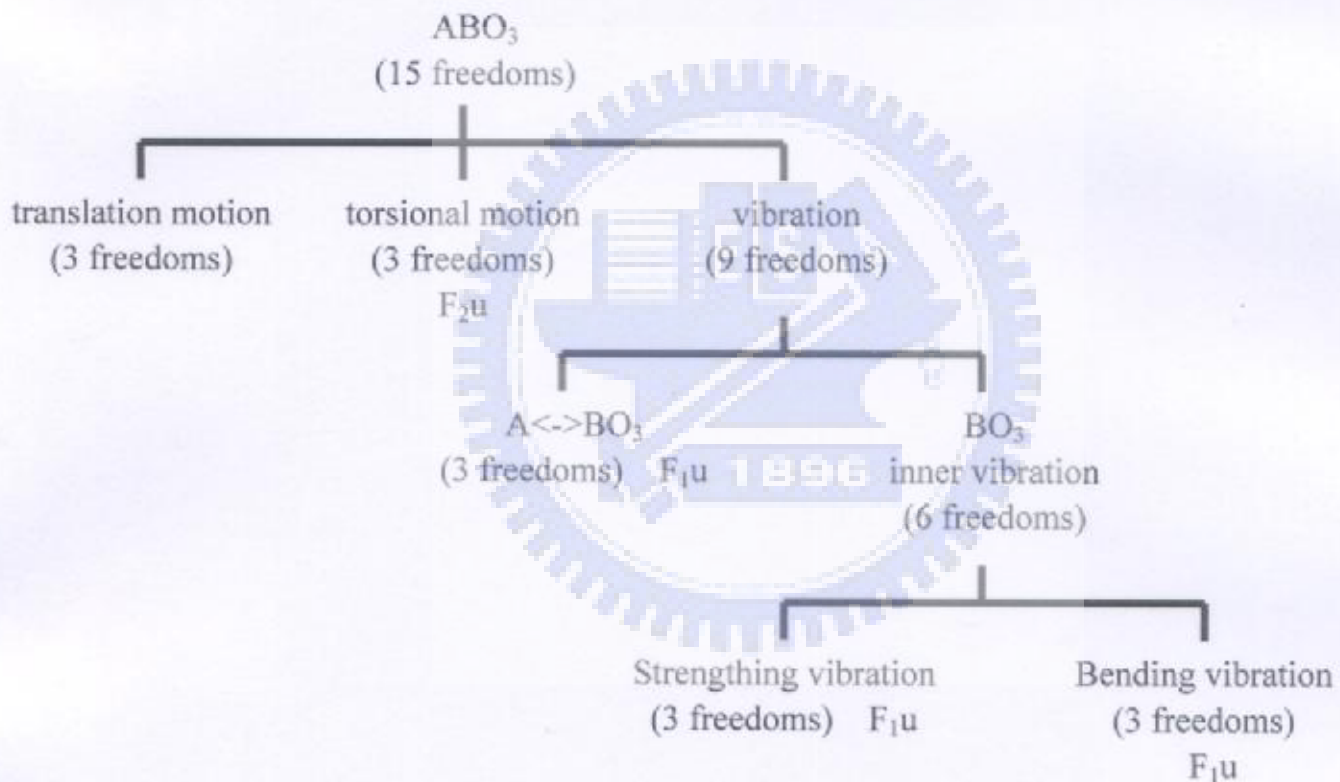
Table 3-2 The structures of perovskite and their vibration modes
[3-15~20].

Structure	point group	Vibration modes					
cubic	O_h	F_{1u}			F_{2u}		
tetragonal	C_{4v}	A_1	E		B_1	E	
orthorhombic	C_{2v}	A_1	B_1	B_2	B_2	A_1	A_2
trigonal	C_{3v}	A_1	E		A_2	E	

Table 3-3 The Raman spectra comparison for the ternary halides $CsGe(Br_yCl_{1-y})_3$ (B-series). The descriptions of the peaks are: "vs" = very strong, "s" = strong, "ls" = less strong, "m" = middle, and "w" = weak. The unit of these Raman peaks was labeled as cm^{-1}.

Specimens	w_1	m	s_1	vs	ls	s_2	w_2	w_3
symmetry	overtone			A_1	E	A_1		overtone
y = 1.00	49	77	91	139	160	210		Ref.[3-6,3-22]
y = 1.00	50.50	78.50	93.99	140.31	159.88	209.79	—	419.21
y = 0.86	51.99	81.71	94.41	141.88	162.22	210.57	264.10	419.51
y = 0.78	52.11	82.57	94.78	141.88	162.22	211.12	264.10	419.97
y = 0.70	52.78	83.18	95.57	142.66	163.00	211.69	263.33	420.67
y = 0.52	53.10	83.76	96.35	145.01	164.57	212.12	264.88	420.74
y = 0.35	54.57	89.27	102.64	152.05	—	212.35	265.65	421.54
y = 0.27	54.86	90.77	105.38	155.58	—	212.54	272.30	422.64
y = 0.19	55.36	91.63	107.36	158.31		230.36	273.78	—
	m	w	m	vs	ls	s		
symmetry				A_1	E	A_1		
y = 0.00	58.50	121.49	146.58	202.79	—	236.98	291.15	—
y = 0.00	57	120	145	200	—	237	290	Ref.[3-6,3-22]

Table 3-4 The Raman spectra comparison for the ternary halides $CsGe(Br_xCl_{1-x})_3$ (C-series). The descriptions of the peaks are: "*vs*" = very strong, "*s*" = strong, "*ls*" = less strong, "*m*" = middle, and "*w*" = weak. The unit of these Raman peaks was labeled as cm^{-1}.

Specimens	w_1	m	s_1	vs	ls	s_2	w_2	w_3
symmetry	*overtone*			A_1	E	A_1		*overtone*
x = 1.00	49	77	91	139	160	210	—	Ref.[3-6,3-22]
x = 1.00	50.50	78.50	93.99	140.31	159.88	209.79	—	419.21
x = 0.82	51.48	81.39	94.29	141.09	161.44	210.35	262.56	420.34
x = 0.79	52.32	82.97	94.78	142.66	163.00	211.25	264.10	421.27
x = 0.68	53.14	83.69	95.57	143.44	163.00	212.47	264.10	421.83
x = 0.51	53.94	84.18	95.57	144.23	163.78	212.90	264.10	421.50
x = 0.35	54.57	90.06	102.64	152.05	—	212.12	265.65	422.02
x = 0.26	55.08	91.27	103.43	152.84	—	212.58	268.48	423.37
x = 0.18	56.13	93.21	109.71	160.66	—	229.39	275.45	—
	m	w	m	vs		ls	s	
symmetry				A_1		E	A_1	
x = 0.00	58.50	121.49	146.58	202.79	—	236.98	291.15	—
x = 0.00	57	120	145	200	—	237	290	Ref.[3-6,3-22]

Table 3-5 The Raman spectra comparison for the ternary halides $CsGe(Br_xCl_{1-x})_3$ and $(Rb_zCs_{1-z})GeBr_3$. The descriptions of the peaks are: "vs" = very strong, "s" = strong, "ls" = less strong, "m" = middle, and "w" = weak. The unit of these Raman peaks was labeled as cm^{-1}.

Specimens	m	w	m	vs		ls	s	
x = 0.00	57	120	145	200(A_1)	—	237(E)	290(A_1)	Ref.[3-6,3-22]
x = 0.00	58.50	121.49	146.58	202.79	—	236.98	291.15	
	w_1	m	s_1	vs	ls	s_2	w_2	w_3
x = 0.27	54.86	90.77	105.38	155.58	—	212.54	272.30	422.64
x = 0.52	53.10	83.76	96.35	145.01	164.57	212.12	264.88	420.74
x = 0.78	52.11	82.57	94.78	141.88	162.22	211.12	264.10	419.97
x = 1.00	50.50	78.50	93.99	140.31	159.88	209.79	—	419.21
x = 1.00	49	77	91	139(A_1)	160(E)	210(A_1)	—	Ref.[3-6,3-22]
z = 0.26	—	—	92.33	139.43	160.38	209.61	—	418.09
z = 0.52	—	—	92.42	138.29	159.33	207.77	—	416.49
z = 0.77	—	—	92.36	139.21	160.37	209.80	—	418.07
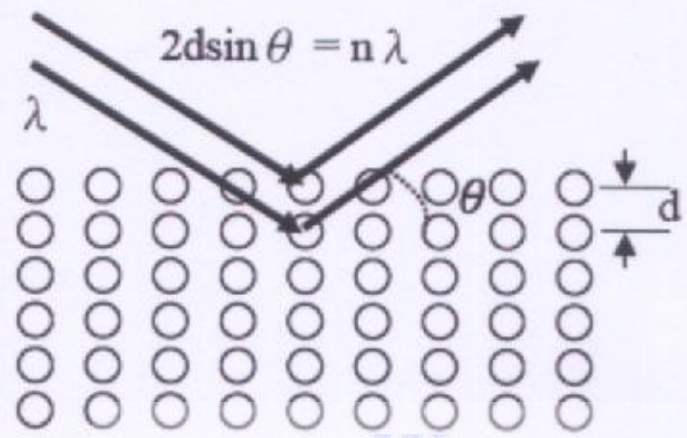
Fig. 3-1 X-ray diffraction from 2-dimensional periodic lattices [3-2].
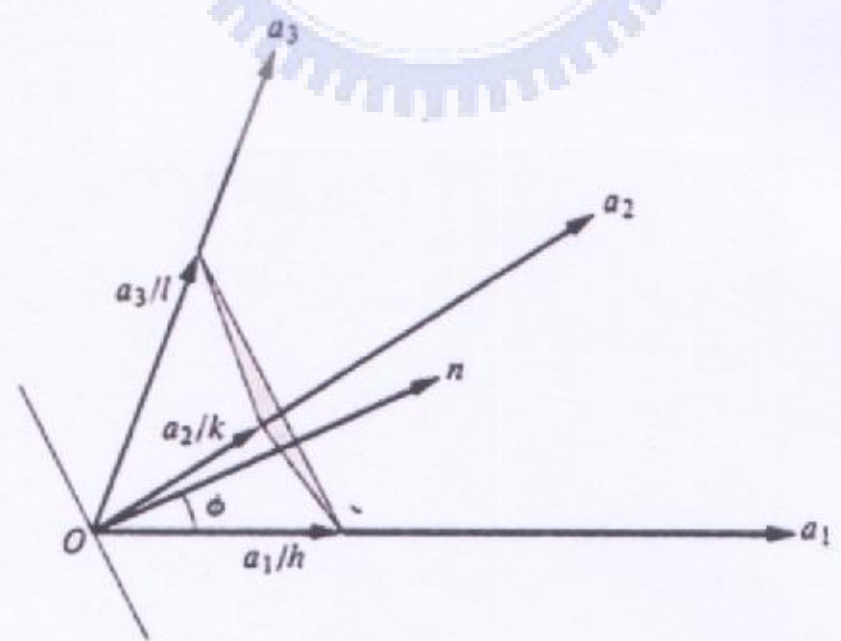
Fig. 3-2 Representation of the crystallographic planes *hkl* [3-2].
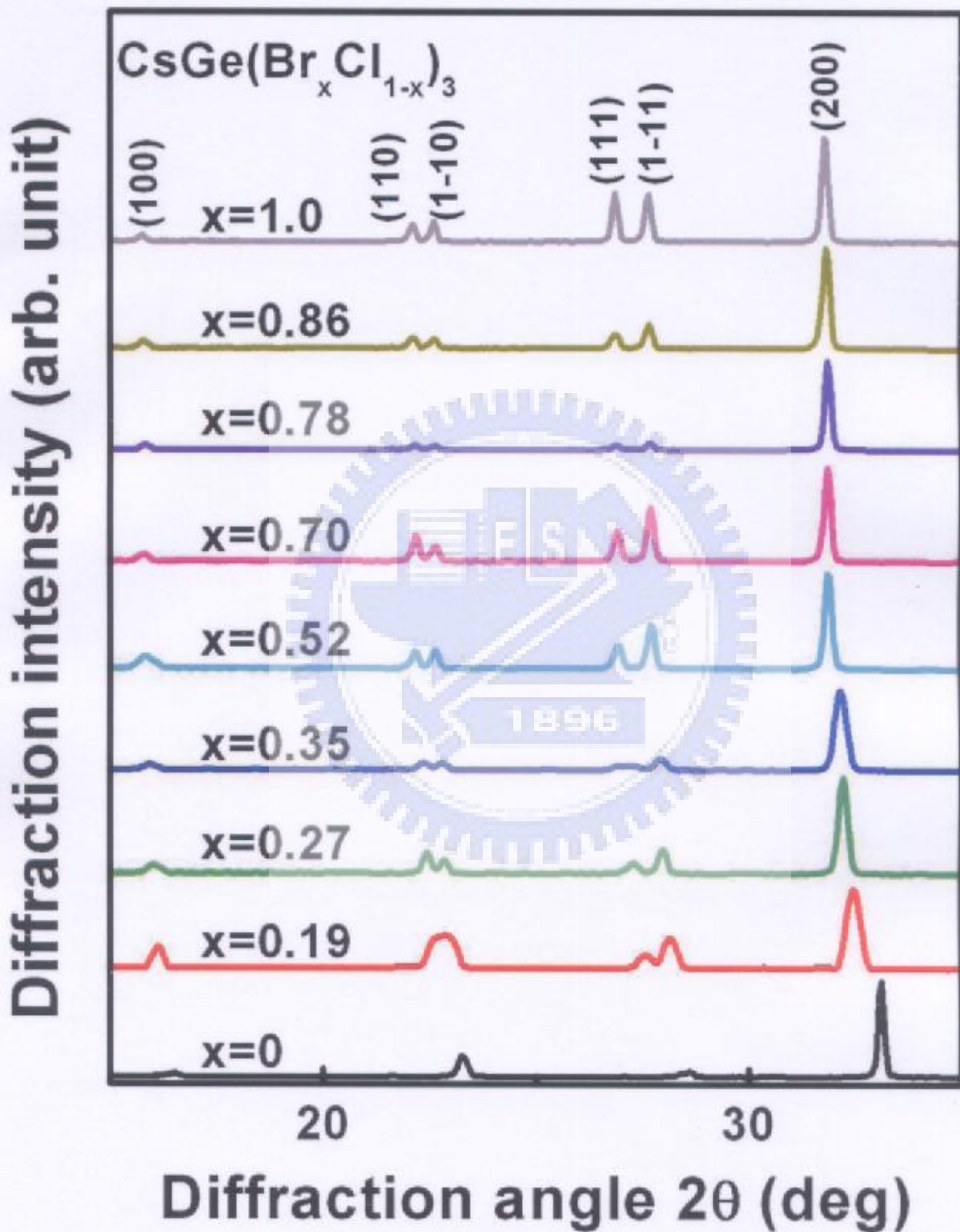
Fig. 3-3 The X-ray powder diffraction results for nonlinear optical crystals CsGe(Br$_x$Cl$_{1-x}$)$_3$.
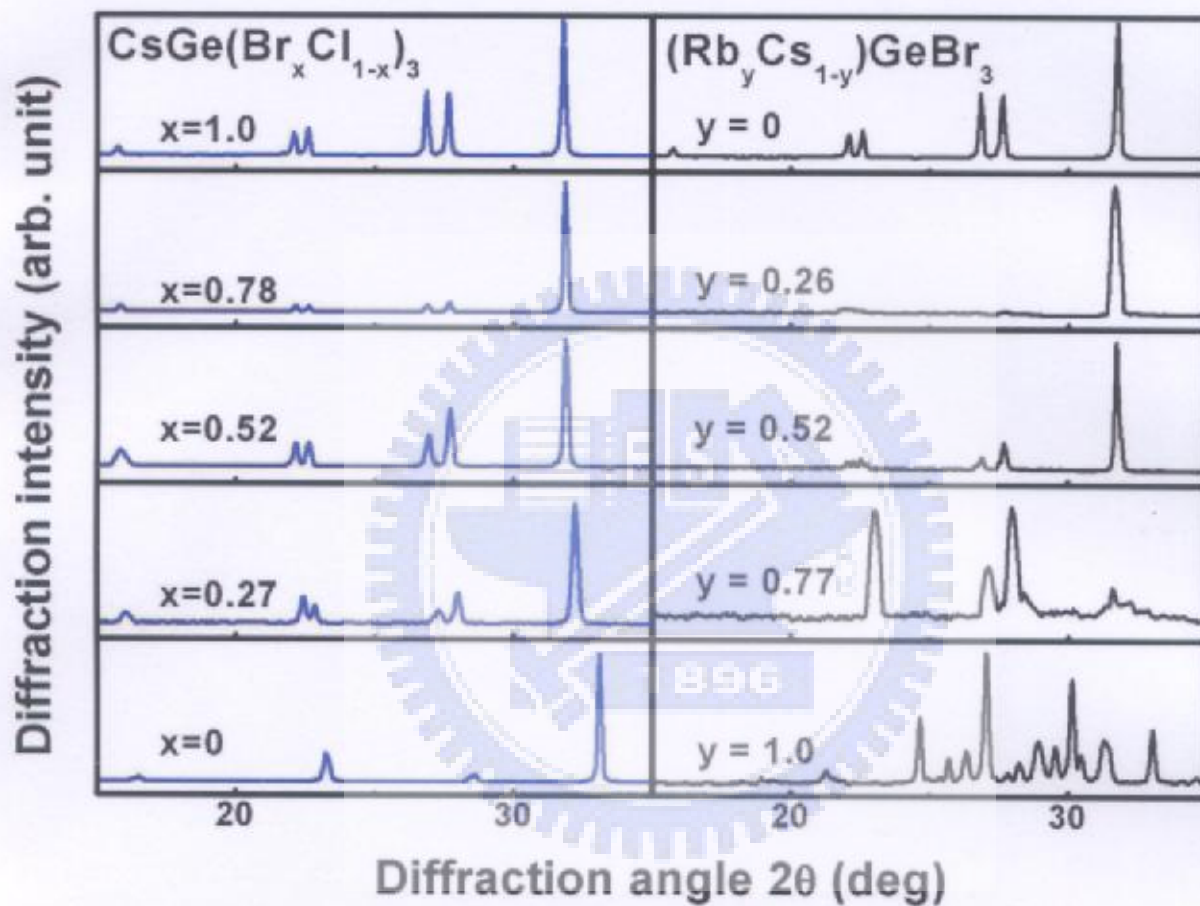
Fig. 3-4 The X-ray powder diffraction results for nonlinear optical crystals $CsGe(Br_xCl_{1-x})_3$ and $(Rb_yCs_{1-y})GeBr_3$.
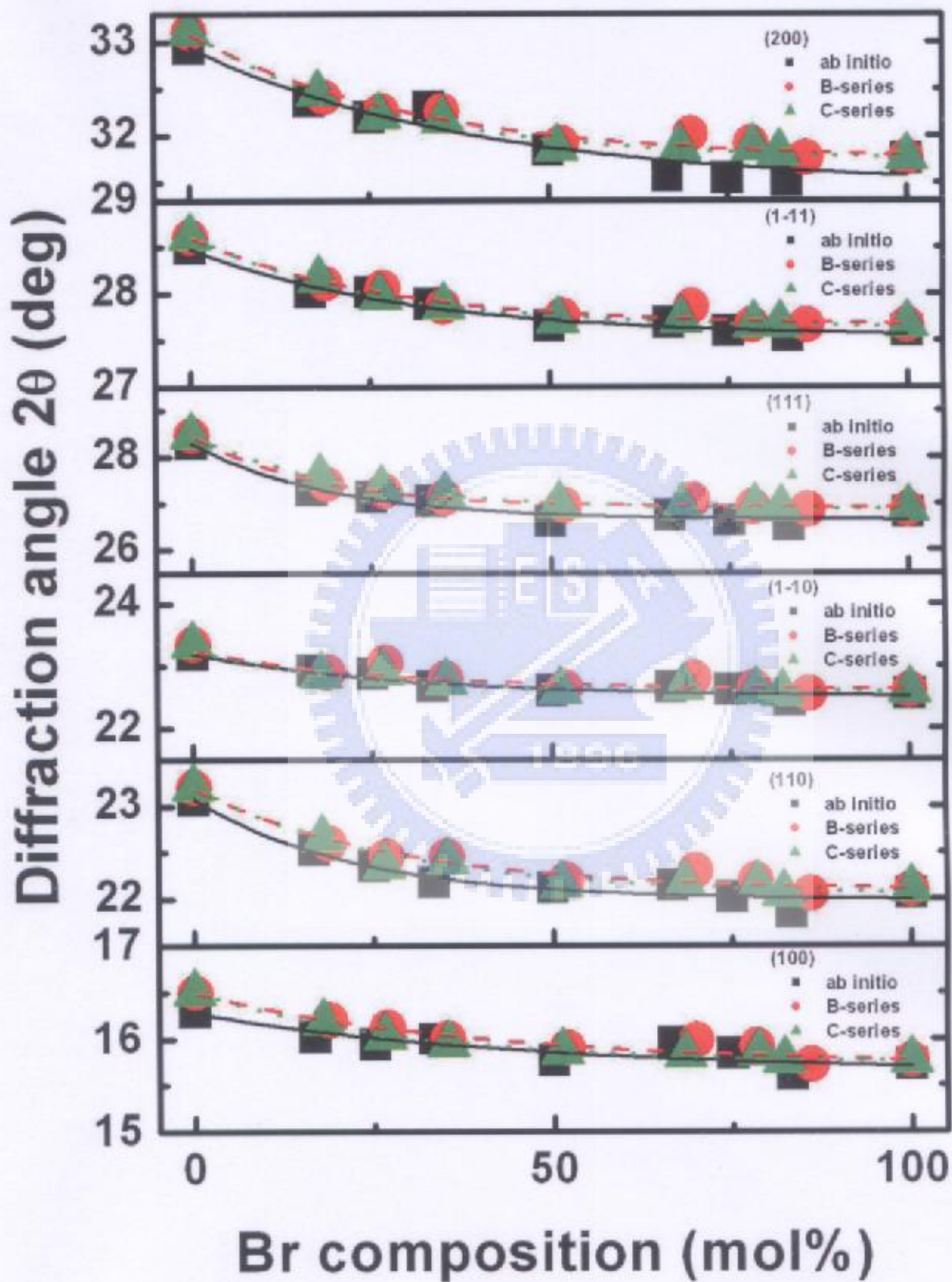
Fig. 3-5 The X-ray diffraction angle of $CsGe(Br_xCl_{1-x})_3$ determined by experiment and simulation.
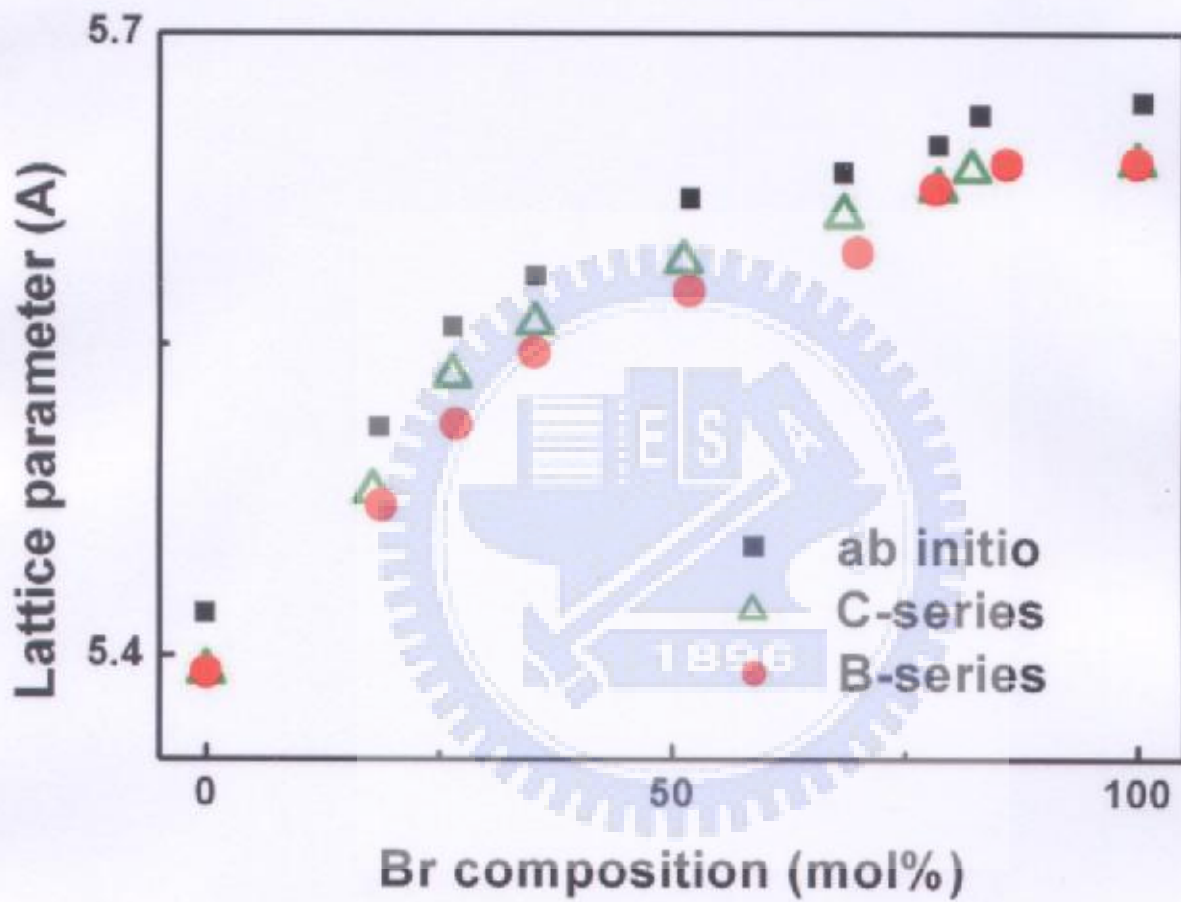
Fig. 3-6 The lattice constant of $CsGe(Br_xCl_{1-x})_3$ unit cell determined by experiment and simulation.
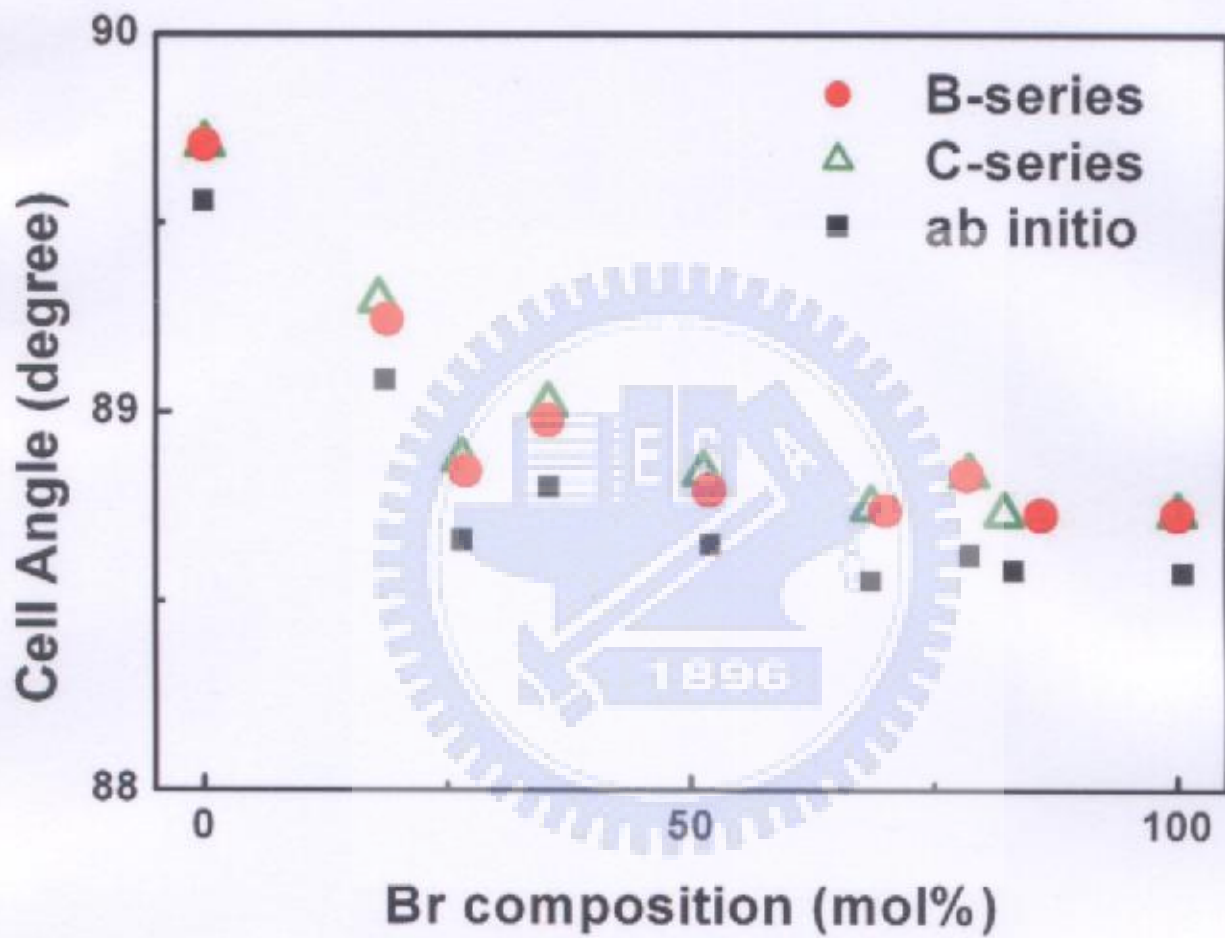
Fig. 3-7 The cell angle of $CsGe(Br_xCl_{1-x})_3$ unit cell determined by experiment and simulation.
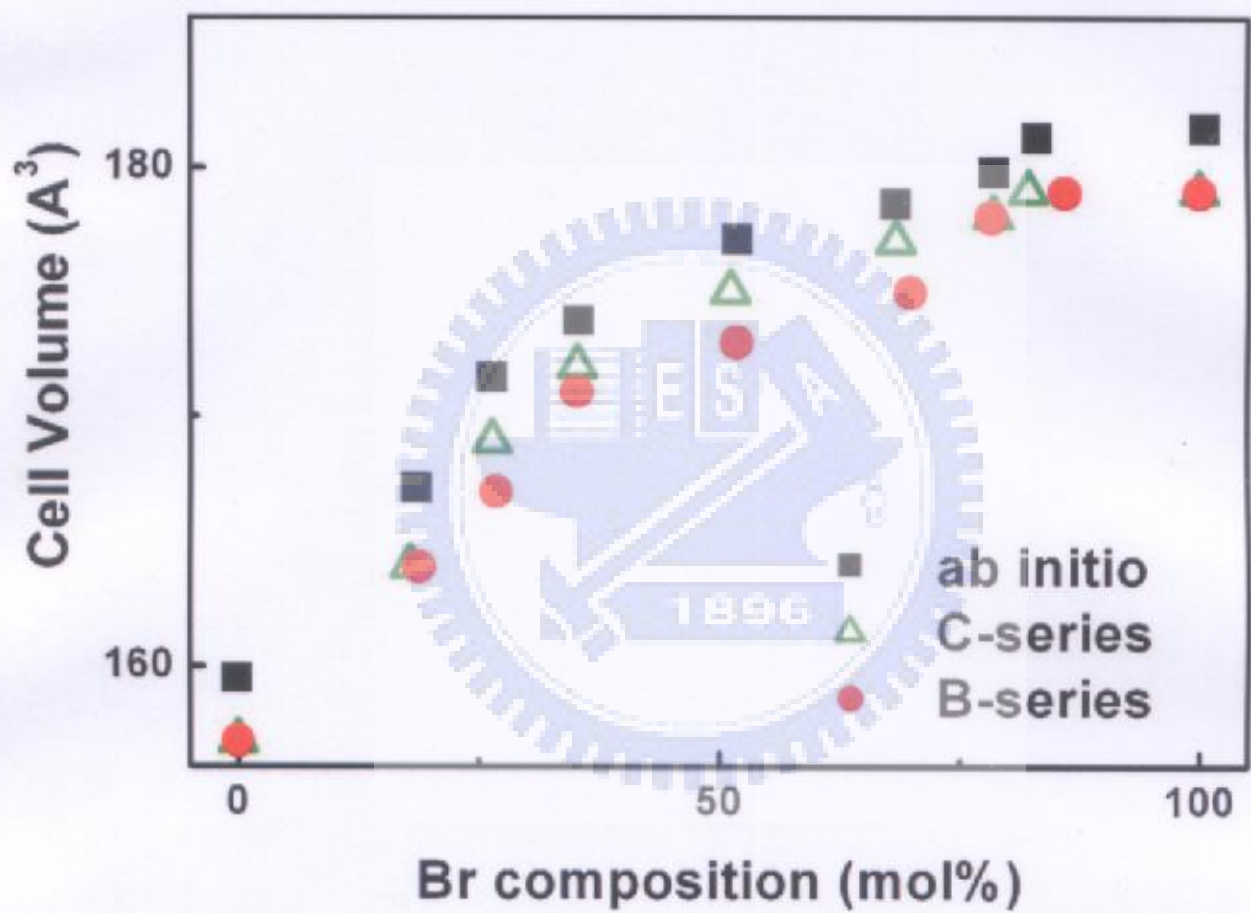
Fig. 3-8 The cell volume of $CsGe(Br_xCl_{1-x})_3$ unit cell determined by experiment and simulation.
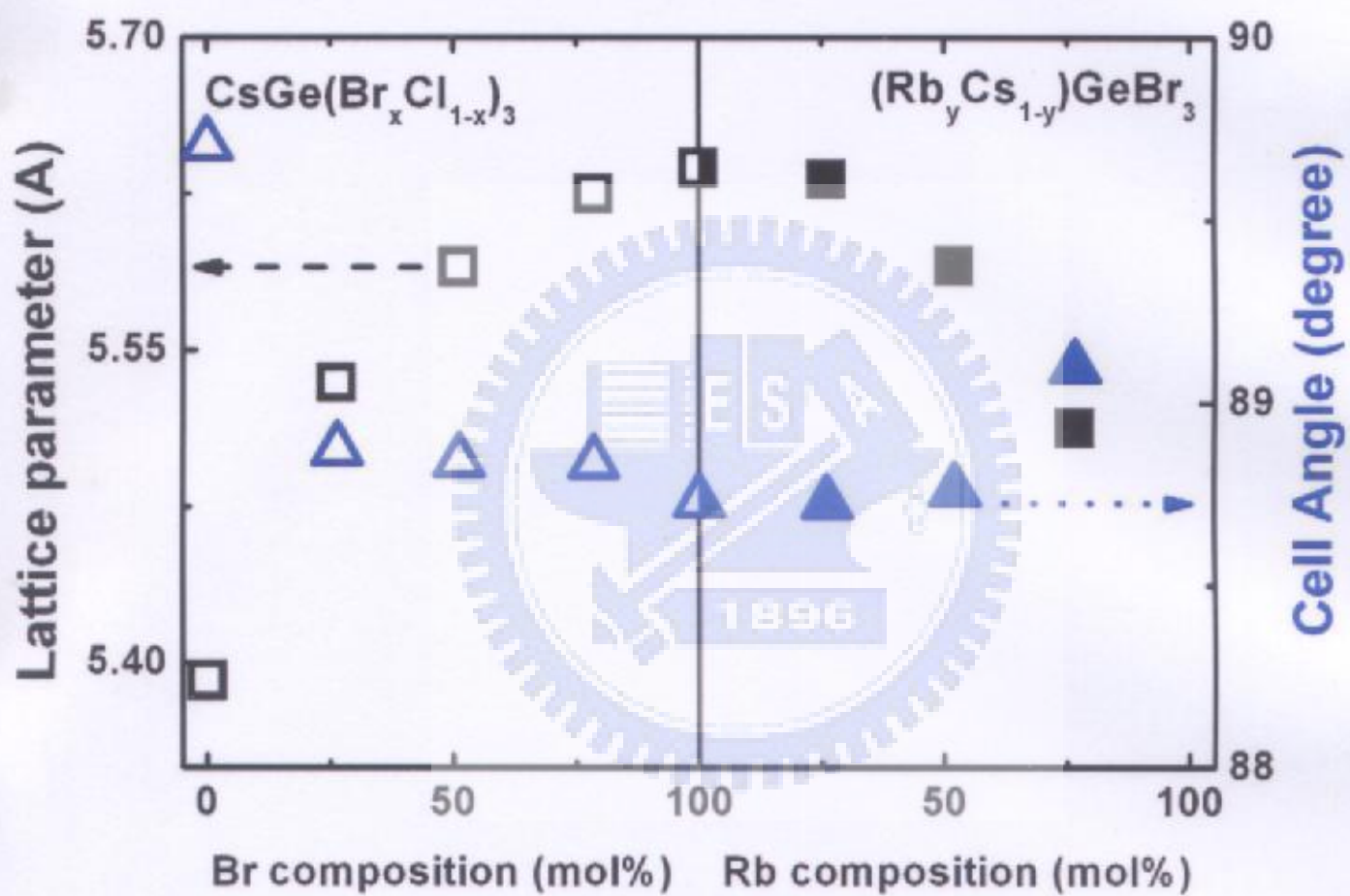
Fig. 3-9 Structural parameters of the NLO crystals $CsGe(Br_xCl_{1-x})_3$ and $(Rb_yCs_{1-y})GeBr_3$.
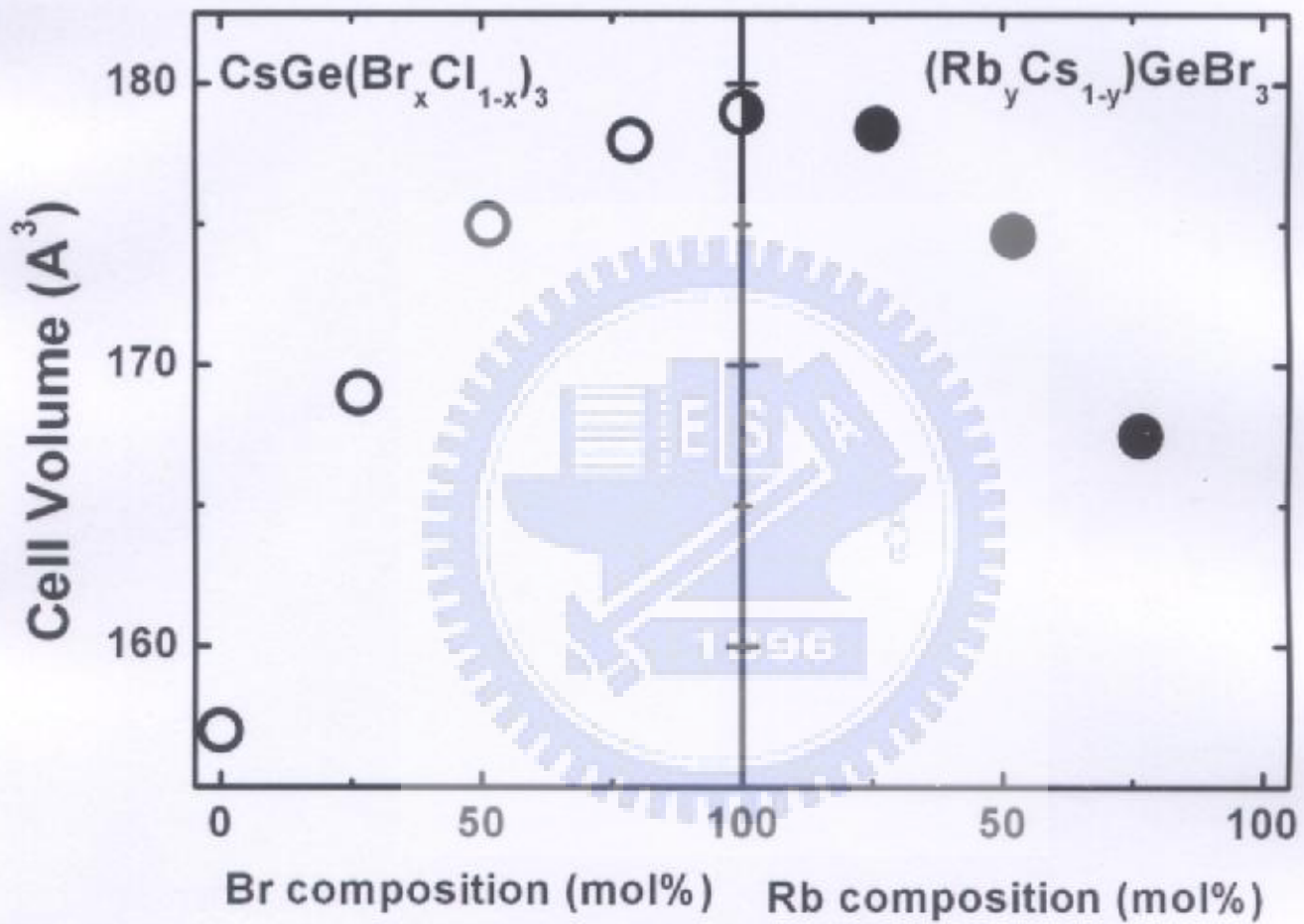
Fig. 3-10 The cell volume of the NLO crystals $CsGe(Br_xCl_{1-x})_3$ and $(Rb_yCs_{1-y})GeBr_3$.

	(hkl)	(200)	(1̄1̄1)	(111)	(1̄1̄0)	(110)	(100)
CGC	2θ	33.11	28.61	28.46	23.35	23.20	16.5
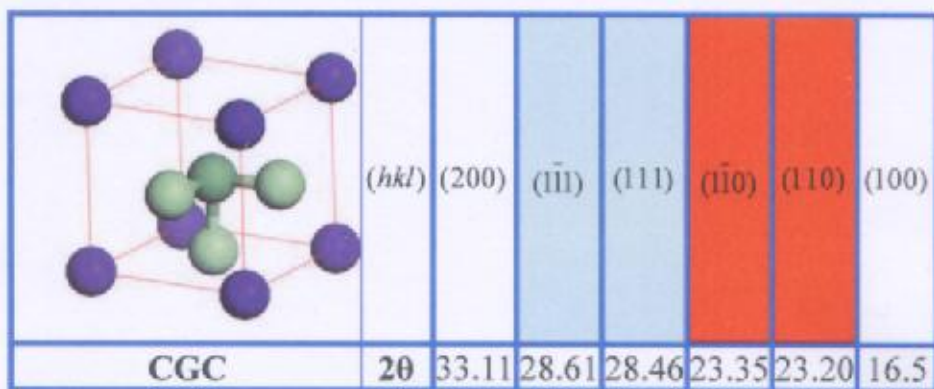
Fig. 3-11 The unit cell of constituent atoms that are input to the calculation for CsGeCl₃.
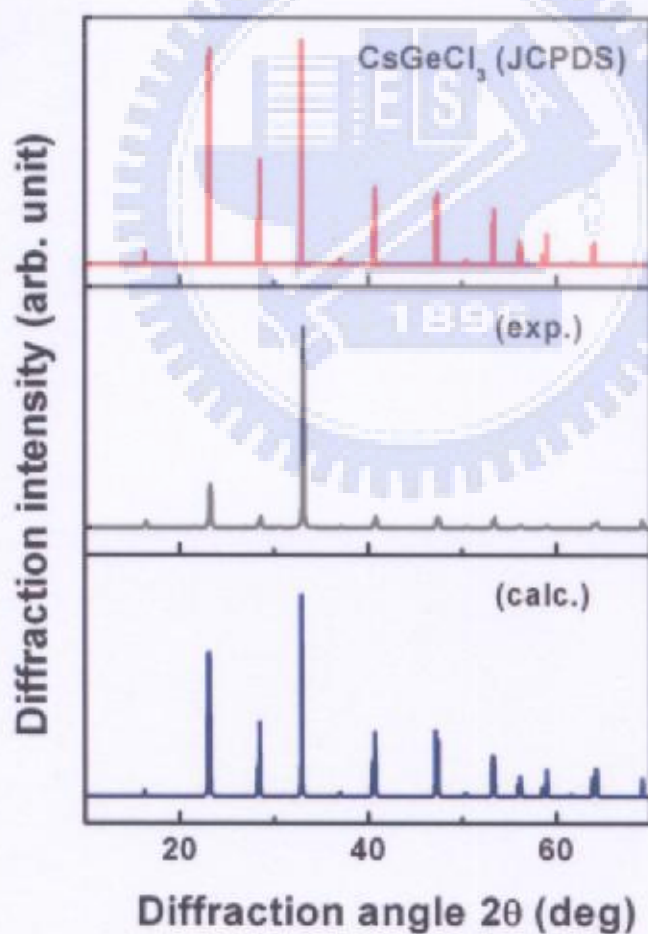
Fig. 3-20 The X-ray diffraction results for CsGeCl₃ determined by experiment and simulation.
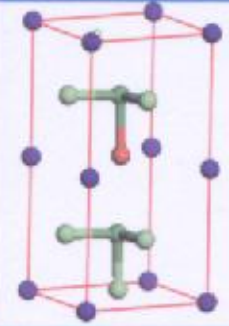
	(hkl)	(200)	(1$\bar{1}$1)	(111)	(1$\bar{1}$0)	(110)	(100)
C16	2θ	32.46	28.16	27.56	22.85	22.65	16.18
B16	2θ	32.41	28.11	27.41	22.90	22.60	16.20

Fig. 3-12 The unit cell of constituent atoms that are input to the calculation for $CsGe(Br_{1/6}Cl_{5/6})_3$.
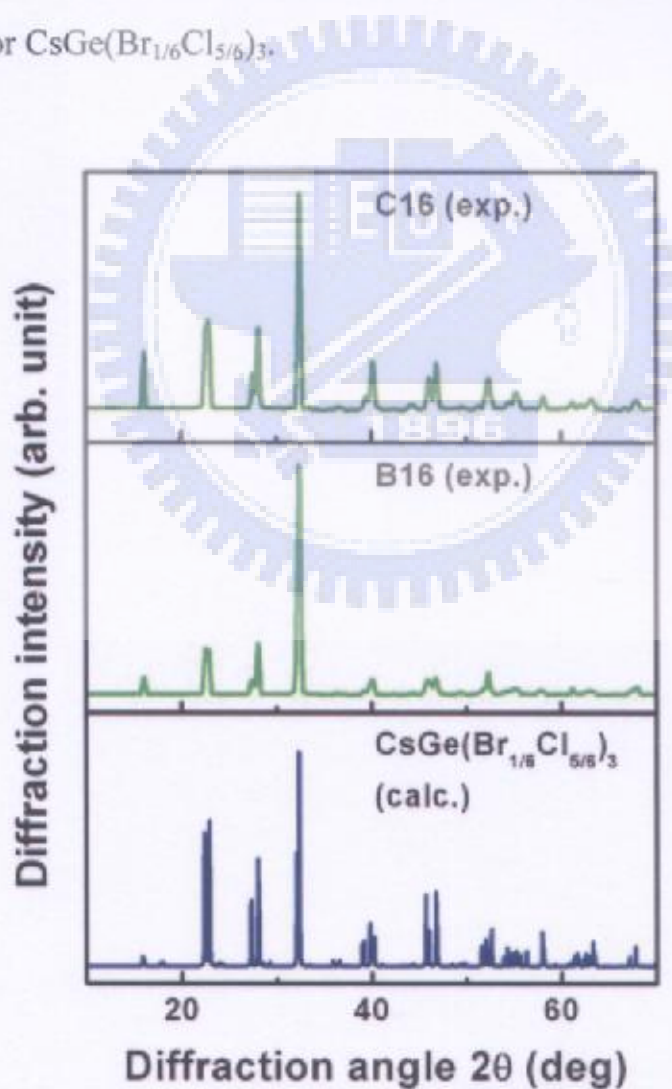
Fig. 3-21 The X-ray diffraction results for $CsGe(Br_{1/6}Cl_{5/6})_3$ determined by experiment and simulation.

	(hkl)	(200)	(1$\bar{1}$1)	(111)	(1$\bar{1}$0)	(110)	(100)
C14	2θ	32.21	27.96	27.31	22.90	22.36	16.02
B14	2θ	32.26	28.06	27.26	23.05	22.45	16.12
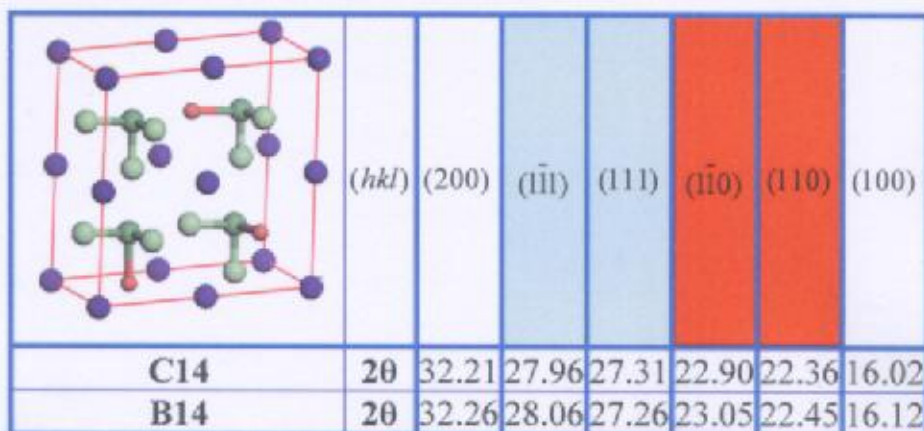
Fig. 3-13 The unit cell of constituent atoms that are input to the calculation for CsGe(Br$_{1/4}$Cl$_{3/4}$)$_3$.
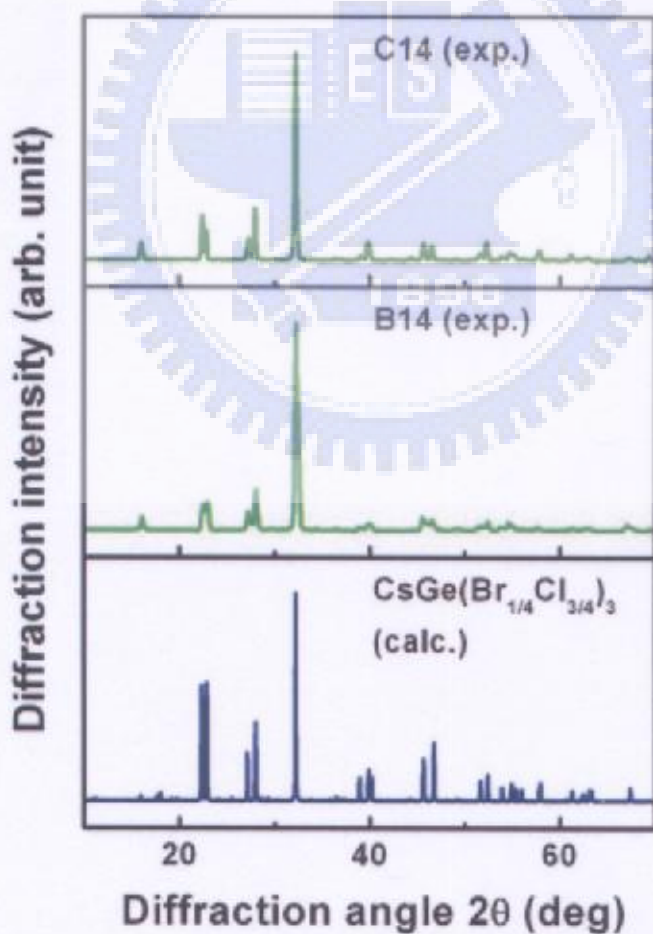
Fig. 3-22 The X-ray diffraction results for CsGe(Br$_{1/4}$Cl$_{3/4}$)$_3$ determined by experiment and simulation.
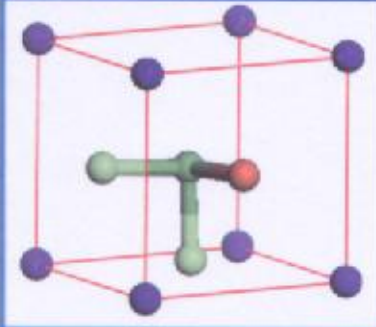
	(hkl)	(200)	$(1\bar{1}\bar{1})$	(111)	$(1\bar{1}0)$	(110)	(100)
C26	2θ	32.16	27.86	27.16	22.75	22.40	15.94
B26	2θ	32.26	27.86	27.11	22.80	22.45	16.00

Fig. 3-14 The unit cell of constituent atoms that are input to the calculation for $CsGe(Br_{2/6}Cl_{4/6})_3$.
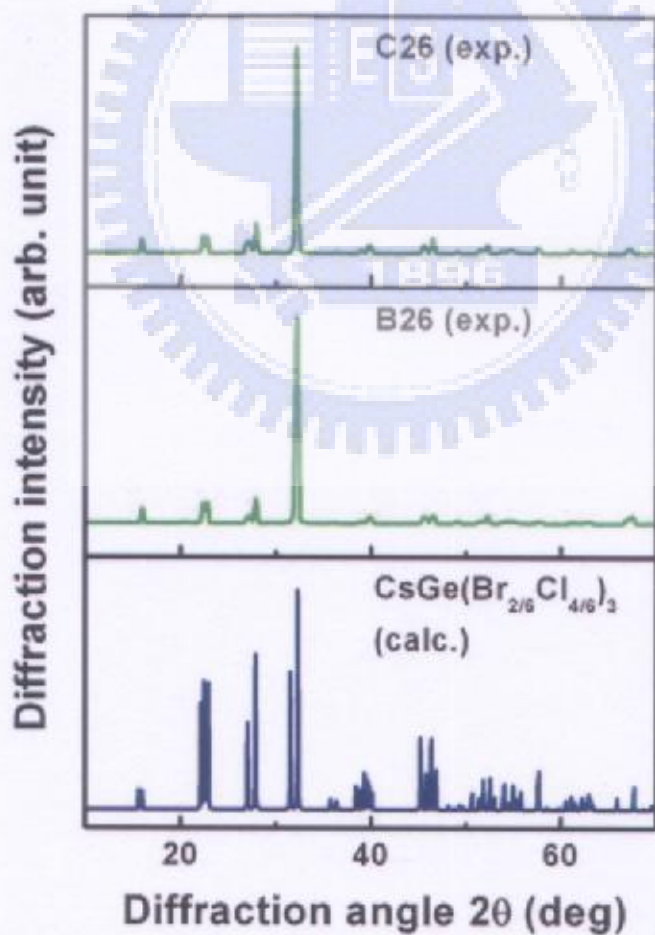
Fig. 3-23 The X-ray diffraction results for $CsGe(Br_{2/6}Cl_{4/6})_3$ determined by experiment and simulation.
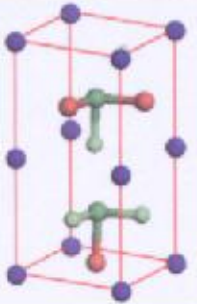
	(hkl)	(200)	(1Ī1)	(111)	(1Ī0)	(110)	(100)
C36	2θ	31.86	27.71	26.96	22.60	22.15	15.86
B36	2θ	31.91	27.76	26.95	22.65	22.20	15.90

Fig. 3-15 The unit cell of constituent atoms that are input to the calculation for $CsGe(Br_{3/6}Cl_{3/6})_3$.
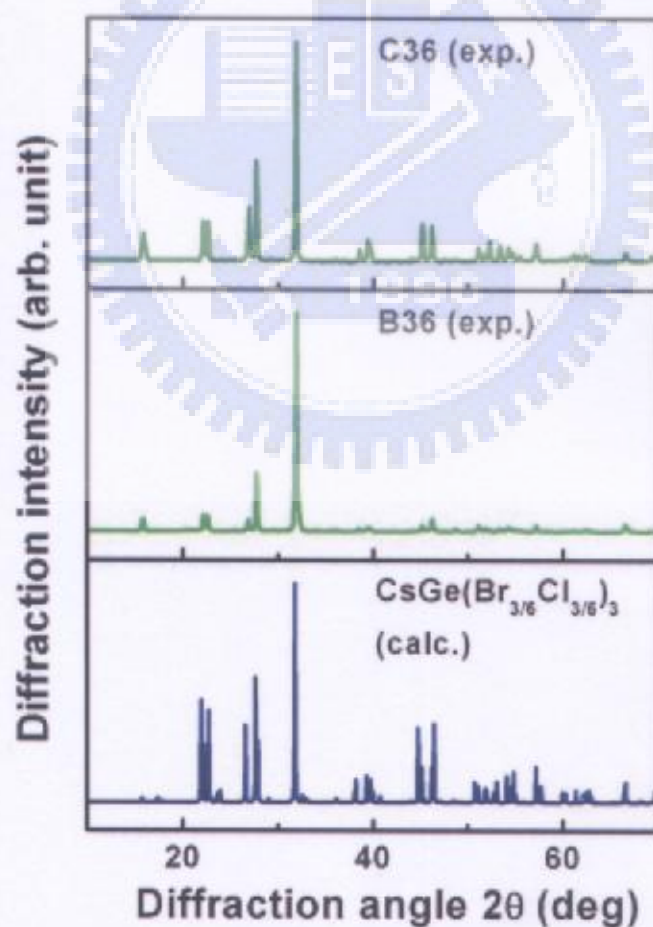
Fig. 3-24 The X-ray diffraction results for $CsGe(Br_{3/6}Cl_{3/6})_3$ determined by experiment and simulation.

	(hkl)	(200)	(1$\bar{1}\bar{1}$)	(111)	(1$\bar{1}$0)	(110)	(100)
C46	2θ	31.86	27.71	26.91	22.65	22.16	15.82
B46	2θ	32.01	27.86	27.06	22.80	22.30	15.98
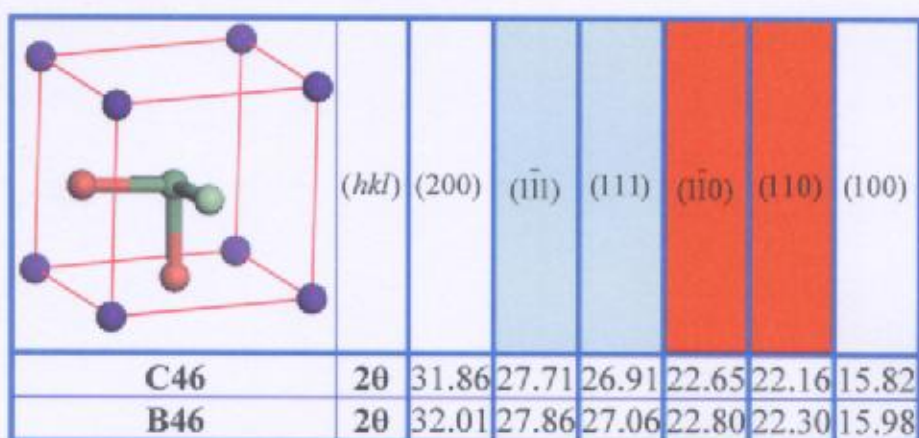
Fig. 3-16 The unit cell of constituent atoms that are input to the calculation for $CsGe(Br_{4/6}Cl_{2/6})_3$.
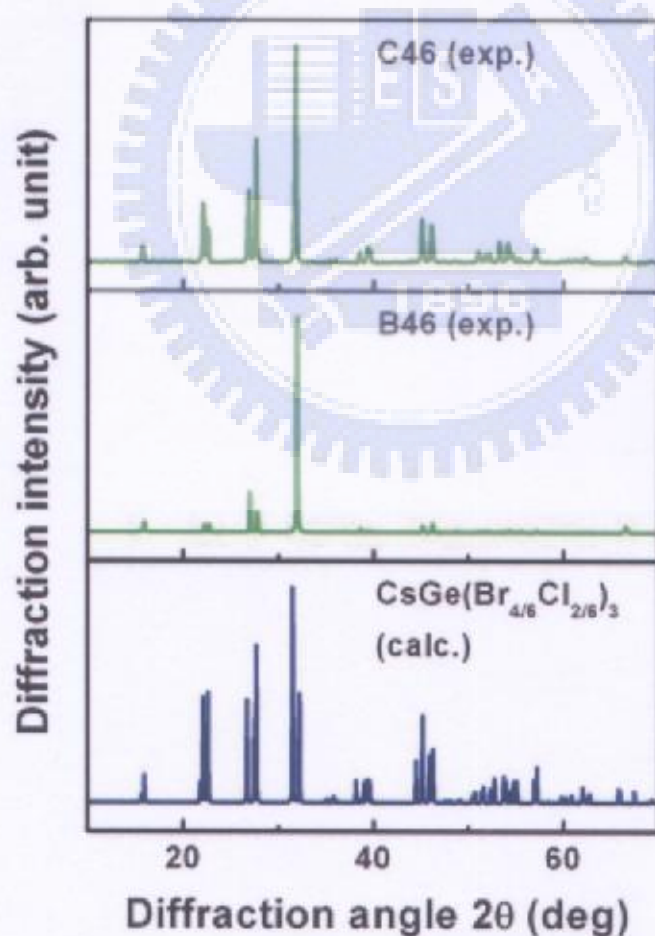
Fig. 3-25 The X-ray diffraction results for $CsGe(Br_{4/6}Cl_{2/6})_3$ determined by experiment and simulation.

	(hkl)	(200)	(1ī1)	(111)	(1ī0)	(110)	(100)
C34	2θ	31.86	27.66	26.91	22.60	22.15	15.84
B34	2θ	31.91	27.66	26.91	22.65	22.20	15.92
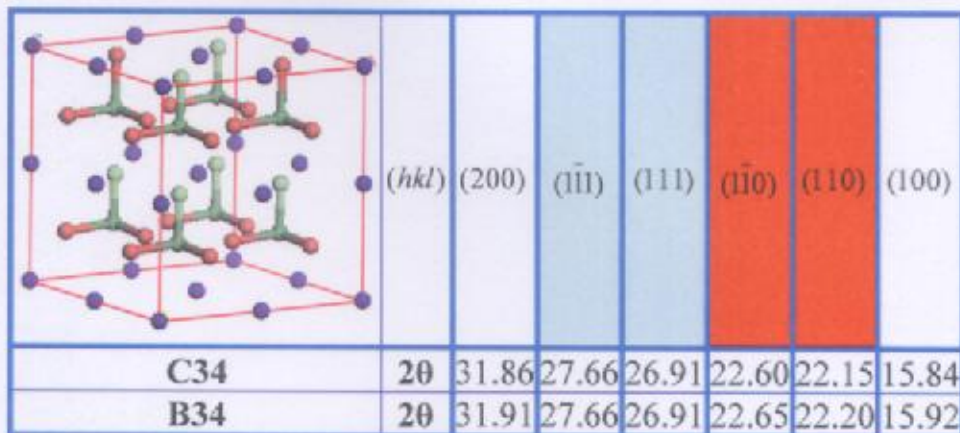
Fig. 3-17 The unit cell of constituent atoms that are input to the calculation for $CsGe(Br_{3/4}Cl_{1/4})_3$.
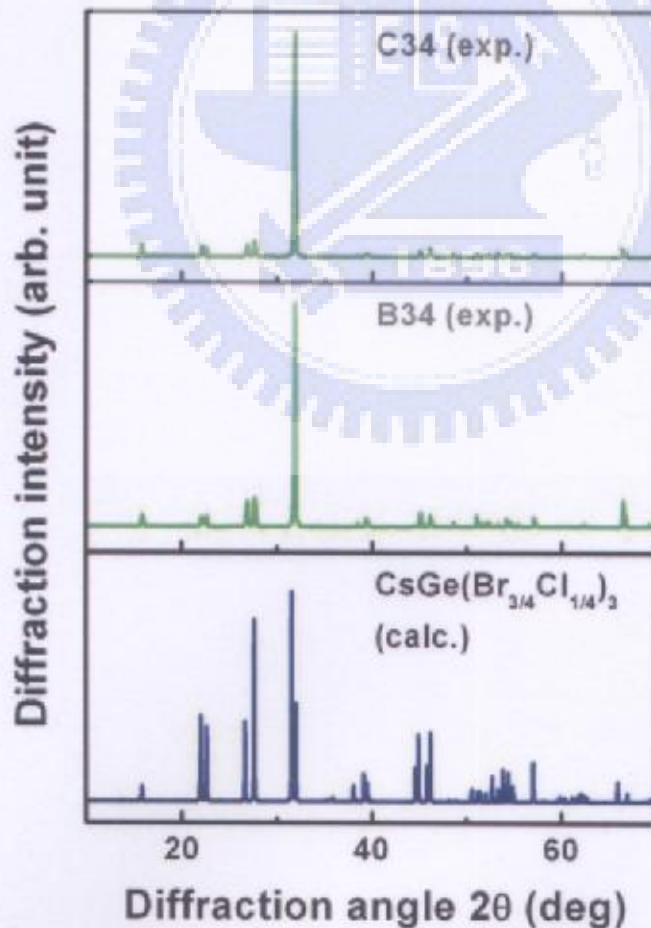
Fig. 3-26 The X-ray diffraction results for $CsGe(Br_{3/4}Cl_{1/4})_3$ determined by experiment and simulation.

	(hkl)	(200)	(1Ī1)	(111)	(1Ī0)	(110)	(100)
C56	2θ	31.81	27.66	26.86	22.55	22.05	15.76
B56	2θ	31.76	27.66	26.86	22.55	22.05	15.72
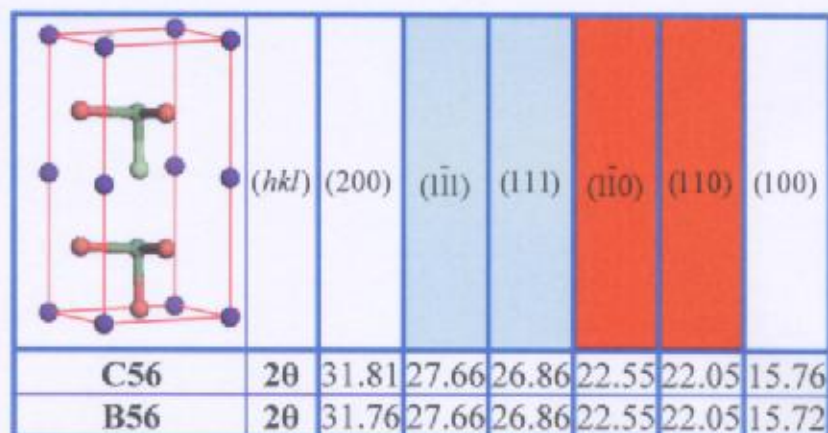
Fig. 3-18 The unit cell of constituent atoms that are input to the calculation for $CsGe(Br_{5/6}Cl_{1/6})_3$.
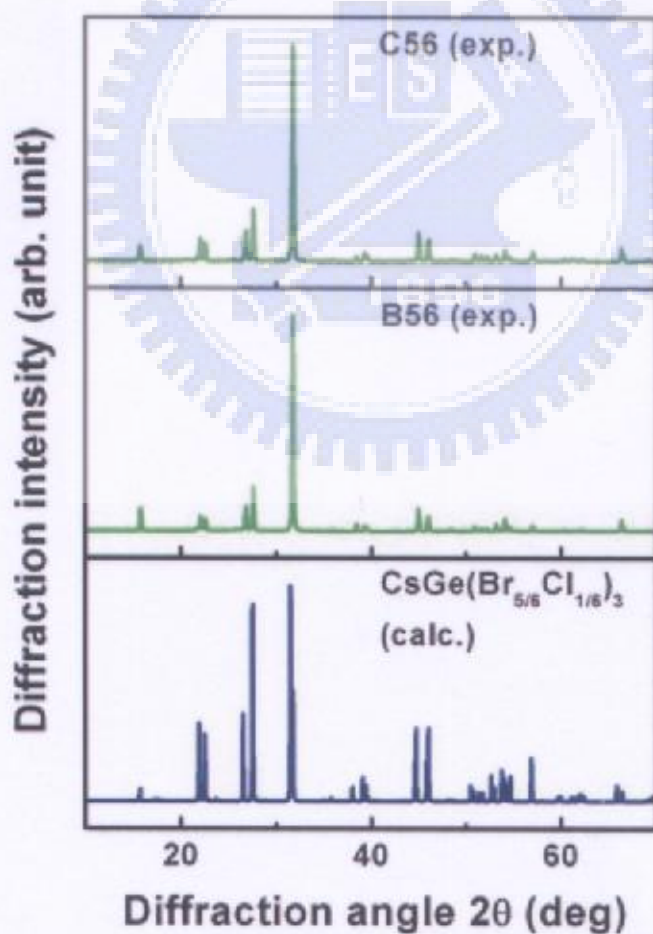
Fig. 3-27 The X-ray diffraction results for $CsGe(Br_{5/6}Cl_{1/6})_3$ determined by experiment and simulation.

	(hkl)	(200)	(1ĪĪ)	(111)	(1Ī0)	(110)	(100)
CGB	2θ	31.76	27.66	26.86	22.60	22.10	15.76
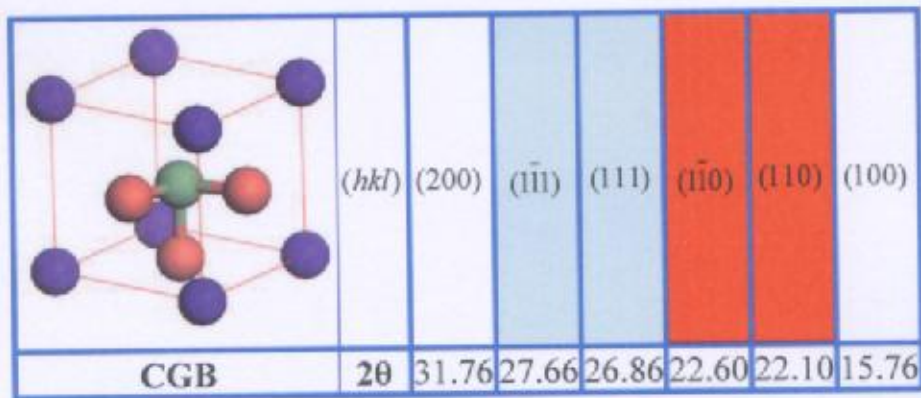
Fig. 3-19 The unit cell of constituent atoms that are input to the calculation for CsGeBr₃.
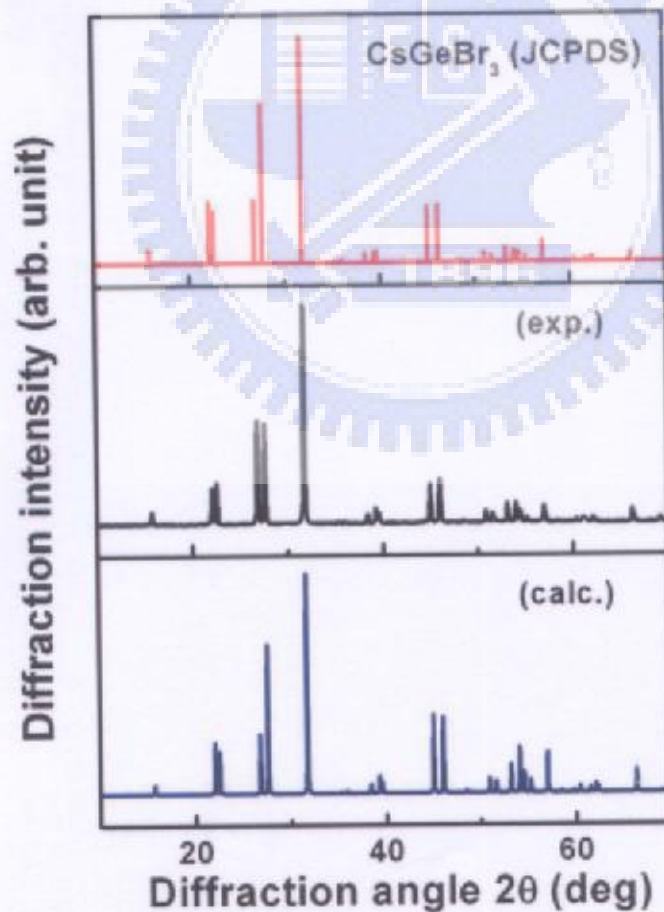
Fig. 3-28 The X-ray diffraction results for CsGeBr₃ determined by experiment and simulation.
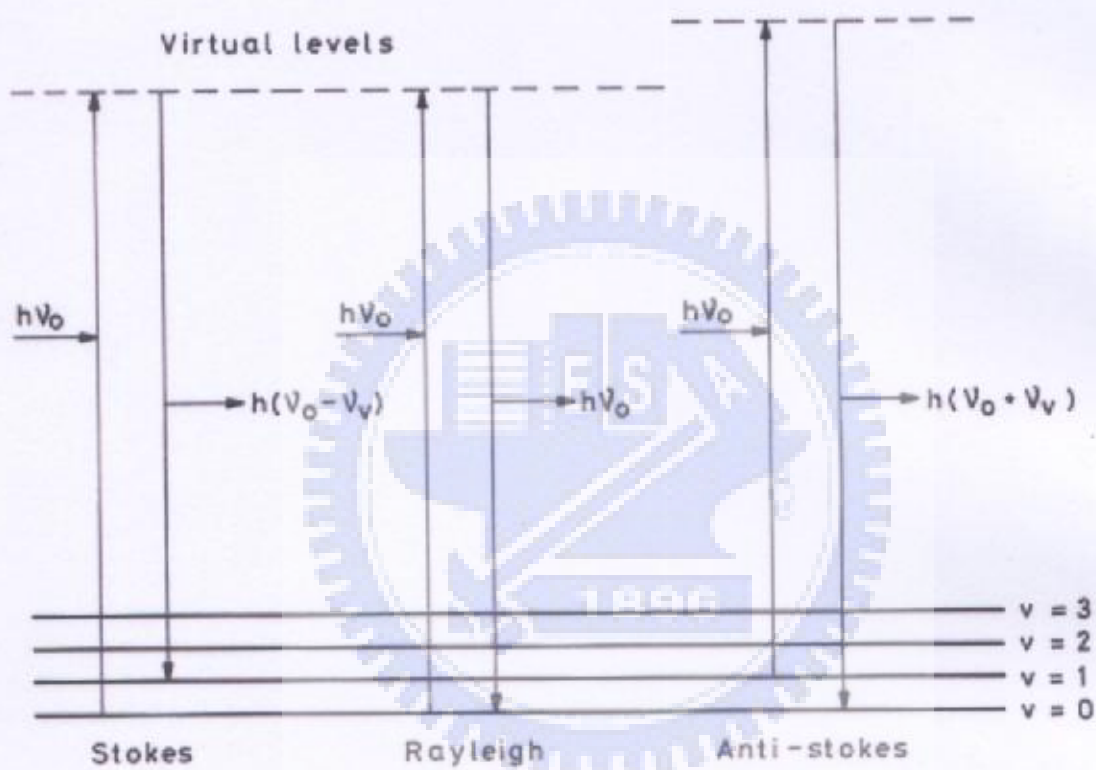
Fig. 3-29 Idealised model of Rayleigh scattering and Stokes and anti-Stokes Raman scattering [3-15].
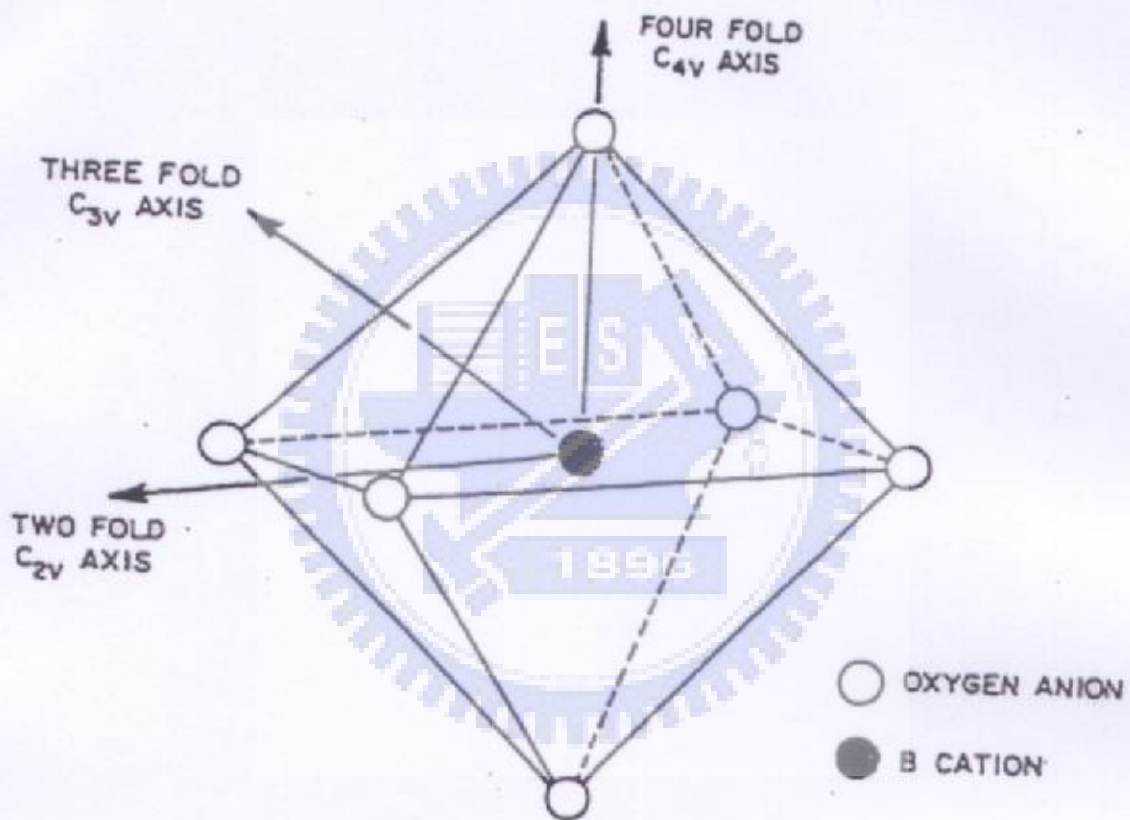
Fig. 3-30 The point groups and symmetry axes of perovskite [3-17].
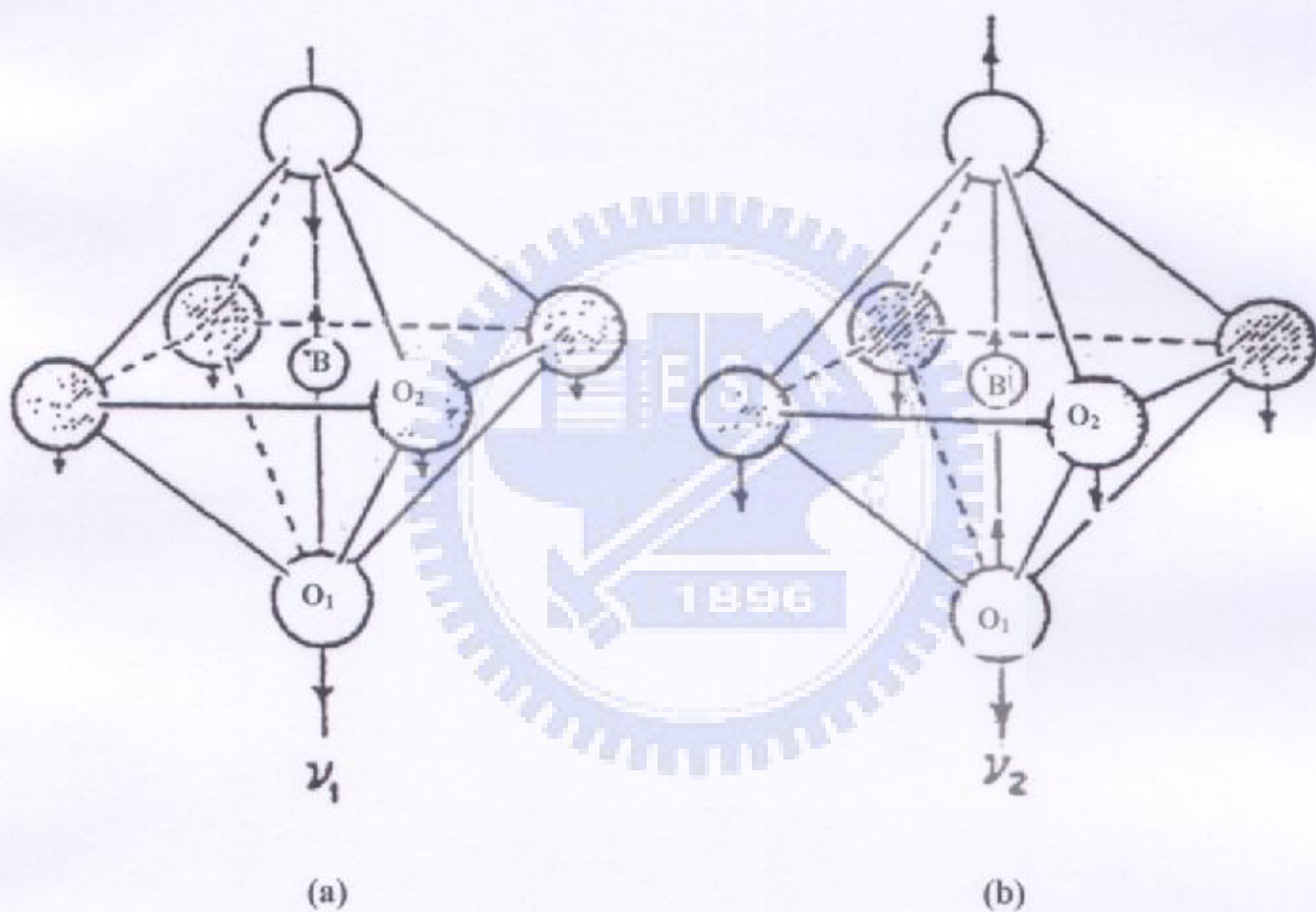
Fig. 3-31 The vibration modes of octahedral structure. (a) Strengthing
vibration, (b) Bending vibration [3-23].
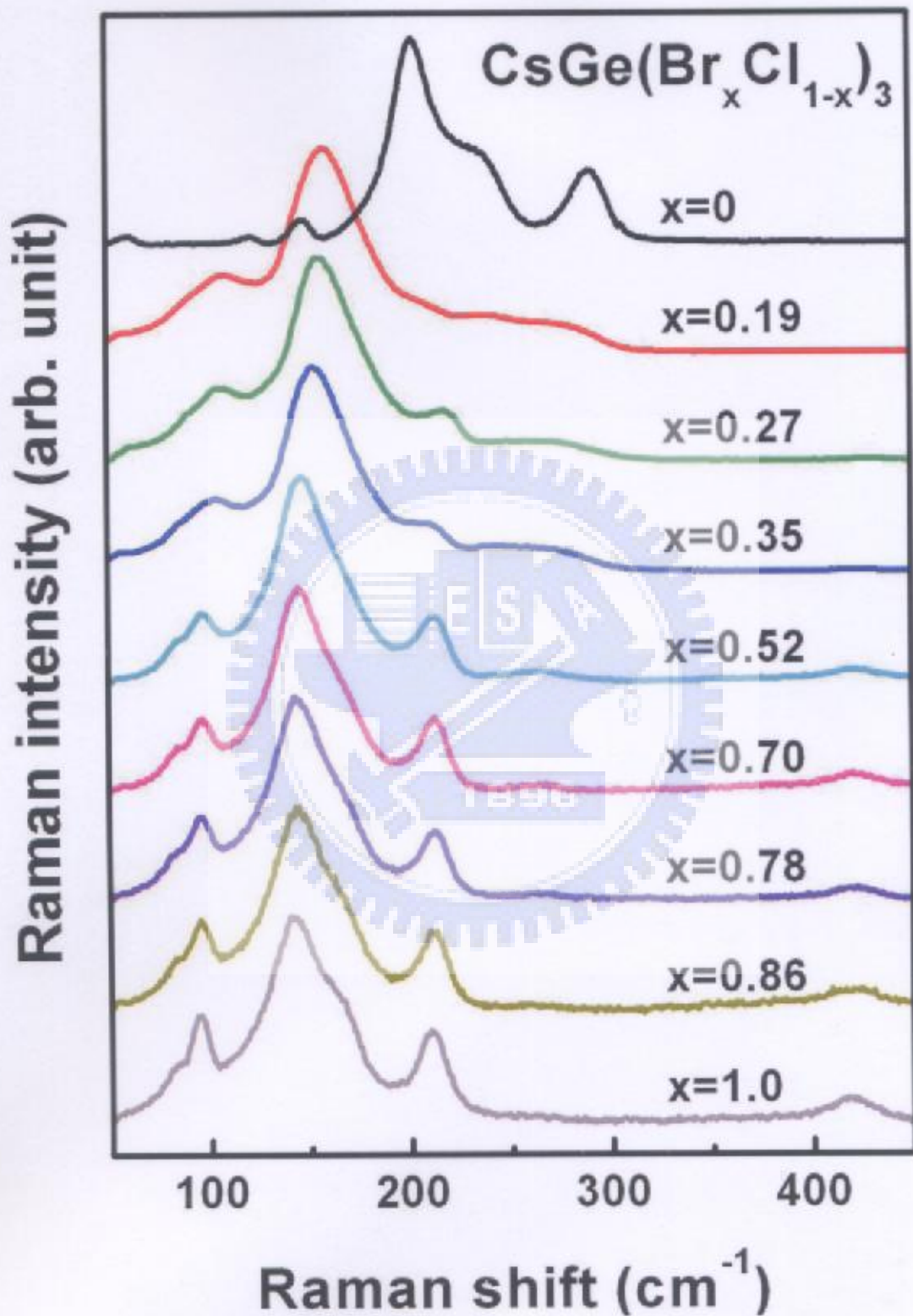
Fig. 3-32 The Raman spectrum of $CsGe(Br_xCl_{1-x})_3$ (R3m) crystals at room temperature.
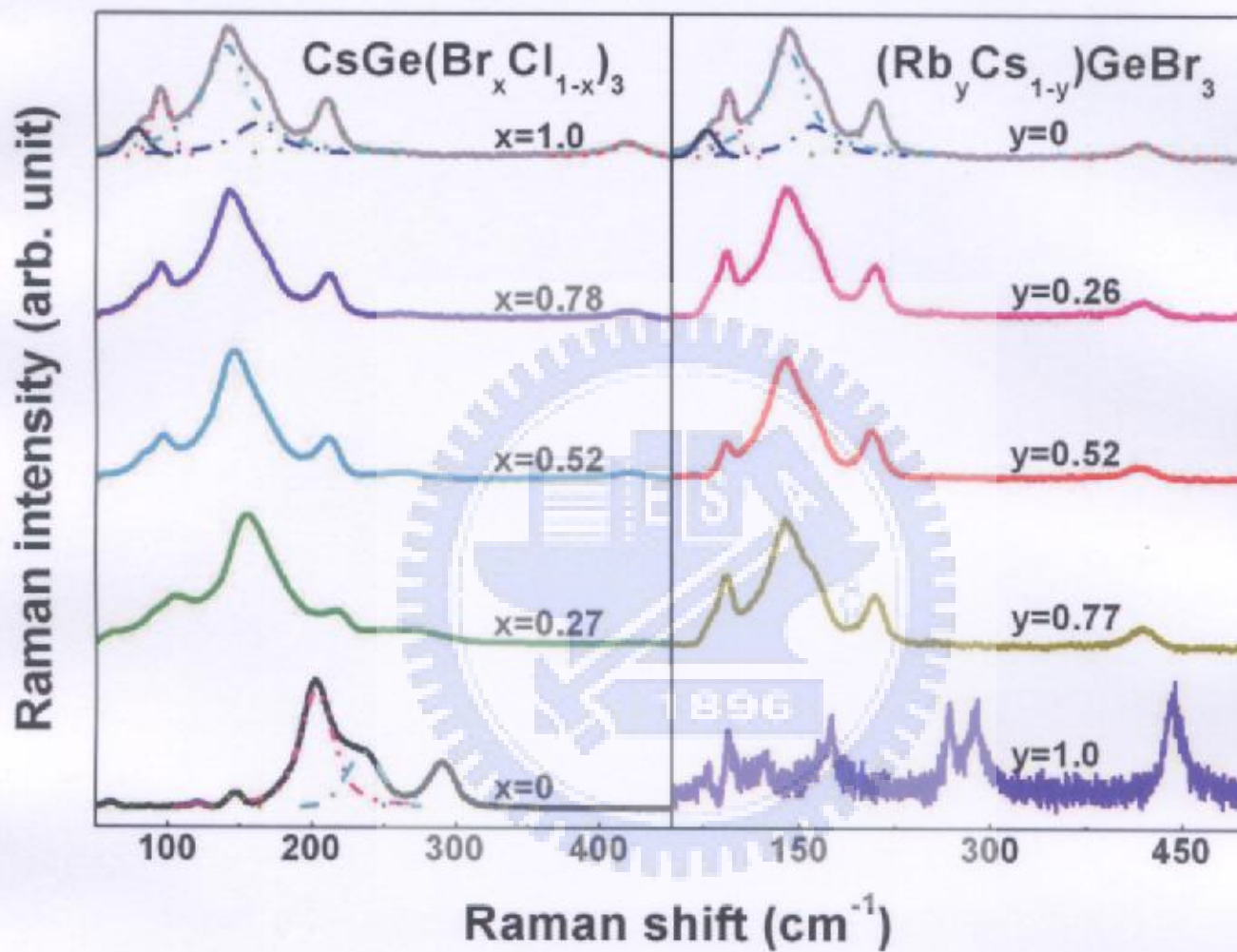
Fig. 3-33 The Raman spectrum of CsGe(Br$_x$Cl$_{1-x}$)$_3$ and (Rb$_y$Cs$_{1-y}$)GeBr$_3$ crystals at room temperature.
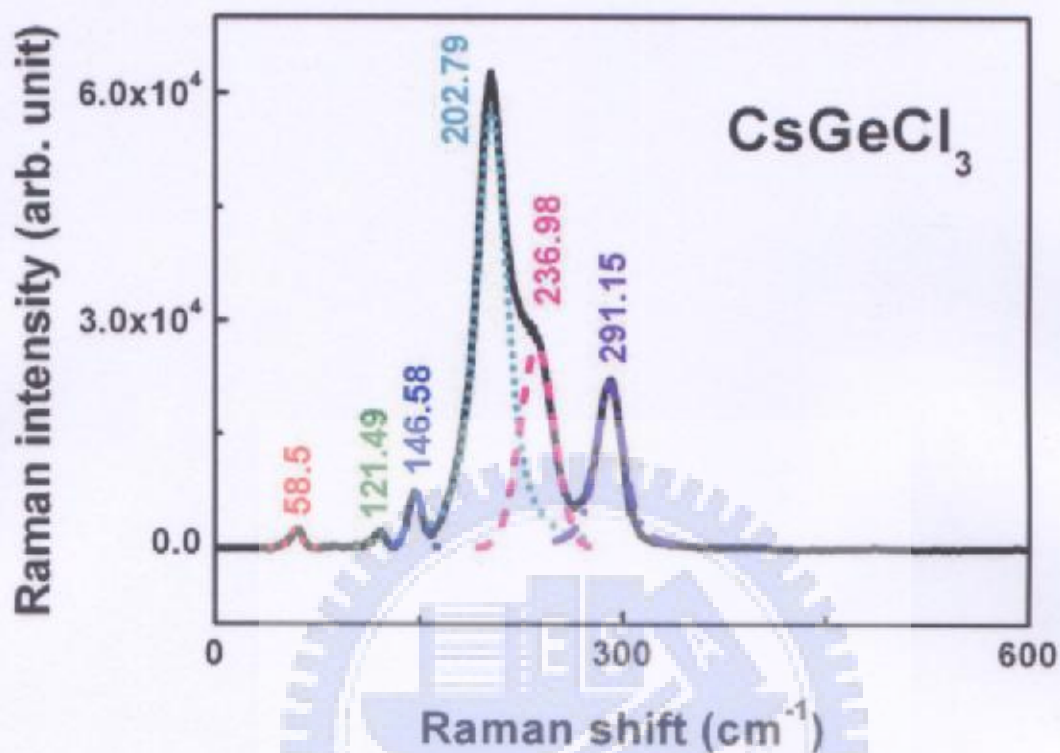
Fig. 3-34 The peak-splitting of CsGeCl₃ (R3m) Raman spectrum.

exp. (cm^{-1})	symmetry	ref. [3-6,3-22]
58.50		57 (*m*)
—		77 (*vw*)
121.49		120 (*w*)
146.58		145 (*m*)
202.79	A_1	200 (*vs*)
236.98	E	237 (*ls*)
291.15	A_1	290 (*s*)
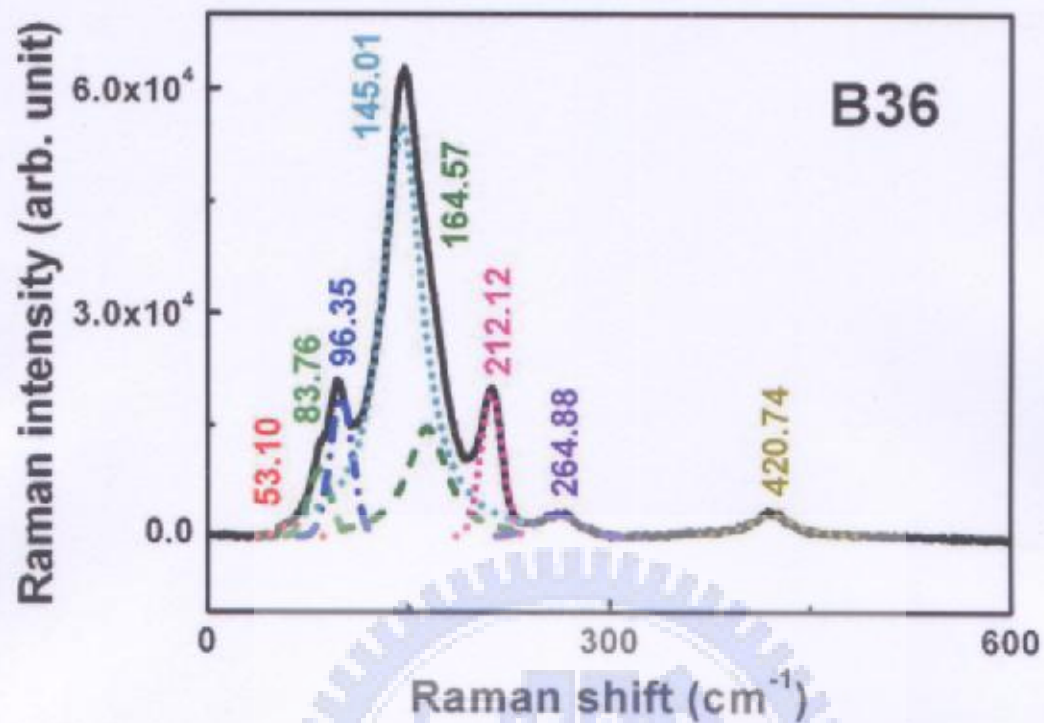
Fig. 3-35 The peak-splitting of $CsGe(Br_{3/6}Cl_{3/6})_3$ (B-series) Raman spectrum.
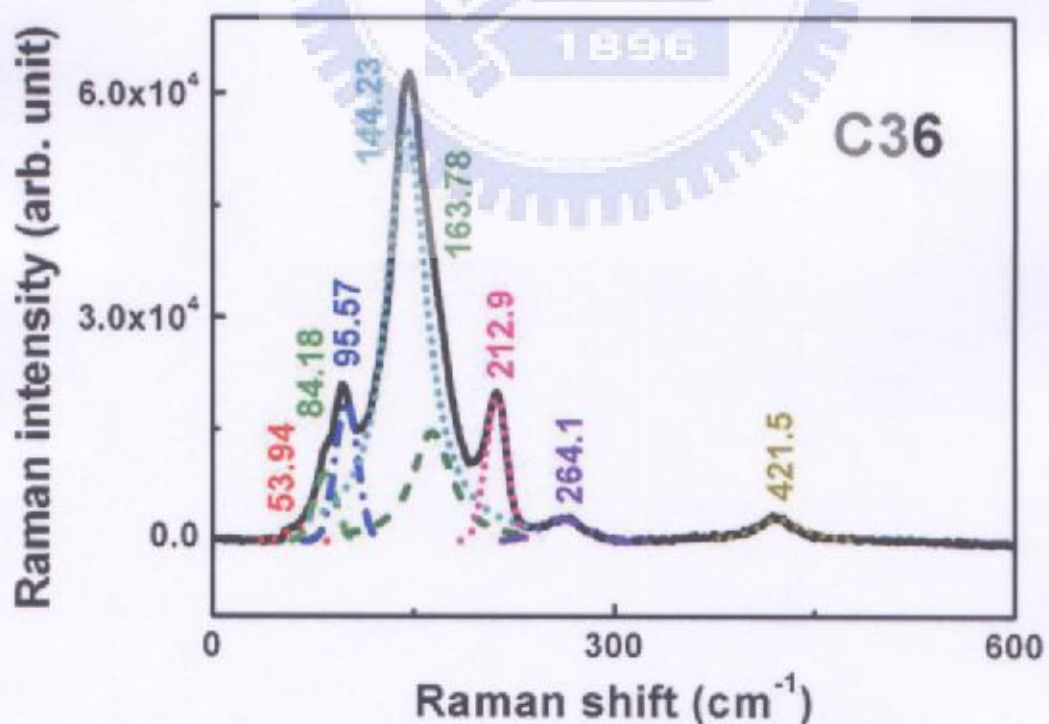
Fig. 3-36 The peak-splitting of $CsGe(Br_{3/6}Cl_{3/6})_3$ (C-series) Raman spectrum.
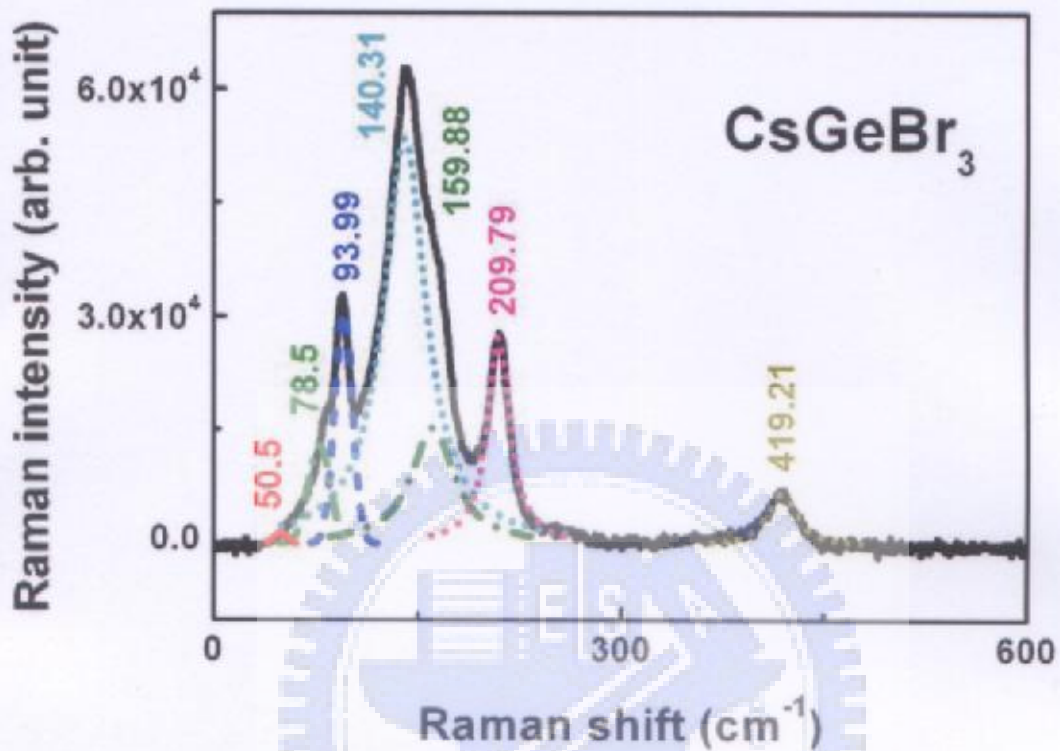
Fig. 3-37 The peak-splitting of CsGeBr₃ (R3m) Raman spectrum.

exp. (cm^{-1})	symmetry	ref. [3-6,3-22]
50.50		49 (*w*)
78.50		77 (*m*)
93..99		91 (*s*)
140.31	A$_1$	139 (*vs*)
159.88	E	160 (*ls*)
209.79	A$_1$	210 (*s*)
419.21		—
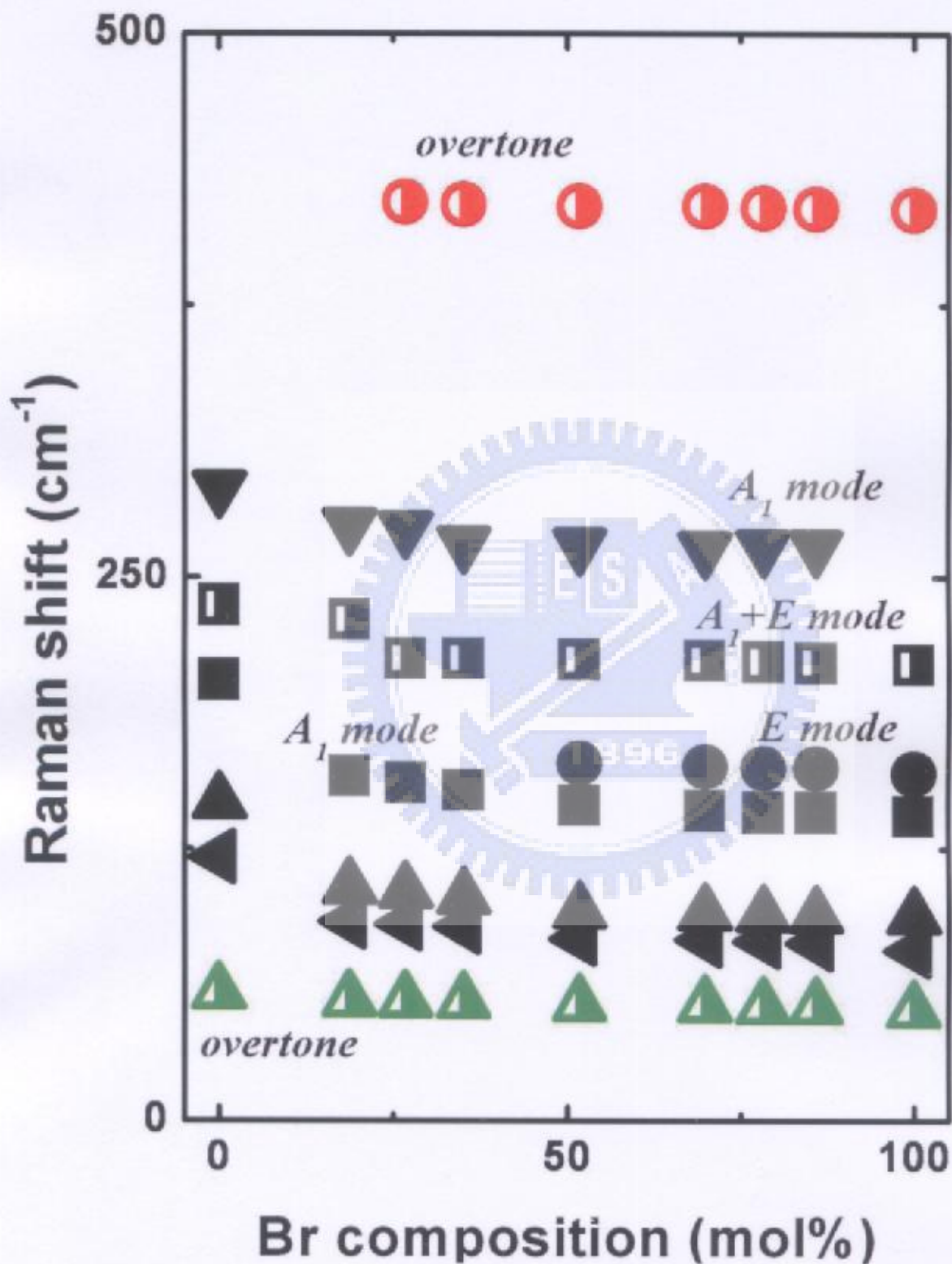
Fig. 3-38 The Raman vibrational modes of CsGe(Br_yCl_{1-y})$_3$ (B-series) crystals at room temperature.
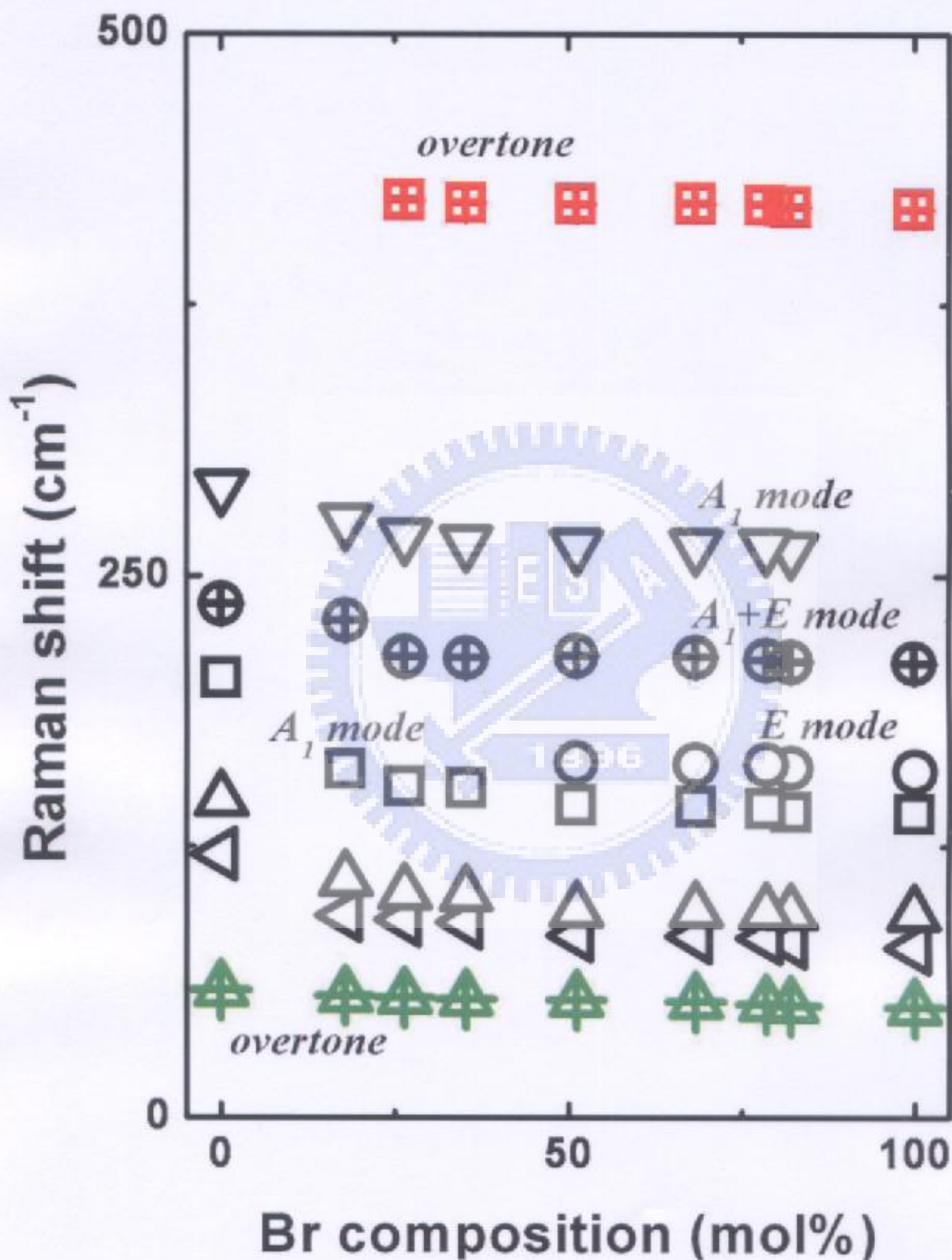
Fig. 3-39 The Raman vibrational modes of $CsGe(Br_xCl_{1-x})_3$ (C-series) crystals at room temperature.
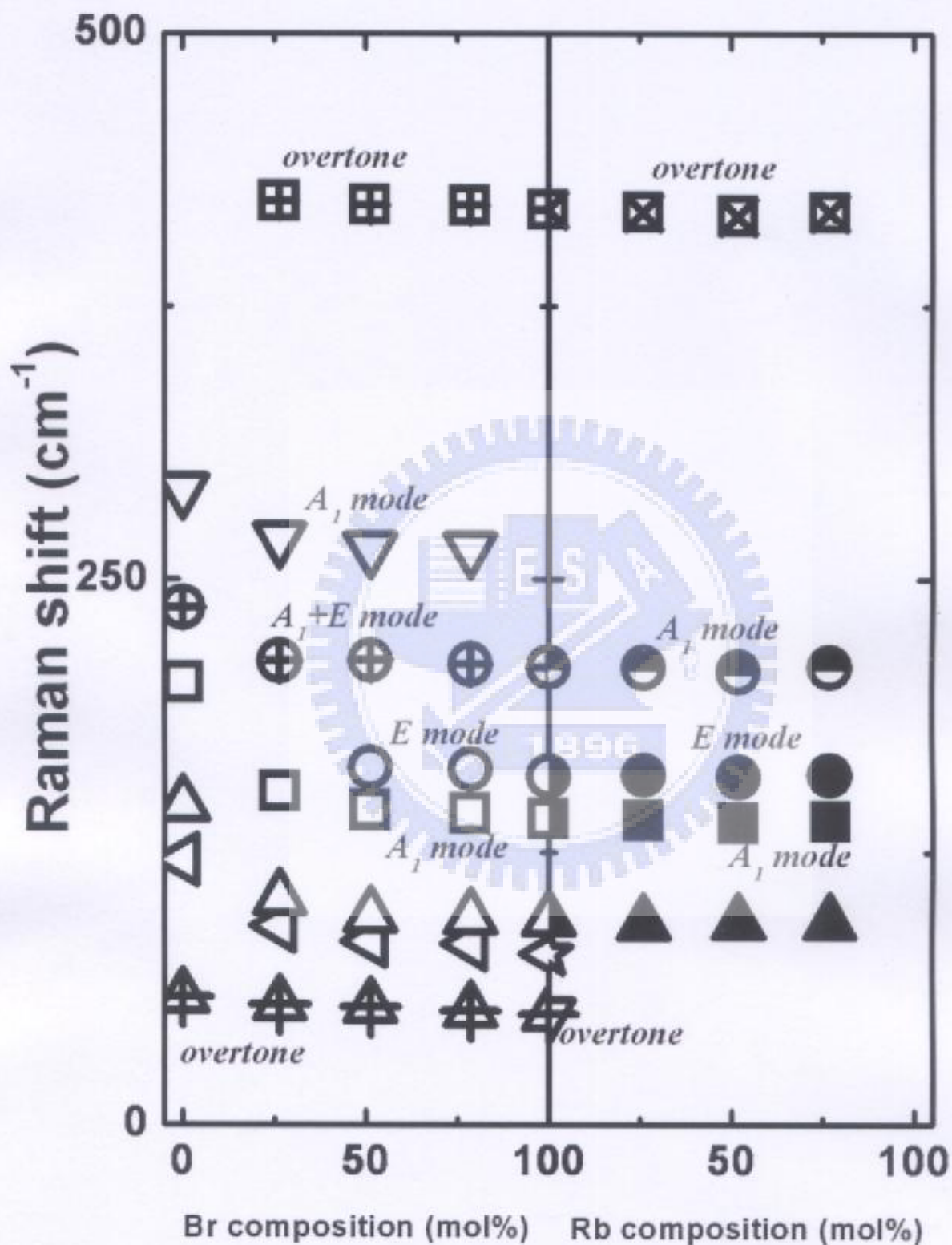
Fig. 3-40 The Raman vibrational modes of $CsGe(Br_xCl_{1-x})_3$ and $(Rb_zCs_{1-z})GeBr_3$ crystals at room temperature.

3.5 References

[3-1] B. D. Cullity, *Elements of X-ray diffraction* (Addison Wesley, Canada, 1978).

[3-2] B. E. Warren, *X-ray diffraction* (1969, ch.2).

[3-3] W. Kraus and G. Nolze, *J. Appl. Cryst.* 29 (1996) 301.

[3-4] U. Schwarz, H. Hillebrecht, M. Kaupp, K. Syassen, H. G. von Schnering and G. Thiele, *Journal of Solid State Chemistry* 118 (1995) 20.

[3-5] U. Schwarz, F. Wagner, K. Syassen and H. Hillebrecht, *Phys. Rev. B* 53 (1996) 12545.

[3-6] G. Thiele, H. W. Rotter and K. D. Schmidt, *Z. Anorg. Allg. Chem.* 545 (1987) 148.

[3-7] G. Thiele, H. W. Rotter and K. D. Schmidt, *Z. Anorg. Allg. Chem.* 559 (1988) 7.

[3-8] D. K. Seo, N. Gupta, M. H. Whangbo, H. Hillebrecht and G. Thiele, *Inorg. Chem.* 37 (1998) 407.

[3-9] R. O. Jones and O. Gunnarsson, *Rev. Mod. Phys.* 61 (1989) 689.

[3-10] M. C. Payne, M. P. Teter, D. C. Allan, T. A. Arias and J. D. Joannopoulos, *Rev. Mod. Phys.* 64 (1992) 1045.

[3-11] G. Kresse, *Phys. Rev. B* 54 (1996) 11169.

[3-12] R. Car and M. Parrinello, *Phys. Rev. Lett.* 55 (1985) 2471.

[3-13] H. J. Monkhorst and J. D. Pack, *Phys. Rev. B* 13 (1976) 5188.

D. J. Chadi and M. L. Cohen, *Phys. Rev. B* 8 (1973) 5747.

S. Froyen, *Phys. Rev. B* 39 (1989) 3168.

J. Moreno and J. M. Soler, *Phys. Rev. B* 45 (1992) 13891.

P. E. Blochl, G. Jepsen and O. K. Anderson, *Phys. Rev. B* 49 (1994) 16222.

[3-14] V. Milman, M. H. Lee and M. C. Payne, *Phys. Rev. B* 49 (1994) 16300.

[3-15] D. J. Gardiner and P. R. Graves, *Practical Raman Spectroscopy* (Springer-Verlag, 1989).

[3-16] G. Burns, *Introduction to group theory with applications* (1977).

[3-17] B. Schrader, *Infrared and Raman spectroscopy - methods and applications* (1995).

[3-18] U. D. Venkateswaran, V. M. Naik, R. Naik, *Phys. Rev. B* 58 (1998) 14256.

[3-19] A. K. Sood, N. Chandrabhas, D. V. S. Muthu, A. Jayaraman, *Phys. Rev. B* 51(1995) 8892.

[3-20] W. Zhong, R. D. King-Smith, and D. Vanderbilt, *Phys. Rev. Lett.*

72 (1994) 3618.

[3-21] G. Burns and B. A. Scott, *Solid State Comm.* 9 (1971) 813.

[3-22] L. C. Tang, C. S. Chang and J. Y. Huang, *J. Phys.: Condens. Matter* 12 (2000) 9129.

[3-23] D. A. Skoog and J. J. Leary, *Principles of instrumental analysis* (Academic Press, New York, 1992).

Chapter 4   Transparency Characteristics

4.1 UV-visible spectra

4.1.1 Theory [4-1, 4-2, 4-4, 4-5]

The absorption of ultraviolet or visible radiation is generally caused by the excitation of bonding electrons. The optical absorption coefficient α is determined by the quantum mechanical transition rate $W_{i \to f}$ in the excitation of an electron in an initial quantum state ψ_i to a final state ψ_f by the absorption of a photon of angular frequency ω. Our goal is therefore to calculate $W_{i \to f}$, and thus to derive the dependence of α on frequency. Fermi's golden rule yields the transition rate:

$$W_{i \to f} = \frac{2\pi}{\hbar} |M|^2 g(\hbar\omega) \tag{4-1}$$

The transition rate thus depends on two factors — the matrix element M, and the density of states $g(\hbar\omega)$.

In the following discussion, the matrix element is considered first, and then $g(\hbar\omega)$ is considered. The matrix element specifies the effect of the external perturbation that is caused by the incidence of the light wave on the electrons. It is given by

$$M = \langle f|H'|i \rangle = \int \psi_f^*(\vec{r}) H'(\vec{r}) \psi_i(\vec{r}) d^3r \tag{4-2}$$

where $H^{'}$ is the perturbation that is caused by the light wave, and $\vec{r}$ is the position vector of the electron. This study utilizes the semi-classical approach in which the electrons are treated quantum mechanically, but the photons are described by electromagnetic waves.

In classical electromagnetism, the presence of a perturbing electric field $\vec{\varepsilon}$ causes a shift in the energy of a charged particle of $-\vec{p}\cdot\vec{\varepsilon}$, where $\vec{p}$ is the dipole moment of the particle. The quantum perturbation that describes the electric dipole interaction between light and the electron is therefore,

$$H^{'}=-\vec{p}_{e}\cdot\vec{\varepsilon}_{photon}$$ (4-3)

where $\vec{p}_{e}$ is the electron dipole moment and equals $-e\cdot\vec{r}$. The light wave is described by plane waves of the form

$$\varepsilon_{photon}(\vec{r})=\varepsilon_{0}e^{\pm ik\cdot r}$$ (4-4)

where the sign in the phase depends on the direction of propagation of the wave. The perturbation is thus

$$H^{'}(\vec{r})=e\varepsilon_{0}\cdot\vec{r}e^{\pm ik\cdot r}$$ (4-5)

Bloch functions describe the electron states in a crystalline solid. Hence, the wave functions can be written as a product of a plane wave and an envelope function that has the periodicity of a crystal lattice. Therefore,

$$\psi_i(\vec{r}) = \frac{1}{\sqrt{V}} u_i(\vec{r}) e^{ik_i \cdot \vec{r}} \tag{4-6}$$

$$\psi_f(\vec{r}) = \frac{1}{\sqrt{V}} u_f(\vec{r}) e^{ik_f \cdot \vec{r}} \tag{4-7}$$

where u_i and u_f are the appropriate envelope functions for the initial and final bands respectively, and V is the normalization volume. k_i and k_f are the wave number of the initial and final electron states.

Substituting the perturbed Eq. 4-5 and the wave functions in Eqs. 4-6 and 4-7 into Eq. 4-2 yields,

$$M = \frac{e}{V} \int u_f^*(\vec{r}) e^{-ik_f \cdot \vec{r}} (\varepsilon_0 \cdot \vec{r} e^{\pm ik \cdot \vec{r}}) u_i(\vec{r}) e^{ik_i \cdot \vec{r}} d^3r \tag{4-8}$$

where the limits of the integration are over the whole crystal. This integral can be simplified by applying conservation of momentum and Bloch's theorem. Conservation of momentum requires that the change in the crystal momentum of the electron must equal the momentum of the photon:

$$\hbar k_f - \hbar k_i = \pm \hbar k \tag{4-9}$$

This criterion is equivalent to requiring that the phase factor in Eq. 4-8 is zero. If the phase factor is not zero, the different unit cells within the crystal will be out of phase with each other and the integral equal to zero. Bloch's theorem requires that u_i and u_f are periodic functions with the same periodicity as the lattice.

97

These two considerations imply that the integral over the whole crystal can be separated into a sum over identical unit cells, because the unit cells are equivalent and in phase. Therefore,

$$|M| \propto \int_{unit\ cell} u_i^*(\vec{r}) x u_f(\vec{r}) d^3r \qquad (4\text{-}10)$$

where the axes are defined such that the light is polarized along the x axis. This matrix element represents the electric dipole moment of the transition. Its evaluation depends on knowledge of the envelope functions u_i and u_f. These functions are derived from the atomic orbitals of the constituent atoms, and so each component must be considered separately.

The conservation of momentum condition in Eq. 4-9 can be simplified further by considering the magnitude of the wave vectors of the electrons and photons. The wave vector of the photon is $2\pi/\lambda$, where λ is the wavelength of the light. Photons of optical frequency therefore have k values of about 10^7 m^{-1}. The wave vectors of the electrons, however, are much larger, because the electron wave vector is related to the size of the Brillouin zone, which equals π/a, where a is the unit cell dimension. Since $a \sim 10^{-10}$ m, the photon wave vector is much smaller than the Brillouin zone. Hence, the photon momentum in Eq. 4-9 is negligible in relation to the electron momentum, and

$$k_f = k_i \qquad (4\text{-}11)$$

A direct optical transition therefore causes a negligible change in the wave vector of the electron so the absorption processes are represented by vertical arrows in the electron E-k diagrams, such as those in Fig. 4-1.

The $g(\hbar\omega)$ factor that appears in Eq. 4-1 is the joint density of states evaluated at the photon energy. The density of states function specifies the distribution of the states within the bands. The joint density of states explains the fact that both the initial and the final electron states lie within continuous bands. For electrons within a band, the range of the density of states per unit energy $g(E)$ is obtained from,

$$g(E)dE = 2g(k)dk, \qquad (4\text{-}12)$$

where $g(k)$ is the density of states in momentum space. The extra factor of two is included because each allowed k-state is associated with two electron spin states.

$$g(E) = \frac{2g(k)}{dE/dk} \qquad (4\text{-}13)$$

where dE/dk is the gradient of the E-k dispersion curve in the band diagram. $g(k)$ is determined by calculating the number of k-states in the incremental volume between shells in k-space of radius k and $k+dk$. This number equals the number of states per unit volume of k-space, $1/(2\pi)^3$,

multiplied by the incremental volume $4\pi k^2 dk$. Therefore, $g(k)$ is given by the standard formula,

$$g(k)dk = \frac{1}{(2\pi)^3}4\pi k^2 dk \Rightarrow g(k)=\frac{k^2}{2\pi^2} \qquad (4\text{-}14)$$

$g(E)$ can now be determined from Eq. 4-13 if the relationship between E and k is known from the band structure of the material. For electrons in a parabolic band with effective mass m^*, $g(E)$ is given by,

$$g(E) = \frac{1}{2\pi^2}\left(\frac{2m^*}{h^2}\right)^{\frac{3}{2}} E^{\frac{1}{2}} \qquad (4\text{-}15)$$

This formula is just the standard formula for free electrons but with the free electron mass m_0 replaced by m^*. The joint density of states factor is finally obtained by evaluating $g(E)$ at E_i and E_f when they are related to $\hbar\omega$ through the details of the band structure.

The dependence of the absorption coefficient on frequency can now be calculated the joint density of states factor, given by Eq. 4-13, is known. This can be determined analytically for the simplified band structure presented in Fig. 4-2. The dispersion of the bands is determined by their respective effective masses — m_e^* for the electrons, m_{hh}^* for the heavy holes, m_{lh}^* for the light holes and m_{so}^* for the split-off holes. It allows us to write the following E-k relationships for the conduction,

heavy hole, light hole and split-off hole bands;

$$E_c(k) = E_g + \frac{\hbar^2 k^2}{2m_e^*} \qquad (4\text{-}16)$$

$$E_{hh}(k) = -\frac{\hbar^2 k^2}{2m_{hh}^*} \qquad (4\text{-}17)$$

$$E_{lh}(k) = -\frac{\hbar^2 k^2}{2m_{lh}^*} \qquad (4\text{-}18)$$

$$E_{so}(k) = -\Delta - \frac{\hbar^2 k^2}{2m_{so}^*} \qquad (4\text{-}19)$$

From Fig. 4-2, conservation of energy during a heavy hole or light hole transition requires that,

$$\hbar\omega = E_g + \frac{\hbar^2 k^2}{2m_e^*} + \frac{\hbar^2 k^2}{2m_h^*} \qquad (4\text{-}20)$$

where $m_h^* = m_{hh}^*$ or m_{lh}^* for the heavy or light hole transition, respectively. The reduced electron-hole mass μ is defined by

$$\frac{1}{\mu} = \frac{1}{m_e^*} + \frac{1}{m_h^*} \qquad (4\text{-}21)$$

Equation 4-20 can be written in simplified form,

$$\hbar\omega = E_g + \frac{\hbar^2 k^2}{2\mu} \qquad (4\text{-}22)$$

$g(E)$ is to be evaluated with $E = \hbar\omega$. The joint electron-hole density of states can be determined by substituting Eq. 4-22 into Eqs. 4-13 and 4-14, which yields,

$$For \ \hbar\omega < E_g, \ g(\hbar\omega) = 0$$

$$\qquad (4\text{-}23)$$

$$For \ \hbar\omega \geq E_g, \ g(\hbar\omega) = \frac{1}{2\pi^2}\left(\frac{2\mu}{\hbar^2}\right)^{\frac{3}{2}}(\hbar\omega - E_g)^{\frac{1}{2}}$$

Therefore, the density of states factor increases as $(\hbar\omega - E_g)^{1/2}$ for photon

101

energies that exceed band gap.

Fermi's golden rule, given in Eq. 4-1, states that the absorption rate of a dipole-allowed interband transition is proportional to the joint density of states given by Eq. 4-23. The following behavior for $\alpha(\hbar\omega)$ is therefore expected.

$$For \quad \hbar\omega < E_g, \quad \alpha(\hbar\omega) = 0$$
$$For \quad \hbar\omega \geq E_g, \quad \alpha(\hbar\omega) \propto (\hbar\omega - E_g)^{\frac{1}{2}}$$

(4-24)

No absorption occurs if $\hbar\omega < E_g$, and the absorption increases as $(\hbar\omega - E_g)^{1/2}$ of photon energy exceeds the band-gap energy. Transitions with larger reduced masses give rise to stronger absorption because Eq. 4-23 includes the factor $\mu^{3/2}$. The predictions of Eq. 4-24 can be compared to the experimental data.

4.1.2 Discussion

Thin plates ($\approx$ 500 μm) of $CsGe(Br_xCl_{1-x})_3$ and $(Rb_yCs_{1-y})GeBr_3$ were used to make the bandgap measurements. Figures 4-3 to 4-5 show the absorption spectra obtained at room temperature using $CsGe(Br_xCl_{1-x})_3$ (x = 0, 1/6, 1/4, 2/6, 3/6, 4/6, 3/4, 5/6, 1) and $(Rb_yCs_{1-y})GeBr_3$ (y = 0, 1/4, 2/4, 3/4, 1) crystals in the UV-visible light

range. The recorded curves can be approximated as straight lines for α^2 as a function of $h\nu$, where α is the absorption coefficient and $h\nu$ is the photon energy. The straight line approximation is applied to the rapidly increasing portions of the curves in Figs. 4-3, 4-4 and 4-5. Thus, the fundamental absorption edge is described by $\alpha = A \cdot (h\nu - E_g)^{1/2}$, where A is a constant and the band-gap E_g can be determined the points of intersection of the straight lines with the abscissa. This dependence corresponds to directly allowed electronic transitions [4-2]. In the insets in Figs. 4-3, 4-4 and 4-5, the band-gap values are plotted versus Br content. Although the absorption edge falls from 3.43 to 2.38 eV as the bromine content (x = 0 to 1), the absorption edge remains fixed for y = 0 to 3/4.

4.2 FTIR spectra

4.2.1 Theory [4-3, 4-6, 4-7, 4-8]

Generally, infrared radiation is not sufficiently energetic to bring about the kinds of electronic transitions that are caused by ultraviolet and visible radiation. The absorption of infrared radiation is thus confined largely to molecular species whose various vibrational and rotational states are separated by small energies.

To absorb infrared radiation, the vibrational or rotational motion of a molecule must cause a net change in dipole moment. Only under these circumstances can the alternating electrical field of the radiation interact with the molecule and change the amplitude of one of its motions.

The energy that is required to cause a change in rotational level is minute and corresponds to a radiation wavenumber of $100 \ cm^{-1}$ or less ($>100 \ \mu m$). Since rotational levels are quantized, absorption by gases in this far-infrared region is characterized by discrete, well-defined lines. In liquids or solids, intramolecular collisions and interactions broaden the lines into a continuum.

Vibrational energy levels are also quantized, and for most molecules the energy differences between quantum states correspond to the

mid-infrared region. The infrared spectrum of a gas usually comprises a series of closely spaced lines, because each vibrational state corresponds to various rotational energy states. However, rotation is extremely restricted in liquids and solids; in such samples, discrete vibrational/rotational lines disappear, leaving only somewhat broadened vibrational peaks.

The relative positions of atoms in a molecule are not exactly fixed but fluctuate continuously as a consequence of numerous vibrations. For a simple diatomic or triatomic molecule, the number and nature of such vibrations can be easily defined and related to energies of absorption. Such an analysis is difficult if not impossible for molecules that comprise many atoms. Not only do large molecules have numerous vibrating centers, but also interactions among these various centers can occur and must be considered.

Vibrations fall into the basic categories of stretching and bending. A stretching vibration involves continuous change in the interatomic distance along the axis of the bond between two atoms. Bending vibrations are characterized by a change in the angle between two bonds and are of four types — scissoring, rocking, wagging and twisting. Figure

4-6 schematically depicts the various vibrations.

The characteristics of atomic stretching vibration can be approximated by a mechanical model that consists of two masses that are connected by a spring. A disturbance of one of these masses along the axis of the spring causes simple harmonic motion.

Consider first the vibration of a single mass that is attached to a spring that is hung from an immovable object (Fig. 4-7(a)). If the mass is displaced by a distance y from its equilibrium position by the application of a force along the axis of the spring, the restoring force F is proportional to the displacement (Hooke's law). That is,

$$F = -ky \qquad (4-25)$$

where k is the force constant, which depends upon the stiffness of the spring. The negative sign indicates that F is a restoring force.

The potential energy E of the mass and spring can be treated as zero when the mass is at rest or in its equilibrium position. As the spring is compressed or stretched, however, the potential energy of this system increases by an amount that equals the work that is required to displace the mass. If, for instance, the mass is moved from some position y to $y + dy$, the work and hence the change in potential energy dE equal the force

F times the distance dy. Therefore,

$$dE = -Fdy \qquad\qquad (4-26)$$

Combining Eqs. 4-26 and 4-25 yields

$$dE = kydy$$

Integrating between the equilibrium position ($y = 0$) and y yields

$$\int_0^E dE = k \int_0^y ydy$$

$$E = \frac{1}{2}ky^2 \qquad\qquad (4-27)$$

The potential-energy curve for a simple harmonic oscillation, derived from Eq. 4-27, is a parabola, as plotted in Fig. 4-7(a). The potential energy is maximal when the spring is stretched or compressed to its maximum amplitude A, and is zero at the equilibrium position.

The motion of the mass as a function of time t can be derived as follows. Newton's second law states that

$$F = ma$$

where m is the mass and a is its acceleration. Since acceleration is the second derivative of distance with respect to time,

$$a = \frac{d^2y}{dt^2}$$

Substituting these expressions into Eq. 4-25 yields

$$m\frac{d^2y}{dt^2} = -ky \qquad\qquad (4-28)$$

A solution to this equation must be a periodic function such that its second derivative equals the original function times $-(k/m)$. A suitable cosine relationship meets this requirement. Accordingly, the instantaneous displacement of the mass at time t can be expressed as

$$y = A\cos 2\pi \upsilon_m t \qquad (4\text{-}29)$$

where υ_m denotes the natural vibrational frequency and A is the maximum amplitude of the motion. The second derivative of Eq. 4-29 is

$$\frac{d^2 y}{dt^2} = -4\pi^2 \upsilon_m^2 A\cos 2\pi \upsilon_m t \qquad (4\text{-}30)$$

Substituting Eqs. 4-29 and 4-30 into Eq. 4-28 gives

$$A\cos 2\pi \upsilon_m t = \frac{4\pi^2 \upsilon_m^2 m}{k} A\cos 2\pi \upsilon_m t$$

The natural frequency of oscillation is then

$$\upsilon_m = \frac{1}{2\pi} \sqrt{\frac{k}{m}} \qquad (4\text{-}31)$$

where υ_m is the natural frequency of the mechanical oscillator. Although it depends on the force constant of the spring and the mass of the attached body, the natural frequency is independent of the energy that is imparted to the system, changes in energy merely cause a change in the amplitude A of vibration.

The equation just developed is readily modified to describe the behavior of a system that comprises two masses m_1 and m_2 that are

connected by a spring. Here, only the reduced mass μ has to be substituted for the single mass m where

$$\mu = \frac{m_1 m_2}{m_1 + m_2} \qquad (4\text{-}32)$$

Hence, the vibrational frequency of such a system is given by

$$\upsilon_m = \frac{1}{2\pi}\sqrt{\frac{k}{\mu}} = \frac{1}{2\pi}\sqrt{\frac{k(m_1 + m_2)}{m_1 m_2}} \qquad (4\text{-}33)$$

The ordinary mechanical equations, such as used above, do not completely specify the behavior of particles of atomic dimensions. For example, the quantization of molecular vibrational energies (and of course other atomic and molecular energies) does not appear in these equations. The concept of the simple harmonic oscillator may be employed to develop the quantum mechanical wave equations. Solutions of these equations for potential energies have the form

$$E = \left(v + \frac{1}{2}\right)\frac{h}{2\pi}\sqrt{\frac{k}{\mu}} \qquad (4\text{-}34)$$

where h is Planck's constant, and v is the vibrational quantum number, which can take only positive integer values (including zero). Therefore, unlike in ordinary mechanics, in which vibrators can have any positive potential energy, quantum mechanical vibrators can have only particular discrete energies.

Interestingly, the term $(k/\mu)^{1/2}/2\pi$ appears in both the mechanical and the quantum equations; substituting Eq. 4-33 into Eq. 4-34 yields

$$E = \left(v + \frac{1}{2}\right)hv_m \qquad (4\text{-}35)$$

where v_m is the vibrational frequency of the mechanical model.

Transitions in vibrational energy levels are assumed to be caused by radiation, if the energy of the radiation exactly matches the difference ΔE between the energy levels of the vibrational quantum states (provided also that the vibration causes a fluctuation in the dipole). This difference is identical between any pair of adjacent levels, because v in Eqs. 4-34 and 4-35 can only be whole numbers; that is,

$$\Delta E = hv_m = \frac{h}{2\pi}\sqrt{\frac{k}{\mu}} \qquad (4\text{-}36)$$

At room temperature, most molecules are in the ground state ($v = 0$); thus, from Eq. 4-35,

$$E_0 = \frac{1}{2}hv_m$$

Promotion to the first excited state ($v = 1$) with energy

$$E_1 = \frac{3}{2}hv_m$$

requires radiation of energy

$$\left(\frac{3}{2}hv_m - \frac{1}{2}hv_m\right) = hv_m$$

The frequency of radiation v that causes this change equals the classical

vibration frequency of the bond v_m. That is,

$$E_{radiation} = hv = \Delta E = hv_m = \frac{h}{2\pi}\sqrt{\frac{k}{\mu}}$$

or

$$v = v_m = \frac{1}{2\pi}\sqrt{\frac{k}{\mu}} \tag{4-37}$$

If wavenumbers $\bar{v}$ of the radiation are required, $\bar{v} = kv$ should be substituted and rearranged to yield

$$\bar{v} = \frac{1}{2\pi c}\sqrt{\frac{k}{\mu}} = 5.3 \times 10^{-12}\sqrt{\frac{k}{\mu}} \tag{4-38}$$

where $\bar{v}$ is the wavenumber of an absorption peak in cm^{-1}; k is the force constant for the bond in Newtons per meter (N/m); c is the velocity of light in cm/s, and μ, which is given by Eq. 4-32, and has units of kg.

As specified by Eqs. 4-35 and 4-36, the energy for a transition from energy level 1 to 2 or from level 2 to 3 should be identical to that for the 0 to 1 transition. Accordingly, quantum theory demonstrates only transitions in which the vibrational quantum number changes by unity can occur; that is, the so-called selection rule states that $\Delta v = \pm 1$. Since vibrational levels are equally spaced, only a single absorption peak should be observed for a given molecular vibration.

Theoretically, the quantum mechanical wave equations allow the

111

derivation of more accurate potential-energy curves for molecular vibrations. Unfortunately, however, the mathematical complexity of these equations precludes their quantitative application to all but the very simplest of systems. Qualitatively, however, the curves must take the anharmonic form, such as that of curve 2 in Fig. 4-7(b). Such curves depart from harmonic behavior by varying degrees, depending on the nature of the bond and the atoms involved. Anharmonicity causes two kinds of deviation. At higher quantum numbers, ΔE is smaller (curve 2 in Fig. 4-7(b)), and the selection rule does not strictly apply; consequently, transitions of $\Delta v = \pm 2$ or ± 3 are observed. Such transitions are responsible for the appearance of overtone lines at frequencies that are approximately two or three times that of the fundamental line; the intensity of overtone absorption is commonly low, and the peaks are not observed. Notably, however, the harmonic and anharmonic curves are almost alike at low potential energies, which fact explains the success of the approximate methods described herein.

4.2.2 Discussion

Infrared spectra were obtained using a spectrometer (Bomem, DA8.3)

in the range from 120 cm^{-1} to 4000 cm^{-1}, or 2.5 μm ~ 83.3 μm, from samples that were pressed into thin plates ($\approx$ 500 μm). The transmittance of CsGe(Br$_x$Cl$_{1-x}$)$_3$ plates exceeded 75% in the mid-infrared range. The FTIR measurements in Figs. 4-8 and 4-9 reveal that the long wavelength limit of the transparent range of the crystals depended similarly on substitute composition. Crystal CsGeCl$_3$ had an infrared cut-off wavelength at approximately 30 μm, which was shorter than the cut-off value of CsGeBr$_3$ (about 47 μm). The infrared absorption edge of CsGe(Br$_x$Cl$_{1-x}$)$_3$ with x = 1/6, 1/4, 2/6, 3/6, 4/6, 3/4, 5/6 lay around from 32 to 38 μm. This result is consistent with the effective-mass concept, based on which the infrared transparency range of CsGeBr$_3$ is expected to exceed that of CsGeCl$_3$ because the Br atom is heavier than Cl. Figures 4-10 and 4-11 show the FTIR measurements at room temperature. The transmission range of the crystals increases with Br content. The absorption of phonons by the crystal typically limits the longest infrared transparency wavelength. The energy band-gap of the crystal limits the absorption edge.

From Figs. 4-12 and 4-13, and Tables 4-1 and 4-2, the actual IR transparency edges for the vibrational IR absorption/Raman spectra of

CsGe(Br$_x$Cl$_{1-x}$)$_3$ are V1 and P1, which are associated with two-phonon

absorption for x = 0 to 3/6. The further absorption V2 is related to the

two-phonon absorption which involves the next vibrational band P2. The

force constants between the Cs^+ and Ge(Br$_x$Cl$_{1-x}$)$_3^{-1}$ oscillations are

calculated from the FTIR peaks (Figs. 4-12 and 4-13) in the range from

290 to 410 cm^{-1} using $\omega = \dfrac{1}{2\pi c}\sqrt{\dfrac{k}{\mu}} = 5.3\times10^{-12}\sqrt{\dfrac{k}{\mu}}$ [4-3], where ω is the

wavenumber of an absorption peak in cm^{-1}; k is the force constant of

the bond in Newtons per meter (N/m); c is the velocity of light in cm/s,

and μ is the reduced mass in kg. The force constant increases as Br

content declines (Fig. 4-14), so the oscillation frequency increases as the

Br content decreases. This result is also consistent with the Raman A$_1$+E

mode (oscillation between Cs^+ and Ge(Br$_x$Cl$_{1-x}$)$_3^{-1}$) (Figs. 3-38 and 3-39).

4.3 Tables and Figures

Table 4-1 The IR absorption/Raman spectra of $CsGe(Br_yCl_{1-y})_3$ (B-series). The unit of these Raman and FTIR peaks was labeled as cm^{-1}. (P : Raman peak, V : FTIR valley)

Specimens (B-series)		Raman peaks (cm^{-1})			FTIR valleys (cm^{-1})	
	y	P1	P2	P1'	V1	V2
(a)	1.00	209.79	159.88	—	212.14	333.25
(b)	0.86	264.10	162.22	—	266.14	336.34
(c)	0.78	264.10	162.22	—	268.45	330.17
(d)	0.70	263.33	163.00	—	272.31	334.80
(e)	0.52	145.01	164.57	—	292.37	334.80
(f)	0.35	152.05	—	—	322.45	—
(g)	0.27	155.58	—	—	315.51	—
(h)	0.19	158.31	—	—	311.65	—
(i)	0.00	146.58	202.79	291.15	305.48	414.25

Table 4-2 The IR absorption/Raman spectra of $CsGe(Br_xCl_{1-x})_3$ (C-series).

The unit of these Raman and FTIR peaks was labeled as cm^{-1}. (P : Raman

peak, V : FTIR valley)

Specimens (C-series)		Raman peaks (cm^{-1})			FTIR valleys (cm^{-1})	
	x	P1	P2	P1'	V1	V2
(a)	1.00	209.79	159.88	—	212.14	333.25
(b)	0.82	262.56	161.44	—	269.23	328.63
(c)	0.79	264.10	163.00	—	269.64	330.94
(d)	0.68	264.10	163.00	—	270.77	332.48
(e)	0.51	144.23	163.78	—	281.57	332.48
(f)	0.35	152.05	—	—	298.54	—
(g)	0.26	152.84	—	—	311.65	—
(h)	0.18	160.66	—	—	311.65	—
(i)	0.00	146.58	202.79	291.15	305.48	414.25
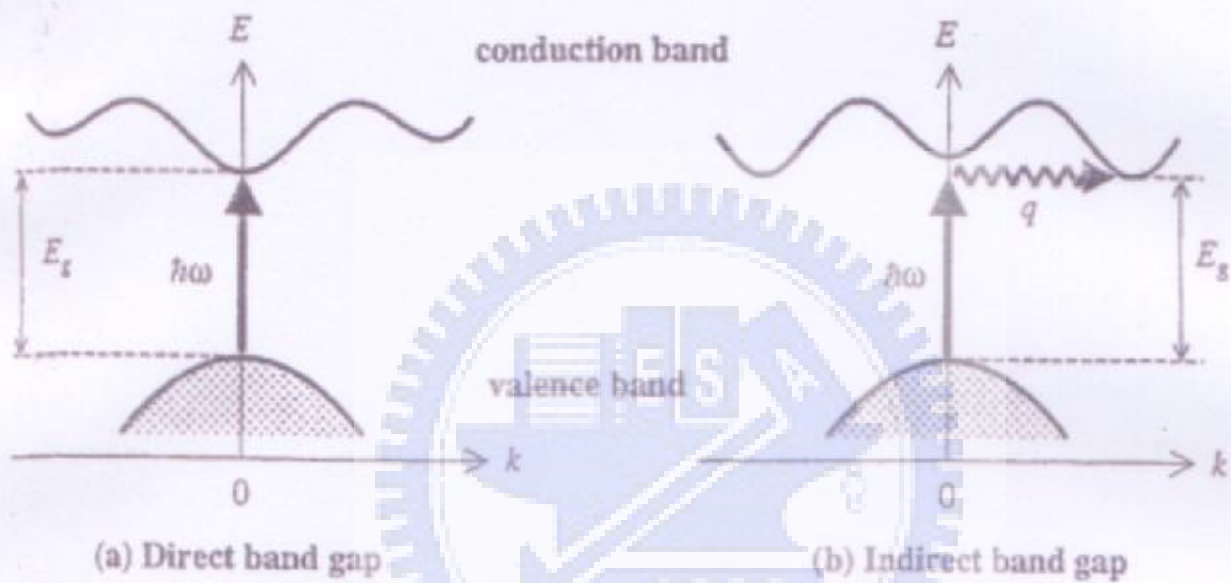
Fig. 4-1 Interband transitions in solids: (a) direct band gap, (b) indirect band gap. The vertical arrow represents the photon absorption process, while the wiggly arrow in part (b) represents the absorption or emission of a phonon [4-1].
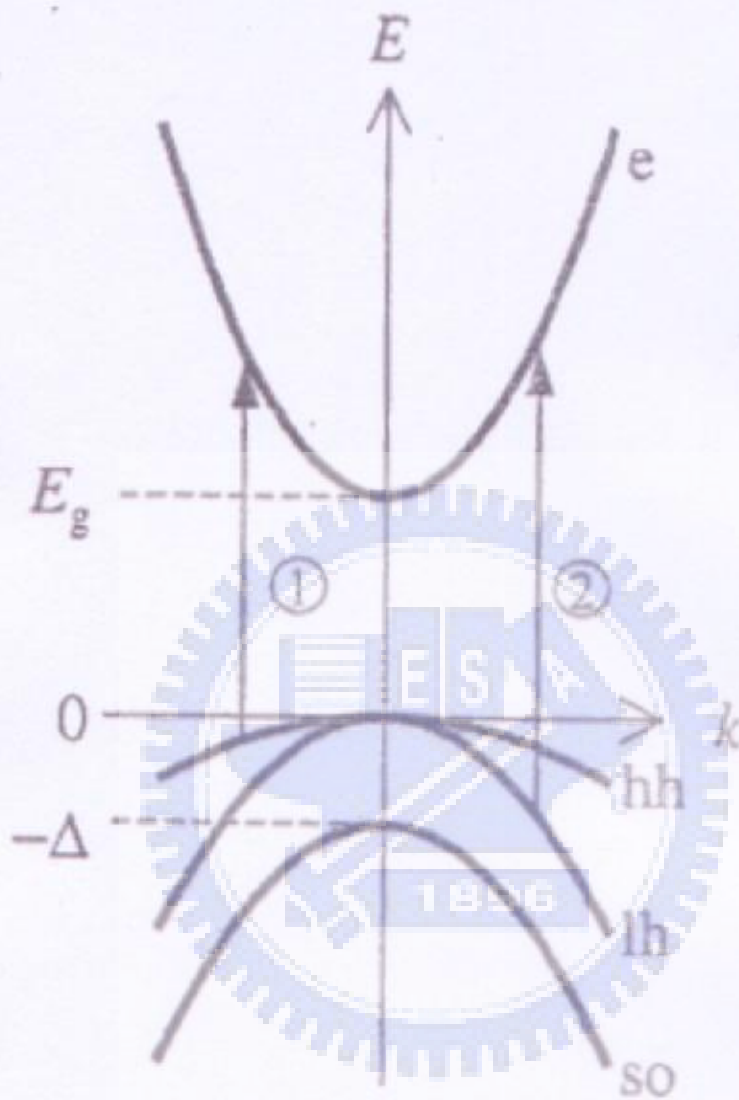
Fig. 4-2 Band structure of a direct gap III-V semiconductor such as GaAs near $k = 0$. $E = 0$ corresponds to the top of the valence band, while $E = E_g$ corresponds to the bottom of the conduction band. Four bands are shown: the heavy hole (hh) band, the light hole (lh) band, the split-off hole (so) band, and the electron (e) band. Two optical transitions are indicated. Transition 1 is a heavy hole transition, while transition 2 is a light hole transition. Transitions can also take place between the split-off hole band and the conduction band [4-1].
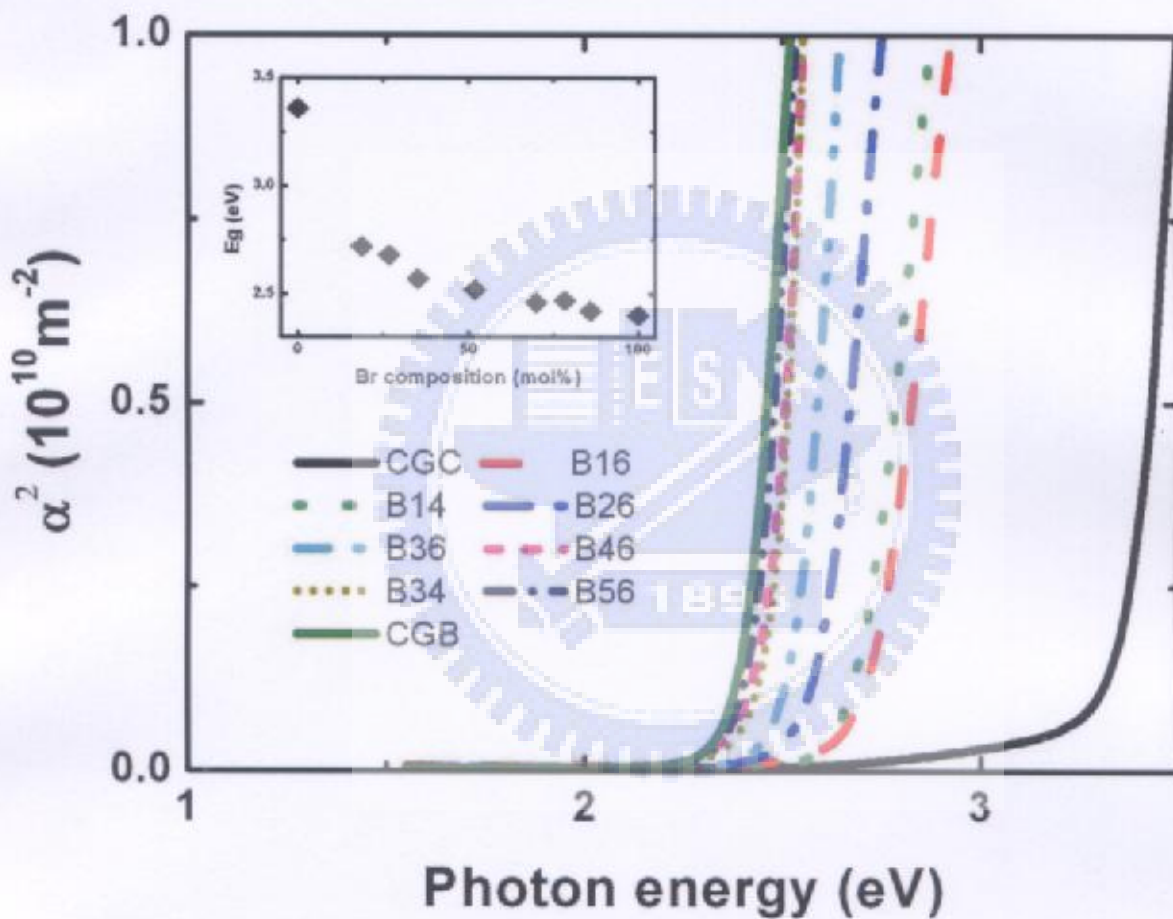
Fig. 4-3 Absorption coefficient near the band edge of $CsGe(Br_yCl_{1-y})_3$ (B-series) plotted in coordinates α^2 and $h\nu$. The inset shows the Br composition dependence of E_g obtained.
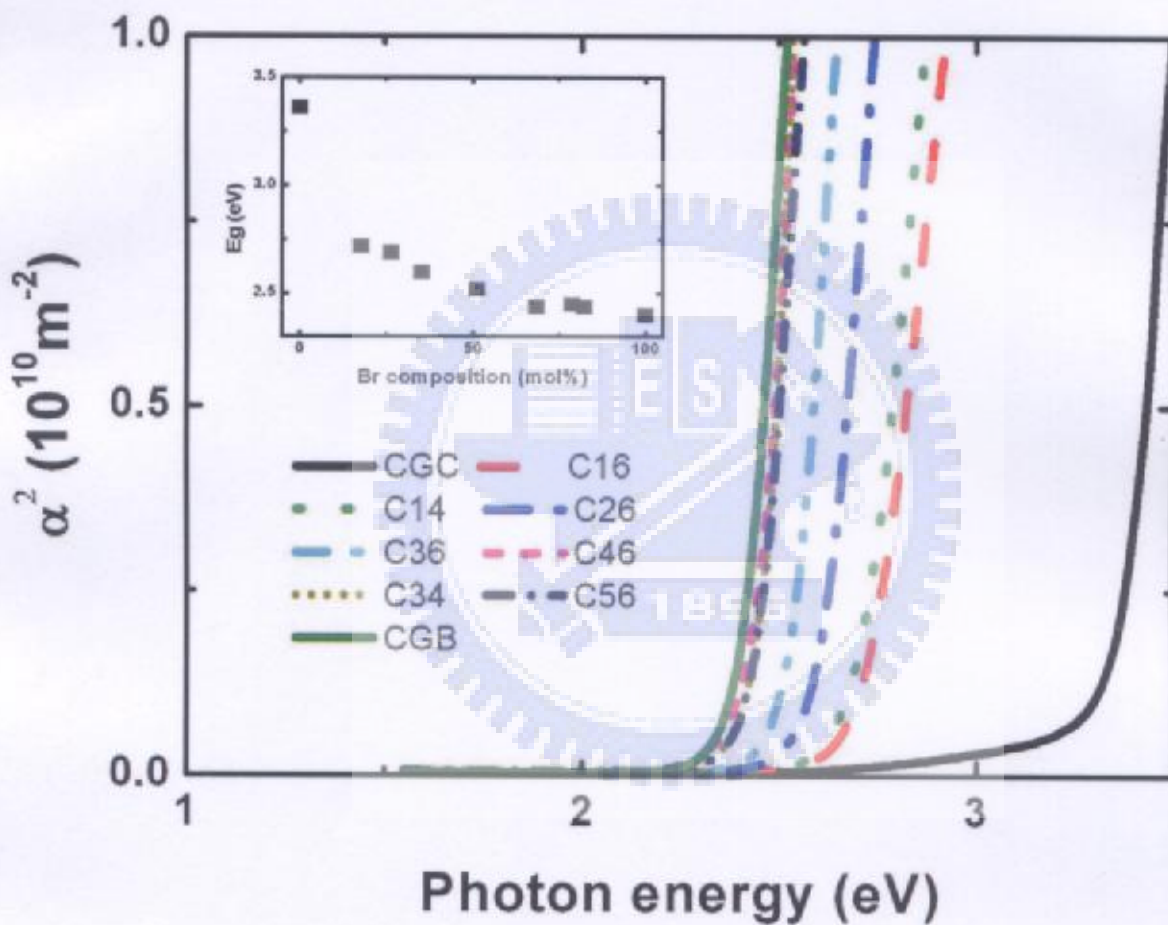
Fig. 4-4 Absorption coefficient near the band edge of CsGe(Br$_x$Cl$_{1-x}$)$_3$ (C-series) plotted in coordinates α^2 and $h\nu$. The inset shows the Br composition dependence of E$_g$ obtained.
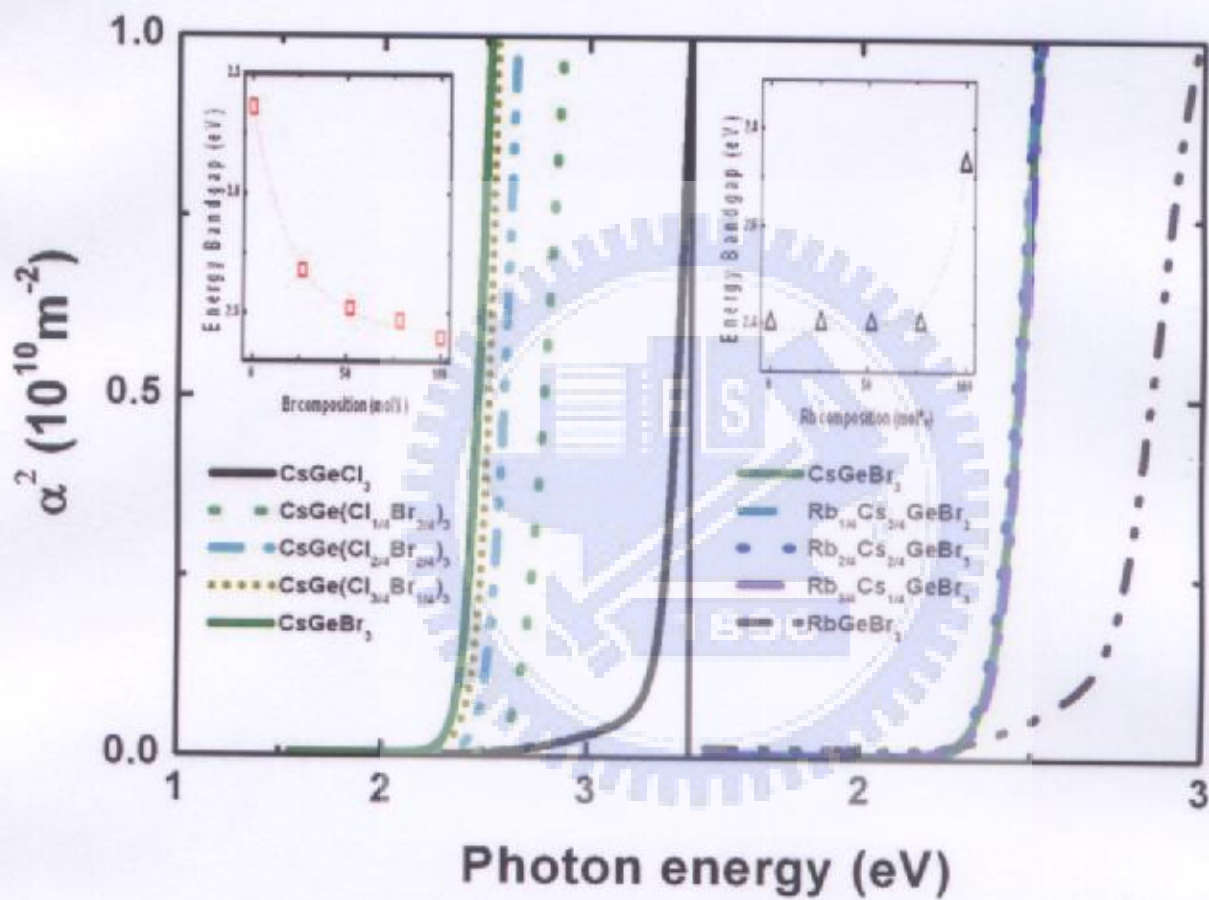
Fig. 4-5 Absorption coefficient near the band edge of CsGe(Br$_x$Cl$_{1-x}$)$_3$ and (Rb$_z$Cs$_{1-z}$)GeBr$_3$ plotted in coordinates α^2 and $h\nu$. The inset shows the substituted composition dependence of E$_g$ obtained.

(a) Stretching vibrations

(b) Bending vibrations
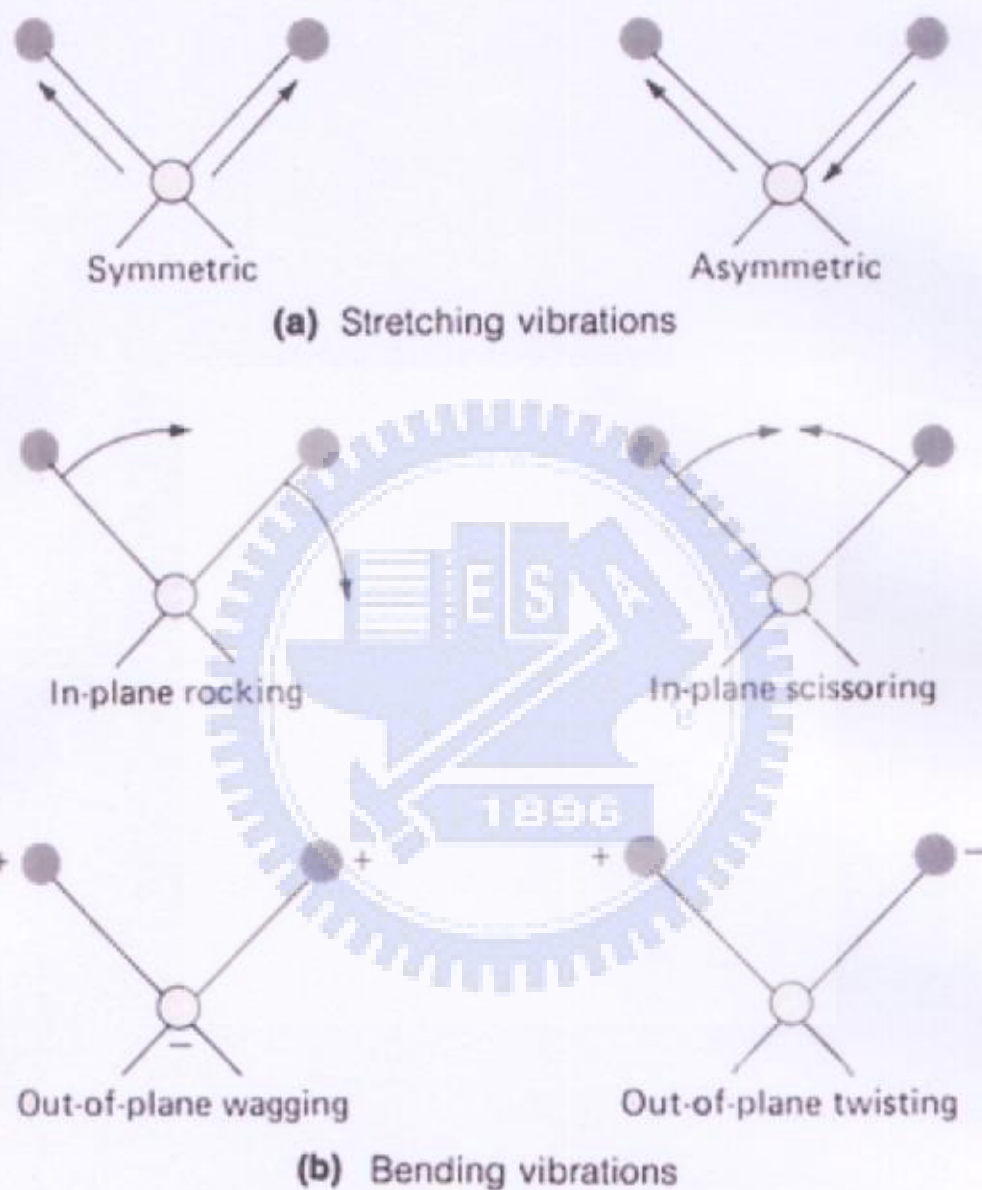
Fig. 4-6 Types of molecular vibrations. Note: + indicates motion from the page toward the reader; - indicates motion away from the reader [4-3].
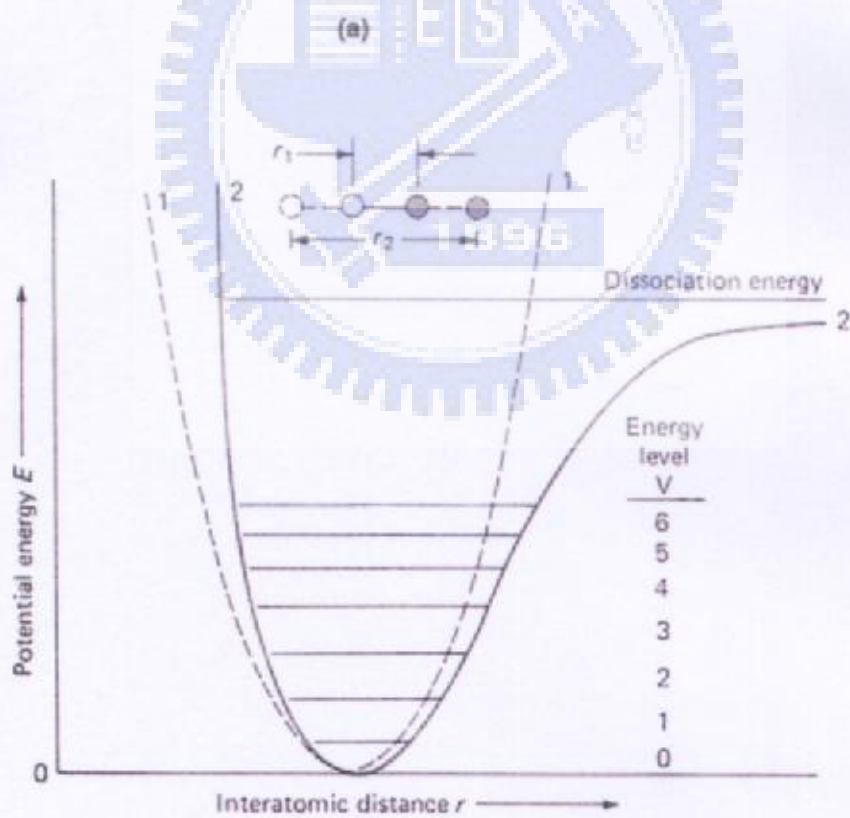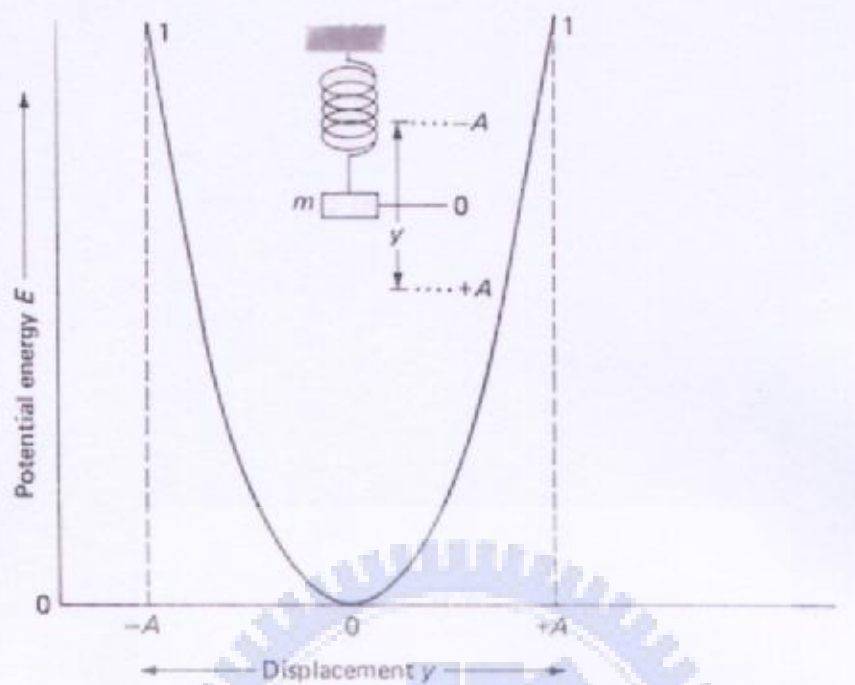
Fig. 4-7 Potential energy diagrams. (a) Curve 1, harmonic oscillator. (b) Curve 2, anharmonic oscillator [4-3].
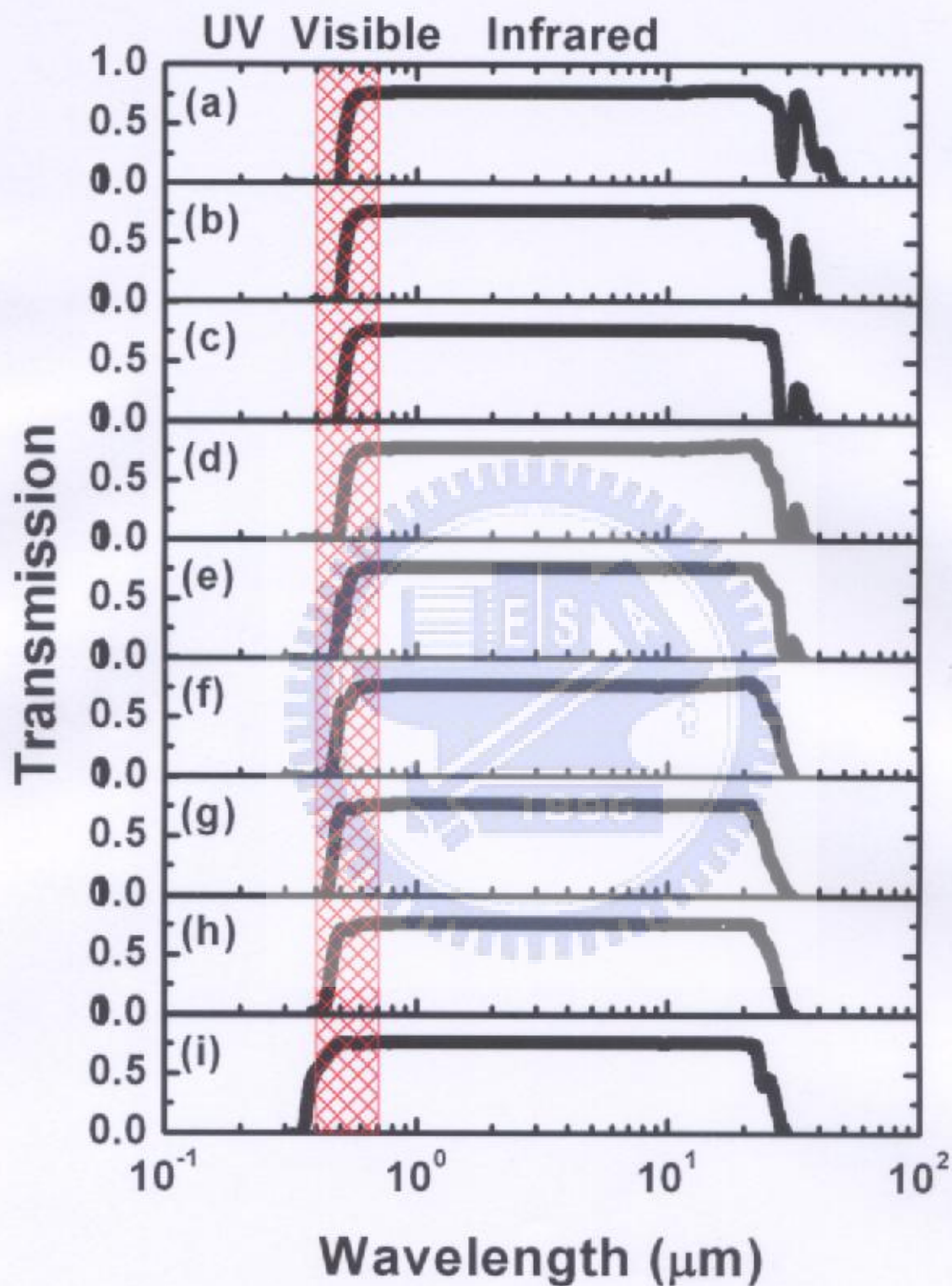
Fig. 4-8 The full transmission range of the nonlinear optical crystals CsGe(Br$_y$Cl$_{1-y}$)$_3$ (B-series) (a) y = 1.0, (b) y = 0.86, (c) y = 0.78, (d) y = 0.70, (e) y = 0.52, (f) y = 0.35, (g) y = 0.27, (h) y = 0.19, (i) y = 0.
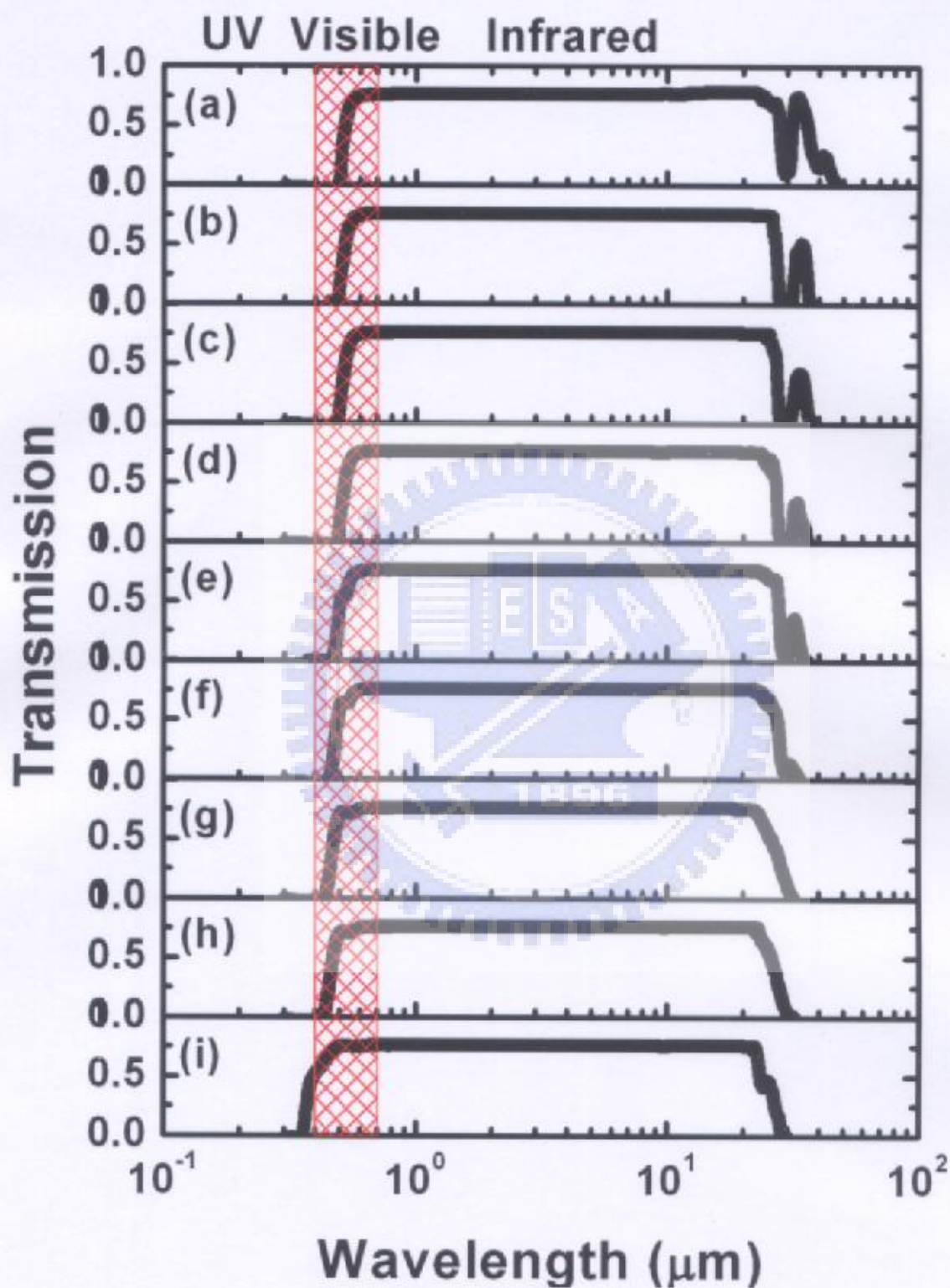
Fig. 4-9 The full transmission range of the nonlinear optical crystals
CsGe(Br$_x$Cl$_{1-x}$)$_3$ (C-series) (a) x = 1.0, (b) x = 0.82, (c) x = 0.79, (d) x = 0.68, (e) x = 0.51, (f) x = 0.35, (g) x = 0.26, (h) x = 0.18, (i) x = 0.
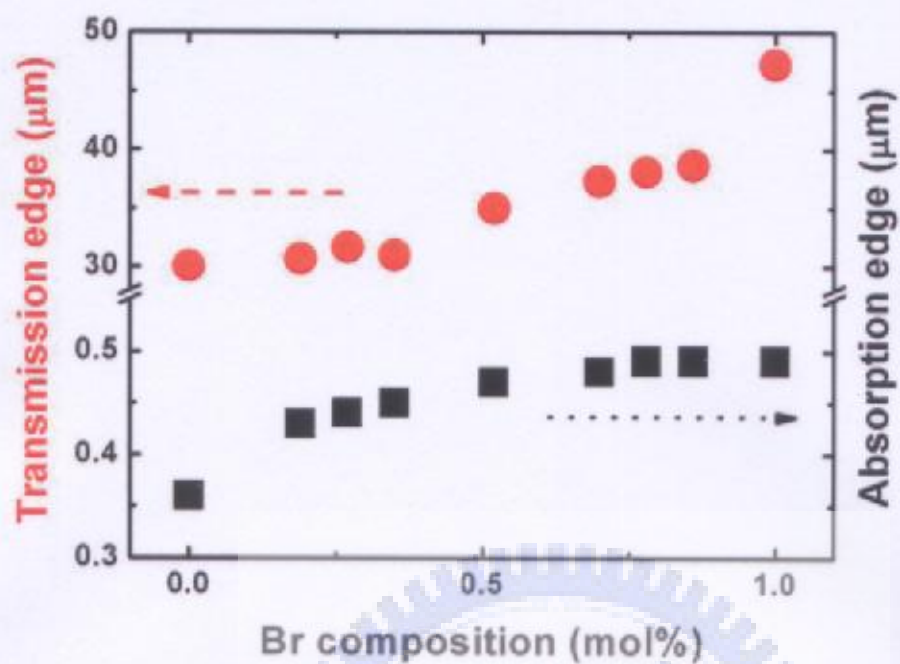
Fig. 4-10 The transmission edge and absorption edge of nonlinear optical crystals $CsGe(Br_yCl_{1-y})_3$ (B-series).
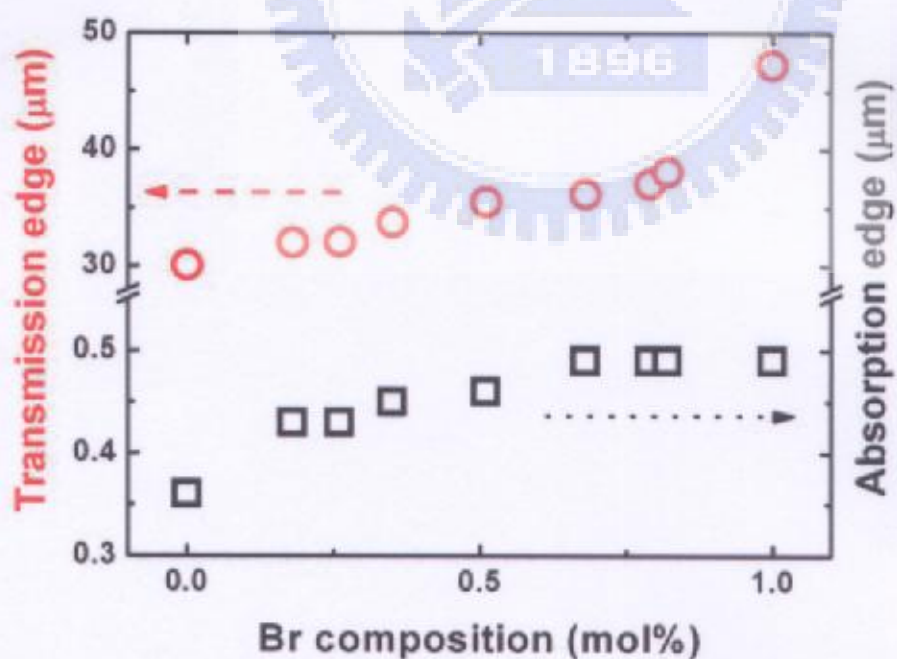
Fig. 4-11 The transmission edge and absorption edge of nonlinear optical crystals $CsGe(Br_xCl_{1-x})_3$ (C-series).
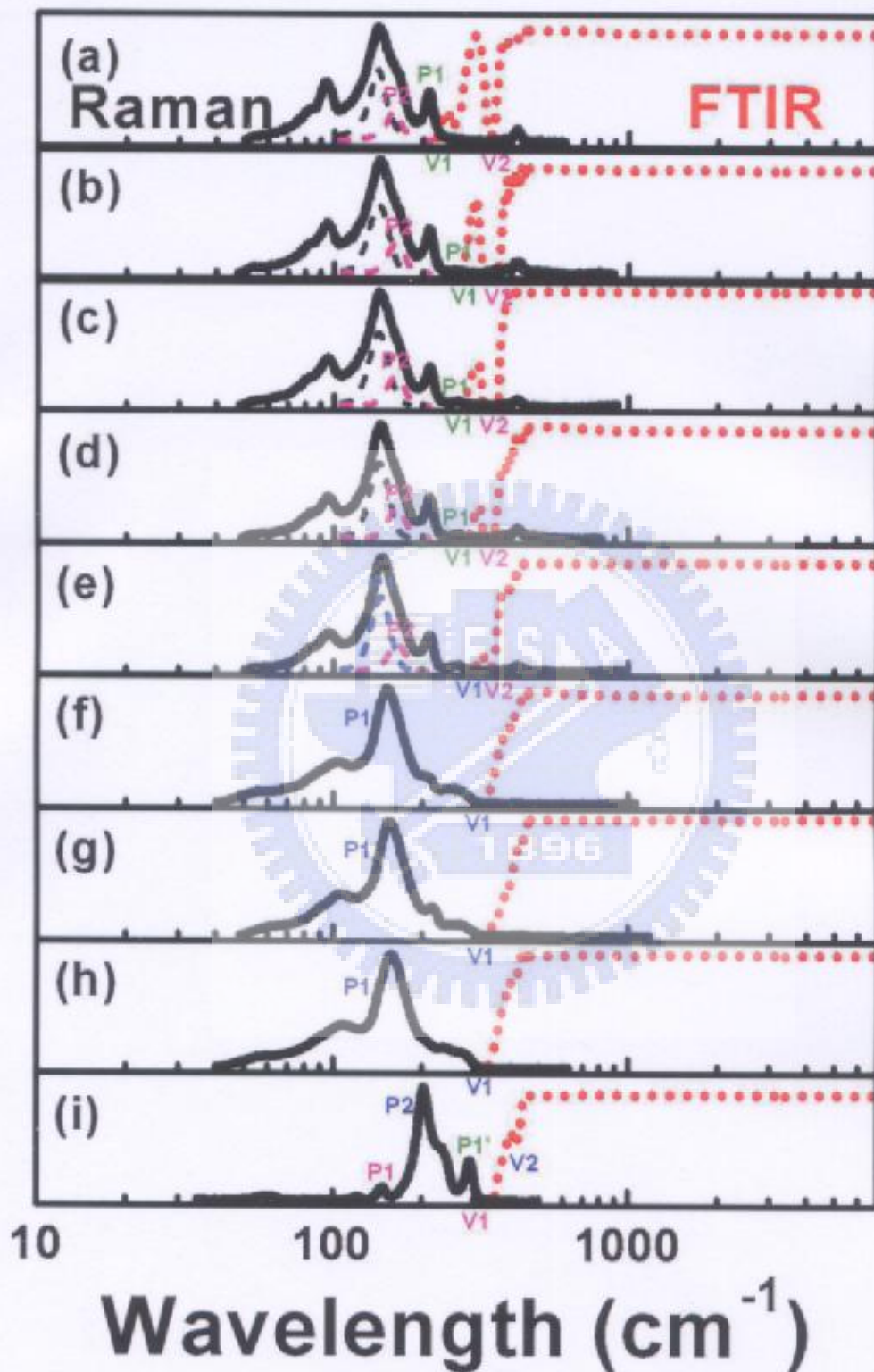
Fig. 4-12 The Raman scattering versus IR absorption spectra of CsGe(Br$_y$Cl$_{1-y}$)$_3$ (B-series). (a) y = 1.0, (b) y = 0.86, (c) y = 0.78, (d) y = 0.70, (e) y = 0.52, (f) y = 0.35, (g) y = 0.27, (h) y = 0.19, (i) y = 0.
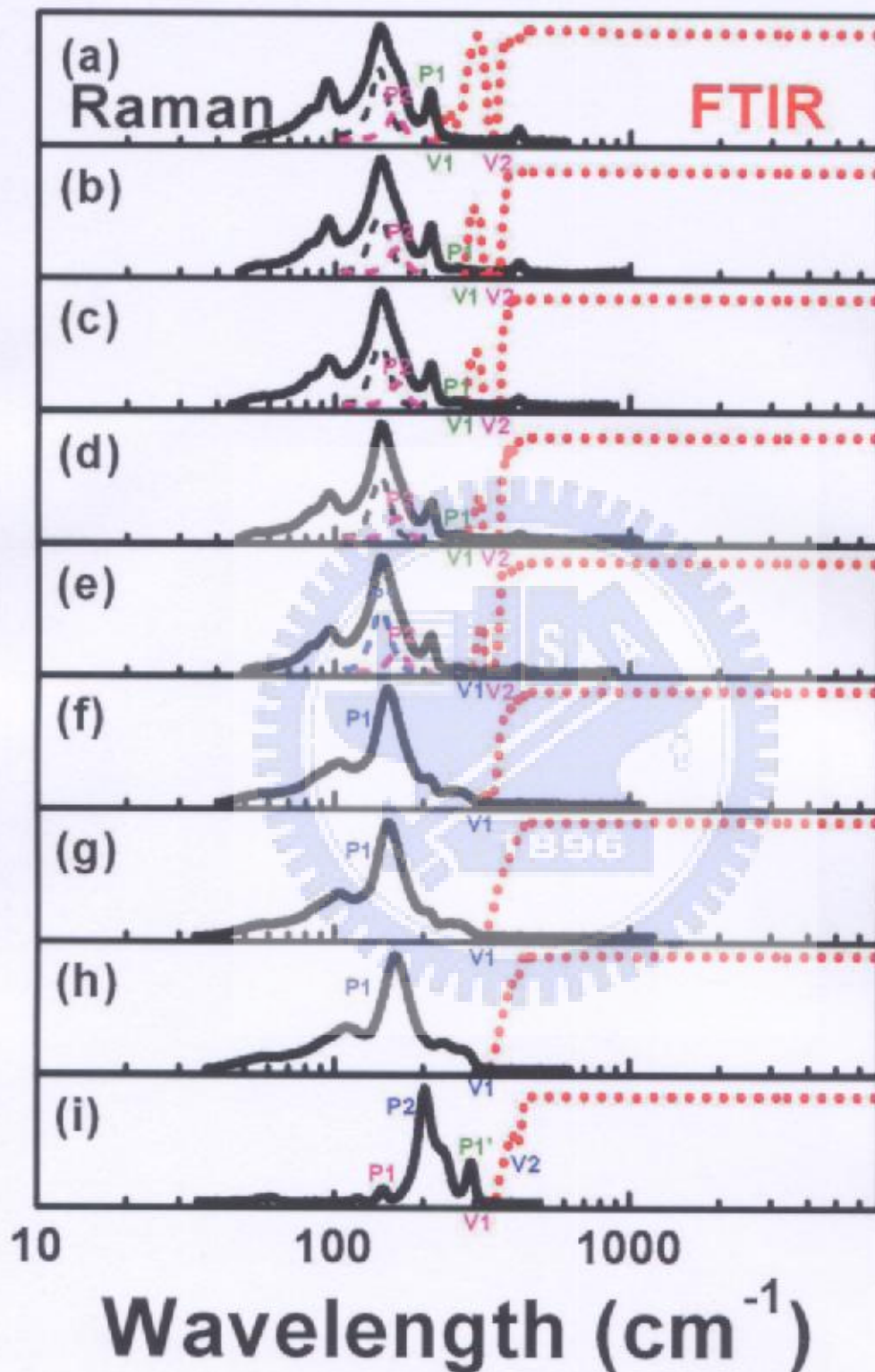
Fig. 4-13 The Raman scattering versus IR absorption spectra of $CsGe(Br_xCl_{1-x})_3$ (C-series). (a) x = 1.0, (b) x = 0.82, (c) x = 0.79, (d) x = 0.68, (e) x = 0.51, (f) x = 0.35, (g) x = 0.26, (h) x = 0.18, (i) x = 0.
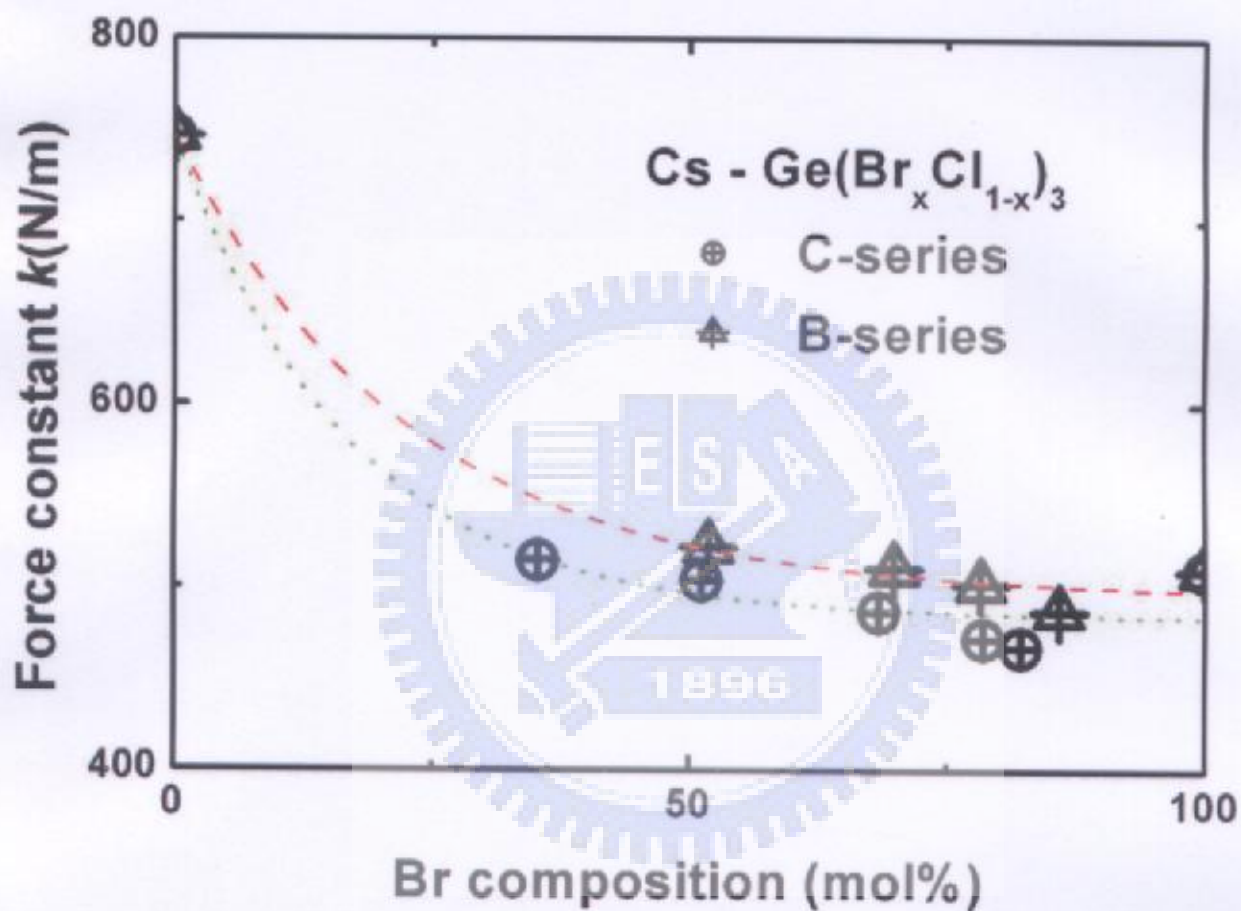
Fig. 4-14 The force constant of bonds between Cs^+ and anion group $Ge(Br_xCl_{1-x})_3^{-1}$ of $CsGe(Br_xCl_{1-x})_3$ crystals.

4.4 Reference

[4-1] Mark Fox, *Optical properties of solids* (Oxford University Press, 2001, Ch. 3).

[4-2] J. I. Pankove, *Optical Processes in Semiconductors* (Prentice-Hall, Englewood Cliffs, NJ, 1971).

[4-3] D. A. Skoog and J. J. Leary, *Principles of instrumental analysis* (Academic Press, New York, 1992).

[4-4] W. O. George and H. A. Willi, *Computer methods in UV, visible, and IR spectroscopy* (Cambridge, UK:Royal Society of Chemistry, 1990).

[4-5] B. J. Clark and, T. Frost, and M. A. Russell, *UV spectroscopy : techniques, instrumentation, data handling* (London; Chapman & Hall,1993).

[4-6] R. Bhargava, *Liquid chromatography FTIR microspectroscopy microwave assisted synthesis* (Berlin : Springer, 2003).

[4-7] A. Vaia, *Global optimization in least squares problems in FTIR spectroscopy and X-ray crystallography* (University of Illinois at Urbana-Champaign, Ph.D. Thesis, 2003).

[4-8] B. Schrader, *Infrared and Raman spectroscopy - methods and applications* (1995).

Chapter 5   Linear Optical Properties

5.1 Photoluminence analysis

5.1.1 Theory [5-1, 5-2, 5-3]

Since PL emission requires that a system be in non-equilibrium, and some means of excitation is required to act on the semiconductor to generate hole-electron pairs, this work considers the fundamental transitions, which occur at or near the band edges.

The ground state of the electronic system of a perfect semiconductor is a completely filled valance band and a completely empty conduction band. This state can be defined as the "zero" energy or the "vacuum" state. Exciting one electron from the above-defined ground state to the conduction band simultaneously generates a hole in the valance band. In this sense, an optical excitation is a two-particle transition, as is the recombination process. An electron in the conduction band can return radiatively or nonradiatively into the valance band only if a free space – a hole – is available. Two quasi-particles are annihilated in the recombination process. Therefore, a description of the excited states of N-particle problem is required to elucidate the optical properties of the

electronic system of a semiconductor. The quanta of these excitations are called "excitons".

5.1.1.1 Wannier excitons

The use of effective mass approximation, Fig. 5-1 suggests that the Coulomb interaction between electron and hole raises a hydrogen-like problem with a Coulomb potential term

$$\frac{-e^2}{4\pi\varepsilon_0\varepsilon|r_e-r_h|} \tag{5-1}$$

Indeed, excitons in semiconductors are, to a good approximation, a hydrogen or positronium-like series of states below the gap. For a simple parabolic band in a direct-gap semiconductor, the relative motion of electrons and holes as well as the actual motion of the center of mass can be separated out, leading to the dispersion relation of excitons;

$$E_{ex}(n_B,K) = E_g - R_y^* \cdot \frac{1}{n_B^2} + \frac{\hbar^2 K^2}{2M} \tag{5-2}$$

where $n_B = 1,2,3\ldots$ is the principal quantum number, $R_y^* = 13.6\frac{\mu}{m_0}\frac{1}{\varepsilon^2}$ is the exciton binding energy, $M = m_e + m_h$, and $K = k_e + k_h$ are the translational mass and wave number of the exciton, respectively.

5.1.1.2 Bound excitons

A real crystal is never perfect. Imperfections such as ion vacancies, interstitials, or substitutional atoms (either native or intentionally

132

introduced) exist in densities of $n_i < 10^{12}$ cm^{-3} in ultrapure crystals. The imperfections can attract excitons that become localized at the defect sites to yield bound excitons. The binding energy of the exciton to the defect is commonly quite small – typically a few meV. Therefore, the bound excitons are best observed at very low temperatures.

An exciton may be bound to a donor, which is a substitutional atom with more valance electrons than the host atom, or to an acceptor, which is a substitutional atom with fewer valance electrons. Donors contribute excess electrons to the crystal, while acceptors tend to capture electrons or equivalently donate holes. Donor or acceptor atoms may be electrically charged or neutral. When the donor atom has given away its initial extra valance electrons, it becomes positively charged and it referred to as an ionized donor. Similarly, when an acceptor atom has captured an electron (or equivalently released a hole), it has a negative charge and is called an ionized acceptor. In contrast, a neutral donor or acceptor has no charge, since it has kept its original number of valance electrons. Excitons may get bound to either an ionized donor or acceptor, or a neutral donor or acceptor by forming complexes, which are depicted schematically in Fig. 5-2. In various crystals, the binding energy of the exciton to a neutral

donor or acceptor is close to a tenth of the donor or acceptor ionization energy, which is the energy that is required to free the extra valence electron of a neutral donor, or the energy that is required to free a hole (to accept an electron) in a neutral acceptor. Bound excitons are characterized by more sharply peaked emission which occurs at a lower energy than the corresponding free exctions, because kinetic broadening is reduced since the bound exciton is spatially localized at an impurity. The emitted binding energy E_{BE} is

$$E_{BE} = E_g - E_E^F - E_E^B \qquad (5\text{-}3)$$

where E_E^B is the energy required to bind the exciton to the center of the defect and E_E^F is the binding energy of the free exciton. Hence, the luminescence of the bound exciton generally dominates the near-band edge emission and occurs on the low-energy side of the free exciton emission.

5.1.2 Discussion

The synthesized crystals were crushed, ground and melted under vacuum into bulks. They were then polished to thin plates ($\doteqdot 1$ mm) and measured using the 325 nm laser line excited with a power of about 4

mW from 17 to 293 K. Figures 5-3 and 5-4 present for $CsGe(Br_xCl_{1-x})_3$ the red-shift in the emission bands A, B and K as the temperature decreases (except $x = 0$).

Seo *et al.* [5-4] demonstrated that the top of the valence band is formed such that each Ge 4s orbital makes σ antibonding interactions with the p orbital of every halogen atom that surrounds the Ge (hereafter referred to as the s* level). The bottom of the conduction band is triply degenerate. The three degenerate orbitals are obtained when each Ge 4p orbital makes σ antibonding interactions with the s orbitals of the two adjacent halogen atoms that lie in the principal direction of the Ge 4p orbital. (The associated level is hereafter referred to as the p* levels). Therefore, each Ge atom has antibonding interactions with six adjacent halogen atoms in the s* level, and with two adjacent halogen atoms in each p* level. A band gap is formed when the s* level is below the p* level, as it does when the energy difference between the Ge 4s and Ge 4p levels is sufficiently large. The energy difference between the valence ns and np levels of Ge is quite large (approximately 7 eV [5-5]). Accordingly, the s* level is expected to lie below the p* level in $CsGeX_3$. An increase in the applied pressure or a drop in the temperature reduces

the cell parameter of $CsGeX_3$ and, hence, the Ge-X bond length. The s*

and p* levels have antibonding interactions between Ge and X, so an

increase in the applied pressure or a decline in the temperature raises both

of them. This increase in energy is slightly larger for the s* level than for

the p* level, since each Ge has more antibonding interactions with the

surrounding X atoms in the s* level. Therefore, the band gap decreases

somewhat as the temperature fell (or the external pressure increases),

which result agrees with the experimental results. The results for $CsGeCl_3$

revealed that the energy was constant as the temperature varied,

indicating that neither cooling nor pressuring easily reduced the lattice

constant [5-4, 5-6]. During the above experiments, drastic changes in

color were observed. For example, $CsGeBr_3$ changed from yellow to

black in a narrow temperature range of 17~60 K. These observations are

consistent with the phenomenon, observed by Schwarz et $al.$ [5-6], that

motivated this investigation of the optical-absorption edges of

$CsGe(Br_xCl_{1-x})_3$. Cooling shifts the large absorption edge to lower energy.

Figure 5-9 displays the PL spectra of $(Rb_yCs_{1-y})GeBr_3$ crystals; the

locations of their emission are almost the same in the range $y = 0 \sim 76.64$.

Their emission bands A, B and K are also red-shifted as the temperature

declines (except y =1) (Fig. 5-10).

Figure 5-5 presents the difference between the measured results obtained from the UV-visible spectra and the PL measurements. The difference is about 0.2~0.4 eV, and is caused by the drop in the lattice constant [5-4]. Since the band gap of the halide declines as temperature falls, reducing the lattice constant, the emission band A is attributable to the electronic transition of the energy band edge.

The CsGeBr$_3$ plate was annealed at 235℃ for 0 hr, 12 hrs, 24 hrs and 36 hrs under vacuum, and then measured at 17 K. Figure 5-6 indicates that peak K was an asymmetric Gaussian peak and that the relative intensity $I_{A band}/I_{K band}$ or $I_{B band}/I_{K band}$, increased with the duration of heat treatment because structural defects were eliminated by annealing. A wide band K was centered around 700 nm after annealing for 36 hrs. Figures 2-7 and 2-8 reveal that the crystals still contain O and P, which produce donor and acceptor states in the crystals. Thus, emission band K was associated with the defects and impurities.

In Fig. 5-4, the variation of peak energy from B almost followed that of the band-gap energy of CsGe(Br$_x$Cl$_{1-x}$)$_3$. These results indicate that the emission band B is attributable to the transition from the conduction band

to the impurity level or from the impurity level to the valence band [5-7].

Figure 5-7 displays the behavior associated with the thermal quenching of

the emission band B. The luminescent intensity gradually fell as the

temperature increased. At temperatures of over 50 K, semi-log plots of

luminescence intensity against reciprocal temperature yielded an almost

straight line. The variation of PL intensity $I(T)$ with temperature T can be

described by the Arrhenius expression [5-8].

$$I(T) = \frac{I_0}{1 + c \cdot exp\left(-\frac{E_a}{kT}\right)} \tag{5-4}$$

where I_0 is the PL intensity as T approaches 0 K; c is a

temperature-independent constant; k is Boltzmann's constant, and E_a is

the activation energy. The solid line in Fig. 5-7 fits the data and the

activation energy obtained from the emission band B of $CsGeBr_3$ is

around 64.2 meV. This value is identical to E_A-E_B in Fig. 5-4. Thus, the

emission band B is attributable to the transition from the conduction band

to the impurity level or from the impurity level to the valence band.

Figure 5-8 depicts the behavior associated with thermal quenching of the

emission band B of $CsGe(Br_{4/6}Cl_{2/6})_3$ and $CsGe(Br_{5/6}Cl_{1/6})_3$. Equation (5-4)

yielded activation energies of about 53 and 58 meV, respectively, which

values were consistent with the values of 53.2 meV ($=E_A-E_B$ of

CsGe(Br$_{4/6}$Cl$_{2/6}$)$_3$) and 58.3 meV (=E$_A$–E$_B$ of CsGe(Br$_{5/6}$Cl$_{1/6}$)$_3$) from Fig.

5-4.

5.2 Ellipsometric analysis

5.2.1 Theory [5-9, 5-10, 5-11, 5-12, 5-13, 5-14, 5-15]

The effects of surface roughness on the measured reflectivities from material surfaces have been examined both theoretically and experimentally. Davies [5-9], and Beckmann and Spizzichino [5-10], derived mathematical models that describe reflectivity from a rough surface based on Kirchhoff diffraction theory, by assuming a statistically random surface and a material with infinite conductivity. The assumption of infinite conductivity facilitates the reduction of the pertinent equations to forms that yield workable solutions. Since a smooth material with infinite conductivity has a reflectivity of one, the mathematical models predict the deviation of the reflectivity from unity due to the diffuse nature of the surface. The complete models proposed by Davies [5-9] and by Beckmann and Spizzichino [5-10] predict the reflectivity of a rough surface with infinite conductivity. Both models require knowledge of two parameters to describe the surface roughness; these are the root-mean-square roughness σ and the correlation length α [5-11]. Davies's model is restricted to small gradients and to the limiting cases of extremely small and extremely large optical roughness. For a material with infinite

conductivity, Davies's model predicts the bidirectional reflectivity as

$$\rho_D = e^{-f} + f\pi(\alpha/\lambda)^2 \cos(\theta)\Delta\omega \qquad (5\text{-}5)$$

where the first and second terms represent the specular and the diffuse components of the reflected radiation, respectively. The term $\Delta\omega$ represents the solid angle of the detection optics, which is defined as the monochromator slit opening, A_s, the distance from the reflection surface, R, and the angle of incidence, θ [$\Delta\omega = A_s \cos(\theta)]/R^2$]. Notably, the angle of incidence θ is measured from the normal to the mean surface plane of the sample. The factor f is related to the ratio (σ/λ) and the angle of reflection is given θ by

$$f = \left[4\pi\cos(\theta)\frac{\sigma}{\lambda} \right]^2 \qquad (5\text{-}6)$$

Over a broader range of roughness values, Houchens and Hering [5-11] suggest the following simplified relation for the reflectivity of the rough surface based on the Beckmann-Spizzichino model;

$$\rho_{BS} = e^{-f} \left[1 + \pi(\alpha/\lambda)^2 \cos(\theta)\Delta\omega \sum_{m=1}^{\infty} \frac{f^m}{m \cdot m!} \right] \qquad (5\text{-}7)$$

Notably, both models assume that the distribution of heights of the surface irregularities is Gaussian about the mean. Moreover, many researchers (such as Bennett and Porteus [5-12], Bennett [5-13] and

141

Ohlidal et al. [5-14]) have found that most randomly generated rough surfaces may in practice be represented by a Gaussian distribution, and the autocovariance function of the surface irregularities is also Gaussian with known standard deviation. For slightly rough surfaces of materials with finite conductivity, both models [Eqs. (5-5) and (5-7)] can be reduced to the specular component alone, which is given by

$$\rho_s = exp\left\{-\left[4\pi\cos(\theta)\frac{\sigma}{\lambda}\right]^2\right\} \qquad (5\text{-}8)$$

In the case of a material with finite conductivity, the angular reflectance of a rough surface may be expressed as the product of a surface-roughness-dependent quantity and a material-dependent quantity [5-10, 5-12, 5-14]:

$$R\left(\overline{m},\theta,\frac{\sigma}{\lambda}\right) = \rho\left(\theta,\frac{\sigma}{\lambda}\right)R_0\left(\overline{m},\theta\right) \qquad (5\text{-}9)$$

where $\rho(\theta,\sigma/\lambda)$ is given by Eq. (5-5) or (5-7) and $R_0(\overline{m},\theta)$ is the reflectivity of a smooth surface with the same refractive index ($\overline{m}$) as the surface of interest. According to Beckmann and Spizzichino [5-10] the function $\rho(\theta,\sigma/\lambda)$ represents a mean value of the reflection coefficient over the surface. The reflectivity $R_0(\overline{m},\theta)$ can be calculated from the Fresnel equations if the complex refractive index ($\overline{m} = n - ik$) is known. Since the reflection approach requires knowledge of both components of

142

polarization, Eq. (5-9) should be applied in both planes of polarization. In this respect, Hensler [5-15] has demonstrated that the roughness factors $\rho(\theta, \sigma/\lambda)$ are identical in both the vertical and horizontal planes of polarization. Under this condition, Eq. (5-9) yields the reflection coefficients.

$$R_{\parallel} = \rho R_{0,\parallel} \qquad (5\text{-}10)$$

$$R_{\perp} = \rho R_{0,\perp} \qquad (5\text{-}11)$$

The subscripts $\parallel$ and $\perp$ indicate polarization parallel and perpendicular to the plane of incidence. Equations (5-10) and (5-11) yield

$$\frac{R_{\parallel}}{R_{\perp}} = \frac{R_{0,\parallel}}{R_{0,\perp}} \qquad (5\text{-}12)$$

Thus, the reflectance ratio from a rough surface equals that from a smooth surface of the same material. This fact implies that the complex refractive index ($\overline{m} = n - ik$) of a rough surface can be determined by measuring the reflectance ratio at a minimum of two angles of incidence and solving the Fresnel equations simultaneously.

5.2.2 Discussion

Tables 5-1, 5-2 and 5-3 display the results. According to Figs. 4-3 and 4-4, the values of the energy gap reveal that $CsGe(Br_xCl_{1-x})_3$ has

different dispersion relationships. The energy gap of $CsGe(Br_xCl_{1-x})_3$ decreased as the proportion of Br, x, was increased. The refractive index of $CsGe(Br_xCl_{1-x})_3$ became abnormal because of the near-bandgap (~2.38 eV) resonance. In this case, the near-bandgap refractive indices became smaller than those for longer wavelengths as the amount of Br, x, was increased.

5.3 Tables and Figures

Table 5-1 The ellipsometry measurements of the rhombohedral NLO crystals $CsGe(Br_yCl_{1-y})_3$ (B-series).

$CsGe(Br_yCl_{1-y})_3$ (B-series)	y								
	0	0.19	0.27	0.35	0.52	0.70	0.78	0.86	1.0
α_{630nm} (1/mm)	1.49	2.75	3.80	2.66	5.26	4.49	4.45	4.86	8.88
n_{630nm}	1.71	1.88	1.89	1.95	1.78	1.67	1.58	1.71	1.63
n_{1260nm}	1.67	1.84	1.86	1.89	1.78	1.68	1.64	1.73	1.68
lc (1/μm)	3.76	3..86	5.88	2.67	24.35	10.69	2.85	6.35	3.58

Table 5-2 The ellipsometry measurements of the rhombohedral NLO crystals $CsGe(Br_xCl_{1-x})_3$ (C-series).

$CsGe(Br_xCl_{1-x})_3$ (C-series)	x								
	0	0.18	0.26	0.35	0.51	0.68	0.79	0.82	1.0
α_{630nm} (1/mm)	1.49	3.04	2.22	5.17	4.48	3.76	6.08	3.43	8.88
n_{630nm}	1.71	1.90	1.91	1.81	1.78	1.55	1.57	1.52	1.63
n_{1260nm}	1.67	1.85	1.84	1.80	1.79	1.59	1.59	1.53	1.68
lc (1/μm)	3.76	3.29	2.33	13.70	14.02	3.31	6.65	12.43	3.58

Table 5-3 The ellipsometry measurements of the rhombohedral NLO crystals $(Rb_zCs_{1-z})GeBr_3$.

$(Rb_zCs_{1-z})GeBr_3$	z				
	0	0.26	0.52	0.77	1.0
α_{630nm} (1/mm)	8.88	3.59	4.60	3.42	–
n_{630nm}	1.63	1.56	1.55	1.50	–
n_{1260nm}	1.68	1.58	1.58	1.53	–
lc (1/μm)	3.58	8.02	4.75	5.11	–
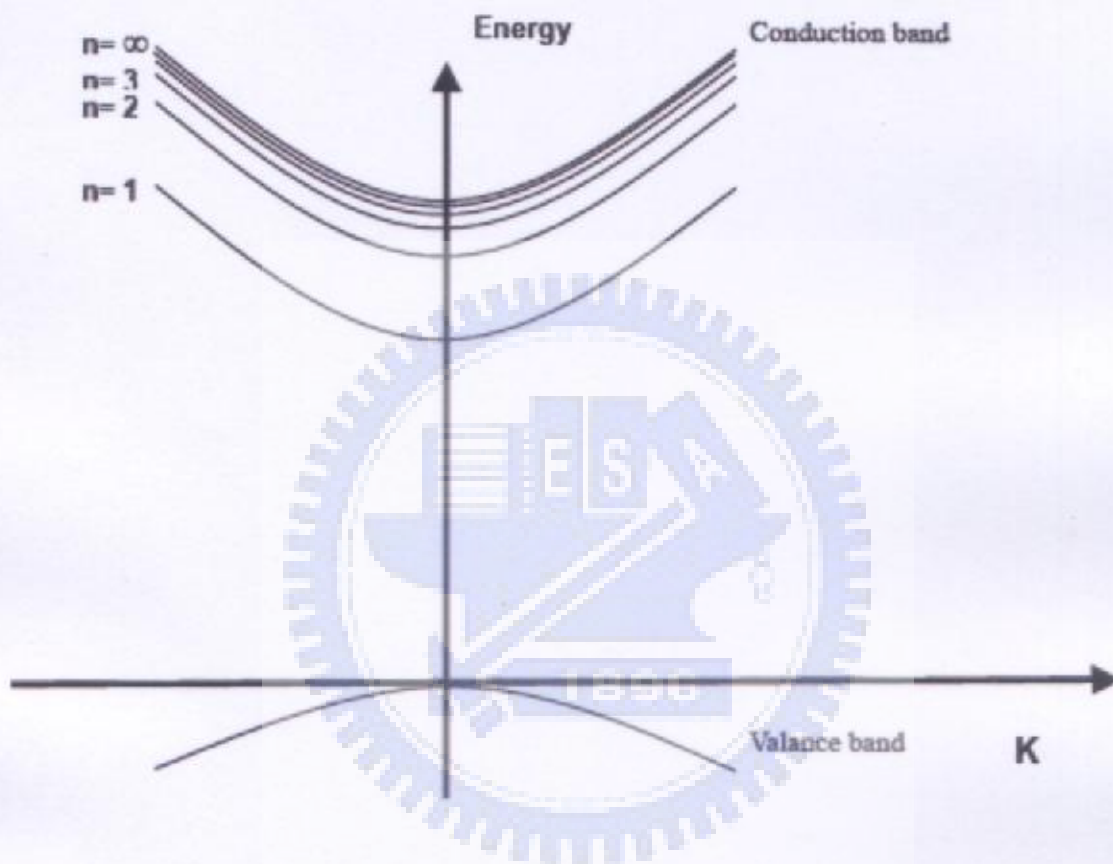
Fig. 5-1 The exciton dispersion in a two-particle (electron-hole) excitation diagram of the entire crystal. The crystal ground state (zero energy and zero momentum) is the point at the origin. Different parabolas represent the kinetic energy bands associated with different terms of the excitonic series [5-1].

(a)   (b)   (c)

⊞ ⊖   ⊖   ⊕   ⊖
⊕   ⊖⊞ ⊕   ▣
                         ⊕   ⊕   ☐ point defect
                                                           ⊖ electron
D⁺X   D⁰X   A⁰X   ⊕ hole
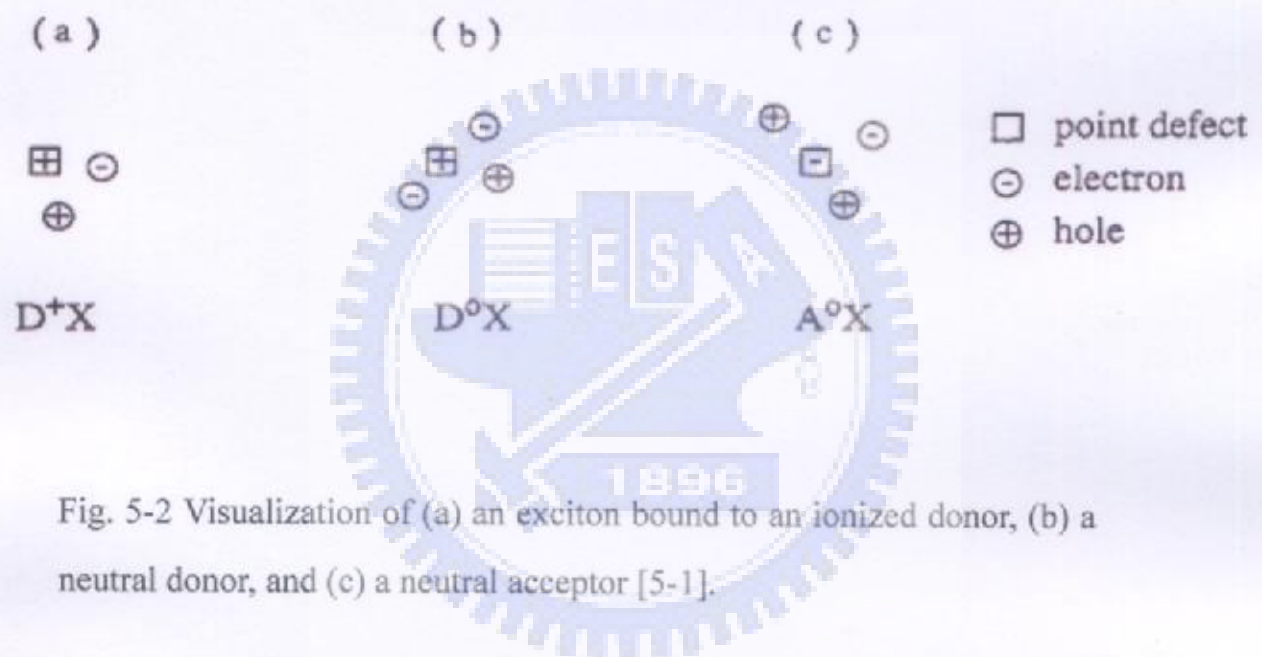
Fig. 5-2 Visualization of (a) an exciton bound to an ionized donor, (b) a
neutral donor, and (c) a neutral acceptor [5-1].

147
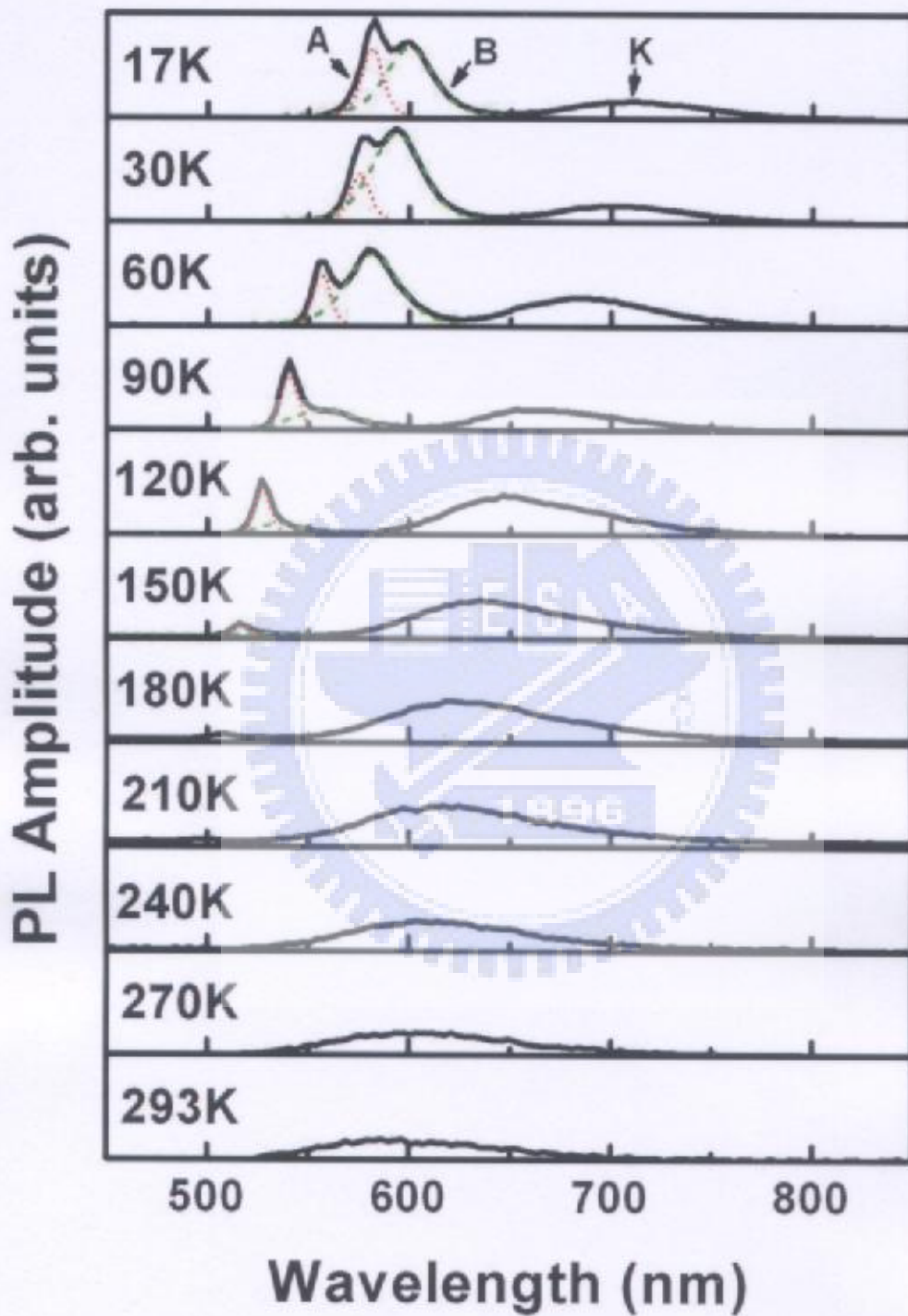
Fig. 5-3 PL spectra of CsGeBr₃ under 325 nm excitation (He-Cd laser, power = 4 mW) in the temperature range of 17 to 293 K.
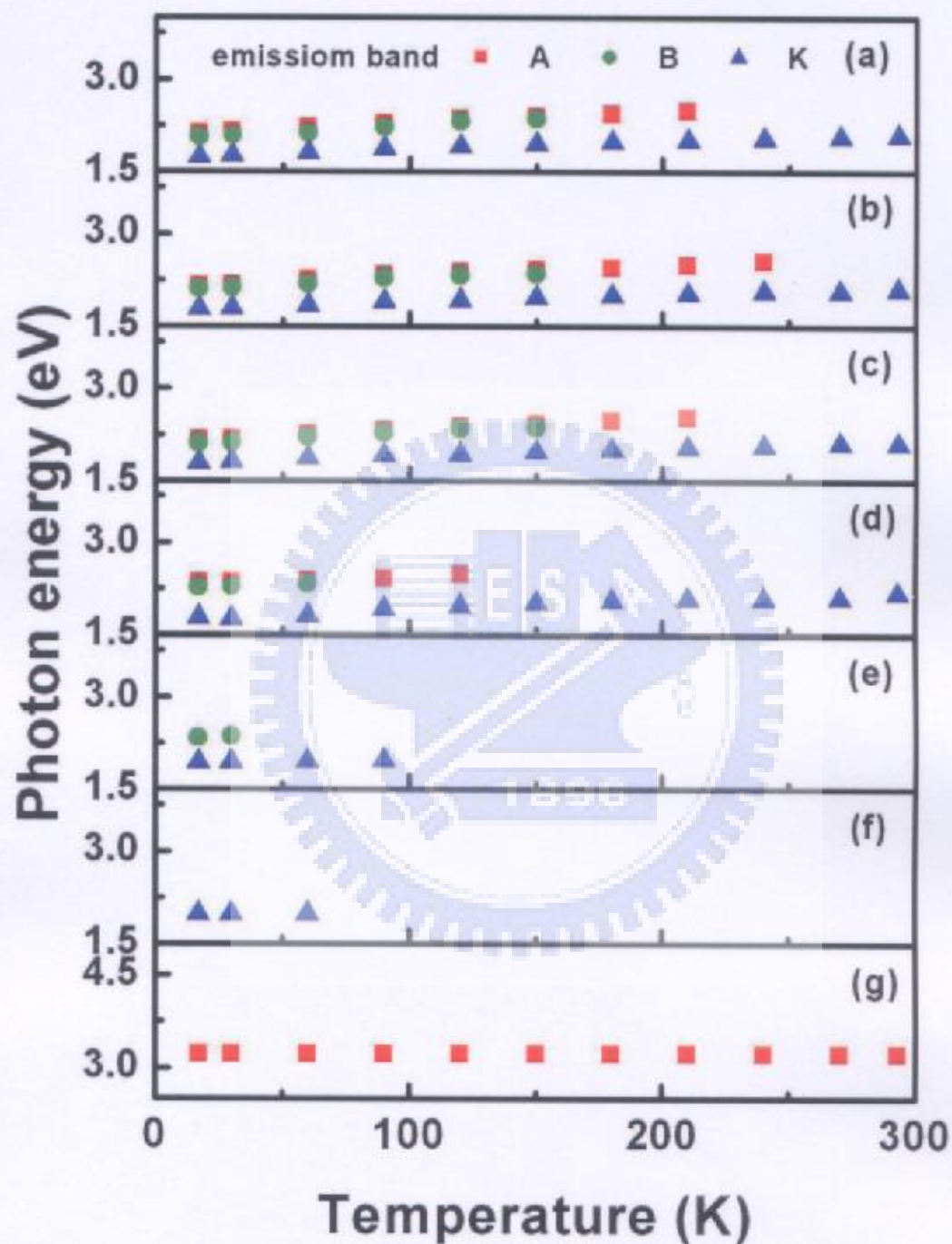
Fig. 5-4 Temperature dependence of the peak energy of emission bands A, B and K of $CsGe(Br_xCl_{1-x})_3$ crystals, (a) x = 1 (b) x = 5/6 (c) x = 4/6 (d) x = 3/6 (e) x = 2/6 (f) x = 1/6 (g) x = 0.
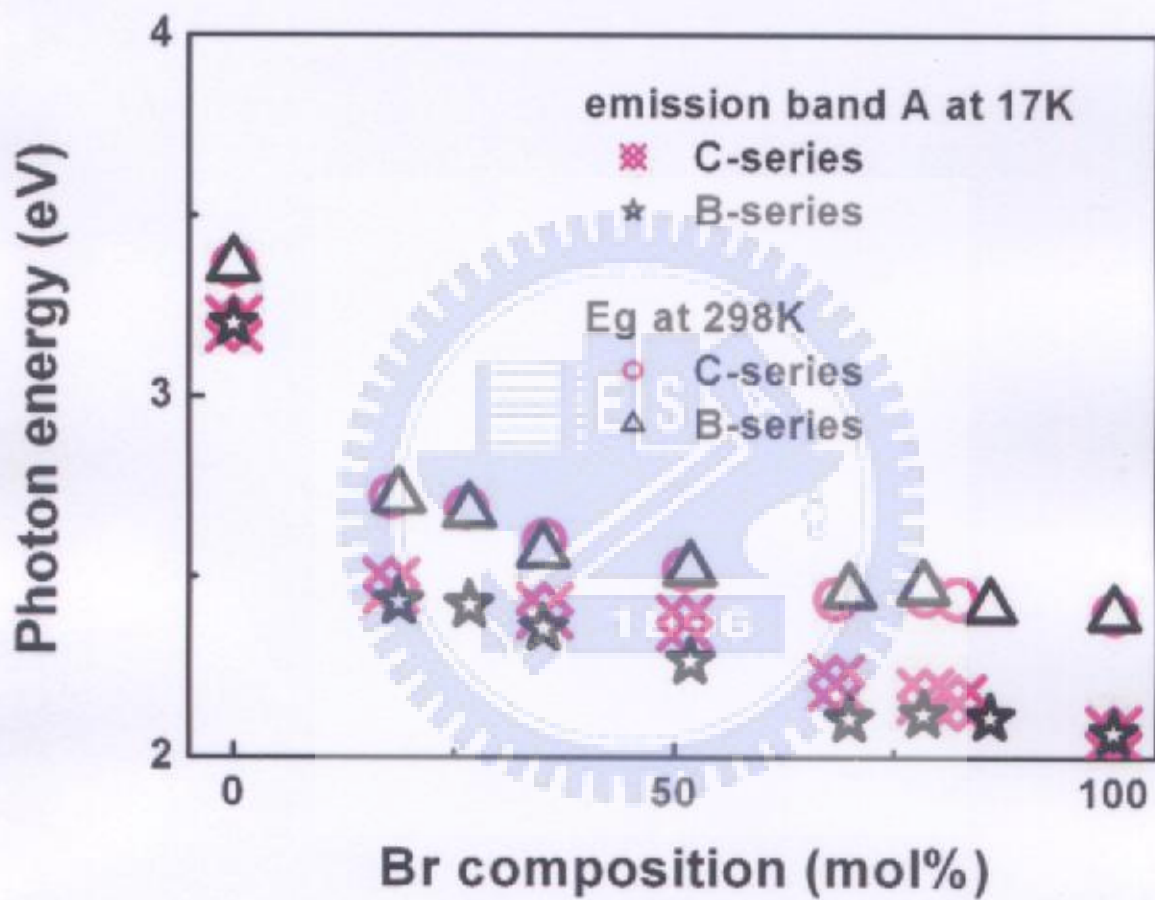
Fig. 5-5 Comparison of Br content dependent photon energy from emission band A with Br content dependent absorption edge from UV-visible spectra.
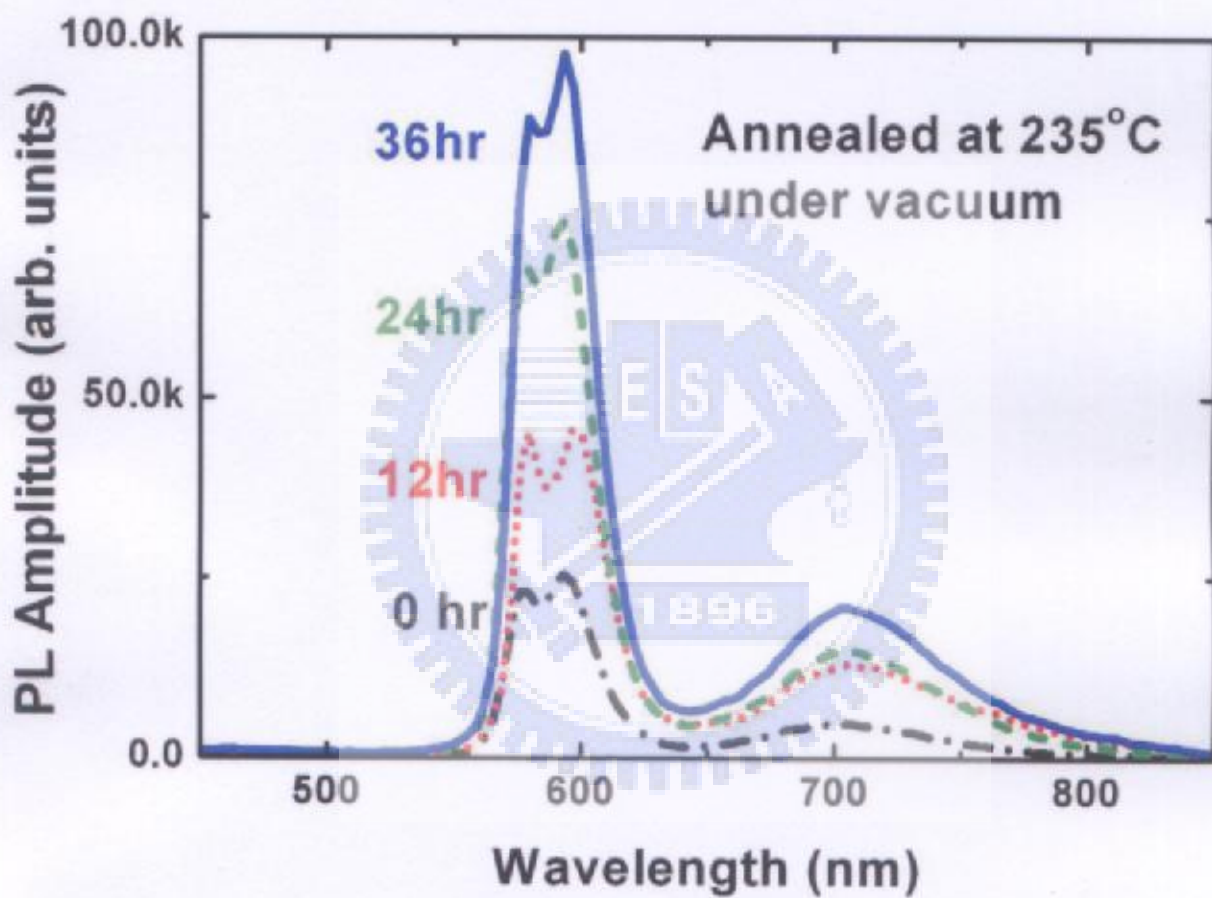
Fig. 5-6 PL spectra of CsGeBr$_3$ annealed at 235°C for 0 to 36 hours under 325 nm excitation (He-Cd laser, power = 4 mW) at 17 K.
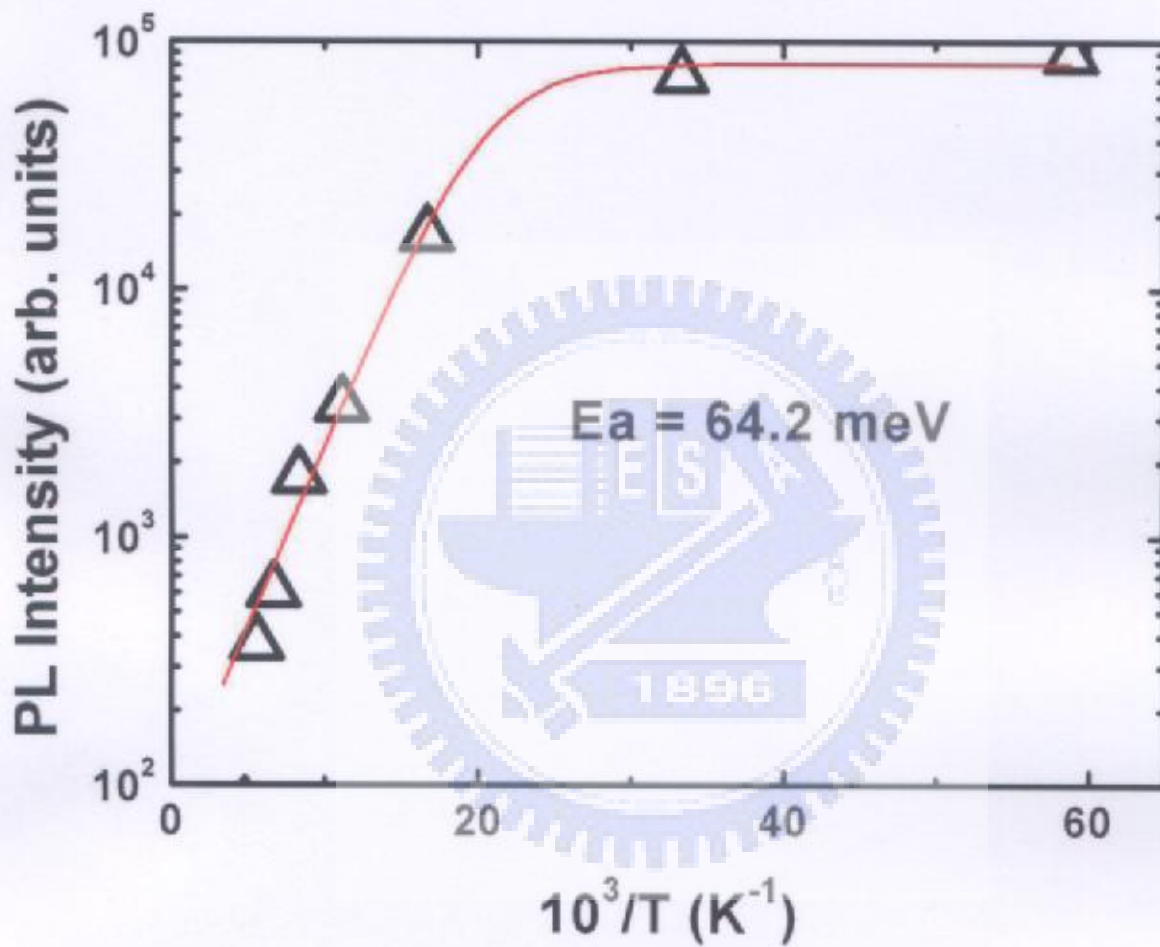
Fig. 5-7 Variation of PL intensity with reciprocal temperature for the emission band B of CsGeBr₃.
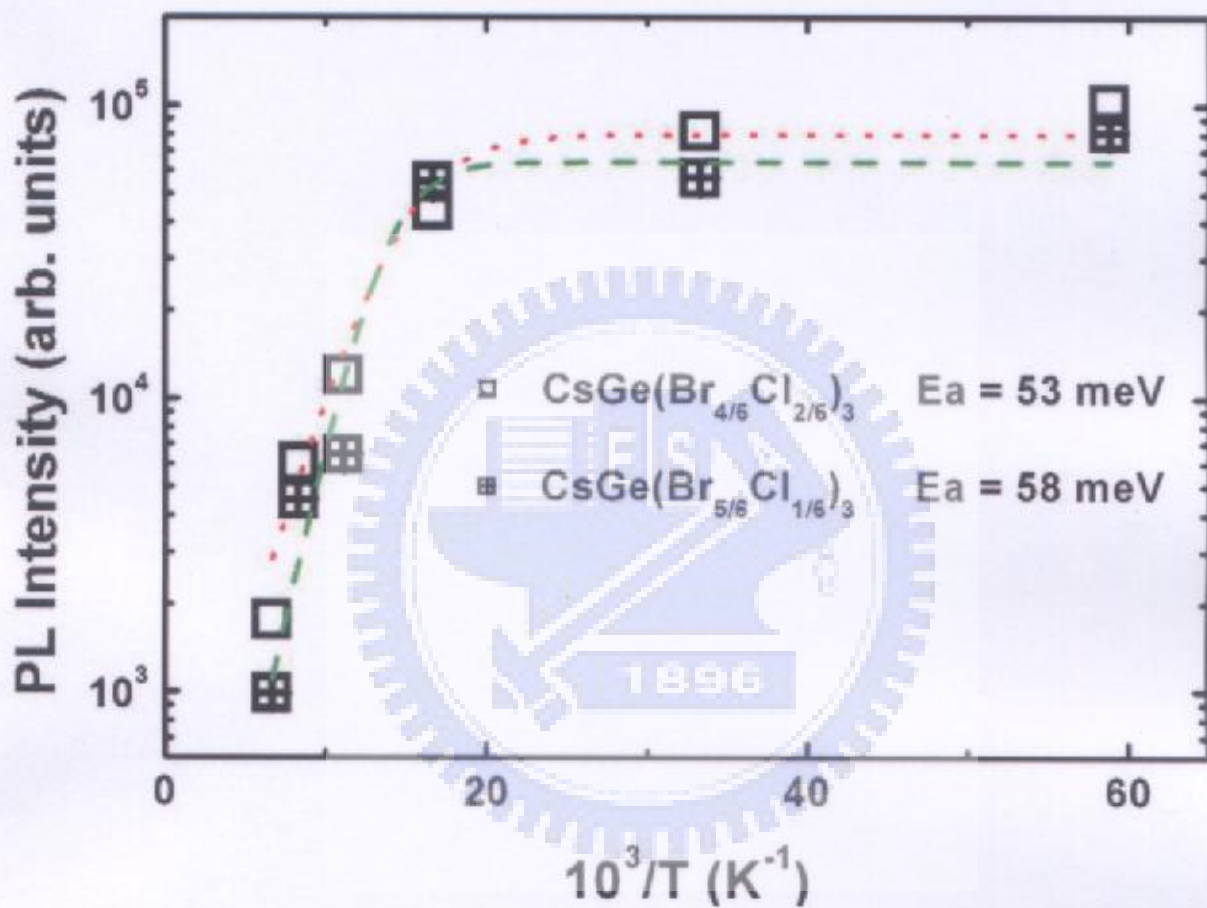
Fig. 5-8 Variation of PL intensity with reciprocal temperature for the emission band B of $CsGe(Br_{4/6}Cl_{2/6})_3$ and $CsGe(Br_{5/6}Cl_{1/6})_3$.
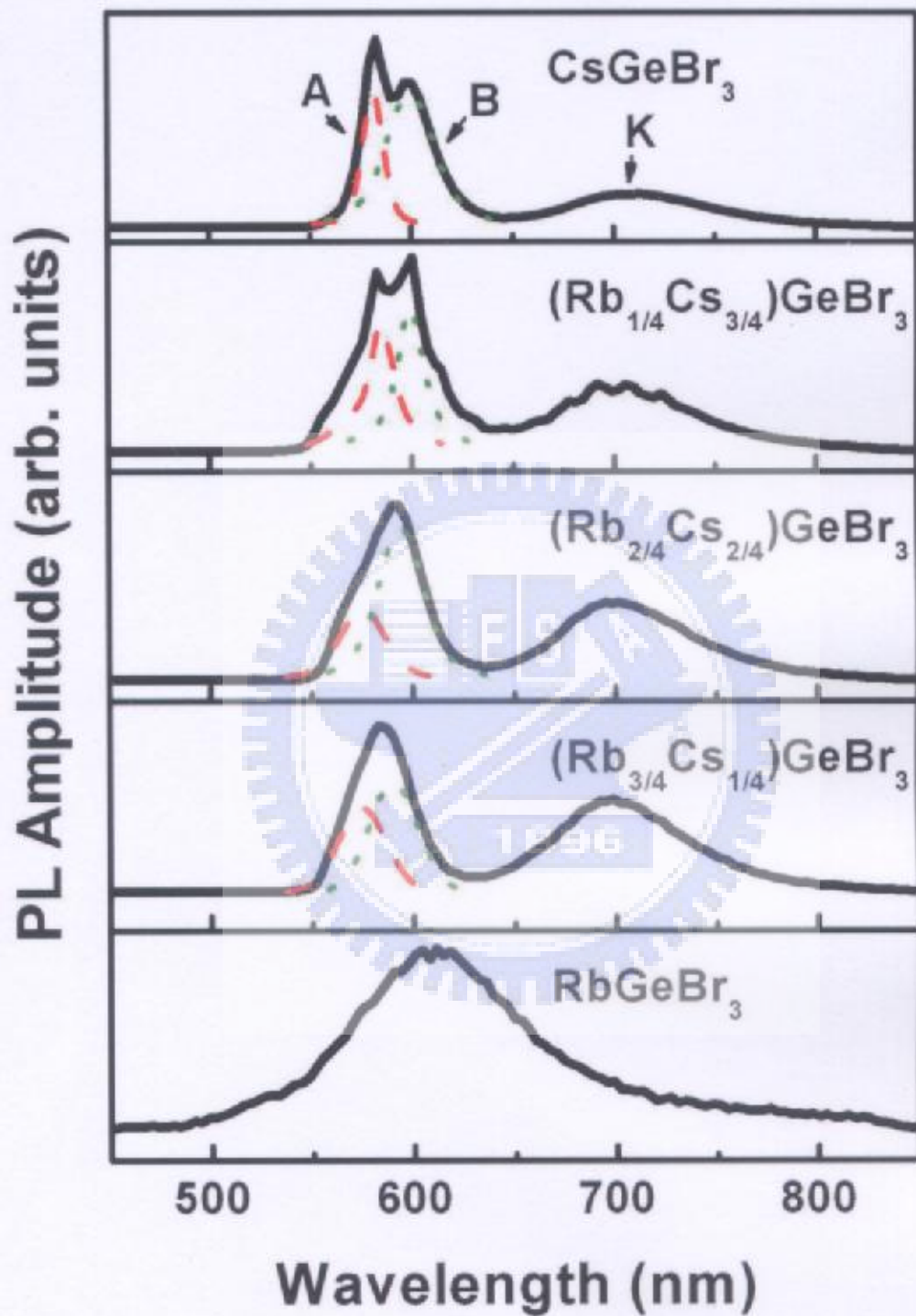
Fig. 5-9 PL spectra of $(Rb_yCs_{1-y})GeBr_3$ under 325 nm excitation (He-Cd laser, power = 4 mW) at 17 K.
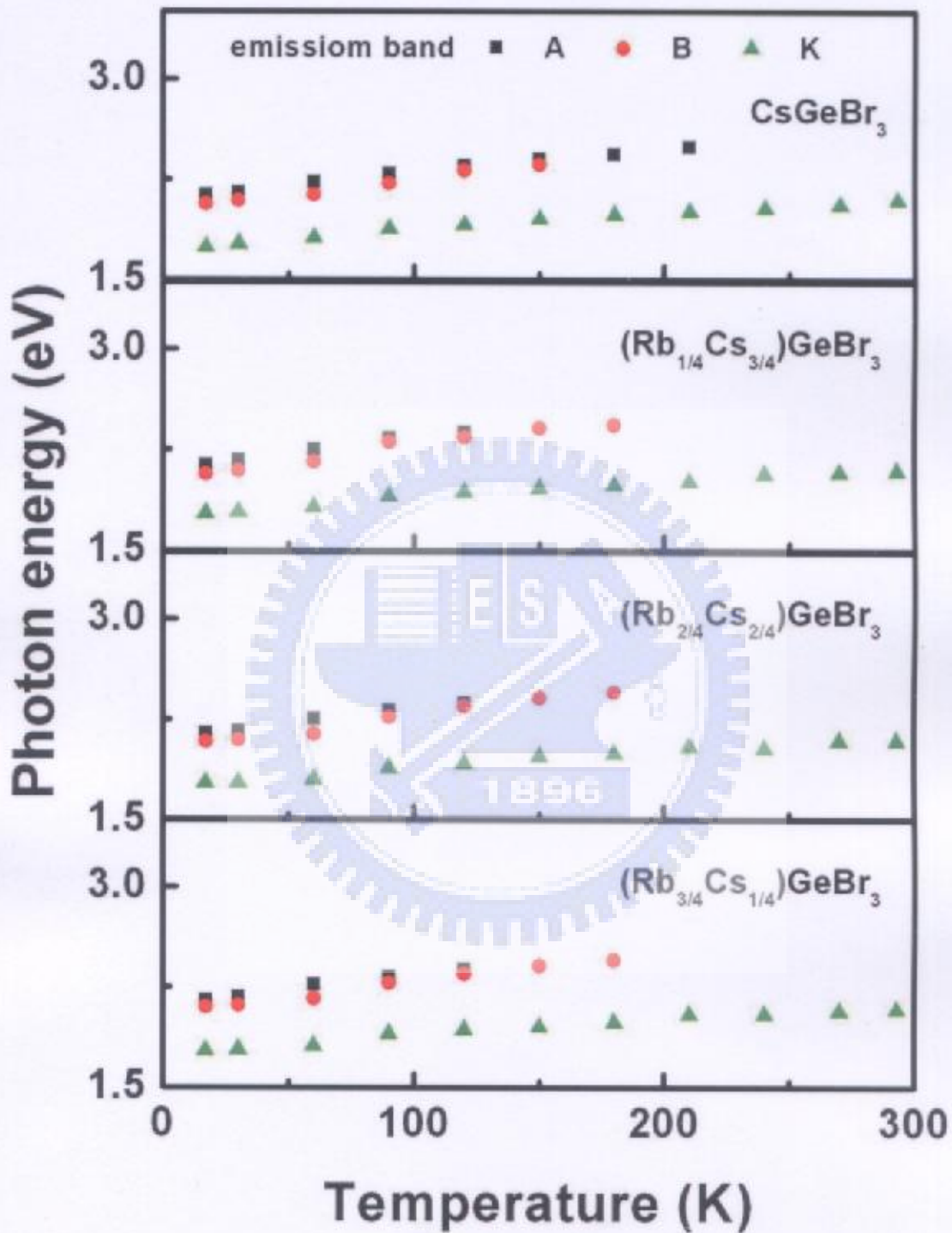
Fig. 5-10 Temperature dependence of the peak energy of emission bands
A, B and K of $(Rb_yCs_{1-y})GeBr_3$ crystals.

5.4 Reference

[5-1] C. F. Klingshirn, *Semiconductor Optics* (Springer, Berlin, 1997).

[5-2] N. Peyghambarian, S. W. Koch, and A. Mysyriwicz, *Introduction to Semiconductor Optics* (Prentice-Hall, New Jersey, 1993).

[5-3] J. I. Pankove, *Optical Processes in Semiconductors* (Dover Publications, New York, 1971).

[5-4] D. K. Seo, N. Gupta, M. H. Whangbo, H. Hillebrecht and G. Thiele, *Inorg. Chem.* 37 (1998) 407.

[5-5] E. Clementi and C. Roetti, *At. Data Nucl. Data Tables* 14 (1974) 177.

[5-6] U. Schwarz, F. Wagner, K. Syassen, and H. Hillebrecht, *Phy. Rev. B* 53 (1996) 12545.

[5-7] S. Shigetomi, T. Ikari and H. Nakashima, *Phys. Status Solidi A* 156 (1996) K21.

[5-8] H. Kressel, *J. Appl. Phys.* 38 (1967) 4383.

[5-9] H. Davies, *Proc. Inst. Electr. Eng.* 101 (1954) 209.

[5-10] P. Beckmann and A. Spizzichino, *The Scattering of Electromagnetic Waves from Rough Surfaces* (Macmillan, New York, 1987).

[5-11] A. F. Houchens and R. G. Hering, *AIAA Thermophysics*

Specialist Conference (Academic, New York, 1967), paper 67-319.

[5-12] M. E. Bennett and J. O. Porteus, *J. Opt. Soc. Am.* 51 (1961) 123.

[5-13] H. E. Bennett, *J. Opt. Soc. Am.* 53 (1963) 1389.

[5-14] I. Ohlidal, F. Lukes and K. Navratil, *Surf. Sci.* 45 (1974) 91.

[5-15] D. H. Hensler, *Appl. Opt.* 11 (1972) 2522.

Chapter 6   Nonlinear Optical Effects

6.1 Theory [6-1, 6-2, 6-3, 6-4, 6-5, 6-6, 6-7, 6-8, 6-9, 6-10]

When an electromagnetic field propagates through a linear medium, its properties are independent of its own intensity and the presence of any other field. However, when different electromagnetic waves propagate through a nonlinear medium, they can interact and the propagation characteristics of one field can be influenced by the other fields. This interaction is the basis of many of the observed nonlinear optical phenomena, including harmonic generation, frequency mixing and parametric generation.

6.1.1 Notation

When an electromagnetic field $\vec{E}(\vec{r},t)$ is applied to a material, the response of the material is a polarization $\vec{P}(\vec{r},t)$ (i.e. the induced dipole moment per unit volume), which is described in general by

$$\vec{P}(\vec{r},t) = \varepsilon_0 \int_{-\infty}^{\infty} \int_{-\infty}^{t} \overline{\overline{\chi}}(\vec{r},\vec{r}',t-t') \vec{E}(\vec{r}',t') d^3\vec{r}' dt' \tag{6-1}$$

where ε_0 denotes the vacuum permittivity and $\overline{\overline{\chi}}$ is the susceptibility

tensor of the material. For systems that exhibit spatial invariance, the dependence on $(\vec{r}, \vec{r}')$ can be replaced by dependence on $(\vec{r} - \vec{r}')$. The time integration must be truncated since the response $\vec{P}(\vec{r}, t)$ is only a function of the electric field in the past. This causality requirement yields the well-known Kramers-Kronig relations [6-1] between the real and imaginary parts of $\overline{\overline{\chi}}$ in the frequency domain. Based on the assumption of spatial invariance, the Fourier transform of Eq. (6-1) with respect to time and space yields

$$\vec{P}(\vec{k}, \omega) = \varepsilon_0 \overline{\overline{\chi}}(\vec{k}, \omega) \vec{E}(\vec{k}, \omega) \tag{6-2}$$

The local response approximation is commonly applied (meaning that the response $\vec{P}(\vec{r}, t)$ is considered to depend only on the field $\vec{E}(\vec{r}, t)$ at spatial coordinate $\vec{r}$). In this case, Eq. (6-2) can be written

$$\vec{P}(\omega) = \varepsilon_0 \overline{\overline{\chi}}(\omega) \vec{E}(\omega) \tag{6-3}$$

If the material is nonlinear, then the susceptibility $\overline{\overline{\chi}}(\omega)$ can be expanded in powers of the electric field and Eq. (6-3) can be written

$$\vec{P}(\omega) = \varepsilon_0 \left(\overline{\overline{\chi}}^{(1)}(\omega) \cdot \vec{E}(\omega) + \overline{\overline{\chi}}^{(2)}(\omega) : \vec{E}(\omega) \vec{E}(\omega) + \cdots \right) \tag{6-4}$$

In the literature, various sets of notation are used. Shen [6-2] adopted Eq. (6-4) directly with $\overline{E}$ and $\vec{P}$ expressed as complex quantities. This notation is simple and appealing. Yariv and Yeh [6-3]

159

used other notation with $\bar{E}$ and $\bar{P}$ expressed as real quantities. This notation is extensively employed and will be applied as follows.

Following Yariv and Yeh [6-3], Eq. (6-4) is frequently written in the form,

$$P_i^r = \varepsilon_0 \left(\chi_{ij} E_j^r + 2 d_{ijk} E_j^r E_k^r + 4 \chi_{ijkl} E_j^r E_k^r E_l^r + \cdots \right) \tag{6-5}$$

where P_i^r and E_i^r are the i'th components of the field, and summation over repeated indices is assumed. The superscript r means that these fields are real fields that can be expressed in terms of their complex amplitudes as follows;

$$P_i^r = \frac{1}{2} \left(P_i^\omega e^{i(\vec{k} \cdot \vec{r} - \omega t)} + c.c. \right) \quad (i = x, y, z) \tag{6-6}$$

where c.c. means complex conjugate.

In the following, only second order nonlinearities are considered, in the term

$$P_i^r = 2 \varepsilon_0 d_{ijk} E_j^r E_k^r \tag{6-7}$$

Consider two fields at frequencies ω_1 and ω_2

$$E_j^r = \frac{1}{2} \left(E_j^{\omega_1} e^{i(\vec{k}_1 \cdot \vec{r} - \omega_1 t)} + c.c. \right) \qquad (j = x, y, z) \tag{6-8}$$

and

$$E_k^r = \frac{1}{2} \left(E_k^{\omega_2} e^{i(\vec{k}_2 \cdot \vec{r} - \omega_2 t)} + c.c. \right) \qquad (k = x, y, z) \tag{6-9}$$

Using these expressions, Eq. (6-7) becomes

160

$$P_i^r = 2\varepsilon_0 d_{ijk}\left(\frac{1}{2}E_j^{\omega_1}e^{i(\vec{k}_1 \cdot \vec{r} - \omega_1 t)} + \frac{1}{2}E_j^{\omega_2}e^{i(\vec{k}_2 \cdot \vec{r} - \omega_2 t)} + c.c.\right)$$
$$\times\left(\frac{1}{2}E_k^{\omega_1}e^{i(\vec{k}_1 \cdot \vec{r} - \omega_1 t)} + \frac{1}{2}E_k^{\omega_2}e^{i(\vec{k}_2 \cdot \vec{r} - \omega_2 t)} + c.c.\right) \qquad (6\text{-}10)$$

The product in Eq. (6-10) that oscillate with both (ω_1+ω_2) and (ω_1-ω_2) appear. Considering only the sum-frequency terms and applying Eq. (6-6), reduces Eq. (6-7) to

$$P_i^{\omega_3 = \omega_1 + \omega_2} = \varepsilon_0 d_{ijk} E_j^{\omega_1} E_k^{\omega_2} + \varepsilon_0 d_{ijk} E_k^{\omega_2} E_j^{\omega_1} \qquad (6\text{-}11)$$

where

$$\omega_3 = \omega_1 + \omega_2 \qquad (6\text{-}12)$$

is assumed, and

$$\vec{k}_3 = \vec{k}_1 - \vec{k}_2 \qquad (6\text{-}13)$$

Widely used notation for nonlinear susceptibilities is introduced to track the frequencies:

$$d_{ijk} = d_{ijk}(-\omega_3, \omega_1, \omega_2) \qquad (6\text{-}14)$$

In this notation, for example, the difference frequency terms are expressed in terms of the $d_{ijk}(-\omega_3, \omega_1, -\omega_2)$ susceptibilities.

In Eq. (6-11), the order in which the fields appear has no physical significance. Therefore,

$$d_{ijk}(-\omega_3, \omega_1, \omega_2) = d_{ikj}(-\omega_3, \omega_2, \omega_1) \qquad (6\text{-}15)$$

and Eq. (6-11) can be written

$$P_i^{\omega_3 = \omega_1 + \omega_2} = 2\varepsilon_0 d_{ijk}(-\omega_3, \omega_1, \omega_2) E_j^{\omega_1} E_k^{\omega_2} \qquad (6\text{-}16)$$

with summation over repeated indices. This is the relationship between

the complex amplitudes of the fields.

Equation (6-16) is valid only if $\omega_1 \neq \omega_2$. In the case of second harmonic generation where $\omega_1 = \omega_2 = \omega$, the field components $E_j^{\omega_1}$ and $E_k^{\omega_2}$ in Eq. (6-10) are in fact components of the same field. Hence, Eq. (6-10) must be written

$$P_i^r = 2\varepsilon_0 d_{ijk} \left(\frac{1}{2} E_j^\omega e^{i(\vec{k}\cdot\vec{r}-\omega t)} + c.c. \right) \left(\frac{1}{2} E_k^\omega e^{i(\vec{k}\cdot\vec{r}-\omega t)} + c.c. \right) \qquad (6\text{-}17)$$

resulting in,

$$P_i^{\omega_3 = 2\omega} = \varepsilon_0 d_{ijk} E_j^\omega E_k^\omega \qquad (6\text{-}18)$$

with summation over repeated indices. Equation (6-18) is valid for the complex amplitudes in cases of second harmonic generation. Equations (6-16) and (6-18) can be combined in terms of the Kronecker delta $\delta_{\omega_1\omega_2}$.

$$P_i^{\omega_3 = \omega_1 + \omega_2} = \left(2 - \delta_{\omega_1\omega_2} \right) \varepsilon_0 d_{ijk} E_j^{\omega_1} E_k^{\omega_2} \qquad (6\text{-}19)$$

The 27 components of the nonlinear second-order d-tensor have numerous symmetry relations that limit the number of independent elements to only a few for most crystals. If the material exhibits inversion symmetry, all the elements are zero, as revealed by Eq. (6-19). Performing an inversion through a center of symmetry does not change the crystal changes the sign of both P and E. When P changes sign, the sign in Eq. (6-19) changes, but when E changes sign, the sign in Eq. (6-19)

162

dose not change. Accordingly,

$$d_{ijk} = 0 \qquad (6\text{-}20)$$

in centrosymmetric crystals, and is true only for bulk materials in the local response approximation. Second-order effects occur at surfaces and, in the case of a non-local response, also in centrosymmetric crystals.

Kleinman [6-4] offered a useful set of symmetry conditions that were derived from an energy function

$$U(E) = -\frac{1}{3} d_{ijk} E_i E_j E_k \qquad (6\text{-}21)$$

from which the polarization is derived as

$$\vec{P} = -\vec{\nabla}_E U \qquad (6\text{-}22)$$

Since a rearrangement of the electric field components in Eq. (6-21) has no physical significance, all of the terms d_{ijk}, which result merely from the rearrangement of the subscripts are equal. Hence,

$$d_{ijk} = d_{kij} = d_{jki} = d_{ikj} = d_{kji} = d_{jik} \qquad (6\text{-}23)$$

Equation (6-15) is contained in Eq. (6-23), but is more general since Eq. (6-23) is valid only in the lossless case for wavelengths away from the resonance wavelengths in the material. The symmetry relation, Eq. (6-15), gives rise to the so-called contracted notation which is analogous to the piezoelectric notation [6-5].

163

$$xx = 1, \quad yy = 2, \quad zz = 3, \quad yz = zy = 4, \quad xz = zx = 5, \quad xy = yx = 6.$$

The resulting d_{ij} tensor yields a 3×6 matrix which operates on the electric fields following the rule,

$$\begin{bmatrix} P_x \\ P_y \\ P_z \end{bmatrix} = \begin{bmatrix} d_{11} & d_{12} & d_{13} & d_{14} & d_{15} & d_{16} \\ d_{21} & d_{22} & d_{23} & d_{24} & d_{25} & d_{26} \\ d_{31} & d_{32} & d_{33} & d_{34} & d_{35} & d_{36} \end{bmatrix} \begin{bmatrix} E_x^2 \\ E_y^2 \\ E_z^2 \\ 2E_z E_y \\ 2E_z E_x \\ 2E_x E_y \end{bmatrix} \tag{6-24}$$

For the usual crystals, many of these terms vanish [6-3].

6.1.2 Anharmonic Oscillator Model

The harmonic oscillator model is extremely useful in solid state physics for modeling the frequency response close to resonance in the material. Similarly, in nonlinear optics, the anharmonic oscillator model is useful.

Consider an elementary charge e with mass m bound to an oppositely charged center with a force constant $m\omega_0^2$ where ω_0 is the angular resonance frequency. The equation of motion is then

$$m\ddot{x} + m\omega_0^2 x + ax^2 = eE_0 \cos \omega t \tag{6-25}$$

where x denotes the displacement of the charge, and $E_0 \cos \omega t$ is the applied electric field. A term ax^2 is added to model the second order

164

nonlinearity.

Consider first the purely harmonic response with $a = 0$.

$$x_1(t) = \frac{e/m}{\omega_0^2 - \omega^2} E_0 \cos \omega t \qquad (6\text{-}26)$$

Since the polarization P of the material is defined as the induced dipole

moment per unit volume,

$$P = Nex = \frac{Ne^2/m}{\omega_0^2 - \omega^2} E_0 \cos \omega t \qquad (6\text{-}27)$$

where N is the number of induced dipoles per unit volume.

Usual linear response theory yields (as the first term of Eq. (6-4))

$$P = \varepsilon_0 \chi^{(1)}(\omega) E_0 \cos \omega t \qquad (6\text{-}28)$$

Therefore, the linear susceptibility is given by

$$\chi^{(1)}(\omega) = \frac{Ne^2}{m\varepsilon_0} \frac{1}{\omega_0^2 - \omega^2} \qquad (6\text{-}29)$$

Similarly, d ($\chi^{(2)}(\omega)$) can be found from Eq. (6-25) in the

approximation in which the term ax^2 is treated as small. Substituting

$ax_1^2(t)$ for ax^2 in Eq. (6-25) where $x_1(t)$ is given by Eq. (6-26), yields

the solution to Eq. (6-25),

$$x(t) = -\frac{a}{2\omega_0^2} \left(\frac{e/m}{\omega_0^2 - \omega^2} \right)^2 E_0^2 + \frac{e/m}{\omega_0^2 - \omega^2} E_0 \cos \omega t$$

$$\qquad (6\text{-}30)$$

$$-\frac{a}{2} \frac{1}{\omega_0^2 - 4\omega^2} \left(\frac{e/m}{\omega_0^2 - \omega^2} \right)^2 E_0^2 \cos 2\omega t$$

In addition to the linear term, previously found, both a DC-term and a

second harmonic term appear. Both of these terms are small since they

are proportional to the a-coefficient.

Separating $x(t)$ in Eq. (6-30) into its complex amplitudes

$$x(t) = x_0 + \frac{1}{2}\left(x_\omega e^{-i\omega t} + c.c.\right) + \frac{1}{2}\left(x_{2\omega} e^{-2i\omega t} + c.c.\right) \qquad (6\text{-}31)$$

and applying Eq. (6-27) yields the second harmonic polarization,

$$P_{2\omega} = Nex_{2\omega} = -\frac{aNe^3}{2m^2} \frac{1}{\left(\omega_0^2 - 4\omega^2\right)\left(\omega_0^2 - \omega^2\right)^2} E_0^2 \qquad (6\text{-}32)$$

Since this term generates the second harmonic signal it can be compared with Eq. (6-18) to yield the nonlinear second-order susceptibility

$$d = -\frac{aNe^3}{2\varepsilon_0 m^2} \frac{1}{\left(\omega_0^2 - 4\omega^2\right)\left(\omega_0^2 - \omega^2\right)^2} \qquad (6\text{-}33)$$

This is the result of the anharmonic oscillator model. The term d is, of course, proportional to the anharmonic force coefficient. It also resonates not only at ω_0, but also at $\omega_0/2$. The corresponding absorption at this frequency is the two-photon absorption. d can be expressed in terms of the linear susceptibility $\chi^{(1)}$, which is given by Eq. (6-29).

$$d = -\frac{am\varepsilon_0^2}{2N^2 e^3} \chi^{(1)}(2\omega)\left(\chi^{(1)}(\omega)\right)^2 \qquad (6\text{-}34)$$

Miller [6-6] generalized this expression as the so-called Miller's rule.

$$d_{ijk}(-\omega_A, \omega_B, \omega_C) = \delta_{ijk}\chi_{ii}(\omega_A)\chi_{jj}(\omega_B)\chi_{kk}(\omega_C) \qquad (6\text{-}35)$$

The parameter δ_{ijk} is remarkably consistent across numerous inorganic materials. Organic materials tend to have values of δ_{ijk} that are 10-100

166

times greater than those of inorganic materials.

6.1.3 Three Wave Mixing

The previous sections considered only the response of the material. This response (the polarization) acts back on the electric field according to Maxwell's equations, forming coupled modes. In the case of second-order nonlinearities, three waves are mixed as described by the coupled nonlinear wave equations. This so-called three wave mixing is responsible for the usual second-order effects like sum and difference frequency generation, parametric amplification and oscillation and others.

The basic equations are Maxwell's equations for non-magnetic materials

$$\nabla \times \vec{H} = \frac{\partial \vec{D}}{\partial t} + \vec{j} \tag{6-36}$$

$$\nabla \times \vec{E} = -\frac{\partial}{\partial t}\left(\mu_0 \vec{H}\right) \tag{6-37}$$

$$\nabla \cdot \vec{H} = 0 \tag{6-38}$$

$$\nabla \cdot \vec{D} = \rho \tag{6-39}$$

and the material equations are

$$\vec{D} = \varepsilon_0 \vec{E} + \vec{P} \tag{6-40}$$

$$\vec{J} = \sigma E \tag{6-41}$$

167

$$\overline{P} = \varepsilon_0 \chi^{(1)} \overline{E} + \overline{P}_{nl} \qquad (6\text{-}42)$$

where σ, the specific conductivity, is introduced to account for losses, and $\overline{P}_{nl}$ is the nonlinear part of the response which for a second-order effect is given by

$$P_i = 2\varepsilon_0 d_{ijk} E_j E_k \qquad (6\text{-}43)$$

as determined by Eq. (6-4). All of the fields are herein expressed in terms of real field amplitudes. In Eqs. (6-36), (6-37), (6-40), (6-41) and (6-42) the usual wave equation for the electric field is obtained:

$$\nabla^2 \overline{E} = \mu_0 \sigma \frac{\partial \overline{E}}{\partial t} + \mu_0 \varepsilon \frac{\partial^2 \overline{E}}{\partial t^2} + \mu_0 \frac{\partial^2 \overline{P}_{nl}}{\partial t^2} \qquad (6\text{-}44)$$

where

$$\varepsilon = \varepsilon_0 \left(1 + \chi^{(1)} \right) \qquad (6\text{-}45)$$

is the linear part of the dielectric constant of the material.

Introducing the complex amplitudes and considering, for simplicity, a scalar approximation yields the real field amplitude in the form,

$$E_i^r = \frac{1}{2} E_i e^{i(k_i z - \omega t)} + c.c. \qquad (6\text{-}46)$$

where i = 1, 2, 3 now refers to one of the three coupled waves, and the second derivative can be written as

$$\nabla^2 E_i^r = \frac{1}{2} \left(\frac{d^2 E_i}{dz^2} + 2ik \frac{dE_i}{dz} - k^2 E_i \right) e^{i(k_i z - \omega t)} + c.c. \qquad (6\text{-}47)$$

The amplitude E_i is typically assumed to vary slowly, such that on

168

the wavelength scale of light, E_i is regarded as almost constant, in which is called the SVEA-approximation (Slowly Varying Envelope Approximation)

$$\left|k^2 E_i\right| \gg \left|k \frac{dE_i}{dz}\right| \gg \frac{d^2 E_i}{dz^2} \tag{6-48}$$

In this approximation, the wave equation can be written

$$\frac{dE_i}{dz} e^{i(k_i z - \omega t)} + c.c. = -\frac{1}{2}\left(\frac{\mu_0}{\varepsilon_i}\right)^{\frac{1}{2}} \sigma_i E_i e^{i(k_i z - \omega t)} + c.c. - i\left(\frac{\mu_0}{\varepsilon_i}\right)^{\frac{1}{2}} \frac{1}{\omega_i} \frac{\partial^2 P_{ne}^r}{\partial t^2} \tag{6-49}$$

where

$$k_i = \omega_i (\mu_0 \varepsilon_i)^{\frac{1}{2}} \tag{6-50}$$

In Eq. (6-49) the P_{ne}^r-term acts as a source which generates the electric field. Obviously, the three terms must oscillate synchronously, meaning at the same frequency. In the case in which

$$\omega_3 = \omega_1 + \omega_2 \tag{6-51}$$

Eq. (6-19) describes the relationship between the complex amplitudes of the second order response;

$$P_{ne} = (2 - \delta_{\omega_1 \omega_2})\varepsilon_0 d E_1(\omega_1) E_2(\omega_2) \tag{6-52}$$

where P_{ne} is the complex amplitude which is defined as

$$P_{ne}^r = \frac{1}{2} P_{ne} e^{i(kz - \omega t)} + c.c. \tag{6-53}$$

Substituting Eqs. (6-52) and (6-53) into Eq. (6-49) yields the following equations for the complex amplitudes;

169

$$\frac{dE_3}{dz} = -\frac{\mu_0 \sigma_3 c}{2n_3} E_3 + \frac{i\alpha\omega_3\mu_0 dc}{n_3} E_1 E_2 e^{i\Delta k z} \qquad (6\text{-}54)$$

$$\frac{dE_1}{dz} = -\frac{\mu_0 \sigma_1 c}{2n_1} E_1 + \frac{i\alpha\omega_1\mu_0 dc}{n_1} E_3 E_2^* e^{-i\Delta k z} \qquad (6\text{-}55)$$

$$\frac{dE_2}{dz} = -\frac{\mu_0 \sigma_2 c}{2n_2} E_2 + \frac{i\alpha\omega_2\mu_0 dc}{n_2} E_3 E_1^* e^{-i\Delta k z} \qquad (6\text{-}56)$$

where

$$\Delta k = k_1 + k_2 - k_3 \qquad (6\text{-}57)$$

$$\left(\frac{\mu_0}{\varepsilon_i}\right)^{\frac{1}{2}} = \mu_0 \frac{c}{n_i} \qquad (6\text{-}58)$$

and

$$\alpha = \frac{1}{2}\left(2 - \delta_{\omega_i \omega_j}\right) \qquad (6\text{-}59)$$

Equations (6-54) ~ (6-56) constitute the basis of second-order nonlinear optics and can be applied in all three wave mixing cases.

6.1.4 Second Harmonic Generation

In the special case of second harmonic generation,

$$\omega_3 = 2\omega \qquad (6\text{-}60)$$

and

$$\alpha = \frac{1}{2} \qquad (6\text{-}61)$$

Neglecting absorption ($\sigma_i = 0$), the coupled Eqs. (6-54) ~ (6-56) reduce to

$$\frac{dE_3}{dz} = \frac{i\omega_3\mu_0 dc}{2n(2\omega)} E_1^2 e^{i\Delta k z} \qquad (6\text{-}62)$$

$$\frac{dE_1}{dz} = \frac{i\omega_1 \mu_0 dc}{2n(\omega)} E_3 E_1^* e^{-i\Delta kz} \qquad (6\text{-}63)$$

with

$$\Delta k = 2k_1 - k_3 = 2\frac{\omega}{c}(n(\omega) - n(2\omega)) \qquad (6\text{-}64)$$

In the approximation in which the fundamental wave is not depleted

(E_1 is regarded as constant), and the solution to Eq. (6-62) is

$$E_3(z) = \frac{i\omega\mu_0 dc}{n(2\omega)} E_1^2 z e^{i\Delta kz/2} \left(\frac{\sin\frac{1}{2}\Delta kz}{\frac{1}{2}\Delta kz} \right) \qquad (6\text{-}65)$$

Since the intensity of a wave is given by

$$I = \frac{n}{2\mu_0 c}|E|^2$$

the intensity of the second harmonic output from a crystal of thickness L

is given by

$$I(2\omega) = KI^2(\omega)L^2 \left(\frac{\sin\frac{1}{2}\Delta kL}{\frac{1}{2}\Delta kL} \right)^2 \qquad (6\text{-}66)$$

where

$$K = \frac{2\mu_0^3 c^3 \omega^2 d^2}{n^2(\omega)n(2\omega)}$$

The depletion of E_1 (determined by solving Eqs. (6-62) and (6-63)

exactly) can be taken into account. The result is then,

$$I(2\omega) = I(\omega)\tanh^2 \left((KI(\omega))^{\frac{1}{2}} L \frac{\sin\frac{1}{2}\Delta kL}{\frac{1}{2}\Delta kL} \right) \qquad (6\text{-}67)$$

Notably, when the beam is focused, the confocal parameter of the beam must exceeds the crystal length L such that Eq. (6-67) is valid. Otherwise, the efficiency of conversion would be reduced, as was discussed by Boyd and Kleinman [6-7].

6.1.5 Phase matching

The condition $\Delta k = 0$ in Eqs. (6-54) ~ (6-56) must be satisfied to achieve sufficient frequency conversion. In the case of second harmonic generation, this condition becomes

$$\Delta k = k(\omega) + k(\omega) - k(2\omega) = \frac{\omega}{c}(n(\omega) + n(\omega) - 2n(2\omega)) \qquad (6\text{-}68)$$

If this phase match condition is satisfied, phase velocities of the fundamental and the second-harmonic waves are equal. In this case, $I(2\omega) \propto L^2$ as revealed by Eq. (6-66) or (6-67). If the condition is not satisfied, a coherence length

$$l_c = \frac{\pi}{\Delta k} \qquad (6\text{-}69)$$

is introduced and the intensity of the generated harmonic, Eq. (6-66), can be rewritten as

$$I(2\omega) = \frac{4K}{\pi^2} I^2(\omega) l_c^2 \sin^2\left(\frac{\pi l}{2 l_c}\right) \qquad (6\text{-}70)$$

Figure 6-1 presents the conversion efficiency obtained for different

172

values of l_c, which leads to the so-called quasi phase matching scheme that is displayed in Fig. 6-2, where the sign of the d-coefficient is reversed periodically by changing the direction of the spontaneous polarization in the non-linear crystal during crystal growth [6-8].

The phase matching condition is typically satisfied by birefringent crystals. Often uniaxial crystals are utilized. In this case, the two refractive indices are given by

$$n_0 \qquad\qquad \text{ordinary index} \qquad\qquad (6\text{-}71)$$

$$n_e(\theta) = \frac{n_0 n_e}{\left(n_0^2 \sin^2\theta + n_e^2 \cos^2\theta\right)^{\frac{1}{2}}} \quad \text{extraordinary index} \qquad (6\text{-}72)$$

where θ is the angle between the optical axis and the direction of propagation and $n_e = n_e(\theta = \pi/2)$. Equation (6-68) can now be satisfied in various ways.

(1) Type I phase matching with positive uniaxial crystals $(n_e > n_0)$:

$$n_0(2\omega) = n_e(\omega, \theta_m) \quad \text{where} \quad \sin^2\theta_m = \frac{\left(n_0(2\omega)\right)^{-2} - \left(n_0(\omega)\right)^{-2}}{\left(n_e(\omega)\right)^{-2} - \left(n_0(\omega)\right)^{-2}} \qquad (6\text{-}73)$$

where θ_m is the angle at which phase matching occurs.

(2) Type I phase matching with negative uniaxial crystals $(n_e < n_0)$:

$$n_e(2\omega, \theta_m) = n_0(\omega) \quad \text{where} \quad \sin^2\theta_m = \frac{\left(n_0(\omega)\right)^{-2} - \left(n_0(2\omega)\right)^{-2}}{\left(n_e(2\omega)\right)^{-2} - \left(n_0(2\omega)\right)^{-2}} \qquad (6\text{-}74)$$

(3) Type II phase matching with positive uniaxial crystals $(n_e > n_0)$:

$$n_0(2\omega) = \frac{1}{2}(n_0(\omega) + n_e(\omega, \theta_m)) \quad \text{where}$$

$$\sin^2 \theta_m = \frac{(2n_0(2\omega) - n_0(\omega))^{-2} - (n_0(\omega))^{-2}}{(n_e(\omega))^{-2} - (n_0(\omega))^{-2}} \tag{6-75}$$

(4) Type II phase matching with negative uniaxial crystals $(n_e < n_0)$:

$$n_e(2\omega, \theta_m) = \frac{1}{2}(n_0(\omega) + n_e(\omega, \theta_m)) \tag{6-76}$$

where θ_m must be determined using iterative methods.

6.1.6 Kurtz powder assessment of nonlinear materials

The Kurtz powder technique is the first real means of screening experimentally large numbers of unknown materials for nonlinear activity, without the need for the slow and expensive task of growing high-quality crystals of each material. Kurtz [6-9, 6-10] demonstrated that measurements can be made on powders to ascertain whether a crystal has large or small nonlinearity and whether it can be phase matched, then given commonly known data on crystal properties, the probability of selecting a material for crystal growth that will subsequently be useful is markedly increased.

Figure 6-3 depicts apparatus used. A laser, typically a Q-switched high-repetition rate Nd:YAG laser, is used to illuminate a large area of a thin layer of the powdered material to be studied. The powder is compacted into a thin cell to define the thickness of the layer. The cell is fixed in an optical system that collects all of the scattered SHG from the sample over 4π radians, and the signal is monitored using a photomultiplier. The measurement approach involves determining the amount of SHG from the powder sample as a function of particle size, and the powder is sieved to a small range of sizes in each test. The laser power must be monitored for control purposes. The required information is obtained by measuring SHG power as a function of particle size, which is compared the results determined for quartz powder samples with identical geometry, because phase-matchable and non-phase-matchable materials exhibit two distinctly different responses.

For very small particles, such that $r \ll l_c$ for all orientations, the total integrated SHG varies with the particle radius r, because the interaction is always effectively phase matched, since the radius is not large enough for any serious phase error to occur. Hence, the interaction efficiency increases rapidly with the radius, but it is somewhat offset by

the drop in the number of particles.

For a non-phase-matchable material, once the particle size surpasses the mean coherence length l_c (such that for most or all orientations, phase-mismatch effects become apparent), the SHG varies inversely with the particle size because the SHG per particle does not increase as rapidly as the number of particles declines. Therefore, a plot of SHG against particle size yields a curve of the form plotted in Fig. 6-4, with a pronounced maximum.

However, for a material that is phase-matchable, when the particle size reaches the average coherence length (averaged for all crystal directions, not just the phase-matching direction), the gain in SHG from the particles that are correctly oriented approximately balances the loss in SHG caused by the drop in the number of particles. The net result is that the overall SHG remains essentially constant, as shown in the second curve of Fig. 6-4. Therefore, when the SHG is plotted as a function of particle size, inspection alone suffices to decide whether a material allows phase matching.

Kurtz used this method to survey very many compounds of potential interest and classified them into one five groups — those with a large

coefficient, those with a small coefficient, phase-matchable compounds,

non-phase-matchable compounds and centrosymmetric materials.

6.2 Discussion

Powder SHG measurements, which were presented by W.K. Chen *et al.* [6-11], were made herein using a modified Kurtz-NLO system [6-9] with 1260 nm light. A mode-locked Cr^{4+}:Forsterite femtosecond laser with a pulse duration of 50 fs, was used in all measurements. The Cr^{4+}:Forsterite oscillator yields pulses with a typical FWHM bandwidth of about 45 nm at a repetition rate of 76 MHz and a mean power of 270 mW. Since the SHG efficiency of powders has been demonstrated to depend strongly on particle size [6-9, 6-12], polycrystalline $CsGe(Br_xCl_{1-x})_3$ and $(Rb_yCs_{1-y})GeBr_3$ were ground and sieved (Newark Wire Cloth Company) into six particle-size ranges — 19~37 μm, 37~74 μm, 74~105 μm, 105~210 μm, 210~420 μm and 420~840 μm (Fig. 6-5). Crystalline KDP was also ground and sieved into the same particle-size ranges to support relevant comparisons with known SHG materials. All of the powders were placed in separate capillary tubes. The SHG radiation (630 nm) was collected in transmission and detected using a

photomultiplier tube (Oriel Instruments). The SHG signal was collected at a data-acquisition (DAQ) interface and was monitored using an analysis program on a personal computer.

When the SHG process was phase-matchable and satisfied type-I phase matching conditions, the intensity of the SHG response could be written as [6-13]

$$I_{2\omega}(\bar{r},\theta) = \frac{128\pi^5 I_\omega^2}{n_\omega^2 n_{2\omega} \lambda_{2\omega}^2 c} \bar{L}\bar{r}\langle d_{eff}^2 \rangle \frac{\sin^2\left[\frac{\pi}{2}\frac{\bar{r}}{\bar{l}_{pm}}(\theta - \theta_{pm})\right]}{\left[\frac{\pi}{2}\frac{\bar{r}}{\bar{l}_{pm}}(\theta - \theta_{pm})\right]} \quad (6\text{-}77)$$

where $\bar{l}_{pm} = \lambda \Big/ \left[4|\Delta n_{B,2\omega}|\sin 2\theta_{pm}\right]$, and θ_{pm} is the phase-matching angle. Here, $\Delta n_{B,2\omega} = n_{E,2\omega} - n_{O,2\omega}$ denotes the birefringence of the material at the second-harmonic wavelength. In the event that $\bar{r} \gg \bar{l}_{pm}$ or $\bar{r} \ll \bar{l}_{pm}$, Eq. (6-77) could be simplified to

$$I_{2\omega} \rightarrow \begin{cases} \left[\left(256\pi^4 I_\omega^2\right)\Big/\left(n_\omega^2 n_{2\omega}\lambda_{2\omega}^2 c\right)\right]\bar{L}\bar{l}_{pm}\langle d_{eff}^2\rangle, \leftarrow \bar{r} \gg \bar{l}_{pm} \\ \left[\left(128\pi^5 I_\omega^2\right)\Big/\left(n_\omega^2 n_{2\omega}\lambda_{2\omega}^2 c\right)\right]\bar{L}\bar{r}\langle d_{eff}^2\rangle, \leftarrow \bar{r} \ll \bar{l}_{pm} \end{cases} \quad (6\text{-}78)$$

The SHG signals became saturated when the average particle size exceeded $\bar{l}_{pm}$, then the SHG signals were independent of the particle size.

Chen *et al.* [6-11] derived a useful empirical formula, associated with the correct asymptotic forms in Eq. (6-78), that describes the overall

178

variation in the second-harmonic intensity with particle size $\bar{r}$

$$I_{2\omega} = \frac{256\pi^4 I_\omega^2}{n_\omega^2 n_{2\omega} \lambda_{2\omega}^2 c} L\bar{l}_{pm} \langle d_{eff}^2 \rangle \sqrt{1 - \exp\left[-\left(\frac{\bar{r}}{A}\right)^2\right]}$$ (6-79)

with $A \approx 9\bar{l}_{pm}$.

Since the absorption coefficient of CsGeBr$_3$ at 630 nm was excessively large, the saturated PSHG intensity decayed. Therefore, the absorption coefficients were used to calculate the real saturated PSHG intensity using $I_{2\omega} = I_{2\omega}^{total} \cdot e^{-az}$. Equation (6-80) yields the square of the effective nonlinearity, $\langle d_{eff}^2 \rangle$, averaged over the orientation distribution of crystalline powders of CsGe(Br$_x$Cl$_{1-x}$)$_3$ using a reference NLO crystal, such as KDP.

$$\langle d_{eff}^2 \rangle_{CGBC} = \langle d_{eff}^2 \rangle_{KDP} \frac{I_{2\omega,CGBC}^{total} n_{\omega,CGBC}^2 n_{2\omega,CGBC}}{I_{2\omega,KDP}^{total} n_{\omega,KDP}^2 n_{2\omega,KDP}} \approx \langle d_{eff}^2 \rangle_{KDP} \frac{I_{2\omega,CGBC}^{total} n_{CGBC}^3}{I_{2\omega,KDP}^{total} n_{KDP}^3}$$ (6-80)

when $n \approx n_\omega \approx n_{2\omega}$.

Powder SHG measurements of sieved polycrystalline CsGe(Br$_x$Cl$_{1-x}$)$_3$ and (Rb$_y$Cs$_{1-y}$)GeBr$_3$ (Figs. 6-6, 6-7 and 6-8) demonstrated that the SHG efficiencies of all the samples exceeded that of KDP. Moreover, all of them were phase-matchable, as was KDP, such that as the particles became substantially larger than the coherence length of the crystal, and the collected SHG intensity no longer increased and

saturated at a particular value. The saturated PSHG intensities were estimated from the transmission signals in particle of various sizes, indicating that the SHG responses were strengthened as the Br content increased, but decayed as the Rb content increased. Since the absorption coefficient of $CsGeBr_3$ in 630 nm was too large, the saturated PSHG intensity decayed. Accordingly, the absorption coefficients (Tables 5-1, 5-2 and 5-3) were used to calculate the real saturated PSHG intensity. The d_{eff} values were calculated (by d_{KDP} (= 0.36 pm/V) [6-14]) and are plotted in Figs. 6-9 and 6-10. The effective powder second-harmonic generation coefficients increased with Br content, but fell as the Rb content increased. The nonlinearity (Figs. 6-11 and 6-12) of d_{eff}^2/n^3 depended similarly on the compositional ratio. Some reasons exist for the significant SHG signals of rhombohedral $CsGe(Br_xCl_{1-x})_3$ and $(Rb_yCs_{1-y})GeBr_3$ crystals. First, the structural distortion and the off-center Ge ion in the unit cell contributed to the SHG response. The XRD results revealed that the lattice constant became larger as Br content increased while the cell angle became smaller. Hence, the structural distortion of $CsGe(Br_xCl_{1-x})_3$ increased with Br content and the position of the B-site cation, Ge, moved closer to the cell corner as the Br increased. However,

increasing Rb content yielded opposite results for $(Rb_yCs_{1-y})GeBr_3$. Then, the nonlinearity increased with Br content, but declined as Rb content increased. Second, the optical non-linearity is approximately inversely proportional to the cube of the bandgap value [6-15]. Therefore, the bandgap values fell and the NLO susceptibilities increased with the atomic weights of the halides.
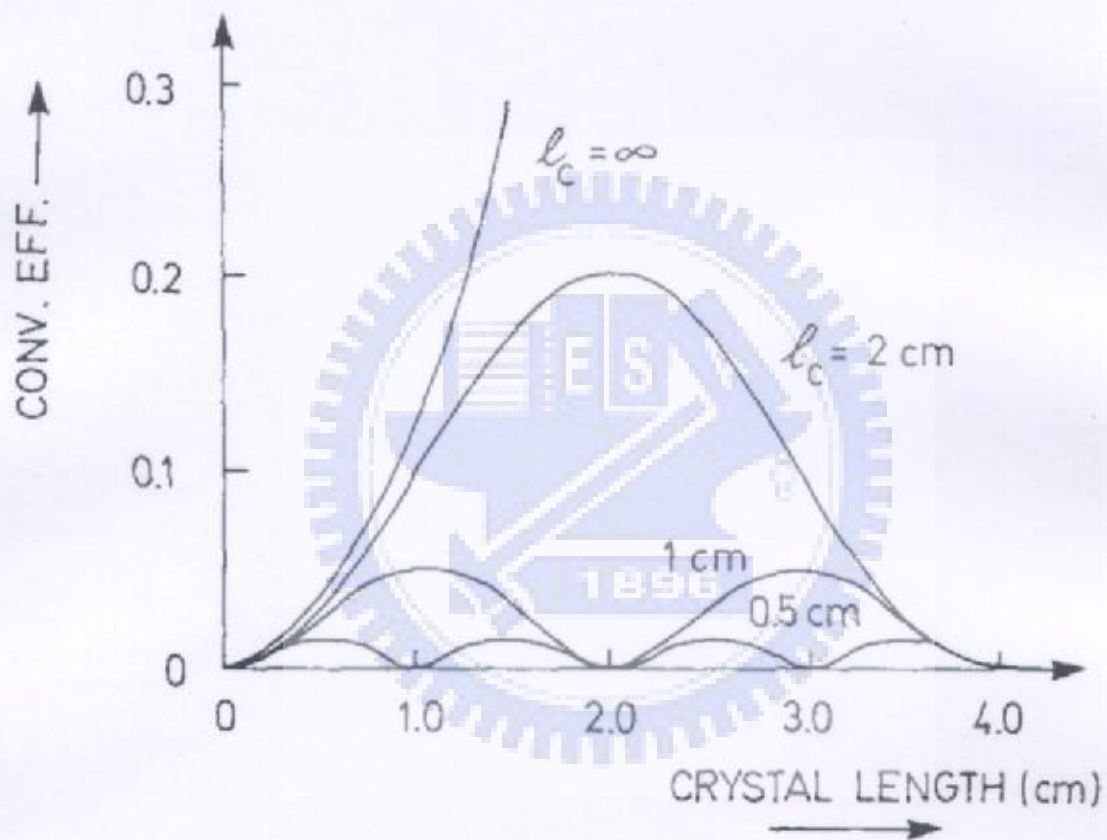
6.3 Tables and Figures

Fig. 6-1 Example of second harmonic conversion efficiency as a function of the length of the nonlinear crystal for various coherence lengths [6-8].
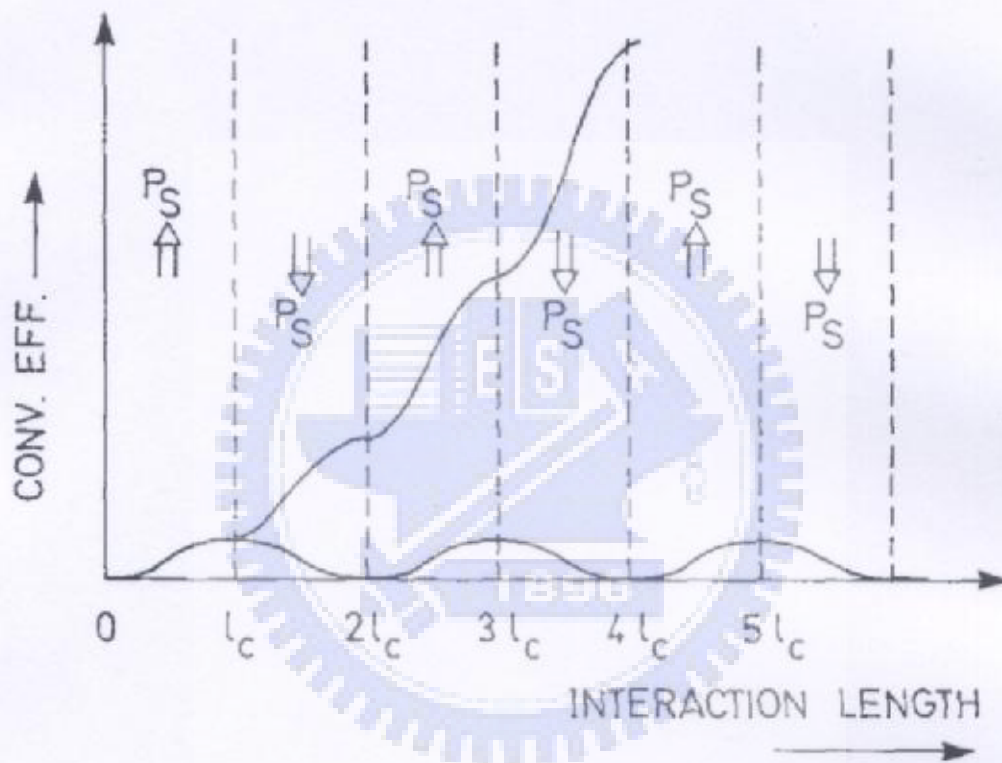
Fig. 6-2 Quasi-phase matching. The sign of the nonlinear susceptibility is reversed periodically with the period equal to the coherence length. P_s is the spontaneous polarization of the crystal [6-8].
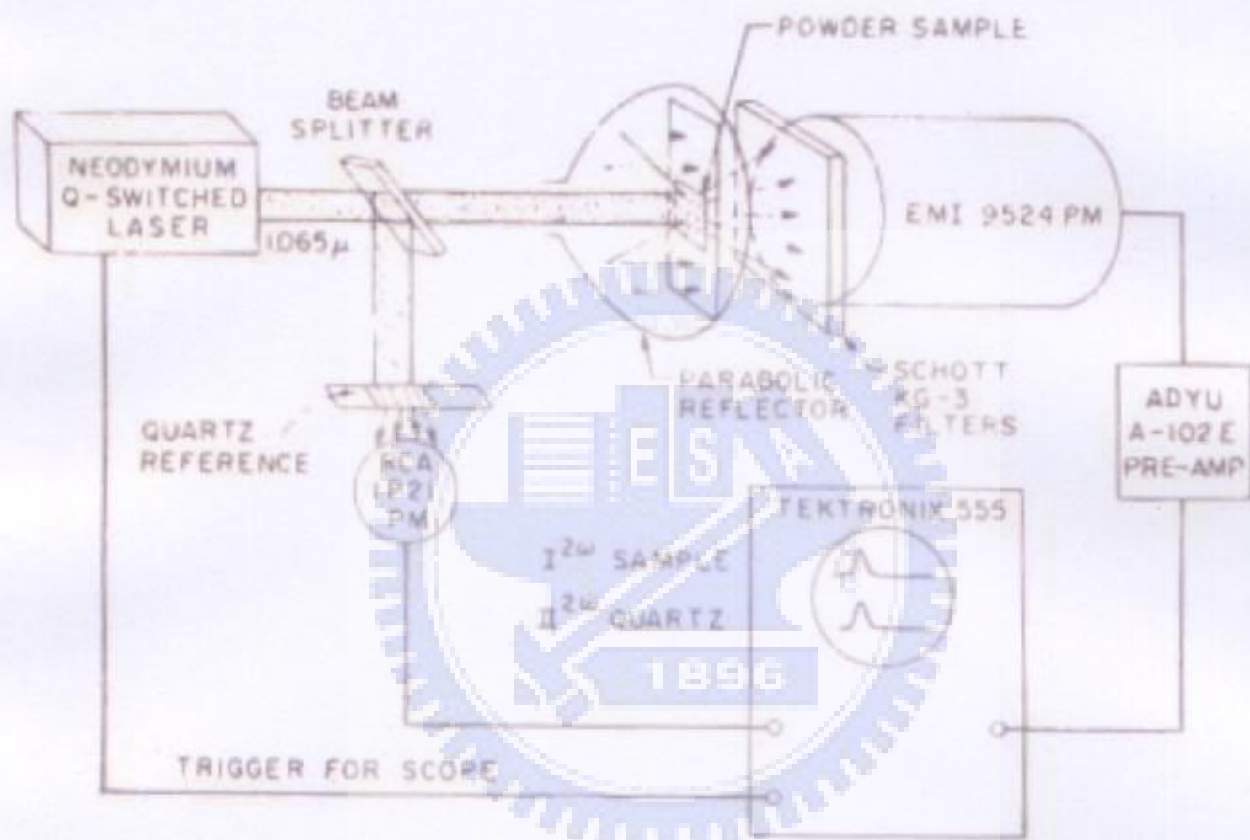
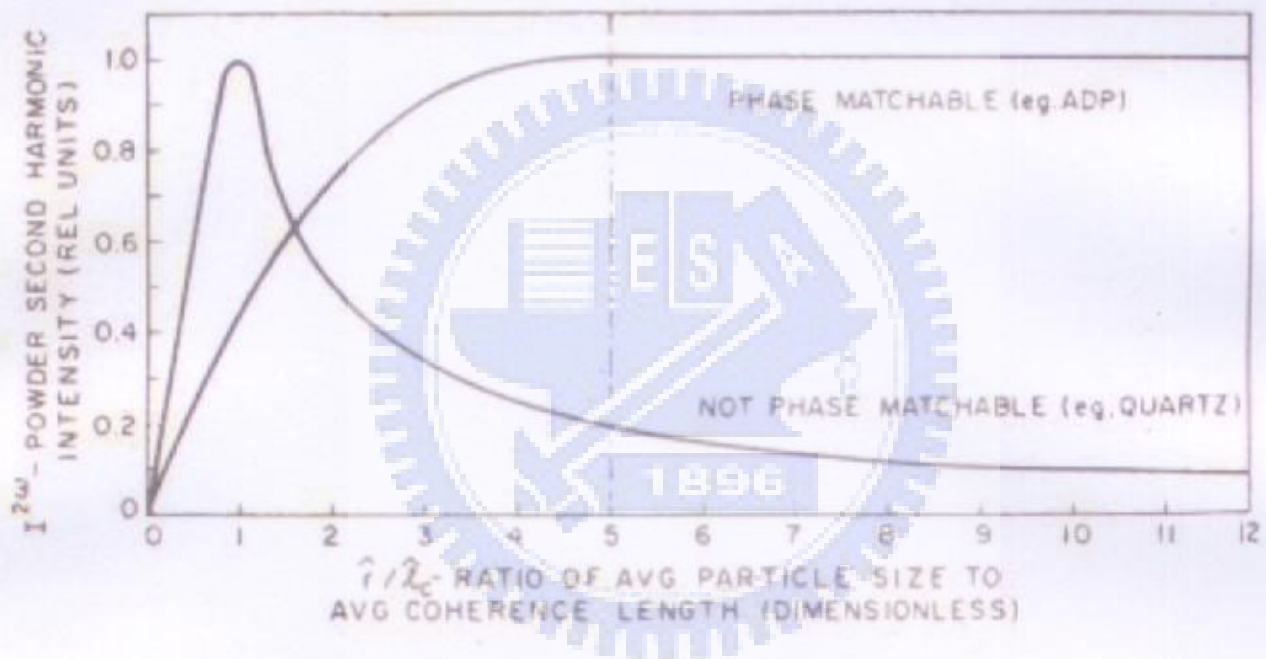Fig. 6-3 Schematic layout of the apparatus for use in the Kurtz powder measurement [6-9].

Fig. 6-4 The typical response for powders of phase-matchable and non-matchable crystals, showing the SHG as a function of particle size [6-9].
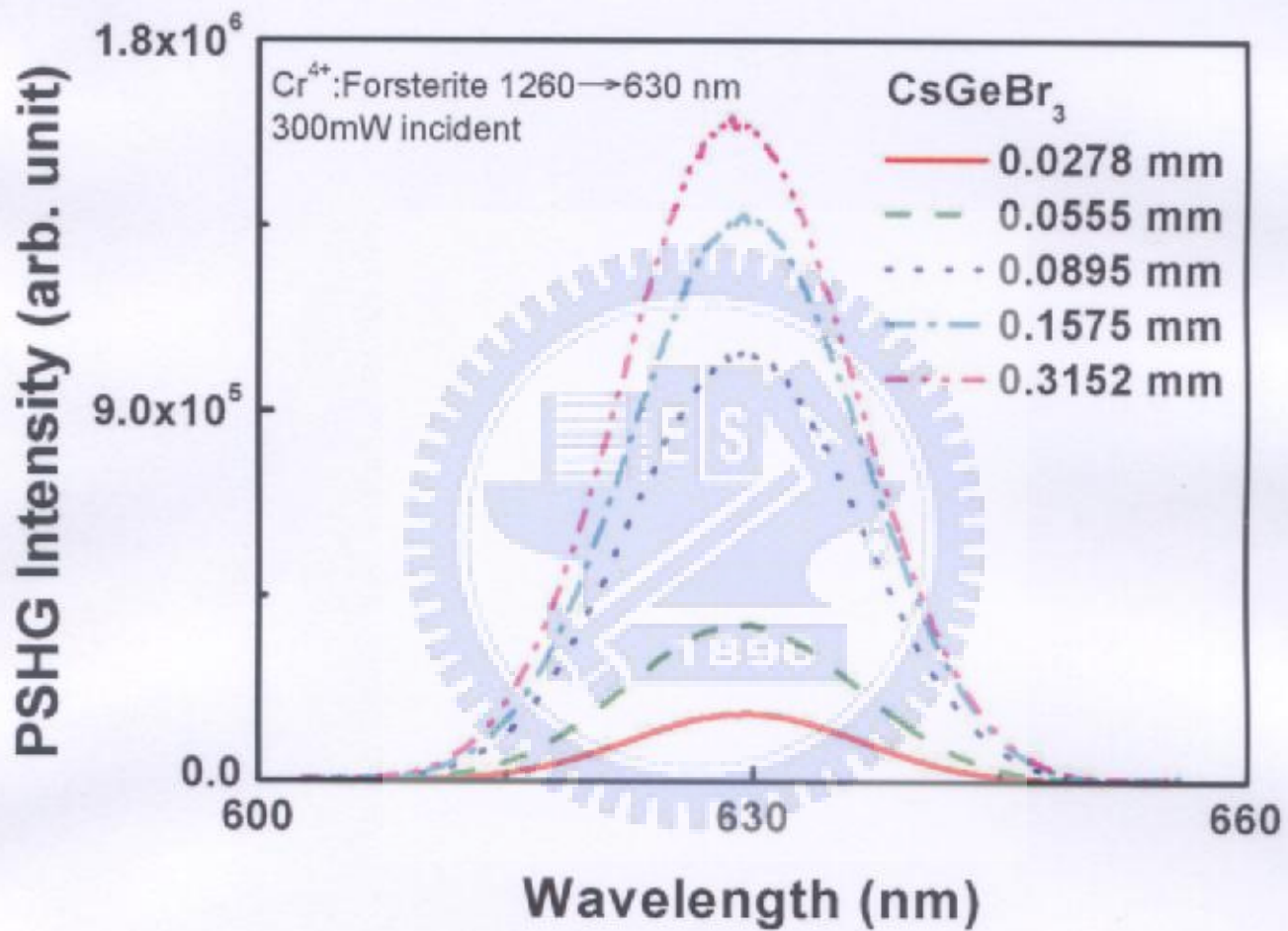
Fig. 6-5 The powder second-harmonic generation results for rhombohedral nonlinear optical crystals CsGeBr₃.
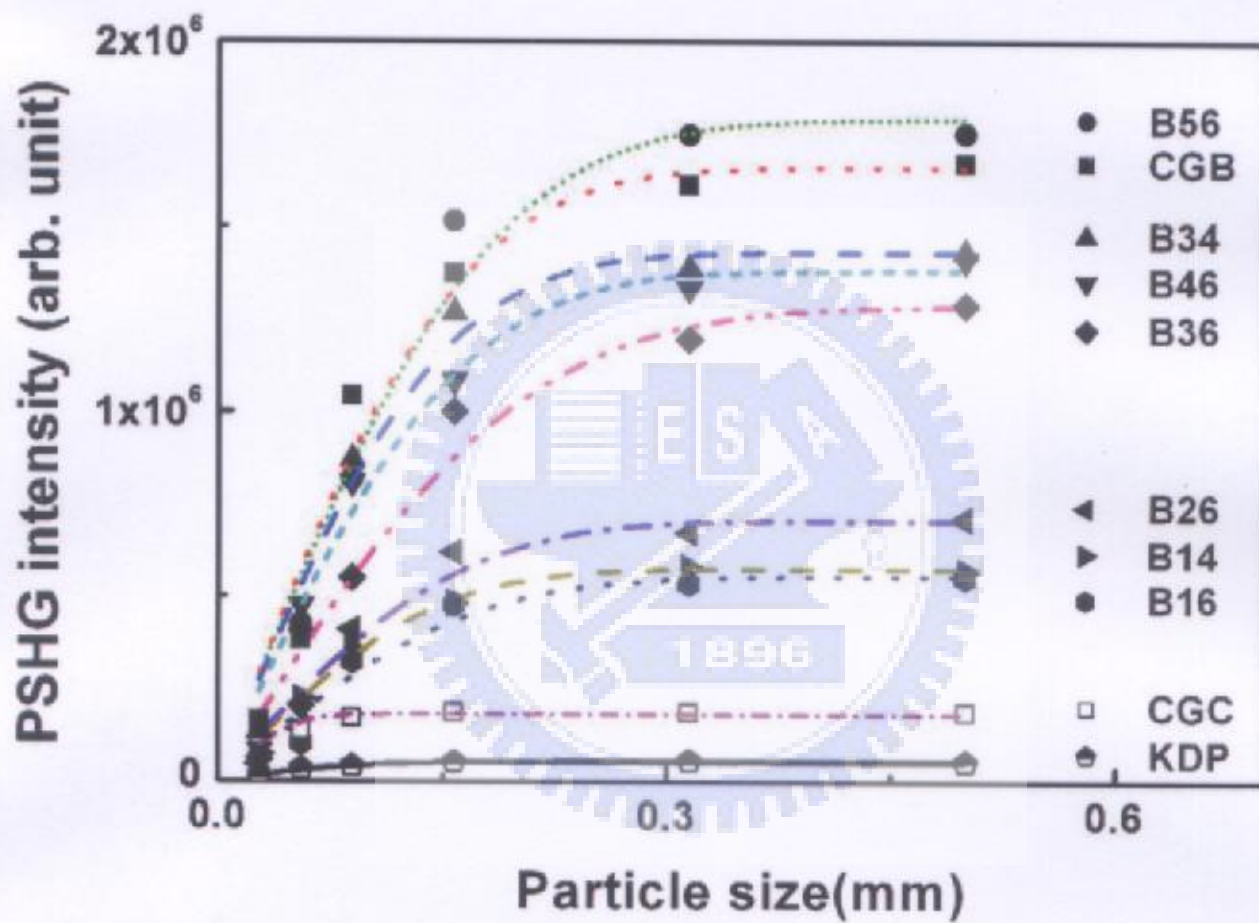
Fig. 6-6 The comparison of integrated powder second-harmonic generation intensity of nonlinear optical crystals KDP and $CsGe(Br_yCl_{1-y})_3$ (B-series).

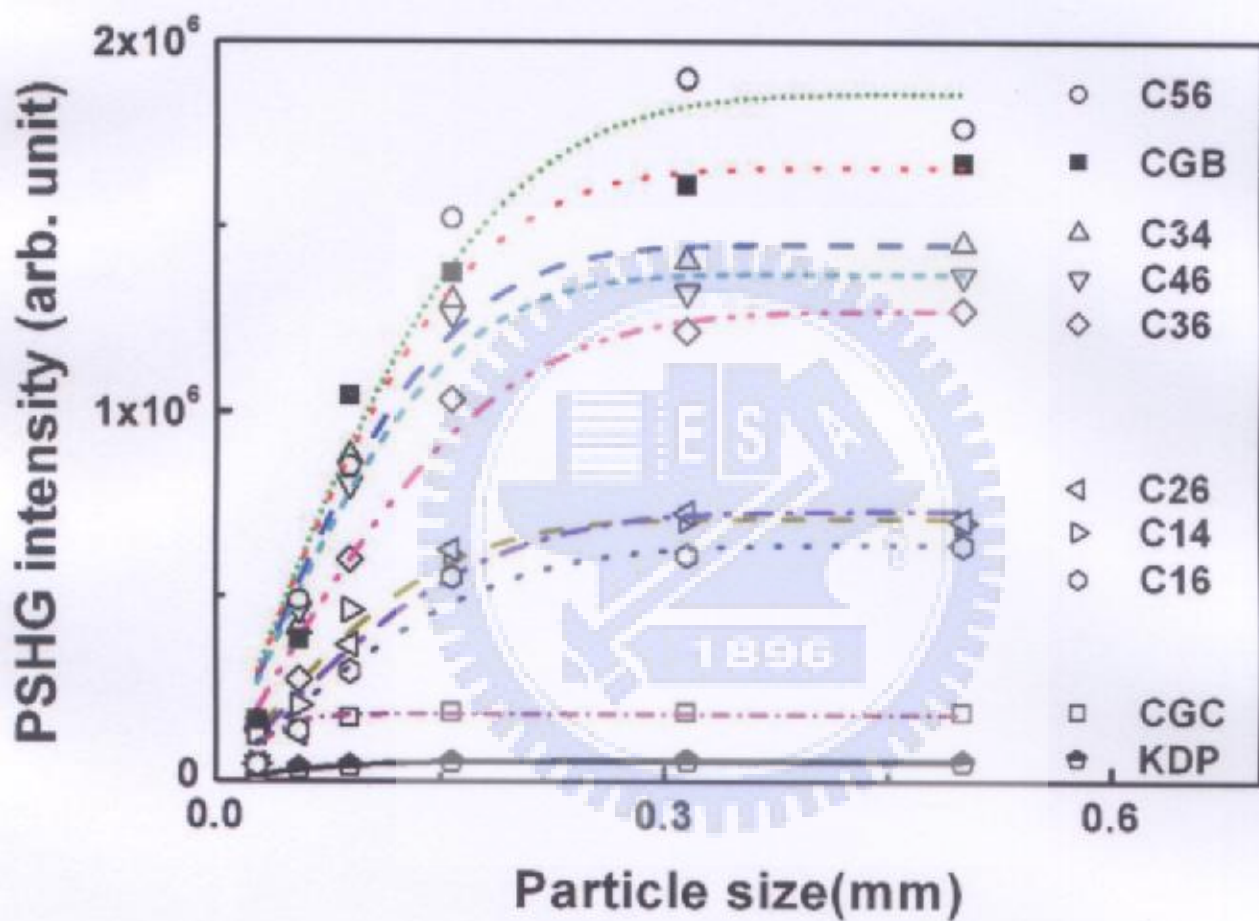Fig. 6-7 The comparison of integrated powder second-harmonic generation intensity of nonlinear optical crystals KDP and CsGe(Br$_x$Cl$_{1-x}$)$_3$ (C-series).
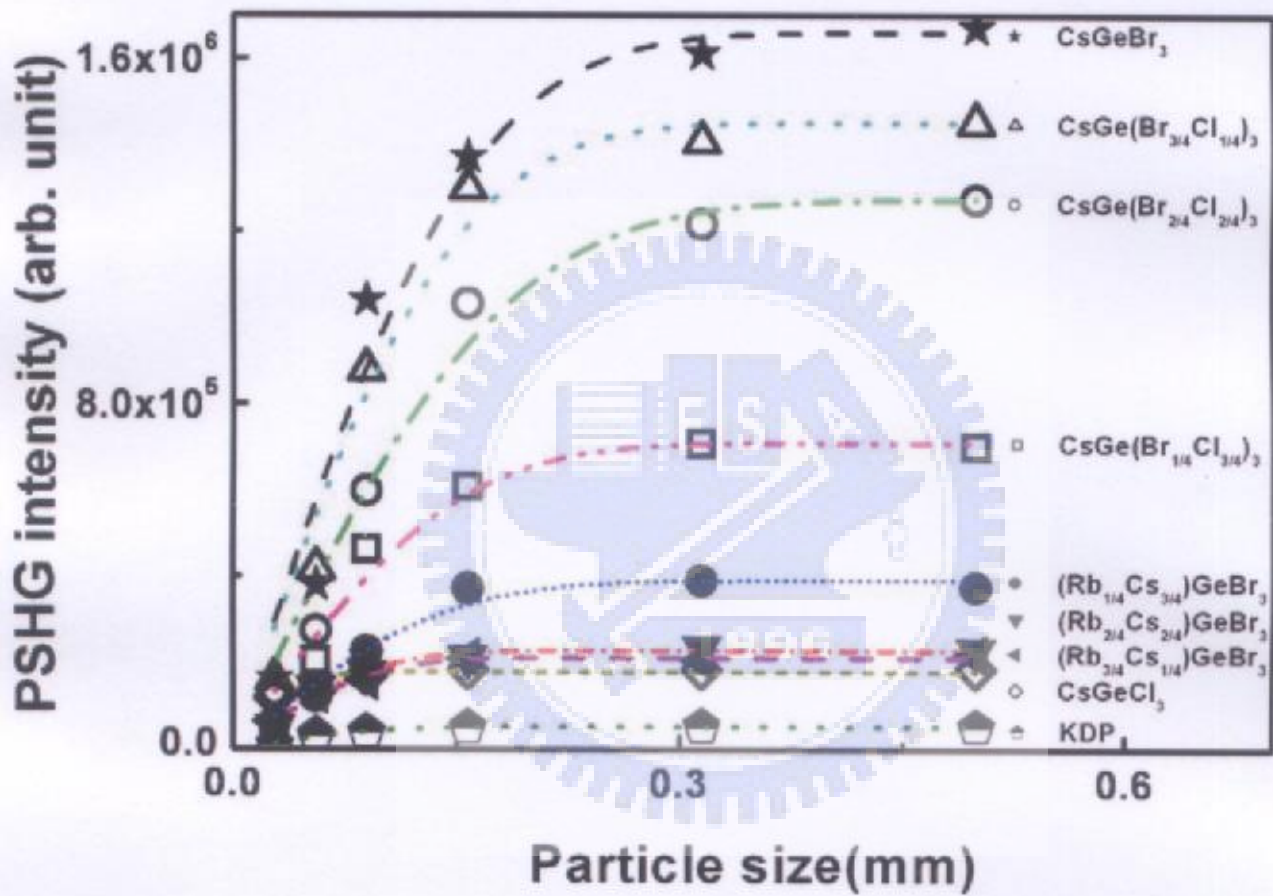
Fig. 6-8 The comparison of integrated powder second-harmonic generation intensity of nonlinear optical crystals KDP, $CsGe(Br_xCl_{1-x})_3$ and $(Rb_zCs_{1-z})GeBr_3$.
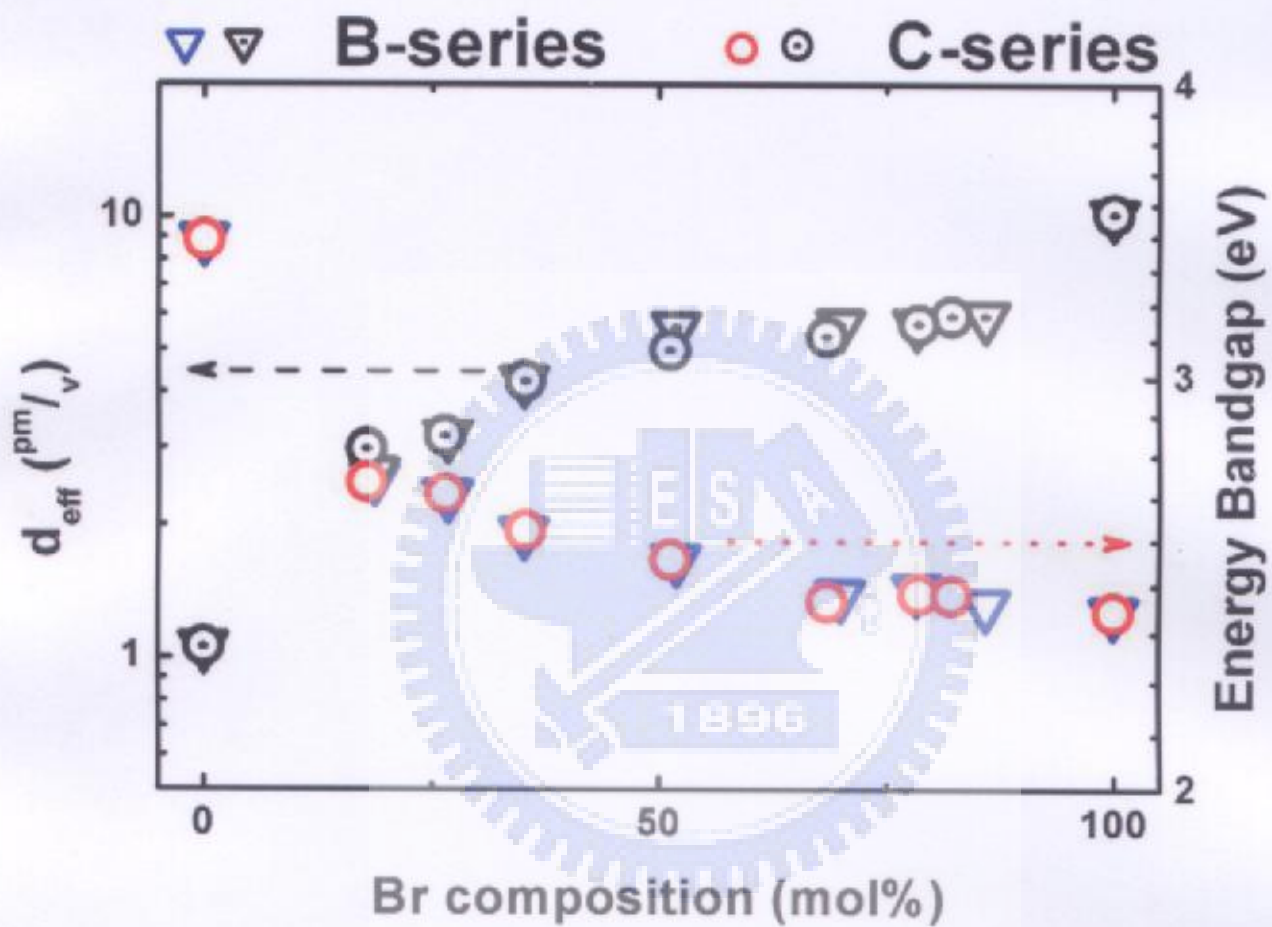
Fig. 6-9 The effective powder second-harmonic generation coefficients and their energy bandgaps of nonlinear optical crystals CsGe(Br$_x$Cl$_{1-x}$)$_3$.
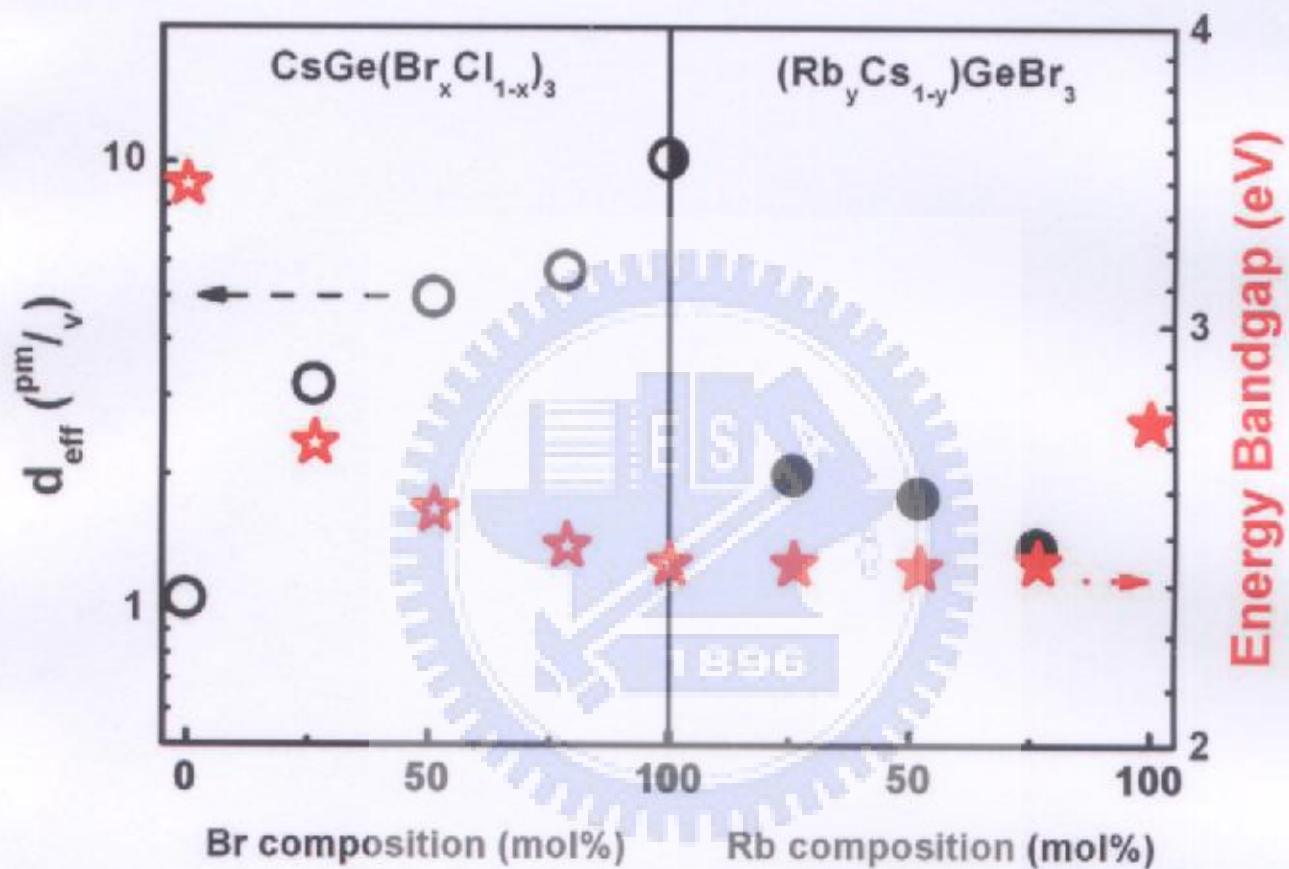
Fig. 6-10 The effective powder second-harmonic generation coefficients and their energy bandgaps of nonlinear optical crystals CsGe(Br$_x$Cl$_{1-x}$)$_3$ and (Rb$_y$Cs$_{1-y}$)GeBr$_3$.

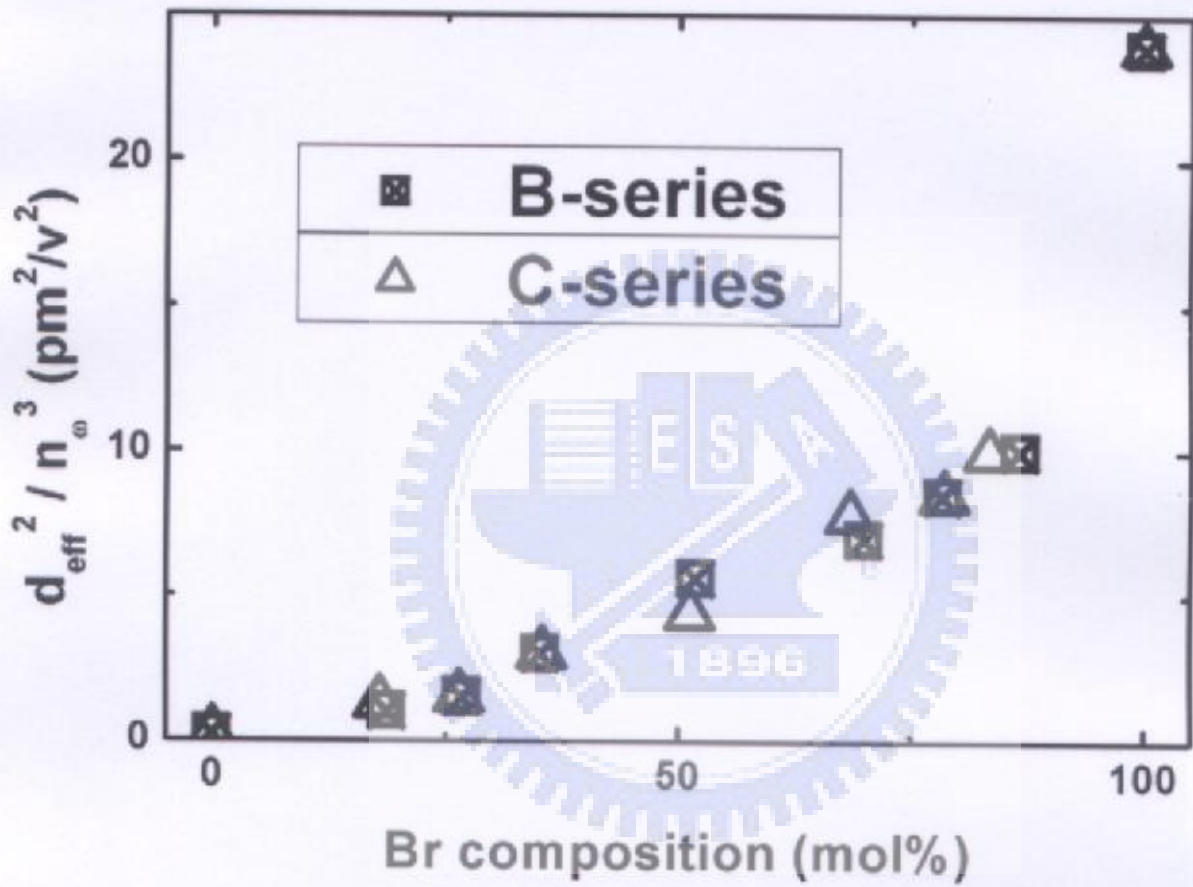Fig. 6-11 The nonlinearity of d_{eff}^2 / n_w^3 for nonlinear optical crystals $CsGe(Br_xCl_{1-x})_3$.

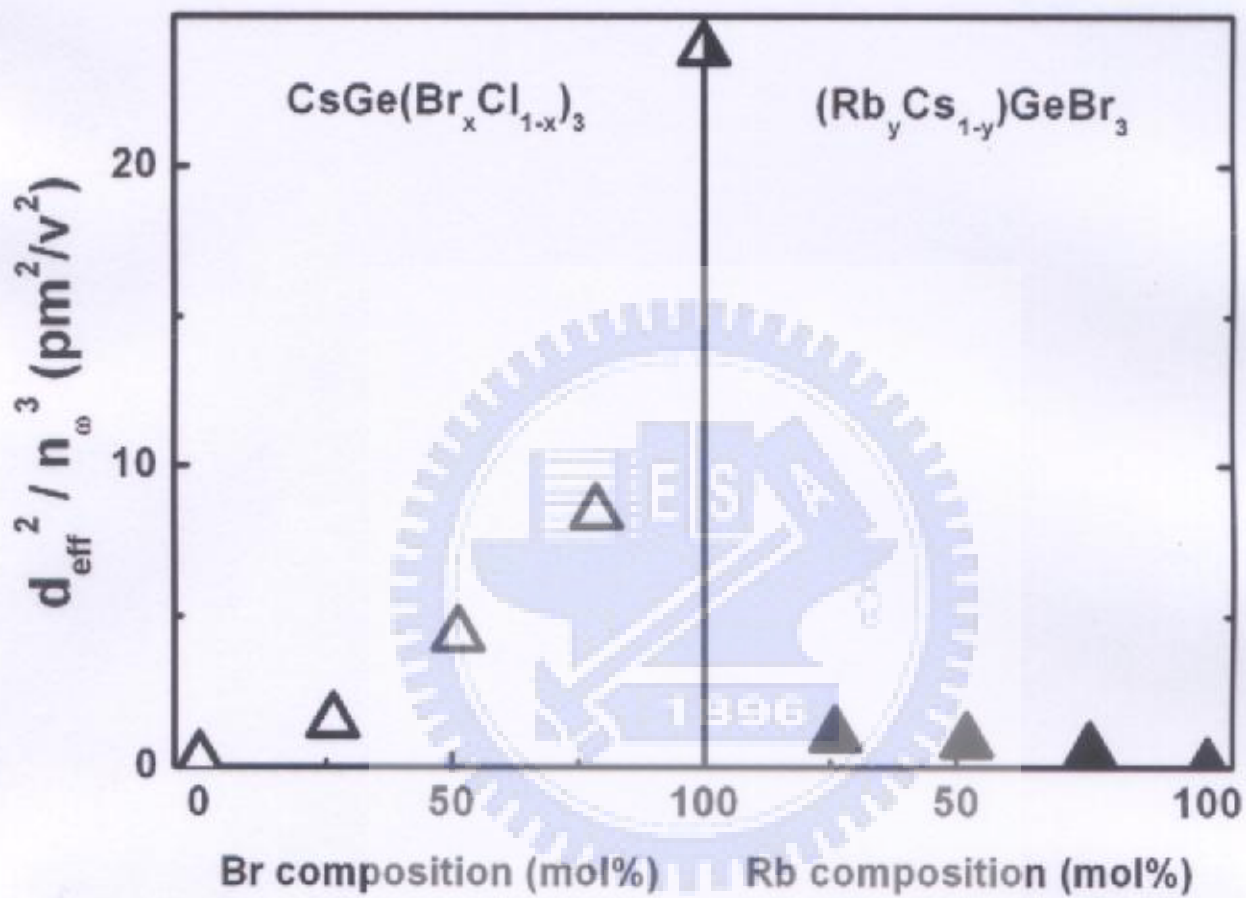Fig. 6-12 The nonlinearity of d_{eff}^2/n_ω^3 for nonlinear optical crystals CsGe(Br$_x$Cl$_{1-x}$)$_3$ and (Rb$_y$Cs$_{1-y}$)GeBr$_3$.

6.4 Reference

[6-1] A. Yariv, *Quantum Electronics* (John Wiley & Sons, New York, 1975).

[6-2] Y. R. Shen, *The Principles of Nonlinear Optics* (John Wiley & Sons, New York, 1984).

[6-3] A. Yariv and P. Yeh, *Optical Waves in Crystals* (John Wiley & Sons, New York, 1984).

[6-4] D. A. Kleinman, *Phys. Rev.* 126 (1962) 1977.

[6-5] J. F. Nye, *Physical Properties of Crystals* (Oxford Univ. Press, London, 1960).

[6-6] R. C. Miller, *Appl. Phys. Lett.* 1 (1964) 17.

[6-7] G. D. Boyd and D. A. Kleinman, *J. Appl. Phys.* 39 (1968) 3597.

[6-8] E. J. Lim, M. M. Fejer and R. L. Byer, *Electron. Lett.* 25 (1989) 174.

[6-9] S. K. Kurtz and T. T. Perry, *J. Appl. Phys.* 39 (1968) 3798.

[6-10] S. K. Kurtz, *IEEE J. Quant. Electr.*, QE-4 (1968) 578.

[6-11] W. K. Chen, C. M. Cheng, J. Y. Huang, W. F. Hsieh and T. Y. Tseng, *J. Phys. Chem. of Solids* 61 (2000) 969.

[6-12] J. P. Dougherty and S. K. Kurtz, *J. Appl. Crystallogr.* 9 (1976)

145.

[6-13] P. N. Prasad and D. J. Williams, *Introduction to Nonlinear Optical Effects in Molecules and Polymers* (Wiley, New York, 1991, chap. 6).

[6-14] L. C. Tang, J. Y. Huang, C. S. Chang, M. H. Lee and L. Q. Liu, *J. Phys.: Condens. Matter* 17 (2005) 7275.

[6-15] Y. R. Shen, *The Principles of Nonlinear Optics* (John Wiley and Sons, 2002).

Chapter 7   Conclusions

The core contribution of this work is the investigation of the growth of NLO crystals in mid- and far-infrared regions. Most studies have examined the structural, linear optical and nonlinear optical properties of the $AGeX_3$ (A = Rb, Cs; X = Cl, Br) crystals by varying the alloy composition to satisfy the demands of specific applications. Their results and discussions are summarized as follows.

In the analysis of components, bromine replaced chlorine in $CsGeCl_3$, and vice versa in $CsGeBr_3$ while cesium was substituted by rubidium in $CsGeBr_3$. According to thermal analysis, the Curie temperature and the melting temperature of the crystals rose with Br content, since the attraction between crystal and its outside electrons increased with the molecular weight which increases with Br content.

The structural analysis indicated that the lattice constant became increased with the amount of Br, while the cell angle decreased. Therefore, the structural distortion of $CsGe(Br_xCl_{1-x})_3$ (R3m) increases with Br content. In contrast, the lattice constant declined as the amount of Rb increased, while the cell angle became larger, revealing that the

structure of $(Rb_yCs_{1-y})GeBr_3$ slowly becomes centro-symmetric as Rb content increases. The results of Raman spectroscopy agree with the expectation based on effective-mass that the oscillation frequency increases as the Br content falls because Br is heavier than Cl. The atomic vibration modes of $AGeX_3$ (A = Rb, Cs; X = Cl, Br) system were also defined herein.

Regarding transparency characteristics, the longest infrared transparency wavelength is typically limited by the phonon absorption of the crystal and the absorption edge is limited by the energy band-gap of the crystal. UV-visible spectra show that the absorption edge declines from 3.43 to 2.38 eV with the composition of bromine (x = 0 to 1), but remains constant for y = 0 to 3/4. The infrared phonon absorption edge of $CsGe(Br_xCl_{1-x})_3$ with x = 0 to 1 is approximately from 30 to 47 μm. This result is consistent with the expectation based on the effective-mass concept, that the infrared transparency range of $CsGeBr_3$ is wider than that of $CsGeCl_3$ because the Br atom is heavier than Cl. Hence, the transmission range of the crystals increases with Br. Furthermore, the force constant increases as the Br content declines, such that the oscillation frequency increases as Br content decreases. The

photoluminence spectra revealed that the emission bands of $CsGe(Br_xCl_{1-x})_3$ and $(Rb_yCs_{1-y})GeBr_3$ were red-shifted as the temperature fell, because cooling reduced the lattice constant.

Detection of the generated second-harmonic of the powder demonstrates that all of the crystals, $CsGe(Br_xCl_{1-x})_3$ (x = 0, 1/6, 1/4, 2/6, 3/6, 4/6, 3/4, 5/6, 1) and $(Rb_yCs_{1-y})GeBr_3$ (y = 1/4, 2/4, 3/4), were phase-matchable. The structural distortion and the off-center Ge ion in the unit cell govern the SHG responses. The XRD results that the lattice constant increased with Br content while the cell angle decreased as Br increased. Therefore, the structural distortion of $CsGe(Br_xCl_{1-x})_3$ increases with Br content and the position of the B-site cation, Ge, becomes closer to the cell corner. However, $(Rb_yCs_{1-y})GeBr_3$ yields opposing results as the Rb content is increased. Hence, the nonlinearity properties increased with Br content, but fell as Rb content increased. This result is identical to that for PSHG, for which that second-order NLO susceptibility increased with Br content, but declined as Rb content increased.

The structural and optical properties of rhombohedral NLO $AGeX_3$ (A = Rb, Cs; X = Cl, Br) crystals were investigated experimentally to

elucidate the anion and cation substitution effect. Based on these results,

a linear increase in x of $CsGe(Br_xCl_{1-x})_3$ increased the lattice constant and

the second-order NLO susceptibility, but reduced the cell angle and

bandgap. Linearly increasing y in $(Rb_yCs_{1-y})GeBr_3$ yielded the opposite

results. Since the optical damage threshold and the range of transparency

of the materials are related to the magnitude of the band gap, while the

optical non-linearity is inversely proportional to the cubic power of the

band gap, the nonlinear susceptibility coefficient, energy bandgap, laser

damage threshold of halides can be modulated simultaneously by anion

substitution but not cation substitution.
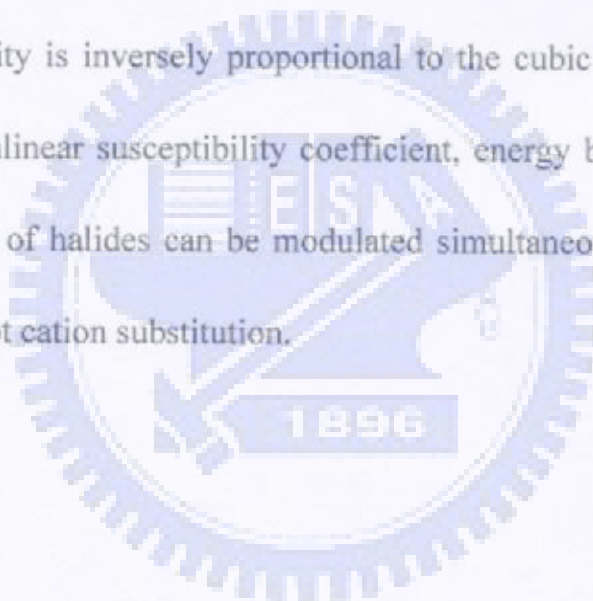
List of Publication

1. <u>Zhi-Guang Lin</u>, Li-Chuan Tang and Chang-Pin Chou, "*Infrared properties of CsGe(Br$_x$Cl$_{1-x}$)$_3$, nonlinear optical rhombohedral semiconductor*" Journal of Physics : Condensed Matter (accepted).

2. <u>Zhi-Guang Lin</u>, Li-Chuan Tang and Chang-Pin Chou, "*Study on Mid-IR NLO Crystals CsGe(Br$_x$Cl$_{1-x}$)$_3$*" Optical Materials (accepted).

3. <u>Zhi-Guang Lin</u>, Li-Chuan Tang and Chang-Pin Chou, "*Characterization and Properties of Novel Infrared Nonlinear Optical Crystal CsGe(Br$_x$Cl$_{1-x}$)$_3$*" Inorganic Chemistry (accepted).

4. <u>Zhi-Guang Lin</u>, Li-Chuan Tang and Chang-Pin Chou, "*Characterization and Properties of Infrared NLO Crystals: AGeX$_3$ (A=Rb, Cs; X=Cl, Br)*" Journal of Crystal Growth (accepted).

2006 SCI Journal Citation Reports

	Abbreviated Journal Title *(linked to journal information)*	ISSN	Total Cites	Impact Factor	Immediacy Index	Articles	Cited Half-life
1	**J PHYS-CONDENS MAT**	0953-8984	24227	**2.038**	0.378	1255	5.1
2	**OPT MATER**	0925-3467	2993	**1.709**	0.370	338	4.2
3	**INORG CHEM**	0020-1669	58002	**3.911**	0.699	1443	8.4
4	**J CRYST GROWTH**	0022-0248	19641	**1.809**	0.346	1012	6.5